CHARACTERISATION OF THE HEATING MECHANISMS IN A CAPACITIVELY COUPLED ARGON RF DISCHARGE

A thesis for the degree of
PHILOSOPHIAE DOCTOR

Presented to
DUBLIN CITY UNIVERSITY

By
CATHERINE M. DEEGAN, B.Sc.
School of Physical Sciences
DUBLIN CITY UNIVERSITY

Research Supervisors
Dr. D. Vender and Dr. M. Hopkins

External Examiner
Dr. G. M. W. Kroesen

July 1999

Declaration

I hereby certify that this material, which I now submit for assessment on the programme of study leading to the award of Philosophiae Doctor is entirely my own work and has not been taken from the works of others save and to the extent that such work has been cited and acknowledged within the text of this work.

Catherine M. Deegan

Catherine M. Deegan

25th July 1999

Acknowledgements

I would like to thank Professor Eugene Kennedy and the Physics department for their support of this work. Thanks also to my supervisors for the support and help they provided during this project. Thank you to Dr. Johnathan Goss for useful discussions and help during the later stages of the work. The technical aspects of this work were realised with the expert help of Alan Hughes and the DCU technical staff. I would also like to thank Bill Lanigan and the Maynooth technical staff for their assistance in the later stages of the project.

Thanks are also due to Dr. Garrard Conway for an interesting and rewarding collaboration. I am grateful to Professor Lawrence Overzet and his research group for the chance to work in an excellent laboratory. Special thanks to Jennifer Kleber and Marwan Khater for their hospitality and assistance while visiting the University of Texas at Dallas. I am indebted to Richard and Martha Dinwiddie for their hospitality and friendship during my stay and since.

Many thanks to the Markhams for their kind support and encouragement over the past few years, in particular Margaret for typing much of the text in this thesis and Edward for proof-reading the thesis. Special thanks are due to Charles for assistance on aspects of the experimental work and the thesis itself. I am also grateful to Seamus Boyle for sound advice.

Thanks to Colette, Frances and Kate for their unrelenting support over the last few years. Last but not least, to my family for always being there.

Dedicated to

Christopher and Kathleen

-my parents

Charles

-my champion

Contents

Abstract

A capacitively coupled rf plasma is investigated in the context of the heating mechanisms that sustain it under various conditions. These mechanisms are critically dependent on gas pressure, applied rf potential, rf current and discharge gap. Pressure ranges of 10 to 300 mTorr and rf potentials from a few Volts to several hundred Volts are investigated.

The argon plasma is generated in two capacitively coupled rf systems. Plasma parameters are measured using a Langmuir probe. A microwave interferometer is used to compare density measurements with that of the probe. A current voltage monitor is used to measure the voltage, current and phase for the purpose of relating the control parameters to the plasma parameters. The design and construction of a retarding field energy analyser is presented. Plasma potential measurements using the analyser are compared with that of the Langmuir probe. Use of the analyser in electron collection mode has revealed a higher electron temperature behind the rf sheath than that measured by the Langmuir probe in the plasma.

Transitions in the heating modes are investigated via plasma parameter and Electron Energy Probability Function (EEPF) measurement in the centre of the discharge. Particular attention is paid to the α-γ transition. The relationship between the current voltage characteristic and the plasma parameters is considered. Pressure effects on the transition are determined.

A model of the diffusion process in the capacitive rf discharge is devised and the resulting density profiles checked against known analytic solutions of the diffusion equation. A procedure to extract the ionisation profiles from experimental density measurements is devised using this model and a reconstruction algorithm. The two-dimensional evolution of density and ionisation profiles is presented at low and high discharge powers over the 10 mTorr to 300 mTorr range. The total ionisation rate is compared with the theoretical ionisation rate calculated using simple particle balance equations. Disagreement in the ionisation rates is attributed to the use of unrealistic models and the assumption of uniform electron energy in the discharge.

Spatially resolved EEPF measurements are made along the discharge axis. Rate coefficients for ionisation are calculated by integrating the product of the measured EEPF and the cross section for ionisation. Spatially resolved ionisation rates obtained from the coefficients are in good agreement with the measured ionisation rate profiles generated using the diffusion model and reconstruction algorithm.

List of Figures

List of Symbols

A	Sheath area, (m)
α	Recombination coefficient, (s^{-1})
A_e	Surface area of electrode, (m^2)
A_{eff}	Effective loss area, (m^2)
A_p	Surface area of probe, (m^2)
B	Generation rate, ($m^{-3}s^{-1}$)
C	Capacitance, (F)
c	Speed of light, (ms^{-1})
D	Diffusion coefficient, (m^2s^{-1})
D_A	Ambipolar diff. coefficient, (m^2s^{-1})
D_e	Electron diffusion constant, (m^2s^{-1})
E	Electric field, (Vm^{-1})
ε	Electron energy, (eV)
ξ	Position of electron, (m)
ε_0	Permitivity of free space, (Fm^{-1})
ε_{iz}	Ionization energy, (eV)
E_A	Ambipolar field, (Vm^{-1})
e	Charge on electron, (C)
$f(\varepsilon)$	EEDF, ($cm^{-3}eV^{-1}$)
$F(\varepsilon)$	EEPF, ($cm^{-3}eV^{-3/2}$)
G	Density gradient, (m^{-4})
G	Particle generation rate, ($m^{-3}s^{-1}$)
Γ	Particle flux, ($m^{-2}s^{-1}$)
h	Attachment coefficient
I_c	Collector current, (A)
I_e	Probe current $V>V_p$, (A)
I_{eret}	Electron retardation current, (A)
I_{esat}	Electron saturation current, (A)
I_{eth}	Electron thermal current, (A)
I_i	Probe current $V<<V_p$, (A)
I_{isat}	Probe Ion Saturation Current, (A)
I_{ith}	Ion thermal current, (A)
I_{probe}	Probe current, (A)
J	Conductivity, ($\Omega^{-1}m^{-1}$)
κ	Complex Dielectric Constant
χ	Probe potential term
χ_{01}	First zero of $J_0(x)=2.405$
K_{iz}	Ionization rate constant, ($m^{-3}s^{-1}$)
k	Boltzmanns constant, (JK^{-1})
k	Phase per unit length, ($rad.m^{-1}$)
k	Rate constant, (m^3s^{-1})
L	Length of plasma, (m)
λ	Mean free path (elastic col.), (m)
λ_ε	Energy relaxation length, (m)
λ^*	Mean free path (inelastic col.), (m)
λ_D	Debye length, (m)
λ_{ionis}	Electron ionisation mfp, (m)
λ_{mfp}	Mean free path, (m)
l	Probe length, (m)
M	Ion Mass, (kg)
m,m_e	Mass of an electron, (kg)
N	Refractive index
ν	Collision frequency, (s^{-1})
ν_a	Attachment collision frequency, (s^{-1})
ν_{ee}	Electron electron collision freq., (s^{-1})
ν_{ei}	Electron ion collision frequency, (s^{-1})
ν_{en}	Electron neutral collision freq., (s^{-1})
ν_{ii}	Ion ion collision frequency, (s^{-1})
ν_{in}	Ion neutral collision frequency, (s^{-1})
n	Number of particles
n_c	Cut off density, (m^{-3})
n_e	Electron density, (m^{-3})
n_{e0}	Electron density, (m^{-3})
n_g	Neutral gas density, (m^{-3})
n_i	Ion density, (m^{-3})
n_{io}	Ion density, (m^{-3})
n_s	Density at sheath edge, (m^{-3})
P	Power, (W)
ϕ	Phase difference (degrees)
φ	Potential, (V)
pD	Pressure-gap product, (mTorr.cm).
R	Chamber radius, (m)
ρ	Charge density, (m^{-3})
R_e	Plasma ground resistance, (Ω)
R_p	Probe sheath resistance, (Ω)
R_{series}	Probe series resistance, (Ω)
S	Microwave signal, (Watts)
$<\sigma v>$	Rate constant, ($m^{-3}s^{-1}$)
$\sigma(\varepsilon)$	Relevant cross section, (m^2)
σ_{ionis}	Ionisation cross section, (m^2)
σ_{iz}	Ionization cross section, , (m^2)
s	Sheath width, (m)
T	Temperature (K)
τ	Decay time constant, (s^{-1})
T_0	Period of wave, (s)
T_e	Electron temperature (eV)

T_{elow}	Temperature of low energy electron group, (eV)
T_i	Ion temperature, (eV)
T_t	Time, (s)
μ	Particle mobility, ($m^2V^{-1}s^{-1}$)
μ_e	Electron mobility, ($m^2V^{-1}s^{-1}$)
u_B	Bohm velocity, (ms^{-2})
V	Discharge volume, (m^3)
V	potential, (V)
V	Probe bias voltage, (V)
ν_{en}	Electron neutral collision frequency, (s^{-1})
V_0	Sheath potential, (V)
V_c	Collector potential, (V)
V_d	Discriminator potential, (V)
V_{det}	Microwave detector output, (V)
V_p	Plasma potential, (V)
V_r	Electron reflected velocity, (m)
V_r	Repeller potential, (R)
V_s	Supressor potential, (V)
$v(\varepsilon)$	Electron velocity, (ms^{-2})
v_e	Mean electron velocity, (ms^{-2})
v_s	Ion acoustic velocity, (ms^{-2})
v_s	Sheath velocity, (ms^{-2})
W	Width of layer, (m)
ω	Microwave frequency, (radians s^{-1})
ω_p	Plasma frequency, (radians s^{-1})
ω	Frequency, (radians s^{-1})
x	Position, (m)
Z	Chamber length, (m)
Z	Impedance, (Ω)

Introduction

Plasma–aided manufacturing encompasses a vast range of industrial applications. It has a direct impact on the world economy in virtually every aspect of high technology industry. Capacitively coupled glow discharges are the most commonly used in industry for semiconductor fabrication. A comprehensive, quantitative understanding of these discharges is required to optimise plasma processes. By combining precise experimental measurements with standard models of plasma processes it is possible to characterise the behaviour of a discharge.

At low pressures the presence of charged particles in the plasma is the most important characteristic used in manufacturing. A discharge reaches the steady state when the charged particle production is balanced by the charged particle loss. The primary generation process in rf plasmas is electron impact ionisation. As the process has an energy threshold, the determination of the dominant heating mechanism of the plasma electrons is an important aspect of rf discharge research.

The aim of this thesis is to describe a systematic experimental investigation of the primary heating mechanisms in capacitive radio frequency (rf) plasmas. Chapter 1 is an introduction to rf plasmas, their uses, types and properties. Some relevant experimental diagnostic techniques are reviewed. A discussion of the heating mechanisms and the loss processes characteristic of the capacitive rf discharge is included.

Chapter 2 describes the experimental systems and the theory and operation of the diagnostics used. The primary diagnostic here is a tuned Langmuir probe. A retarding-field energy analyser and microwave interferometer are included as supplementary diagnostics. Results are presented to demonstrate the reproducibility and reliability of the Langmuir probe. In addition, comparisons between the diagnostic methods are made. The remainder of the thesis presents the experimental results and comparisons with model calculations where appropriate.

An investigation of the transitions in heating mechanisms is presented in Chapter 3. Particular attention is paid to the transition from ohmic to secondary electron dominated heating, the so-called α-γ transition. The effect of pressure on the transition is examined.

The plasmas investigated in this thesis are diffusion dominated for most of the pressure and density ranges used. Ambipolar diffusion is assumed to be the primary loss mechanism. Chapter 4 discusses ambipolar diffusion and one and two-dimensional models are devised to examine the process in a cylindrical geometry relevant to the experimental system used in this work. A procedure is devised using the diffusion model and a reconstruction algorithm to acquire the ionisation source distribution from the experimental density measurements.

Chapter 5 details spatially resolved measurement of plasma parameters in argon. The potential and temperature distributions are presented. To further examine the operating regimes, the charge density profiles are used to determine the ionisation profiles in two dimensions using the numerical method developed in Chapter 4. The ionisation rates obtained from experiment are compared with that of simple particle balance calculations.

Chapter 6 describes spatially resolved EEPF measurements made in all three of the heating regimes and compares density determinations from the EEPF and the ion and electron saturation current. The rate constant for ionisation is obtained by numerically integrating the measured EEDF with the relevant ionisation cross section. The corresponding ionisation rate is then compared with that obtained using the inverse method.

A summary of the main findings and suggestions for further work are included in the final section.

Chapter 1

Introduction to RF Plasmas

1.1 Plasma Processing

In the past, plasma research was mainly directed towards the achievement of controlled fusion; other applications have been as diverse as flames in combustion devices and plasmas in gas lasers, in high current ion sources, or in microwave power sources. More recently, plasmas have been harnessed for material processing, exploiting the capability of energetic plasma charges for removal (etching), deposition or implantation when exposed to material surfaces.

Low pressure, non-equilibrium, weakly ionised gas discharge plasmas are used for a variety of surface materials processing applications. The most extensive applications are in microelectronics manufacturing, where plasma sputtering, etching, stripping, cleaning and film deposition play key roles in this growing industry [1-3]. It has been estimated that up to 30% of all process steps in the manufacture of integrated circuits involve plasmas [4]. For example, in the process of depositing and patterning aluminium interconnects. The first step is to deposit the aluminium film by sputtering. Then, a polymer film (photoresist) is deposited and exposed. The elimination of the exposed regions is increasingly done with plasmas (replacing development with a liquid). Plasma etching of aluminium follows development. Finally, the resist is stripped with an O_2 plasma [3].

The drive to manufacture ever-smaller devices is largely responsible for the great interest in plasma processing. From the early 1970's to the 1990's the minimum device dimension dropped from 6μm to less than 1μm. This is attributable to the use of plasma etching, as this process is capable of removing material anisotropically. This makes possible the etching of features that cannot be done by liquid etchants. When device features are relatively large, the structures have a relatively small aspect ratio (height to width ratio). Wet chemical etchants etch isotropically. This results in an undercut of the mask, but as long as the feature device ratio is small this undercutting may be tolerated. However, as feature minimum dimensions are decreasing (to allow move devices per chip and hence reduce cost), the undercutting process is no longer acceptable and the anisotropic etch achievable with plasmas is essential. This point is illustrated in figure 1.1.

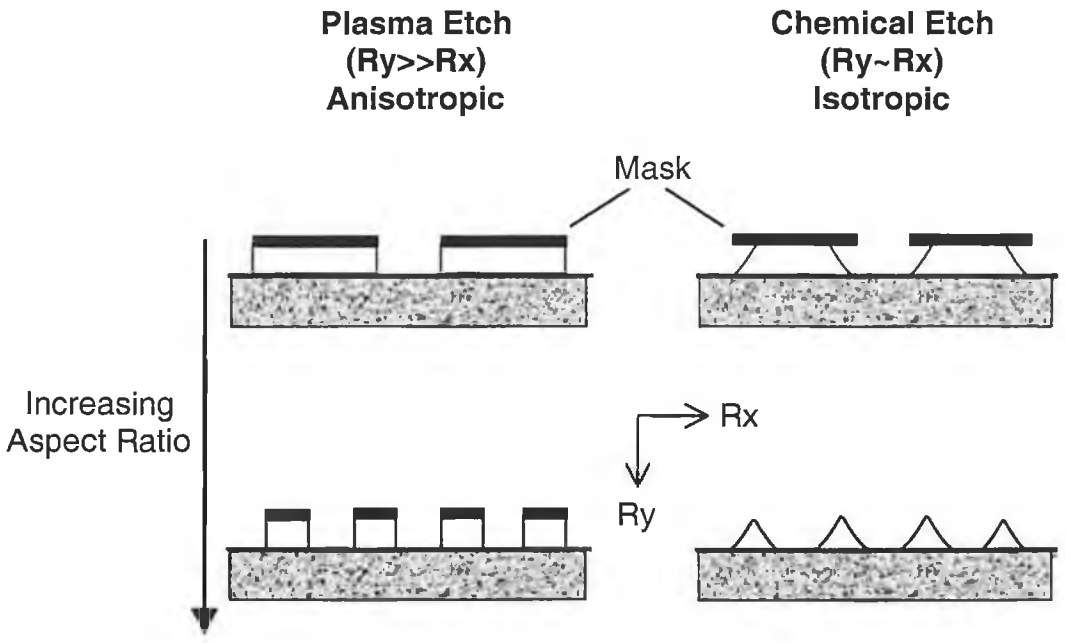

Figure 1.1: Illustration of the advantage of plasma etching over chemical, "wet" etching. When the aspect ratio is small, isotropic etching from the chemical process is acceptable. When the feature size decreases and the aspect ratio increases, anisotropic etching using plasmas becomes essential.

Plasma-based processes have other advantages. Because plasmas are gaseous, the mass of waste products generated during processing is considerably less than for liquid processes. Another advantage is that if all processes are kept "dry", wafers may remain in vacuum and be less susceptible to contamination. This simplifies automated wafer handling.

1.2 Radio Frequency Plasmas

Introduction

In most industrial applications, high frequency power supplies drive plasma processes. DC glow discharges suffer disadvantages such as lack of spatial uniformity and low discharge current densities. DC discharges are sustained by secondary electron emission that depends on electrode surface composition. This can lead to undesirable process variations [5,6]. Radio frequency generated plasmas are more often used in industry as they may be operated at lower pressures. They have the ability to etch or sputter insulating surfaces. Radio frequency discharges are also more efficient at promoting ionisation and sustaining the discharge. For a set pressure, the impedance of a discharge decreases with increasing frequency, so for a given voltage, more current may be driven through the discharge [5,7].

1.2.1 Capacitively Coupled Discharges

The most commonly used reactor today is the capacitively coupled rf discharge. The frequency of operation is usually 13.56MHz, a standard industrial frequency that was chosen to avoid interference with broadcasting and communications bands. Simple schematics of conventional, capacitively coupled sources are shown in figure 1.2. Generally, one electrode is driven and the other is at ground potential. A system is termed asymmetric if the electrodes are of uneven area; usually the electrodes are of similar size while the walls of the chamber are at ground potential. In practice, the walls are electrically connected to the ground electrode producing an asymmetric configuration.

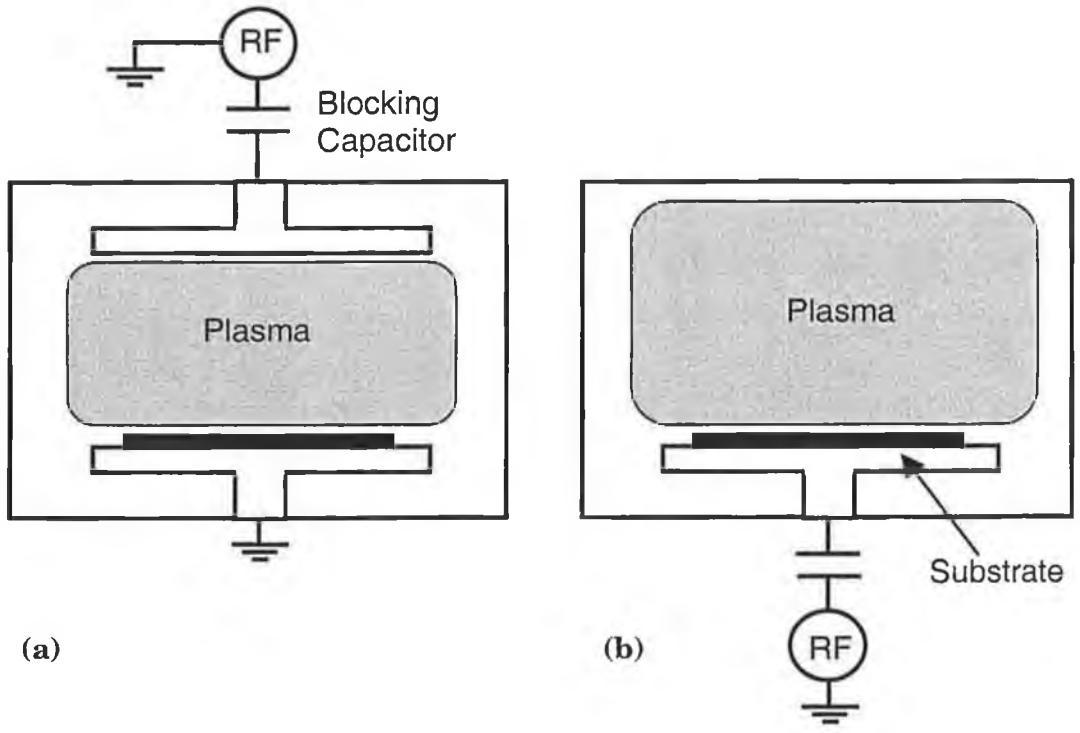

Figure 1.2: Schematic of (a) a typical plasma etching source, substrate on ground electrode and (b) a 'reactive ion etching' (RIE) system where the self-bias on the powered electrode increases the ion impact energy on to the substrate.

The plasmas studied in this thesis are not in thermodynamic equilibrium, the electrons have a temperature of approximately 3 eV (23,000K) while the ions and neutrals are in equilibrium, approximately 300K. The electrons, with their higher mobility and higher energy, will leave the plasma more rapidly than the ions and so to conserve quasineutrality, positive space-charge sheaths form between the walls and the plasma. In radio frequency plasmas, these sheaths have a capacitance of $\varepsilon_0 A/d$, where A is the electrode area and d is the sheath width. In the case of symmetric discharges, the electrode areas are equal. This results in the rf voltage being dropped equally across

both sheaths. Therefore, there is an equal ion bombardment of both electrodes. In the case of asymmetric discharges the powered electrode is usually smaller than the ground electrode. This means that the capacitance of the powered electrode is much less than the capacitance of the ground electrode. The voltage dropped across the powered sheath is much greater than the voltage across the ground sheath.

The electrons have a much greater mobility than the ions due to their smaller mass and so more leak out of the system during the first few rf cycles. Placing a blocking capacitor on the powered electrode prevents the electrons leaving the system altogether so a net negative charge builds up on the powered electrode. This is the dc self-bias on the powered electrode that impedes the electron flow and accelerates the ions to the electrode, so the total charge flow per cycle sums to zero [5,8,9]. The dc bias is of the order of $-V_{RF}/2$ and results in highly energetic ion bombardment of the powered electrode.

This self-bias is observable by considering a simple equivalent-circuit model of a capacitively coupled discharge; see figure 1.3(a) [5,10,11]. The application of an ac voltage to the powered electrode end of the circuit (waveform (i)) results in the formation of a negative dc bias (waveform (ii)) on the powered electrode. Equivalent circuit models have been used by several authors to aid the understanding of capacitively coupled plasmas [9,12-14].

A plot of the dc bias *versus* applied rf potential is shown in figure 1.4 for the capacitive system described in section 2.2, Chapter 2. The dc bias *versus* rf potential is linear over a range of input powers (10 to 100 Watts). The dc bias increases with rf potential because initially, more electrons leave the system via the powered electrode with increasing applied potential. The dc bias increases to balance this and to maintain the net charge flow at zero. At the same rf potential but at a lower pressure, the dc bias is observed to increase in both experiment and simulations [14,15]. This is due to the reduced confinement of the discharge at lower pressures, more current flows to the grounded walls so a larger dc bias is required to maintain a zero net current.

The primary limitation of the capacitively coupled reactors shown in figure 1.2. is that the bombarding ion flux and corresponding ion energy may not be independently varied. This is because in order to increase the ion flux, the rf voltage is raised, but this also raises the plasma potential that simultaneously raises the ion energy impacting the substrate. This can result in damage to the substrate. There are two solutions to this problem currently used in plasma processing [3,11]. The first, pictured in figure 1.5(a),

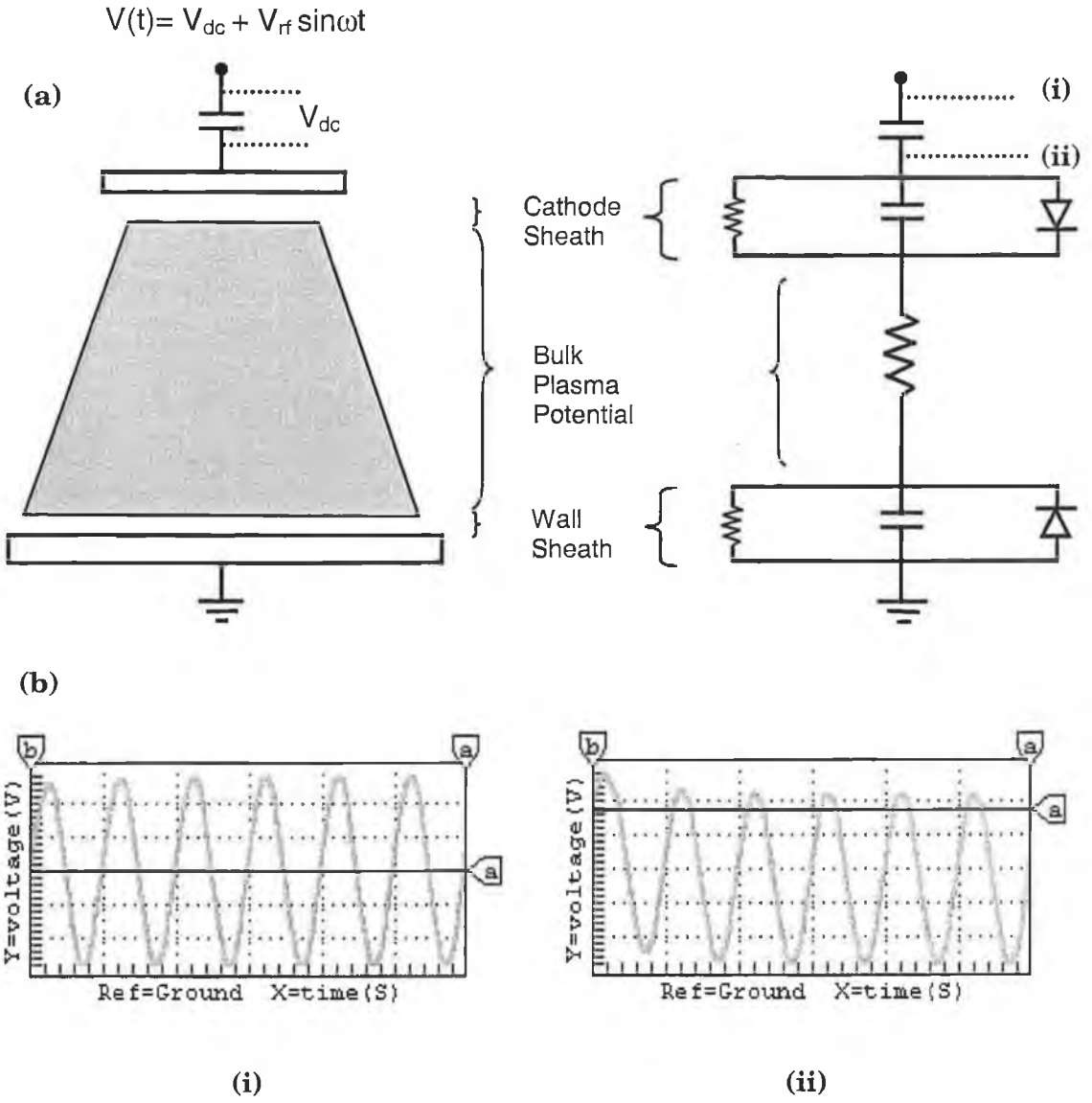

Figure 1.3: (a) Simple equivalent circuit of a capacitively coupled rf system. The plasma is primarily resistive. The sheaths are mainly capacitive but losses due to ion acceleration are accounted for using small impedances. The sheath rectifies the convection current flowing through it due to the disparity in electron and ion mobilities.
(b) Development of the dc bias in an rf system. Waveform (i) is the applied rf signal; waveform (ii) is the RF signal on the powered electrode. A negative dc bias forms after a few rf cycles. Circuit model and waveforms produced using PSPICE.

uses a magnetic field, applied parallel to the powered electrode and slowly rotated in the plane of the wafer. The magnetic field increases the efficiency of power transfer from source to plasma and aids plasma confinement. This results in a reduced sheath voltage and increased plasma density at lower gas pressures. A second option, figure 1.5(b), is a triode system, where a second rf electrode is incorporated to increase the plasma density independently of the driving potential. A variation on this system would be to place the substrate on the ground electrode and using a second rf source to bias the electrode [11].

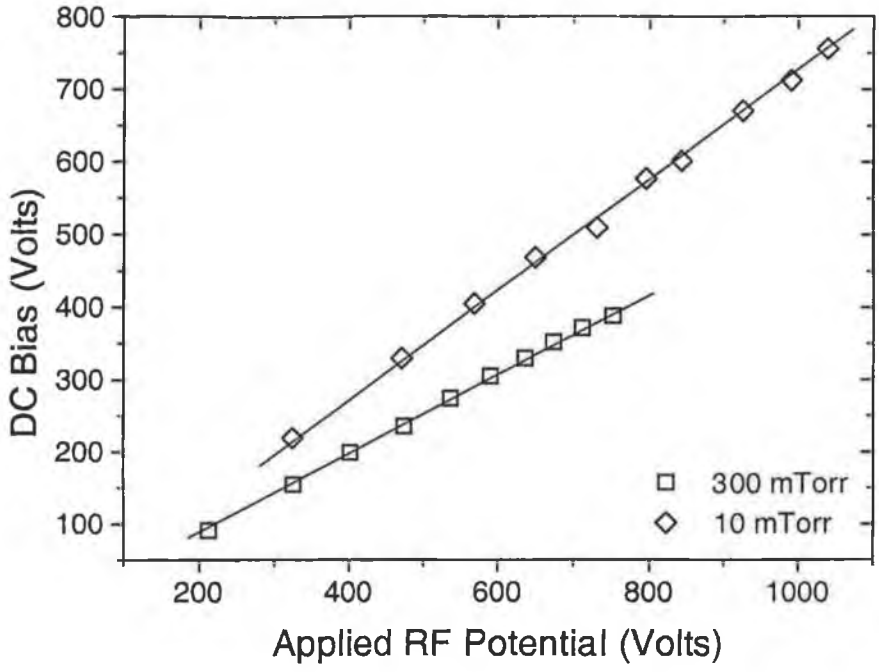

Figure 1.4: DC bias measurements on a capacitively coupled system.

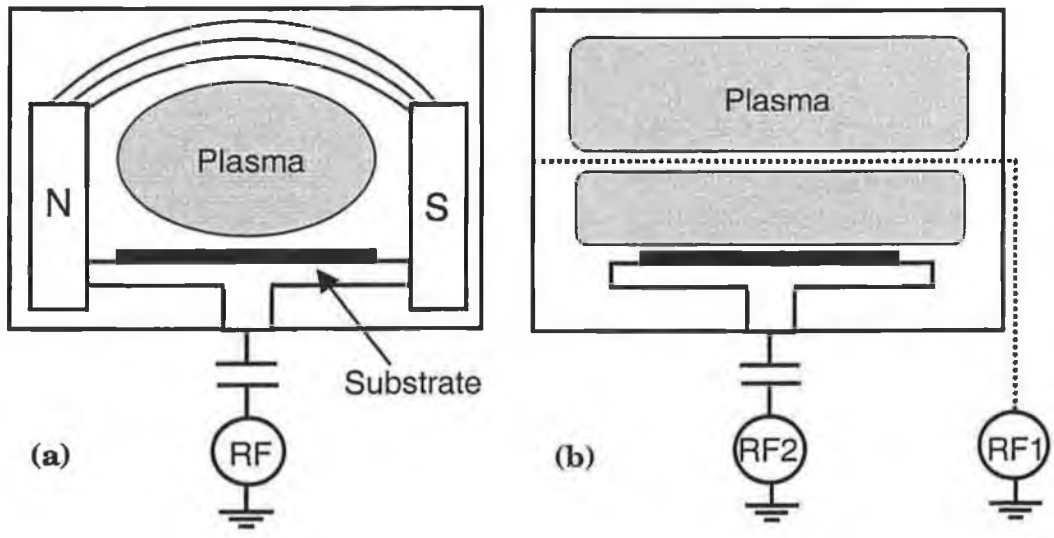

Figure 1.5: Schematic of (a) a magnetically enhanced ion etcher (MERIE) and (b) a triode configuration. RF1 maintains plasma density while RF2 changes the substrate self-bias potential.

1.2.2 Low Pressure, High Density Sources

Many other configurations have been applied to plasma processing. The undesirable high sheath voltage in capacitive plasmas has resulted in the development of new sources in which the rf power is coupled to the plasma across a dielectric rather than by direct connection to the plasma. This has the advantage that the non-capacitive coupling results in low voltages across the sheaths at the electrodes and walls. The

usual method of controlling bombarding ion energy is to independently bias the substrate holder, while the high densities required are generated by the source power. A great deal of interest is being shown in the use of inductively coupled plasmas for this reason [16-19]. Several types of coil design are possible, the most common design from an industry point of view is the flat spiral coil, see figure 1.6. RF power is supplied to the coil through a matching network. The plasma is excited by the induced rf electric field. Capacitive coupling is eliminated (if required) by placing a Faraday shield between the coil and the plasma. This type of coupling results in sheath voltages of the order of the mean energies of the electrons. This type of configuration produces a more uniform ion density near the substrate surface that results in a more homogeneous etch process [20].

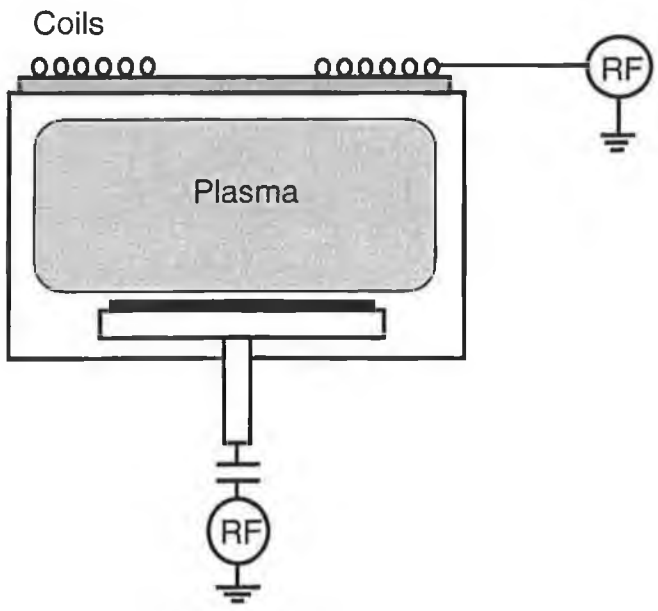

Figure 1.6: Schematic of a planar inductively coupled plasma etching tool.

An example of a source used commercially is the Hitachi Electron Cyclotron Resonance (ECR) reactor [3]. The basic source design is shown in figure 1.7. A magnetron microwave source operating at 2.45GHz transfers power to the plasma chamber. Solenoid coils around the cylindrical source generate an axially varying dc magnetic field. A separate rf bias at the substrate controls the ion energy to the substrate.

Another relatively new source design is the helicon source, a schematic of which is shown in figure 1.8 [21]. Helicon wave modes are excited by an rf antenna and propagate along the axial magnetic field. The substrates are typically placed downstream of the source in a plasma that is confined by permanent magnets. The most complete theory of helicon propagation and absorption has been given by Chen [22,23].

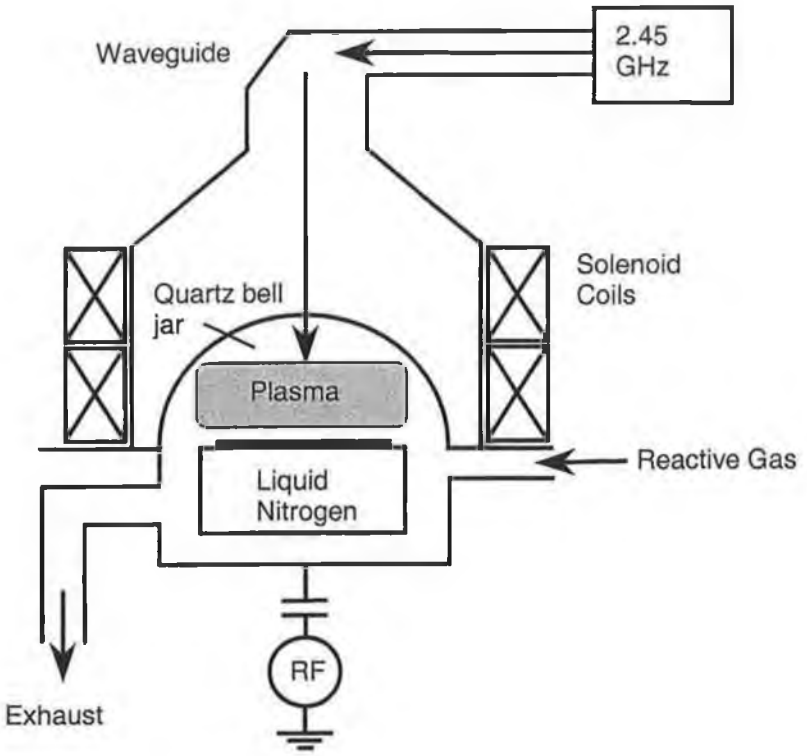

Figure 1.7: Schematic of the Hitachi electron cyclotron resonance tool.

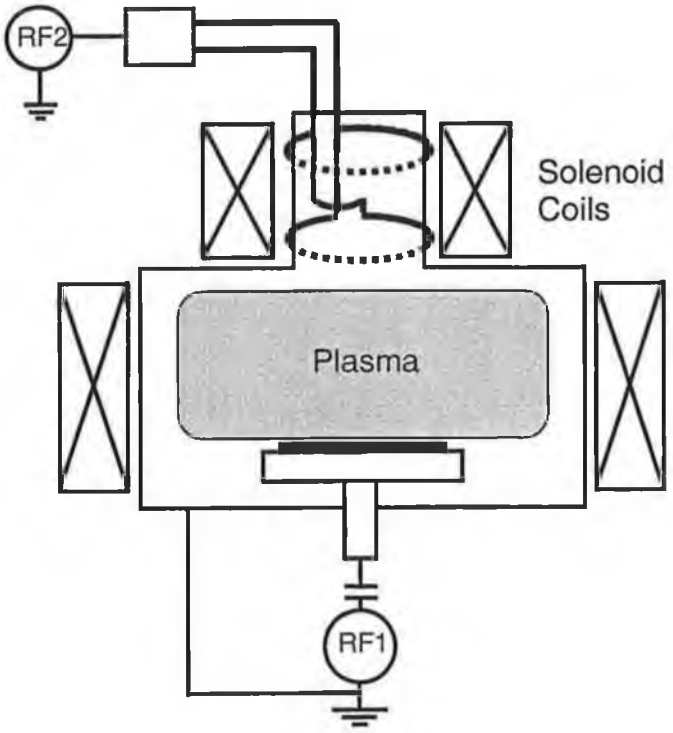

Figure 1.8: Helicon source. The rf antenna at the top launches a helicon wave in the magnetised plasma.

Other high-density sources include the helical resonator which is a variation on the inductively coupled plasma, see figure 1.9. An rf coil is placed around a dielectric tube but does not require a magnetic field. A grounded co-axial shield around the tube can set up a resonant system that efficiently couples power to the plasma [24].

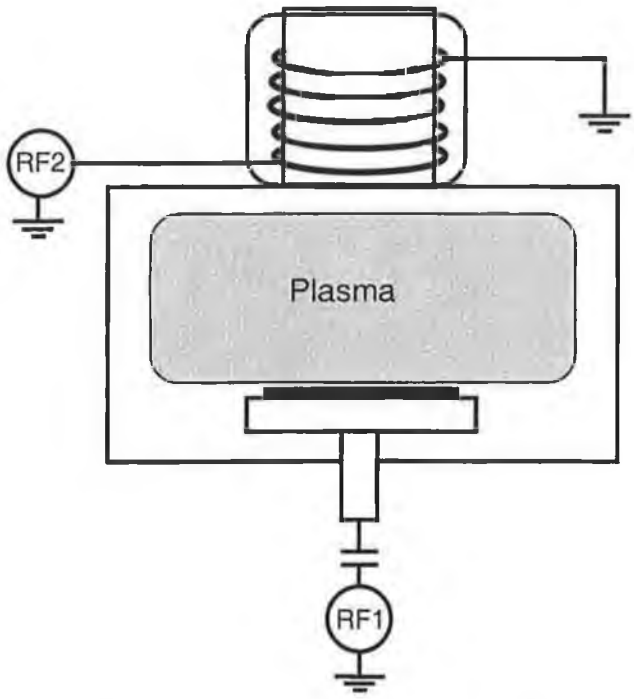

Figure 1.9: Schematic of a helical resonator. RF1 controls the ion impact energy as before.

1.3 Radio Frequency Plasma Diagnostics

Introduction

There are many types of plasma diagnostics and several ways in which they may be grouped when discussing them. This section will limit discussion of plasma diagnostics to those most commonly used in radio frequency discharges, while acknowledging that many more exist. Several textbooks deal with a range of diagnostics in some detail [25-28].

1.3.1 Probe Diagnostics

By far the earliest and most commonly used diagnostic tool is the electrostatic probe such as that first used and developed by Irving Langmuir in the 1920s [29]. There are now many types of probe in common use; collecting, emissive and capacitive probes are the most popular.

The simplest form of collecting probe, usually called a Langmuir probe, is a single wire immersed in the plasma. When biased at positive and negative potentials

relative to the plasma, the current drawn by the wire can provide information about the plasma parameters. This type of diagnostic therefore requires a potential reference point when applying a bias voltage to the probe. This is usually the grounded metallic wall of the discharge chamber. In the event that a potential reference is not available, such as on an electrodeless discharge, a double probe must be used [30-33].

Single Langmuir probes are used in many types of discharges. They have the advantage that they provide local information on plasma parameters. Most other techniques provide information that is averaged over a large plasma volume and is confined to the measurement of one parameter. For example, microwave interferometry usually provides the line-of-sight average of the electron density only. Some spectroscopic measurements are also limited in this manner. The greatest drawback of probe techniques is that they are an invasive diagnostic and so care is required not to disturb the plasma itself. Probe theory in itself is complex and is further complicated when probes are used in rf and magnetised discharges. The original work of Langmuir and Mott-Smith did much to aid understanding of the role of the sheath in probe diagnostics. In many cases the plasma probe sheath may be considered a thin layer near the probe surface [29]. Their approach resulted in a simple theory that is most applicable to planar probes. However, planar probes have the drawback that their large surface area perturbs the discharge so cylindrical probes are often used instead. Work by Laframboise modified the probe theory to allow for an expanding sheath around a cylindrical probe [34]. The theories of Langmuir and Laframboise are discussed in more detail in Chapter 2, section 2.3.

Emissive probes are primarily used to measure the plasma potential. They consist of a refractory wire loop placed in the plasma. The wire is heated to thermionic emission by a current. When the wire is sufficiently positive, ($>V_s$, the space potential) the electrons emitted will be drawn back to the probe and the collected electron current will be unaffected by the thermionic emission. When the probe is negative relative to the plasma potential, the emitted electrons will escape and result in an apparent ion current to the probe. The probe will float at the point where emission and collection are balanced; i.e. at the plasma potential. Emissive probes have the advantage in that, unlike collecting probes, they may be used in the sheath regions of the plasma, also in magnetised plasmas [35].

Some types of plasmas, e.g. those in strong magnetic fields, are more suited to capacitive probe measurements. If the impedance of the probe is high compared to the

source impedance, the probe can track the time-varying plasma potential without loading the plasma [36-38].

In general, electrostatic probes are limited to measurements of electron temperature, density and the electron energy distribution function. Obviously, the ion energy and distribution function at the electrode surface is of great interest to all processing applications. Several methods of ion and electron energy measurement using gridded energy analysers have been developed [39-42]. In many experiments, the gridded (two-to-four grids) analyser is housed in either the powered or grounded electrode in the system [43-46]. Ions or electrons are sampled via a small orifice plate. The ions then pass through a series of grids, one that has a ramped retarding potential in order to select ions at a particular energy. The operation of a four-grid analyser is described in Chapter 2. This analyser is set into the ground electrode of a capacitively coupled, parallel plate system. Gridded analysers may be made compact enough to fit in a probe which has the added advantage of the ability to make spatially-resolved measurements [47].

Gridded probes are often incorporated into mass spectroscopy systems. Mass spectrometry is one of the primary diagnostics for optimising and process monitoring of plasma discharges used in industry. On extraction from the plasma, the plasma particles may be both energy and mass analysed by a retarding field energy analyser and a quadrupole mass spectrometer. Experiments have demonstrated the necessity of simultaneous mass and energy separation, rather than nonmass resolved ion energy distribution measurements [48]. Detailed experiments using these systems are described in references [48-50].

1.3.2 Optical Diagnostics

Optical emission from plasma discharges has long been used as a diagnostic of plasma physics and chemistry. At the simplest level, the bright and dark regions in a discharge provide some information on the motions of ions and electrons in response to spatially varying electric fields. Optical techniques have the advantage of being non-invasive and having relatively simple apparatus; a monochromator to disperse the light emission, lenses/mirrors to image light onto the detector and the detector itself. Most emission studies to date in argon have been performed in the visible-UV region (300-700mm), where the emissions originate from the fraction of plasma species electronically excited to higher states. Plasma induced emission can arise from electron

impact excitation, electron impact dissociation or an ion impact process [26]. Electron concentrations and energies change dramatically during an rf cycle. This leads to a high degree of modulation in emissions excited by electron impact. Ion motion becomes limited at much lower frequencies (approximately 3MHz) for typical ions while electron motion can be modulated up to 100MHz. This means that time and space resolved emission spectroscopy can distinguish between the various processes that result in emission [51,52].

The optical emission apparatus may be easily adapted for absorption measurements. Absorption spectroscopy gives information on the absolute concentration of various species in a discharge. Molecules and some atoms have absorption lines in the visible, infrared or microwave frequency ranges. Visible light techniques have been used to measure concentrations of metastable argon atoms in a low-pressure inductive plasma [53].

Another popular optical diagnostic is laser-induced fluorescence. This technique has the advantage that the absolute density may be obtained provided that a transition starting from a ground state is pumped [54].

A diagnostic technique that requires the use of both probes and an optical setup is photodetachment. This diagnostic is used primarily to measure the negative ion density in electronegative plasmas such as CF_4 and hydrogen [55,56]. A photon of light with enough energy to detach an electron from a negative ion causes the local electron density to increase. If the laser intensity is enough to detach electrons from all negative ions in its path, the density of the negative ions will be proportional to the increase in electron density. This increase in electron density is measured using a Langmuir probe. The photon energy of the laser must be large enough to cause detachment of the electron from the ion but not so large as to cause photoionisation or photoemission [56].

1.3.3 Microwave Diagnostics

The refractive index of a plasma may be used to infer the electron density. Interferometry is the primary experimental technique for measuring the plasma's refractive properties. The basic principle is that the presence of a plasma in one arm of an interferometer results in a phase shift in the microwave arm that is directly related to the electron density in the plasma. The theory of the interaction of an electromagnetic with a plasma, plus the operation of an interferometer is presented in Chapter 2.

Several types of interferometer are used. The most popular configurations are the Michelson interferometer, the Mach-Zehnder configuration and the Fabry-Perot interferometer. The Michelson interferometer configuration is shown in figure 1.10(a). It is a two-beam interferometer; the beams travel in both directions through the plasma. It also has two outputs, one of which is along the input. The arms are usually microwave waveguides. Phase differences between the two components of one of the output beams arise by changes in refractive index N, in one of the arms of the interferometer – due to the presence of a plasma. The Mach-Zehnder configuration is also a two-beam interferometer but has two arms in which the beams travel in only one directon. Both outputs are separated from the input, see figure 1.10(b). Again, phase changes are caused by the presence of a plasma in one arm. The Fabry-Perot interferometer is a multiple-beam interferometer in which there are two beam splitters and two composite output beams. Because it has multiple beams (see figure 1.10(c)), the output is not a simple cosine dependence as in two-beam interferometers (see Chapter 2, section 2.5.2). This makes phase-shift interpretation more difficult, so it is less often used in plasma measurements [25,57].

Microwave interferometry has been used by several workers for density measurements [58-64]. As the information obtained using this technique is usually spatially averaged across the plasma and conveys no information about the electron energy distribution function, it is often compared to and used with the information supplied by Langmuir probes [65-67]. Microwave interferometry has the advantage of being a fast diagnostic and is excellent for pulsed discharge measurements. Recently, spatially localised density measurements have been made using a specially designed experimental system and Abel inversion [67].

Microwave reflectometry is an alternative technique that measures plasma density as a function of position. At densities higher than the critical density, the wave is evanescent, it is therefore reflected back. Detection of the reflected wave makes measurement of the plasma density possible. Measurement of the relative phase of the reflected and incident waves gives us information about where the reflection occurs, hence about density as a function of position. Interferometry is usually the more popular option for laboratory plasmas [25].

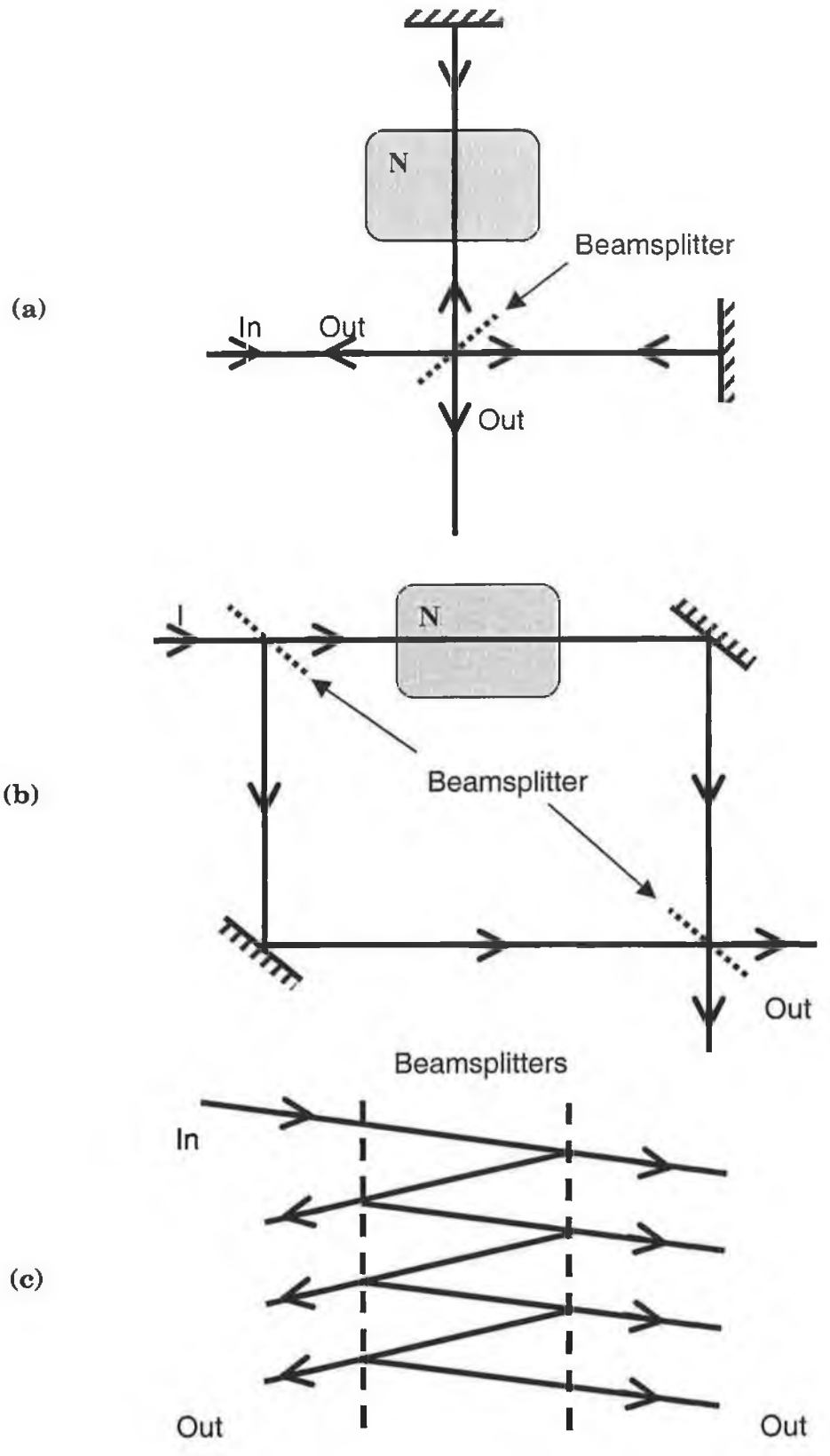

Figure 1.10: (a) Michelson Interferometer, (b) Mach-Zehnder interferometer, (c) Fabry-Perot configuration.

1.3.4 External Electrical Diagnostics

For electrical discharges in low-pressure gases, the external electrical characteristics of the system may be measured directly. The most common external electrical measurements are that of voltage and current on the powered electrode. The electrical impedance of the plasma carries global information about the plasma in terms of the bulk conductivity and the capacitance of the sheaths [68].

The participants of the Gaseous Electronics Conference (GEC) reference reactor programme have performed many measurements of current, voltage and phase at the powered electrode of the GEC parallel-plate reactor [69,70]. Comparisons of data taken from several reactors have shown excellent agreement [71]. This agreement in measurements has allowed reproducible plasmas to be created, resulting in meaningful comparisons of other diagnostic techniques in separate cells. The GEC workers have constructed and calibrated their own current-voltage probes. A schematic of a typical probe is shown in figure 1.11.

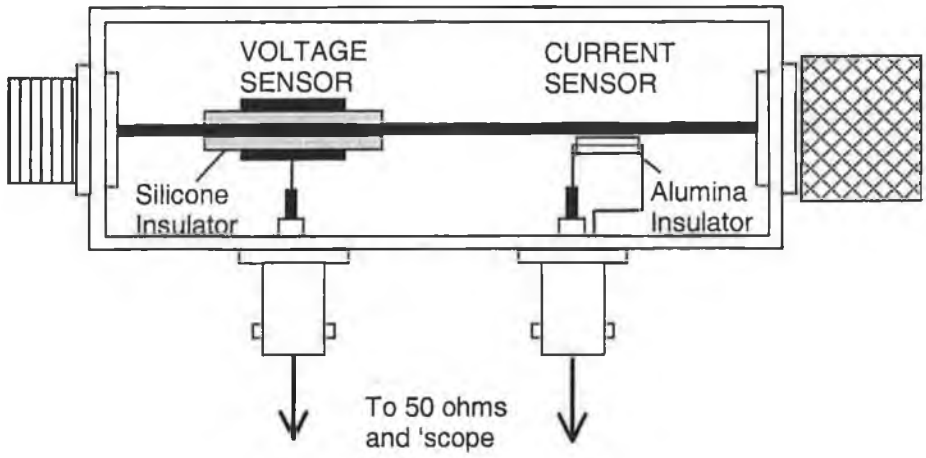

Figure 1.11: Schematic of inductive current probe and capacitive voltage probe inserted in-line on a GEC reference cell.

The methods of measuring current and voltage in this thesis are described in detail in Chapter 2. Typically, the current-voltage waveforms are determined just outside the vacuum chamber, between the matching network and the powered electrode. As most practical matching units will absorb some of the input power, this allows a measurement that more accurately reflects the actual power delivered to the plasma.

1.4 Production Mechanisms in RF Plasmas

Introduction

The primary production mechanism in low pressure rf plasmas is electron impact ionisation. As the ionisation energy of argon is 15.76 eV, the electrons need to be heated in order to sustain the plasma. The exact mechanisms by which the plasma electrons are heated can be complicated but work done on capacitively coupled plasmas to date has done much to improve the understanding of the heating mechanisms. It has been determined that the capacitively coupled rf plasma has three distinct regimes or 'modes' of operation. These regimes are determined by gas type and pressure, electrode gap and material, driving frequency and current density/applied power. An important plasma parameter in determining the primary heating mechanism is the electron ionisation mean free path, λ_{ionis}

$$\lambda_{ionis} = \frac{1}{n_g \sigma_{ionis}} \qquad 1.4.1$$

Where σ_{ionis} is the ionisation cross section. This is shown in figure 1.12 as a function of electron energy in argon [11].

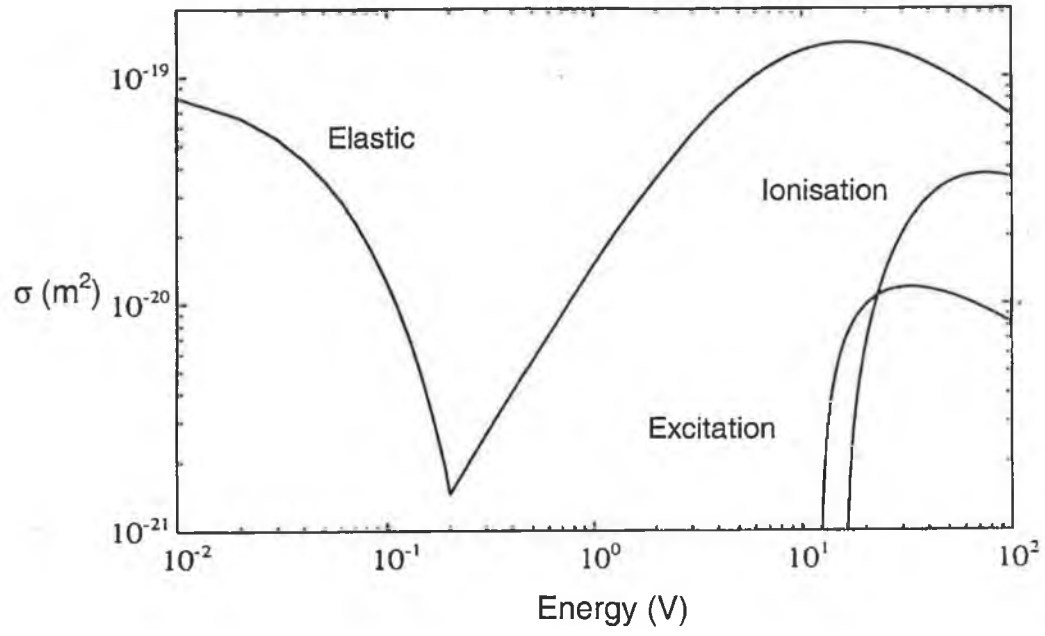

Figure 1.12: Cross-sections for ionisation, excitation and elastic scattering for electrons with neutrals in argon [11].

1.4.1 Sheath Heating

For a given gas, electrode material, gap length and driving frequency, the discharge conditions may be determined by the gas pressure and discharge current density [72]. At low pressures and current densities a regime exclusive to rf discharges

has been examined by several workers [73-76]. It appears that the sheath oscillations which are characteristic of rf discharges also constitute an important source of energy for the electrons. This low-pressure sheath heating has been termed stochastic heating and occurs where the electron mean free path is the order of or greater than the gap length. In this regime, the electron is more likely to interact with the sheaths than to undergo a collision with a gas molecule. The simplest description of the electron's interaction with the sheath is the 'hard wall' model that is simply of a ball bouncing elastically between rigid moving walls [11,77]. Electrons gain energy if they collide with the sheath while it is expanding and lose energy if they collide while it is retreating. On average, there is an energy gain. Modeling work has demonstrated that heating can occur on the retreating part of the cycle. This is called anomalous sheath heating [78].

At very low pressures, the entire discharge is nearly collisionless and the heating mechanism is termed stochastic heating. Increasing the pressure a little results in the plasma becoming more collisional while the sheath is still collisionless. This is sheath oscillation or simply sheath heating.

Models of plasmas that are fully 'collisionless' (collisionless plasma and sheath) have been developed by Goedde *et al* [79]. These workers determined that an rf discharge for which stochastic heating was the only mechanism would have a pD (pressure times the electrode gap) of approximately 10 mTorr.cm at f_{rf}=13.56MHz. The lowest pressure examined in this thesis is 10 mTorr at gaps of 3-7 cm so sheath heating is understood to be the dominant heating mechanism at low pressures.

1.4.2 Ohmic Heating

At higher pressures, the sheath and the plasma become collisional and the plasma sustaining mechanism changes. At higher gas pressures, approximately greater than 50-100 mTorr in the systems studied here, the mean free paths of the plasma electrons are less than the chamber dimensions. In this situation ionisation occurs in the plasma bulk. The bulk electrons with energies below the ionisation threshold are heated by the bulk plasma electric field and contribute to ionisation. It is in this regime, the low current, relatively high-pressure regime, that the rf plasma closely resembles a dc positive column [75,80]. This regime is termed ohmic heating and is essentially the passage of current through a resistive plasma.

In asymmetric higher-pressure discharges, light emission studies, probe measurements and computer simulations have indicated enhanced emission and ionisation at the sheath edge [Chapter 5]. This is attributable to ohmic sheath heating [81] and has also been termed 'wave riding' [75]. At high pressures, fast electrons generated at the sheath edge lose energy at or very near the sheath edge. The localised glow at the sheath edge is observed in most capacitive rf discharges at higher pressures and results from the short mean free paths for inelastic collisions (excitation/relaxation).

1.4.3 The γ Mode

Increasing the voltage to a higher-pressure capacitive rf discharge results in an increase in secondary electron emission by ion impact on the powered electrode. Since the powered electrode is negative with respect to the plasma, the secondary electrons generated at the electrode are accelerated across the sheath to the plasma. At high pressures, these secondaries undergo collisions in the sheath region. Much of this enhanced ionisation takes place at the plasma-sheath boundary, though a marked increase in discharge luminosity indicates that enhanced emission and ionisation in the plasma bulk also occurs [51,82,83].

The 'turning on' of the γ mode has been likened to a secondary breakdown of the gas [84]. Secondary electron emission by ion impact is the primary sustaining mechanism of the cathode region; the 'negative glow' of a dc discharge [5,75,84]

Since ion impact onto the powered electrode is such an inherent feature of the capacitively-coupled discharge, secondary emission will always be present to a certain extent. At very low pressures it may be assumed that secondaries do not play a significant role as their large mean free path results in them being lost from the discharge before significant ionisation can occur [11].

1.4.4 Transitions in Heating Mechanisms

The point where the discharge changes from one regime to another may be inferred from the changes in appearance and measured discharge parameters as the discharge changes from one regime to another. These transitions have been investigated by experiments [83,85-90] and simulations [91,92]. An experimental investigation of these transitions is the topic of Chapter 3 in this thesis. The heating mechanisms described in rf plasmas may be divided into two types, low current and high current.

For a fixed low current density and gap length, the regime of operation is defined by the gas pressure.

At low pressures, the electrons are heated by the oscillatory motion of the sheaths. The electron energy distribution function (EEDF) is bi-Maxwellian, with low energy and high-energy electron populations. The average electron energy in this regime is usually low, in the region of 0.5 to 1eV [72,73,76]. Increasing the gas pressure results in a change in shape of the EEDF to the Druyvesteyn form characteristic of discharges sustained by ohmic heating. For the noble gases the transition from ohmic to sheath heating is enhanced by the Ramsauer effect. This is a minimum in the cross section for elastic collisions for low energy electrons [93]. The low energy electrons therefore have a low electron-atom collision frequency. These electrons do not contribute to ionisation but oscillate collisionlessly in the plasma bulk, unable to gain energy from either the sheaths or the rf field. The higher energy electrons can however ionise atoms and compensate for energy losses through collisions with the expanding plasma sheath [11,94].

The transition from sheath to ohmic heating occurs at a point that depends on the pressure, p times the length, D of the plasma. Typical values of pD for argon are in the range 200-300mTorr cm [72,73,76].

This transition has been studied experimentally by Godyak and co-workers [73]. It has also been examined by others using computational models [86,88]. Verification of the pD parameter for the transition is detailed in Chapter 3.

Increasing the applied rf voltage to an intermediate (>100mTorr) discharge causes a dramatic change in both the appearance and behaviour of the discharge. Early observations of this were reported by Levitskii, who proposed that the dramatic change in emission intensity and electrical characteristics were due to distinctly different ionisation processes [86]. At relatively low rf voltages, Joule heating in the plasma dominates and the plasma is in what is commonly termed the α-mode. At higher discharge voltages secondary electron emission contributes more to the ionisation (hence the term γ-mode, from the secondary emission coefficient). The discharge exhibits a marked increase in emission intensity and electron density. This transition is also marked by a change in shape of the EEDF from a Druyvesteyn to a bi-Maxwellian distribution. The appearance of the high-energy 'tail' in the EEDF is interpreted as indirect evidence of secondary electrons [82,83].

Several workers have studied the fact that two forms of capacitively-coupled rf discharges exist in the intermediate pressure range. Raizer [84] and Yatsenko [87,88] have measured the current-voltage characteristics. The evolution of the plasma density, temperature and EEPF has been monitored by the probe measurements of Godyak [82] and by the author [83] as well as other workers [92]. Experimental investigations of the α-γ transition have also been performed using optical emission spectroscopy [51] and Thomson scattering [90].

1.5 Loss Mechanisms in RF Plasmas

Introduction

The primary electron loss processes in glow discharges are recombination, attachment and diffusion [5,95,96]. The following sections discuss these mechanisms and their relevance to the plasmas studied in this thesis.

1.5.1 Recombination

In higher pressure, higher density discharges, recombination is a significant loss process. Recombination is basically the joining of an electron and positive ion to form a neutral molecule or atom in the ground state. The electron loss rate for a quasi-neutral plasma is

$$\frac{dn}{dt} = -\alpha n_e^2 \qquad 1.5.1$$

where α is the recombination coefficient. The solution to this equation is

$$n = \frac{1}{\frac{1}{n_o} + \alpha t} \qquad 1.5.2$$

where n_0 and n are the peak density and the electron density respectively. There are several processes by which energy and momentum may be conserved and this gives rise to several types of recombination. Radiative recombination is recombination of an electron and ion with photon emission. This process is unlikely due to difficulties in conserving energy and momentum. The probability of an electron and ion recombining is greatly increased if a third body is present. There are two important three-body recombination processes, electron collisional-radiative recombination and neutral collisional-radiative recombination; the latter is only conceivable in high-pressure ionised media [96]. The last and most dominant recombination process in gas discharges is dissociative recombination, where a molecular ion plus an electron make a

transition to an unstable state of the molecule which causes the atoms forming the molecule to move apart and gain kinetic energy due to their mutual repulsion. In this type of recombination, the positive ion provides its own 'third body' to aid energy and momentum conservation.

1.5.3 Attachment

Electron attachment is an important loss process in electronegative gases such as oxygen and chlorine. This process involves the capture of electrons by electronegative gas atoms or molecules, resulting in the formation of negative ions. For this process, the electron loss rate is:

$$\frac{dn_e}{dt} = -\nu_a n_e = -h\nu_e n_e \qquad 1.5.3$$

where ν_a is the collision frequency for attachment, ν_e is the electron-neutral collision frequency and h is the attachment coefficient. Like recombination, attachment resulting in negative ion formation may occur via several processes; radiative attachment, three-body attachment and dissociative attachment [96].

1.5.1 Diffusion

When the density of charged particles is very low, the charges of opposite sign diffuse independently of each other. This is termed free diffusion. Electrons, being more mobile, diffuse more quickly than ions. If the charged particle densities are not so low, a space charge is formed as a result of charged particle separation and the generated field (the ambipolar field) thus impedes further departure from charge neutrality. This field retards the high-mobility electrons and accelerates the slower ions.

The transition from free to ambipolar diffusion is gradual (over about 5 orders of magnitude of electron/ion density). Ambipolar diffusion cannot apply when the degree of ionisation is very high, i.e. the number of neutral particles is so small that collisions between ions and electrons exceed those with neutrals. Therefore, there are two transition regions separating the three types of diffusion processes, see figure 1.13 [95].

Exponential time decays in density occur in both diffusion and attachment dominated discharges. One can qualitatively distinguish between different loss processes by observing the spatial dependence of the electron density. The diffusion process gives rise to spatial distributions that usually have a maximum near the centre of the discharge. Recombination and attachment are volume loss processes so the

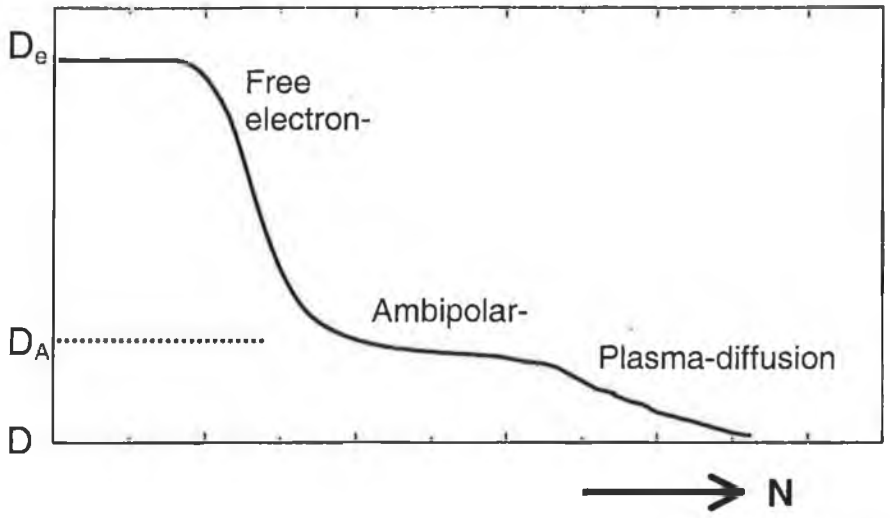

Figure 1.13: Free electron, ambipolar and plasma diffusion as a function of the electron density at constant electron temperature [95].

recombination/attachment rate depends on local electron density. This tends to result in a uniform density profile [96].

It is essential to determine the type of diffusion because free and ambipolar diffusion coefficients differ by a factor of ten or more [80]. This is relevant to the calculations detailed in Chapters 4 and 5. For the electron flux not to exceed the ion flux, the polarization field that appears in ambipolar diffusion equals (see section 4.1)

$$E_A \approx \frac{-D_e}{\mu_e}\frac{1}{n}\frac{dn}{dx} \qquad 1.5.4$$

Using Einstein's relation $-D_e/\mu_e=T_e$, where D_e is the electron diffusion coefficient, μ_e is the electron mobility and T_e is the electron temperature in eV. Equation 1.5.1 may then be written

$$E_A = \frac{-T_e}{R} \qquad 1.5.5$$

where $n=Rdn/dx$ is the plasma density. R is the distance over which the electron or ion density varies considerably, e.g. the radius of a cylindrically symmetric plasma [80]. Using Gauss's Law

$$\nabla \cdot E = \frac{\rho}{\varepsilon_0} \Rightarrow \frac{dE}{dx} = \frac{e(n_i - n_e)}{\varepsilon_0} = \frac{edn}{\varepsilon_0} \qquad 1.5.6$$

$dE/dx \approx E_A/R$, therefore

$$\frac{dn}{n} = \frac{\varepsilon_0}{ne}\frac{E_A}{R} \qquad 1.5.7$$

Using 1.5.5,

$$\frac{dn}{n} = \frac{\varepsilon_0}{ne}\frac{-T_e}{R^2} = \left(\frac{\lambda_D}{R}\right)^2 \qquad 1.5.8$$

where $\lambda_D=(\varepsilon_0 T_e/ne)^{1/2}$ is the Debye length of the plasma. This quantity gives the distance over which a density gradient exists. If large density differences appear over distances greater than the Debye length, then $\delta n/n << 1$ and the diffusion is ambipolar. In this work the density ranges from $9x10^8 cm^{-3}$ to $4x10^{11} cm^{-3}$ and the average temperature from 1eV to 4eV so equation 1.5.5 yields values for dn/n ranging from $1x10^{-7}$ to $9.6x10^{-11}$. This confirms that ambipolar diffusion is the primary loss process for most of the plasmas described in this thesis. However, a condition for ambipolar diffusion is also that the ion mean free path be considerably less than the discharge dimensions. In the 10 mTorr case (see Chapter 5) the ion mean free path is approximately 3 cm so is of the order of the discharge length. In this case, the assumption that ambipolar diffusion is the primary loss process may not be strictly accurate.

The Debye length is also the characteristic defining length of a plasma. The condition $(\lambda_D/R)^2<<1$ is the quantitative criterion that distinguishes a plasma (an electrically neutral ionised medium) from the other instances of the presence of charges in a gas.

References

[1] J. Coburn, IEEE Trans. Plasm. Sci. 19(6), 1048-62, (1991).

[2] J. Shohet, IEEE Trans. Plasm. Sci. 19(5), 725-733, (1991).

[3] D. Graves, IEEE Transactions on Plasma Science, 22(1), 31-42, (1994).

[4] J. Proud and R. A. Gottscho, *Plasma Processing of Materials, Scientific Opportunities and Technological Challenges*, National Academy, National Research Council Rep., Washington DC, (1991).

[5] B. A. Chapman, *Glow Discharge Processes*, New York, Wiley, (1980).

[6] J. Scanlan, PhD Thesis, Dublin City University, (1990).

[7] C. J. Beneking, Appl. Phys. 68(9), 4461-4473, (1990).

[8] K. Al-Assadi, Vacuum, 43(4), 287-290, (1992).

[9] K. Köhler, J.W. Coburn, D.E. Horne and E. Kay, J. Appl. Phys. 57(1), 59-66, (1985).

[10] Y. P. Song, D. Field and D. F. Klemperer, J. Phys. D: Appl. Phys. 23, 673-681, (1990).

[11] M. Lieberman, and A. Lichtenberg, *Principles of Plasma Discharges and Materials Processing*, Wiley Interscience, (1994).

[12] J. Forster, Appl. Phys. Lett., 62(26), 1993, 3249

[13] A.J. Van Roosmalen, W.G.M. van Hock and H. Kalter, J. Appl. Phys. 58(2), 653-658, (1985).

[14] S. Rauf and M. J. Kushner, J. Appl. Phys., 83(10), 5087-5094, (1998).

[15] M. Chandhok, J. Grizzle, IEEE Trans. Plasma. Sci., 26(2), 181-189, (1998).

[16] D. F. Beale, A. E. Wendt and L. J. Mahoney, J. Vac. Sci. Technol. A 12, 2775, (1994).

[17] R.A. Stewart, P.Vitello and D. B. Graves, J. Vac. Sci. Technol. B 12, 478, (1994).

[18] J. Hopwood, Plasma. Sces. Sci. Technol 1, 109, (1992).

[19] J. Hopwood, C. R. Guarnieri, S. J. Whitehair and J. J. Cuomo, J. Vac. Sci. Technol. A. 11, 152, (1993).

[20] Y.Ra, S.G. Bradley and C.H. Chen, J. Vac. Sci. Technol. A, 12(4), 1328-1333, (1994).

[21] R.W. Boswell, Phys. Lett. 33A, 457-458, (1970).

[22] F.F. Chen, J. Vac. Sci. Tech. A, 10, 1389-1401, (1992).

[23] F. F. Chen and C.D. Decker, Plasma Phys. Controlled Fusion, 34, 635-640, (1992).

[24] D.L. Flamm, D.E. Ibbotson and W.L. Johnson, US Patent no. 4368 092, April 17 (1990).

[25] R. H. Huddlestone and S. L. Leonard, *Plasma Diagnostic Techniques.* Academic Press, New York, (1965).

[26] I. H. Hutchinson, *Principles of Plasma Diagnostics*, Cambridge University Press, (1987).

[27] V. M. Donnelly, *Plasma Diagnostics*, ed. By O. Auciello and D. Flamm, Volume 1, Academic Press, (1989).

[28] L. Schott in *Plasma Diagnostics,* ed. by W. L. Holtgreven, North Holland, Amsterdam, (1968).

[29] I. Langmuir and Mott-Smith, Phys. Rev. 28, 727, (1926).

[30] E. O. Johnson and L. Malter, Phys. Rev. 80, 58-68, (1950).

[31] A. M. Pointu, Appl. Phys. Lett. 48, (12), 762-763, (1986).

[32] D. M. Manos, J. Vac. Sci. Technol. A., 3(3), 1059-1065, (1985).

[33] F. F. Chen, Rev. Sci. Instrum., 35(9), 1208-1212, (1964).

[34] J. G. Laframboise, UTIAS report no. 100, (1966).

[35] N. Hershkowitz, IEEE Trans. Plasma Sci. 22(1), 11-21, (1994).

[36] N. Benjamin, Rev. Sci. Instrum. 53(10), 1541-1543, (1982).

[37] S. E. Savas and K. G. Donohoe, Rev. Sci. Instrum. 60(11), 3391-3395, (1989).

[38] R. R. J. Gagné and A. Cantin, J., Appl. Phys. 43, 2639, (1972).

[39] D. D. Neiswender and F.C. Konout, Rev. Sci. Instrum, 43(10), 1475-1480, (1972).

[40] Y. Sakai and I. Katsumata, Jap. J. of Appl. Phys., 24(3), 337-341, (1985).

[41] J. W. Coburn, Rev. Sci. Instrum., 41, 1219, (1970).

[42] D. Bolshukhin, D. Meyer, F. Petriconi, I. Vinogradov, K. Wieseman, Contrib. Plasma Phys. 36 S, 95-102, (1996).

[43] S. G. Ingram and N. St. J. Braithwaite, J. Phys. D. Appl. Phys. 21, 1496-1503, (1988).

[44] C. Wild and P. Koidl, J. Appl. Phys. 69(5), 2909-2922, (1991).

[45] C. Böhm and J. Perrin, Rev. Sci. Instrum. 64(1), 31-44, (1993).

[46] U. Flender and K. Wieseman, J. Phys. D. Appl. Phys. 27, 509-521, (1994).

[47] G.D. Conway, A.J. Perry and R.W. Boswell, Plasma Sces. Sci. Technol. 7, 337-347, (1998).

[48] R.J.M.M. Snijkers, M.J.M. van Sambeck, G.M.W. Kroesen and F.J. de Hoog, Appl. Phys. Lett. 63(3), 308-310, (1993).

[49] J. Olthoff, R.J. van Brunt, S.B. Radanov, J.A. Rees and R. Suroviec, J. Appl. Phys. 75(1), 115-125, (1994).

[50] M. Zeuner, H. Neumann and J. Neichsner, J. Appl. Phys. 81(7), 2985-2994, (1997).

[51] R. Flohr and A. Piel, Phys. Rev. Lett. 70(8), 1108-1111, (1993).

[52] T. Kitajima, M. Izawa, N. Nakano and T. Makabe, J. Phys. D. Appl. Phys. 30, 1783-1789, (1997).

[53] A. Pierre, J. Stittsworth and A. Wendt, Program for 42nd National Symposium of the AVS, 210, (1995).

[54] J. P. Booth, G. Hancock, N. D. Perry and M. Toogood, J. Appl. Phys. 66, 5251, (1989).

[55] J. L. Jaberteau, G. J. Meeusen, M. Haverlag, G. M. W. Kroesen and F. J. de Hoog, Appl. Phys. Lett., 55(25), 2597-2599, (1989).

[56] K. N. Mellon, PhD Thesis, Dublin City University, (1993).

[57] M. A. Heald and C. B. Wharton, *Plasma Diagnostics with Microwaves*, Krieger Publishing Company, Huntington, New York, (1978).

[58] R. A. Doyle, PhD Thesis, Dublin City University, (1994).

[59] J. A. Kleber, MSc Thesis, University of Texas at Dallas, (1997).

[60] L. Overzet, J. Res. Natl. Inst. Stand. Technol. 100, 401, (1995).

[61] L. Lindberg and A. Eriksson, J. Phys. E. Sci. Instrum. 15, 548-554, (1982)

[62] E. Hotson and M. Seidl, J. Sci. Instrum. 42, 225-230, (1965).

[63] L.J. Overzet and J.T. Verdeyn, Appl. Phys. Lett. 48, 695-697, (1986).

[64] K.E. Greenberg and G.A. Hebner, J. Appl. Phys. 73, 8126-8133, (1993).

[65] L. J. Overzet and M. B. Hopkins, J. Appl. Phys. 74(7), 4323-4330, (1993).

[66] M. Tuszewski and J.A. Tobin, Plasma Sces. Sci. Technol. 5, 640-647, (1996).

[67] N. Niemöller, V. Schulz-von der Gathen, A. Stampa, H.F. Döbele, Plasma Sces, Sci. Technol. 6, 437, (1997).

[68] N. St. J. Braithwaite, Plasm. Sces. Sci. Technol, 6, 133-139, (1997).

[69] J. K. Olthoff and K. E. Greenberg, J. Res. Natl. Inst. Stand. Technol. 100, 327, (1995).

[70] M. A. Sobolewski, J. Res. Natl. Inst. Stand. Technol. 100, 341, (1995).

[71] P. J. Hargis, K. E. Greenberg, P.A. Miller, J. B. Gerardo, J. R. Torczynski, M. E. Riley, G. A. Hebner, J. R. Roberts, J. K. Roberts, J. K. Olthoff, J. R. Whetstone, R. J. van Brunt, M. A. Sobolewski, H. M. Anderson, M. P. Splichal, J. L. Mock, P. Bletzenger, A Garscadden, R. A. Gottscho, G. Selwyn, M. Dalvie, J. E. Heidenreich, J. W. Butterbaugh, M. L. Brake, M. L. Passow, J. Pender, A. Lujan, M. E. Elta, D. B. Graves, H. H. Sawin, M. J. Kushner, J. T. Verdeyen, R. Horwath, T. R. Turner, Rev. Sci. Instrum. 65(1), 140-154, (1994).

[72] V. A. Godyak, R. B. Piejak and B. M. Alexandrovich, Plasma Sces. Sci. Technol. 1, 36-58, (1992).

[73] V. A. Godyak and R. B. Piejak, Phys. Rev. Lett., 65, 996, (1990).

[74] M. A. Lieberman, IEEE Trans. Plasm. Sci., 16(6), 638, (1988).

[75] M. J. Kushner, IEEE Trans. Plasma Sci., 14, 188, (1986).

[76] C. M. Deegan and M. B. Hopkins Poster presentation at the 47th Annual Gaseous Electronics Conference, San Francisco, (1995).

[77] O. A. Popov and V. A. Godyak, J. Appl. Phys. 57, 53, (1985).

[78] M. M. Turner and M. B. Hopkins, Phys. Rev. Lett., 69, 24, 3511-3514, (1992).

[79] C. G. Goedde, A. J. Lichtenberg and M. A. Lieberman, J. Appl. Phys. 64, 4375, (1988).

[80] Y. Raizer, *Gas Discharge Physics*, Springer-Verlag, (1991).

[81] Ph. Beluenger and J. P. Boeuf, Phys. Rev. A, 41, 4447, (1990).

[82] V. A. Godyak, R. B. Piejak and B. M. Alexandrovich, Phys. Rev. Letts. 68, 40, (1992).

[83] C. M. Deegan, J. P. Goss, D. Vender and M. Hopkins, Appl. Phys. Letts., 74(4), 1969, (1999).

[84] Y. Raizer, M. N. Schneider and N. A. Yatsenko, *Radio-Frequency Capacitive Discharges,* CRC Press, (1995).

[85] R.A. Doyle, M.B. Hopkins and M.M. Turner, Conference paper at the 45th Annual Gaseous Electronics Conference, Boston, (1992).

[86] S.M. Levitskii, Sov. Phys. Tech. Phys. 2, 887, (1957).

[87] N.A. Yaksenko, Sov. Phys. Tech. Phys. 26(6), 678, (1982).

[88] N.A. Yaksenko, Sov. Phys. Tech. Phys. 27(6), 741, (1982).

[89] E. Tatarova, E. Stoykova, K. Bachevm I. Zhelyazkov, IEEE, Trans. 26, 2, 167-174, (1998).

[90] H.J. Weßeling and B. Kronast, J. Phys. D. 29, 4, 1035-1039, (1996).

[91] M. Surendra and D.B. Graves, Phys. Rev. Lett. 66, 11, 1469-1472, (1991).

[92] M.M. Turner, R.A. Doyle and M.B. Hopkins, Appl. Phys. Lett., 62(25), 3247-3249, (1993).

[93] V. E. Golant, A. P. Zhilinsky and A. E. Sakharov, *Fundamentals of Plasma Physics*, ed. S. C. Brown, Wiley, (1977).

[94] V.A. Godyak, Sov. Phys. Tech. Phys. 16, 1073, (1972).

[95] A. von Engel, *Ionised Gases*, AIP Press, New York, (1994).

[96] B. E. Cherrington, *Gaseous Electronics and Gas Lasers*, Pergamon Press, London, (1979).

Chapter 2

Experiment and Diagnostics

Introduction

The purpose of this chapter is to describe the experimental systems employed and to describe the diagnostics used to determine the plasma parameters. The theory specific to each diagnostic method is explained and the applicability to the plasmas under investigation is determined.

Argon plasmas are generated in two capacitively-coupled systems that are described in detail in sections 2.1 and 2.2. The first system is used to examine the transitions in heating mechanisms characteristic of capacitively coupled plasmas. System 2 allows spatial investigations of the discharge. The primary diagnostic used here is a tuned Langmuir probe described in section 2.3. A retarding field energy analyser is installed in the ground electrode of the system and used to measure ion and electron energy distributions. Measurements of the plasma potential using both diagnostics are compared. A microwave interferometer is used to measure the electron density in the plasma centre. These measurements are compared with those measured with the Langmuir probe. A current-voltage (*IV*) monitor on both systems allows plasma conditions to be kept constant in the course of the experiments. Some measurements using the *IV* monitor are also presented.

2.1 Experimental System 1

This system configuration is shown in figure 2.1. It is a cylindrical aluminium chamber, 180 mm in height by 280 mm in diameter (internal dimensions). The driven electrode is 200 mm while the grounded electrode is 240 mm. The walls of the chamber are therefore connected with the ground plate, resulting in an asymmetric configuration.

The chamber is evacuated by a Varian 170 l/s turbomolecular pump and a two-stage rotary pump. This results in a base pressure of 2×10^{-6} Torr. Argon gas is introduced into the chamber via a MKS7560 mass flow controller and monitored using an MK247C flowmeter. The gas pressure is set using an MKS 2506 meter which is connected to an MKS Baratron capacitance manometer. The pressure is set using the meter and Baratron in conjunction with a 'smart' valve. This is a butterfly type valve that opens or closes to equalise the set pressure and actual pressure in the chamber.

An ENI ACG3 rf generator is used to form the plasma. This generator is connected to an L-type matching network, which in turn connects to the powered electrode via the current-voltage monitor. This monitor is a prototype of the plasma impedance monitor (PIM™) under development by Scientific Systems Ltd. and is described in more detail in section 2.6. This device is connected to a Hewlett-Packard 5400B 100MHz oscilloscope that has a GPIB interface to a computer, allowing current, voltage and power measurement.

Two Langmuir probes are installed in this system. One is an early model of the ceramic-body probe designed by Scientific Systems Ltd. The other is a glass-body Langmuir probe described in [9] and connected using a Wilson seal. The latter probe is used as a reference probe; it monitors the floating potential of the discharge while the former, the main probe, is biased. The theory and operation of these probes are described in detail in section 2.3.

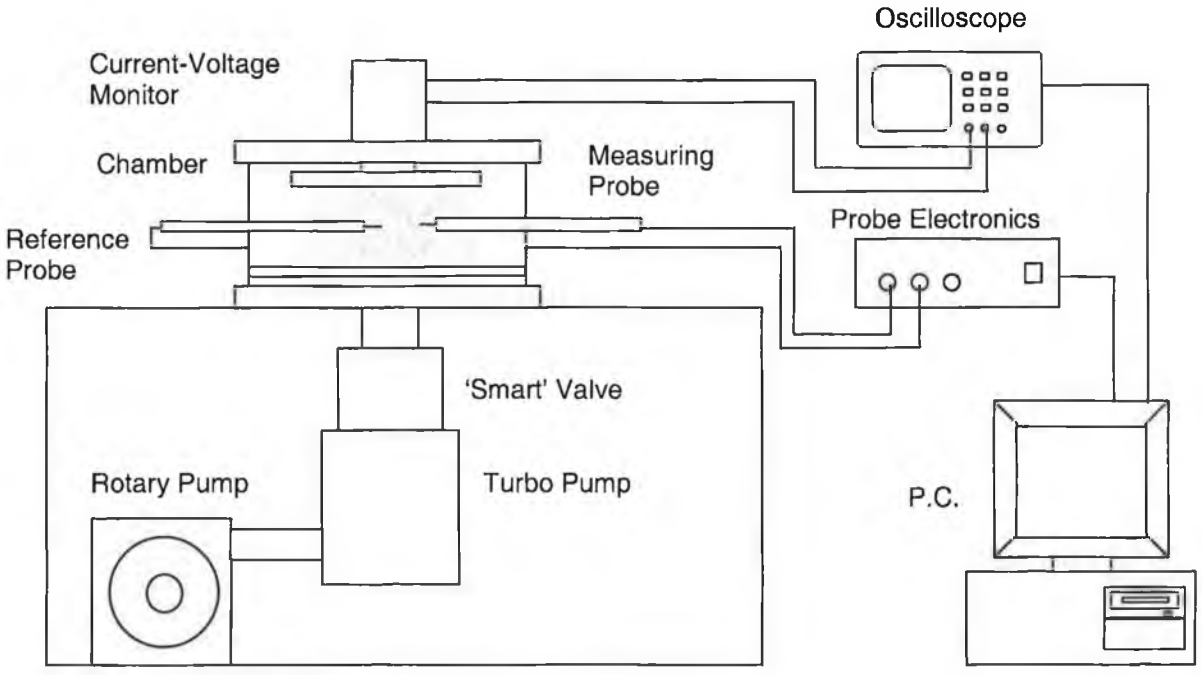

Figure 2.1: Outline of the main components of experimental system 1.

2.2 Experimental System 2

The second experimental system is also a capacitively-coupled system, the main features are shown in figure 2.2. The spatial measurements detailed in Chapter 5 were made in this system. It is a cylindrical stainless-steel chamber. In this case the powered electrode is mounted on the side of the chamber. It is 143mm in diameter and is closely

surrounded (0.5mm gap) by a 1mm thick 'ground shield' whose function it is to ensure no plasma production behind the electrode and also to prevent large sheaths forming along the electrode sides (a narrow ground sheath does form). The powered electrode is mounted on a bellows assembly to allow movement of the electrode while the chamber is evacuated. The chamber is pumped by a Varian 340 l/s (model 969-9424) Turbo pump and operated using a Varian 300HT controller. This, coupled with a two-stage rotary pump achieves base pressures of typically 4 x 10^{-7} Torr. Four mass flow controllers (1179A MKS) that are controlled by an MKS 247D 4-channel readout, regulate the gas flow into the chamber. Several gauges are installed on the system. An MKS cold cathode vacuum gauge system (type 937) plus an MKS 122A Baratron pressure gauge are installed. The Baratron and an MKS 153C throttle valve are used with an MKS 651C pressure controller to set the gas pressure.

The same ENI generator as described in section 2.1 is used to form the plasma. It is connected to the powered electrode via a Bird Instruments in-line power meter, an RFPP AM20 matching network, and a Scientific Systems plasma impedance monitor. Since the bellows assembly varies in length, depending on the plate separation, the cylindrical shield can slide along the inside of the assembly, so preventing rf leakage into the laboratory.

In this system, one Langmuir probe is installed. This has the reference probe installed along the same shaft (see figure 2.7), an important feature for spatially resolved measurements. This is connected to the chamber via a Conflat™ connector and mounted on a bellows assembly, which allows movement of the probe in both the axial (z) and radial (r) directions. Axial measurement is restricted by the probe port so most spatially-resolved measurements were performed on gaps of 55mm or less to allow the probe access near to the powered electrode.

This system also has a compact retarding-field energy analyser installed in the ground plate. The analyser grids and amplifier circuit are connected a P.C. and power supply. This device is described in more detail in section 2.4. Figure 2.3 shows a block diagram of the setup of the Langmuir probe, the current-voltage monitor and the energy analyser on system 2.

An 11.5 GHz microwave interferometer is set up on a platform around the chamber, with the horns touching the windows. This instrument is sensitive to vibrations so the horns are supported by platforms and aligned opposite to each other

and next to the windows using perspex supports. The interferometer configuration is described in more detail in section 2.5.

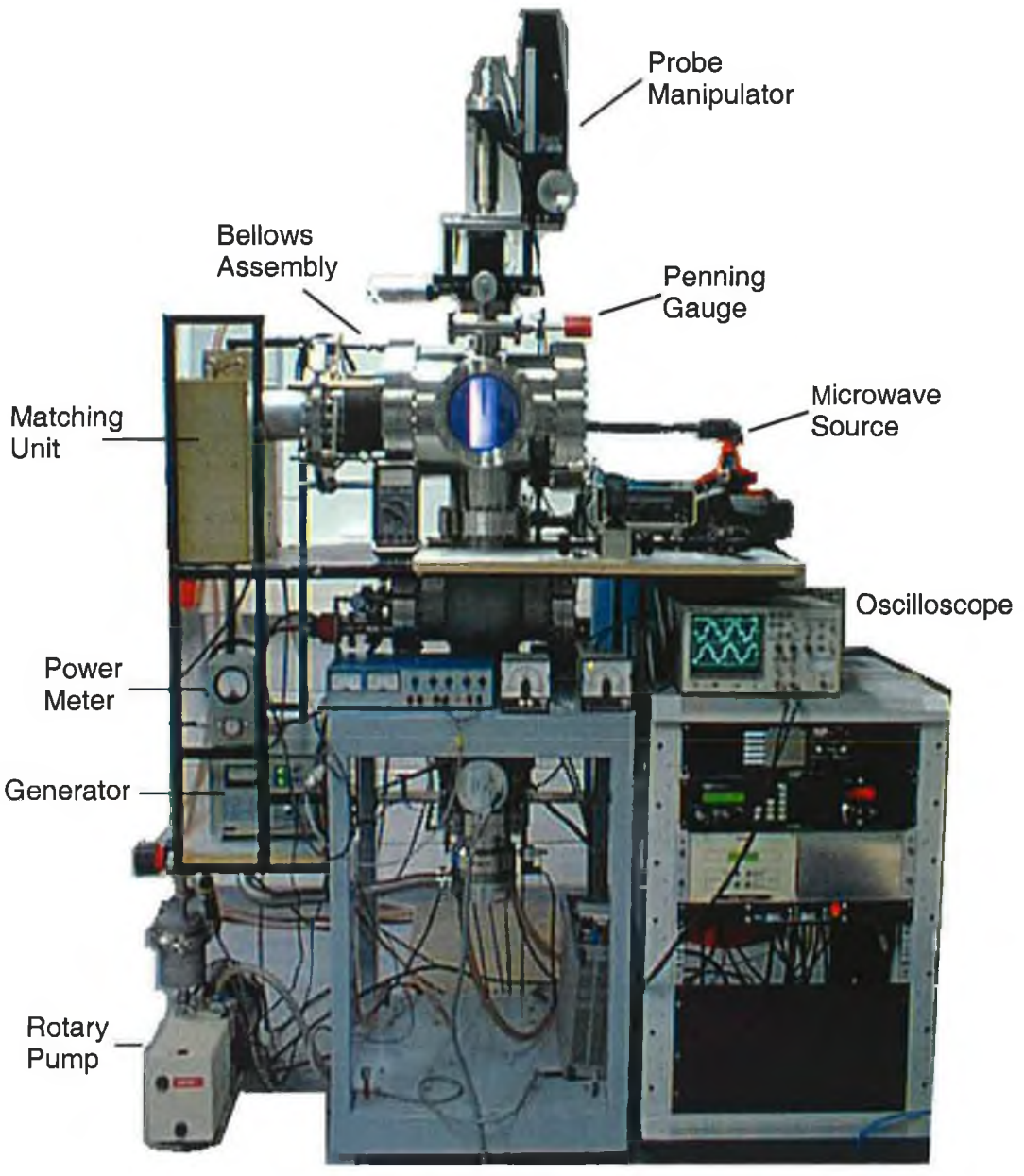

Figure 2.2: Picture of experimental system 2.

2.3 The Langmuir Probe

Introduction

In its simplest form, a Langmuir probe is a refractory metal wire placed in a discharge. The most basic probe method is to measure the current drawn from the plasma as a

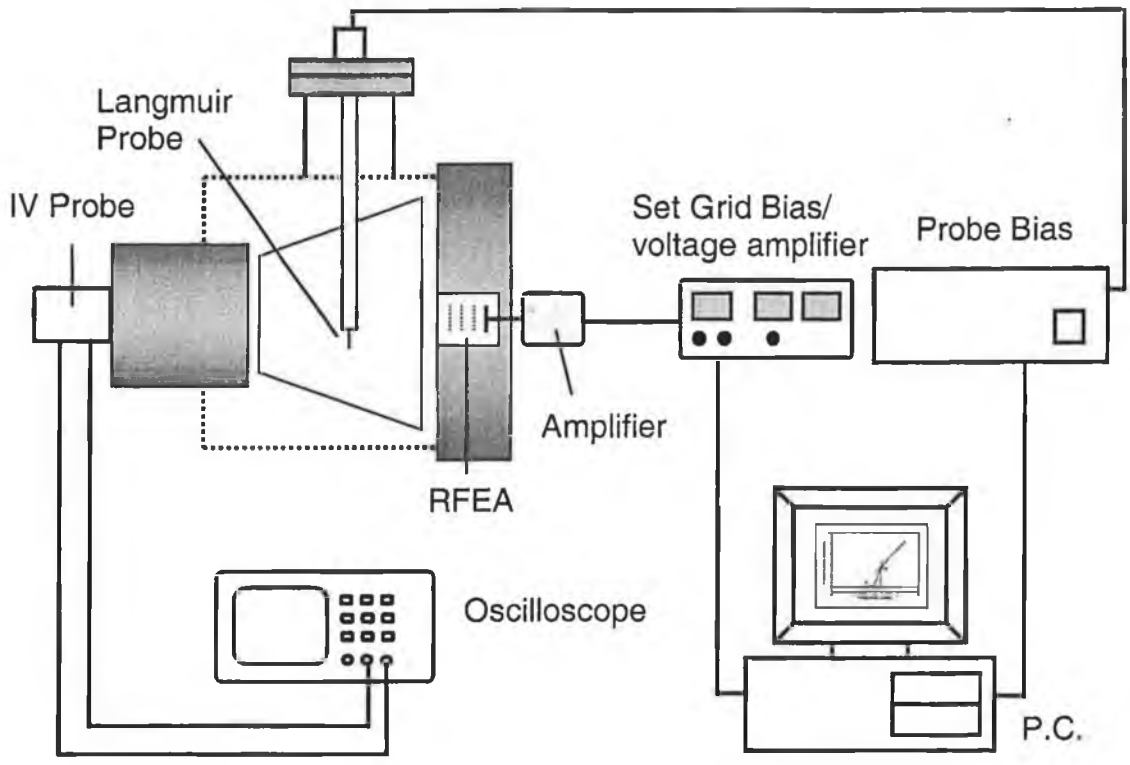

Figure 2.3: Schematic of the Langmuir probe, retarding–field energy analyser and the current voltage monitor on system 2.

function of the applied probe bias. This bias is set relative to a reference electrode that is usually the grounded chamber wall.

Langmuir probes may be plane, spherical or cylindrical. The cylindrical type is most commonly used as it has several advantages over the others. It may be easily employed in both spatial and temporal determination of plasma parameters. These types of probes are relatively easily constructed and have a small surface area so as to minimise disturbance to the plasma.

Biasing the probe results in the sheath that surrounds it increasing in width so the particle collection changes from being radial to orbit motion limited. In this instance, all particles entering the sheath are not necessarily collected [1]. The theory of Laframboise is used here to account for the expansion of the sheath with the probe bias [2]. This theory is described in section 2.3.2. The primary drawback of this theory is that it does not take collisions into account, so it is only valid at low pressures or a small sheath.

2.3.1 Langmuir Theory

The theory detailed here is the classical theory developed by Langmuir and Mott-Smith [6]. The theory assumes that the potential difference between the probe and plasma is dropped across the sheath that forms around the probe tip. The theory used depends on the probe radius, r_p, the Debye length, $\lambda_D=(T_e\varepsilon_0/ne)^{1/2}$ and the mean free path, λ_{mfp}. There are four regimes [4]

$r_p/\lambda_D >> 1$; collisionless thin sheath; $\lambda_{mfp}/\lambda_D > 1$

$r_p/\lambda_D >> 1$; collisional thin sheath; $\lambda_{mfp}/\lambda_D < 1$

$r_p/\lambda_D << 1$; collisionless thick sheath; $\lambda_{mfp}/\lambda_D > 1$

$r_p/\lambda_D << 1$; collisional thick sheath; $\lambda_{mfp}/\lambda_D > 1$

In our case, the probe tip radius is 0.19mm. The maximum operating pressure for experiments is 300mTorr. The mean free path at 300mTorr is 0.125mm. Assuming an electron temperature of 2 eV and a density of 7 x 10^9cm^{-3}, the Debye length is 0.11 mm. This results in $r_p/\lambda_D \approx 1.7$. When $r_p/\lambda_D=1$ the region of operation is known as orbital motion limited [1]. At 300 mTorr the probe is operating on the threshold of a thin sheath/orbital motion limited regime. The theory of Laframboise is used to infer plasma parameters, as this assumes no collisions the density measurements at 300 mTorr are then underestimated. This is further considered in section 2.5.

There are several simplifying assumptions made regarding the plasma when interpreting probe data. It is assumed that all charged particles have Maxwellian velocity distributions and that the electron temperature is much greater than the ion temperature. It is assumed that all charged particles reaching the probe are absorbed and that no magnetic fields are present. The discharge is assumed to exhibit collective behaviour and be quasineutral, homogeneous and infinite in extent [5]. Probe data requires careful interpretation, particularly as the simplifying assumptions mentioned are not always met.

As mentioned, the simplest probe method is the measurement of current drawn as a function of the bias voltage applied to it. A typical cylindrical probe current voltage characteristic and an 'ideal', plane probe characteristic are shown in figure 2.4. In region A, the probe is biased strongly negative, it will only collect ions. This bias should be negative enough to collect ions only; it should repel any contribution from high-energy electrons. In this ion saturation region, the current to the probe is given by

$$I_{isat} = \frac{n_{i0} e A v_s}{4} \qquad 2.3.1$$

where n_{io} is the ion density, A is the sheath (surrounding the probe tip) area, e is the electronic charge and v_s is the ion acoustic velocity given by

$$v_s = \left(\frac{kT_e}{m_i} \right)^{1/2} \qquad 2.3.2$$

This is the minimum velocity that the ions must have to enter the sheath, i.e. the Bohm velocity [6].

Region B of the curve in figure 2.4 is the electron retardation region. As the probe bias is made less negative, fast electrons start to be collected. At a certain point equal fluxes of electrons and ions are collected and the probe is at the floating potential, V_f. As the probe is biased more positively it begins to collect electrons, the faster ones first. The density of electrons in the ion sheath is governed by Boltzmann's law

$$n_e = n_{e0} \exp\left[\frac{eV_p}{kT} \right] \qquad 2.3.3$$

where n_{e0} is the electron density in the plasma, V_p the plasma potential and T the temperature in Kelvin. The electron current at the sheath edge is given by I_{eret}

$$I_{eret} = -\frac{n_e e A v_e}{4} \qquad 2.3.4$$

where all symbols have the same meaning as in 2.3.1 except v_e, this is the average electron velocity calculated using a Maxwell-Boltzmann velocity distribution

$$v_e = \left(\frac{8kT_e}{\pi m} \right)^{1/2} \qquad 2.3.5$$

The electron current in part B of the characteristic, I_{eret} is

$$I_{eret} = -n_{e0} \exp\left[\frac{e(V - V_p)}{kT} \right] \frac{eAv_e}{4} \qquad 2.3.6$$

$$= -I_{isat} \exp\left[\frac{e(V - V_p)}{kT} \right] \qquad 2.3.7$$

where V is the probe potential. The total current to the probe is then

$$I_{probe} = I_{isat} - I_{eret} \exp\left[\frac{e(V - V_p)}{kT}\right] \qquad 2.3.8$$

At a certain positive probe bias V_p, the probe is at the same potential as the plasma and there is no sheath around the probe tip. The movement of the electrons and ions to the probe is due to their thermal velocity only. At values of probe voltage above the plasma potential (section C of the *IV* characteristic), the characteristic is called the electron saturation region and the electron current is ideally

$$I_{esat} = -\frac{n_{e0} e A v_e}{4} \qquad 2.3.9$$

Equation 2.3.9 implies that the probe current is constant for probe voltages greater than the plasma potential. This occurs only for large area probes that deplete the plasma and so are unsuitable for measurements. Figure 2.4 shows a typical (small area) probe characteristic that does not have a well defined electron saturation region. This is because not all electrons entering the sheath are collected by the probe, some pass by and escape from the sheath without being detected. If the probe is small compared to the radius of the sheath around it, the electron current continues to increase over V_p. The higher the probe potential, the stronger the force pulling the electrons to the probe, so the electron saturation current increases with *V*.

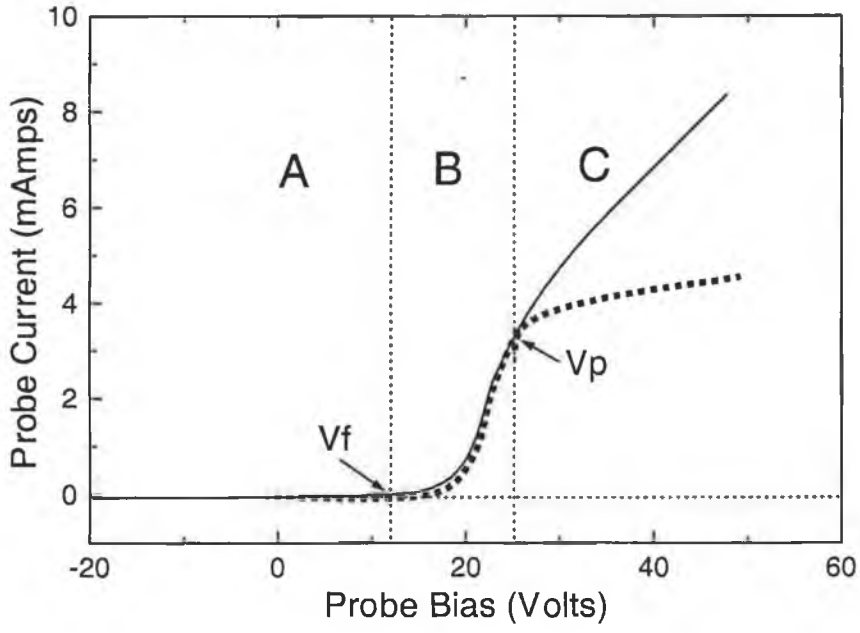

Figure 2.4: Typical Langmuir probe current-voltage characteristic (solid line) compared to an ideal characteristic (dashed line).

2.3.2 Extraction of Plasma Parameters using Laframboise Theory

While it is clear that a simple current-voltage characteristic yields some information about a plasma, accurate calculation of plasma parameters requires further analysis. The simplified Langmuir theory discussed in the previous section is not exact for several reasons. The ion saturation region is difficult to describe quantitatively. In this region not all the probe bias is dropped across the sheath so a sharp, constant sheath edge may not be assumed. As the probe bias becomes more negative, the sheath and therefore the effective collection area expands. Laframboise's theory takes these factors into account and gives a numerical solution for the ion saturation current. A cylindrical probe has the advantage over a plane probe in that it causes less perturbation to the plasma. The expansion of ion current to the probe may be described as a function of applied potential, V as follows

$$\frac{I_i}{I_{ith}}(V) = f\left(\frac{r_p}{\lambda_D}, \chi\right), \qquad V < V_p \qquad 2.3.10$$

$$\frac{I_e}{I_{eth}}(V) = f\left(\frac{r_p}{\lambda_D}, \chi\right), \qquad V > V_p \qquad 2.3.11$$

Where I_{ith} and I_{eth} are the random ion and electron thermal currents and are given by

$$I_{ith} = n_i l r_p e\left(\frac{2\pi k T_e}{m_i}\right)^{1/2} \qquad 2.3.12$$

$$I_{eth} = n_e l r_p e\left(\frac{2\pi k T_e}{m_e}\right)^{1/2} \qquad 2.3.13$$

$f(r_p/\lambda_D,\chi)$ is the expansion factor as calculated by Laframboise in the zero ion temperature limit $T_i << T_e$, n_i and n_e are the ion and electron densities respectively, r_p is the probe radius and l is the probe length. This factor f is derived from numerical fits to Laframboise curves [2]. χ is the (non-dimensional) probe voltage, and is given by

$$\chi = \frac{e(V - V_p)}{kT} \qquad 2.3.14$$

In order to use these equations to determine plasma parameters, V_p, kT_e and λ_D must be known. This requires iteration to be used. V_p, kT_e and λ_D are estimated by taking an IV probe characteristic using a coarse voltage resolution and applying simple Langmuir

theory to it [7]. The plasma potential is determined from the peak in the first derivative of the *IV* characteristic. The electron current to a probe in a retarding field is

$$I_{eret} = I_{esat} \exp\left[\frac{e(V - V_p)}{kT}\right] \qquad 2.3.15$$

$$\Rightarrow \ln I_{eret} - \ln I_{esat} = \frac{eV}{kT} - \frac{eV_p}{kT} \qquad 2.3.16$$

$$\Rightarrow \frac{d}{dV}(\ln I_{eret}) = \frac{e}{kT} \qquad 2.3.17$$

So a plot of *ln* I_{eret} *versus* V_{probe} gives a slope of e/kT, the reciprocal of which is T_e in eV. $\chi(V)$ is then calculated and a value for r_p/λ_D is determined by fitting the probe current, $I(\chi)$, to the theoretical predictions of Laframboise [8]. This fitting occurs at a very negative voltage where it is assumed that there is no contribution of fast electrons to the current. The actual electron and ion densities may now be calculated as follows by substitution

$$n_i = \frac{I_i(\chi)}{er_p l\left(\frac{2\pi kT}{m_i}\right)^{1/2} f\left(\frac{r_p}{\lambda_D}, \chi\right)}, \chi < 0 \qquad 2.3.18$$

$$n_e = \frac{-I_e(\chi)}{er_p l\left(\frac{2\pi kT}{m_e}\right)^{1/2} f\left(\frac{r_p}{\lambda_D}, \chi\right)}, \chi > 0 \qquad 2.3.19$$

Where $I_e(\chi)$ is the current at a positive voltage with respect to the plasma potential and $I_i(\chi)$ is the current measured at a strongly negative voltage [8,9]. The calculation of V_p using the maximum of the first derivative has a problem in that this point is usually below the saturation point. So a new value of V_p is obtained by extrapolating the electron saturation and retardation regions. This method of intersecting slopes yields a new value for V_p

$$V_{p(new)} = V_{p(old)} + \frac{kT}{e} \ln\left(\frac{I_{e(new)}}{I_{e(old)}}\right) \qquad 2.3.20$$

A new value for T_e is calculated using the $(\chi) - I_i(\chi)$; of electron current using

$$I_{e(new)}(\chi) = I_{e(old)}(\chi) - I_i(\chi) \qquad 2.3.21$$

The above analysis is used in determining plasma parameters for some of the data in Chapter 3, using a purpose-written, Quickbasic™ program. The remainder of data presented in this thesis is obtained using Scientific System's 'Smartsoft 'program. The probe bias throughout the whole iteration cycle is corrected for series resistance, R_{series}, due to inductors, leads, etc. The probe bias is also corrected for changes in the plasma potential, ΔV_{ref}, measured by the reference probe caused by the plasma-ground sheath resistance. The probe bias is then given by [10]

$$V_{corrected} = V_{probe} - IR_{series} - \Delta V_{ref} \qquad 2.3.22$$

R_{series} is 8.5 Ohms for the probe used here. An explanation for and measurements of the plasma-ground sheath resistance are presented in Chapter 3.

In the newer software, the initial, 'glance' analysis that precedes the Laframboise analysis is similar to what has been described except there is a choice of how the plasma potential is determined. If 'second derivative' is selected then the 'glance' analysis works as follows. V_p is defined as the voltage at which $d^2I/dV^2 = 0$. V and I are fitted to a least-squares fit

$$I = AV^2 + BV + C \qquad 2.3.23$$

over a moving spline of fixed width (user defined). When the spline reaches a point where $2A=0$, I''=0 and the spline centre = V_p. The electron temperature is determined using integration

$$\frac{\int_{Vf}^{Vp}\int_{Vf}^{V} e^{-eV/kT}\,dVdV}{\int_{Vf}^{Vp} e^{-eV/kT}\,dV} = \frac{kT}{e} \qquad 2.3.24$$

$$\Rightarrow \frac{\int_{Vf}^{Vp}\int_{Vf}^{V} I(V)\,dVdV}{\int_{Vf}^{Vp} I(V)\,dV} \approx \frac{kT}{e} \qquad 2.3.25$$

This technique has the advantage that it is not sensitive to noise. In this case n_e, the electron density is evaluated using [10]

$$n_e = \frac{I(V_p)}{A}\left(\frac{2\pi m_e}{e^2 kT_e}\right)^{1/2} \qquad 2.3.26$$

Where, A is the probe surface area, m_e is the electron mass, e the charge on the electron and T_e the electron temperature as calculated in equation 2.3.23. The floating potential, V_f, is obtained from a spline fit of $I=aV+b$. The spline is fitted to the region where $I(V)$ changes sign.

If the intersecting slopes method is chosen then a different procedure is used to determine the parameters, T_e is calculated from a least square fit of *ln I versus V* over a pre-determined region on the *IV* curve. The electron and ion densities are determined using the Laframboise theory as before.

The software also allows user selection of the plasma potential that is useful in the event of a poorly defined electron saturation region in the *IV* characteristic. This is a common occurrence in probe measurements. All density measurements presented in this thesis are that of ion density because this region is clearly defined as is shown in figures 2.4 and 2.5.

The zero-crossing point of the second derivative is usually used as it is considered the most accurate method of determining the plasma potential [11]. However, the intersecting slopes method is useful for noisy plasmas where zero crossing point of the second derivative may not be well defined. The probe software determines the particle density and temperature from a theoretical fit to the *IV* characteristic that assumes a single Maxwellian temperature distribution. If the fit is not exact in the electron saturation region, then the electron density is over/underestimated. It has been found that using the zero-crossing point a theory curve is produced which often does not fit the experimental curve in the electron saturation region. For this reason, the intersecting slopes and select V_p methods are used to determine electron density, otherwise the ion density alone is presented. Figure 2.5 illustrates this point.

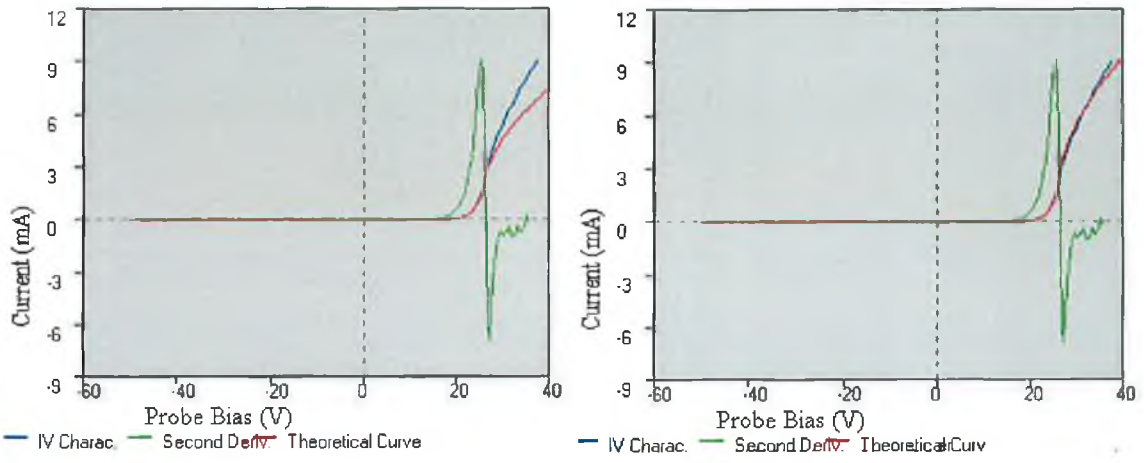

Figure 2.5: The same IV characteristic analysed using (a) the zero second derivative method and (b) the intersecting slopes method.

2.3.3 Evaluation of the Electron Energy Probability Function

Measurement of the electron energy probability function is one of the most fundamental methods of characterising a discharge for several reasons. In many discharges, particularly capacitively-coupled discharges, the energy probability function is not a single Maxwellian. Since probe theory and the estimation of parameters such as electron temperature assumes a Maxwellian distribution, knowledge of the probability function is then necessary to examine the separate temperature groups in the plasma [12,13]. Calculation of the probability function is also important for the calculation of the rate coefficients of important plasma processes such as ionization, excitation and recombination [14]. Rate coefficients may be obtained by integrating over the relevant cross-section after weighting the cross section with the normalised EEPF. The rate coefficient is obtained as follows

$$\langle \sigma v \rangle = \int f(\varepsilon)\sigma(\varepsilon)v(\varepsilon)d\varepsilon \qquad 2.3.27$$

where $f(\varepsilon)$ is the electron distribution function (obtained from the probability function, the EEPF is the EEDF times $(\varepsilon)^{-1/2}$), $\sigma(\varepsilon)$ is the cross-section for the relevant reaction and $v(\varepsilon)$ is the electron velocity.

Assuming that the electron energy probability function is isotropic, it is given by equation 2.3.28 which is known as the Druyvesteyn method of calculating the EEPF [15].

$$f(\varepsilon) = \frac{m_e}{e^2 \pi r_p l}\sqrt{\frac{2}{m_e}}\frac{d^2 I_e}{dV^2} \qquad 2.3.28$$

From this relation it is clear that simply differentiating the *IV* characteristic twice gives the EEPF. The electron density and energy are then calculated using

$$n_e = \int_0^\infty \sqrt{E} f(E) dE \qquad 2.3.29$$

$$\bar{\varepsilon} = \frac{\int_0^\infty E^{3/2} f(E) dE}{\int_0^\infty \sqrt{E} f(E) dE} \qquad 2.3.30$$

EEPFs measured in argon are often non-Maxwellian. Figure 2.6 shows an EEPF measured in a 15 watt argon plasma at 300 mTorr. It is the Druyvesteyn form typical of such discharges.

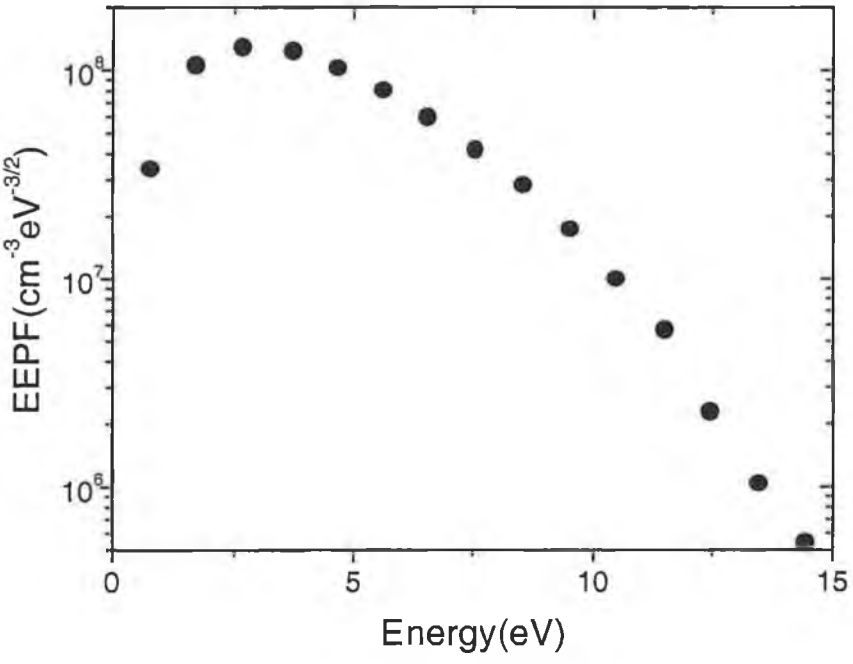

Figure 2.6: EEPF measured in a 15 watt argon plasma at 300 mTorr.

2.3.4 Operation of the Tuned Probe

One of the main problems with probes in rf plasmas is that the plasma potential, V_p, fluctuates with time. Therefore, if the probe is at a fixed bias, the fluctuating voltage across the probe sheath results in a time-varying current being measured. A large rf voltage appearing across the probe sheath shifts the floating potential to a more negative value and distorts the *IV* characteristic. This results in distortion of the electron energy distribution that results in an over-estimation of T_e and under-estimation of n_e [1,5,16].

A second issue with the use of Langmuir probes in rf discharges is the prevention of loading of the plasma. This occurs also because the current collected is a function of time and is oscillating at 13.56MHz. A typical co-axial cable has a

capacitance of approximately 100pF per metre and a capacitive impedance of approximately 100Ω at the rf frequency. For this reason the impedance between probe and ground needs to be greatly increased.

There are several probe techniques used to eliminate the problems caused by rf distortion of the probe characteristic. One approach records the time dependence of the probe current so that the instantaneous distributions of the electrons reaching the probe are obtained [17]. Another approach removes the rf modulation of the probe sheath by either actively driving the probe tip in tandem with the applied rf signal or by increasing the probe impedance at the rf frequency [18,19]. The method of choice for this probe is a passively compensated, tuned Langmuir probe [16,19].

High voltage capacitive discharges such as those examined in the following chapters are subject to sputtering that increases the effective probe area should a layer of the conducting sputtered material form on the ceramic probe holder and touch the probe tip. A hollow cavity around the probe tip inside the ceramic support prevents this. A schematic of the probe is shown in figure 2.7. Another feature of the probe is an automatic clean routine that allows routine cleaning of the tip to avoid contamination from sputtered material.

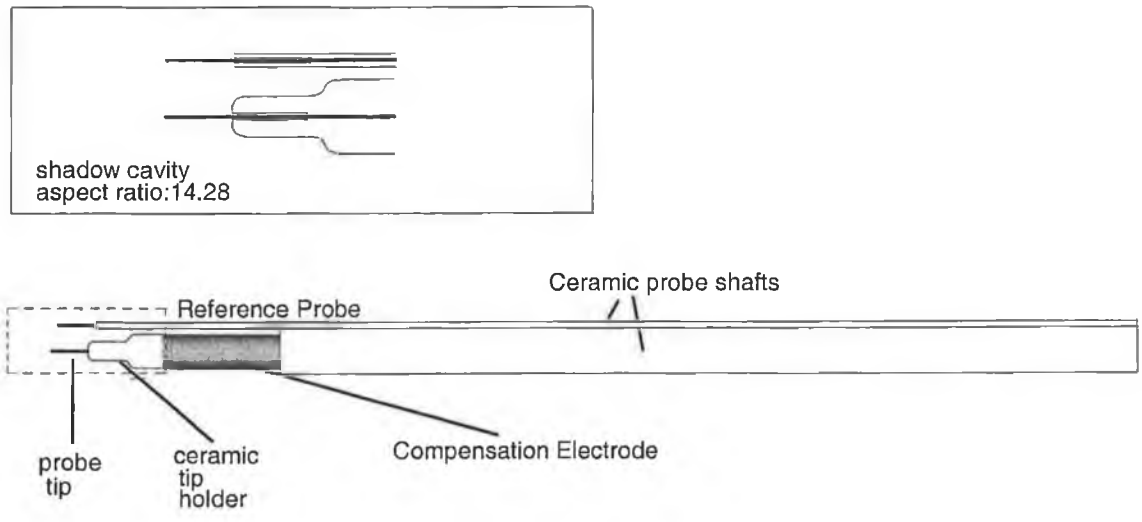

Figure 2.7: Schematic of the Langmuir probe used in system 2. Inset: shadow cavity that prevents sputtered material from increasing the probe tip area.

The operation of the tuned probe is best explained using an equivalent circuit, figure 2.8. The rf voltage across the sheath is minimised by making the impedance of the sheath small compared to the probe-ground impedance so that the probe floats at the rf potential.

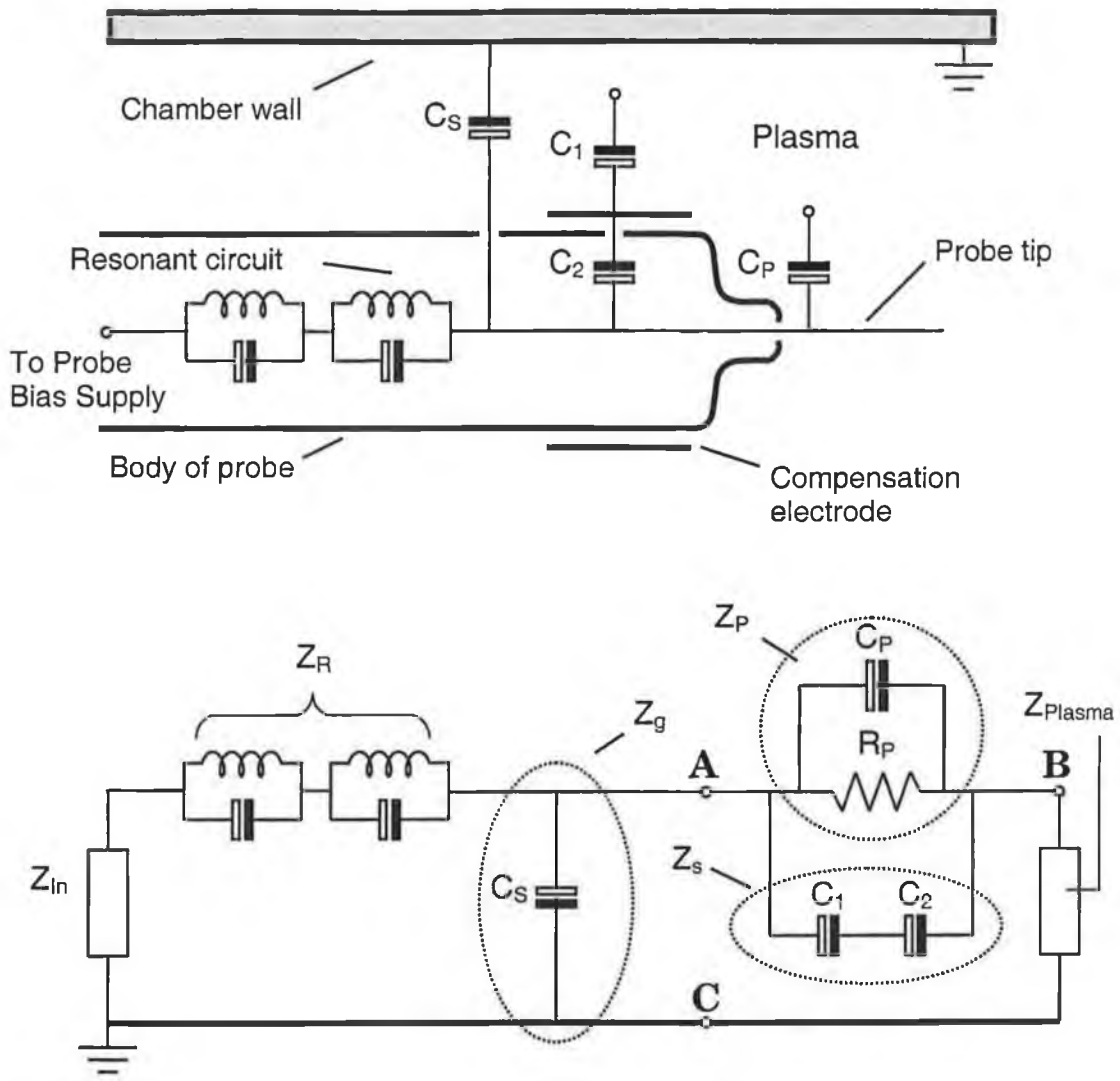

Figure 2.8: Probe schematic and equivalent circuit illustrating compensation circuit. Z_p=Plasma-tip impedance, Z_g=probe-ground impedance, C_2=shunt capacitance, C_s parasitic capacitance. A = Probe tip, B = Plasma (outside tip sheath), C = Chamber wall.

Z_p, the plasma tip impedance, must be much less than Z_g, the probe-ground impedance so the tip will be forced to float at the rf potential. When ω, the excitation frequency, is greater than ω_i, the ion plasma frequency, the rf sheath is essentially capacitive [14]. The value of the sheath capacitance is therefore [9,16]

$$C_p = \left[\frac{2\pi\varepsilon_0 l}{\ln\left[\frac{r_s + r_p}{r_p}\right]} \right] \qquad 2.3.31$$

Where l is the tip length, r_s is the sheath width and r_p is the probe radius. Using Langmuir's equation, r_s may be calculated

$$r_s \cong \lambda_D \left(1+\frac{V}{kT_e}\right)^{1/2} \qquad 2.3.32$$

Assuming a T_e of 3 eV and n_e of 7 x10^9cm^{-3}, r_s is approximately two Debye lengths. Assuming that $r_s=2\lambda_D$ and taking l=5mm and r_p=0.19mm, C_p is 2.76pF. This results in a plasma-tip impedance of 4.25kΩ. The probe-ground impedance, Z_g is made up of the rf chokes in parallel with both the capacitances associated with the chokes and an additional parasitic capacitance C_s. When Z_p/Z_g is very small, very little rf potential can appear across the plasma-tip sheath (i.e between points A and B).

Z_p is further reduced by capacitively-coupling to a large conducting surface (a cylindrical aluminium sleeve) represented by C_2 [18]. The value of C_2 is

$$C_2 = \left[\frac{2\pi\varepsilon_0 l}{\ln\left[\frac{\lambda_D + r_p}{r_p}\right]}\right] \qquad 2.3.33$$

Since this quantity is independent of the probe bias, having it in parallel with C_p shunts Z_p and also makes the probe tip capacitance independent of the probe bias voltage [16,20]. C_2 in this instance is 20pF, corresponding to an impedance of 587Ω at 13.56 MHz. C_2 and C_p in parallel result in a reduced impedance of 515Ω, so the impedance across the plasma-tip interface is significantly reduced. The ratio Z_p/Z_g may be further reduced by reducing parasitic capacitances and maximising the inductor impedances at the rf frequency. This is done by placing the inductors close to the tip [16]. Since the inductors resonate at or close to 13.56 MHz, Z_g is of the order of 1x10^5Ω. This type of probe set up results in an unconvoluted characteristic.

2.3.5 Probe System Hardware and Data Acquisition

The probe system is fully automated. As shown in figure 2.3, it consists of the Langmuir probe (with reference probe), which is connected to the data acquisition unit and interfaced to a personal computer. This unit includes two 14-bit ADC's to measure voltage and current and send it to the P.C. and one DAC to bias the probe according to the program settings. The probe current is measured as a potential across one of five resistors (measurable current 30μAmps to 300mAmps). The probe bias is measured before the resistor. The probe bias is set to go from a very negative voltage to ensure

the ion saturation region is measured. The maximum probe bias is set to a few volts above the plasma potential as biasing a probe high above the plasma potential results in breakdown and heating, even cleaning of the probe tip. This bias voltage is corrected for series resistance and the changes in plasma potential as described in section 2.3.2. There are typically 120 samples per point taken when acquiring an *IV* characteristic (i.e. one scan). Five scans are taken per measurement, with the final result being the average and the error bar the standard deviation of the five measurements. Standard deviations of less than one percent are usual in a measurement so the error bars are not plotted in the data presented in this thesis. The automatic clean function prevents probe tip contamination by regular cleaning by electron bombardment.

Results obtained using the Langmuir probe will be presented in detail in subsequent chapters. An issue with probe measurements in the past has been stability and reproducibility. A feature of the probe system is that it can perform temporally resolved measurements. Before an experiment was undertaken it was usual to perform a temporal scan of the basic plasma parameters for 20 to 30 minutes. Deviations of less than 5 percent are typical in the data presented here. A demonstration of the day to day reproducibility of the data is shown in figure 2.9.

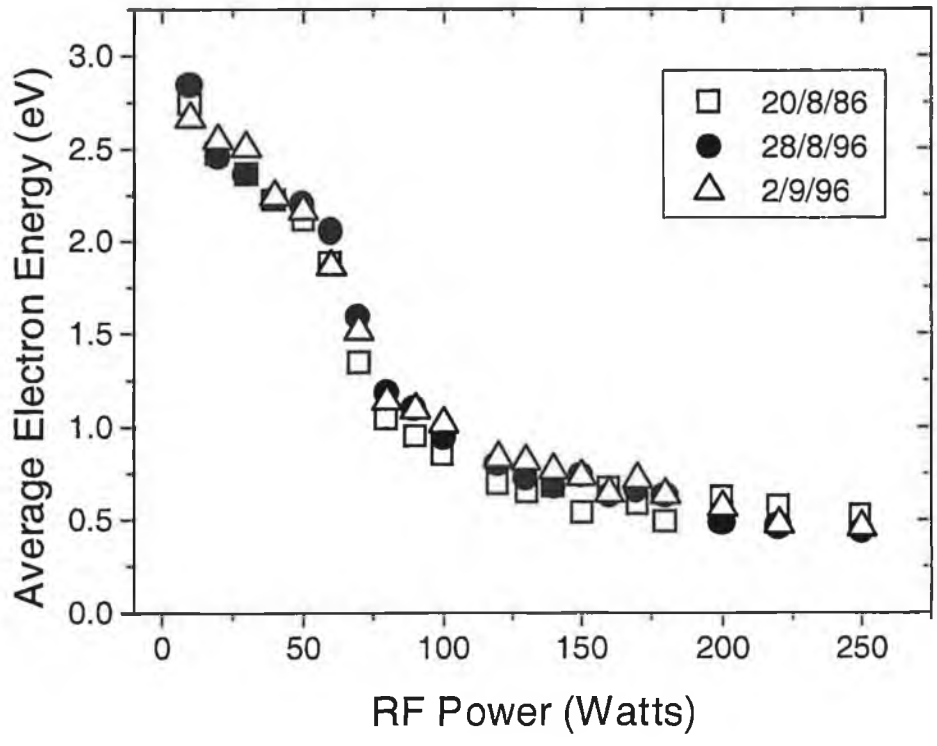

Figure 2.9: Electron temperature measured using the Langmuir probe on three different dates.

2.3.6 Results and Discussion

Probe measurements in radio-frequency plasmas can difficult to perform and interpret for reasons already discussed. The simple Langmuir theory is not enough to correctly infer plasma parameters so the more complicated theory of Laframboise is used. A tuned probe is used to minimise the effect of the rf plasma potential on the measurements. The probe is carefully designed and constructed so as to minimise the disturbance to the plasma. Features such as the automatic clean function and the shadow cavity allow measurements in high-voltage plasmas where sputtering of the electrode material onto the probe surface becomes an issue. Sections 2.4 and 2.5 discuss alternative methods of measuring plasma parameters. It will be shown that agreement with the probe data is excellent over the operating parameters used. It is the ability of the probe to measure locally the plasma parameters that makes it the most utilised diagnostic in this work.

The reproducibility of probe data was shown in figure 2.9. Another test of probe quality is of energy resolution and dynamic range. The energy resolution is demonstrated in figure 2.10, where notable features in the EEPF are resolved. A set of nitrogen EEPFs measured in a capacitive system (section 2.2) are shown. A minimum at approximately 3-4eV is clearly seen. This is characteristic of nitrogen at 100 mTorr and is due to the large cross section for inelastic collisions involving the vibration excitation of the N_2 molecule [16,21].

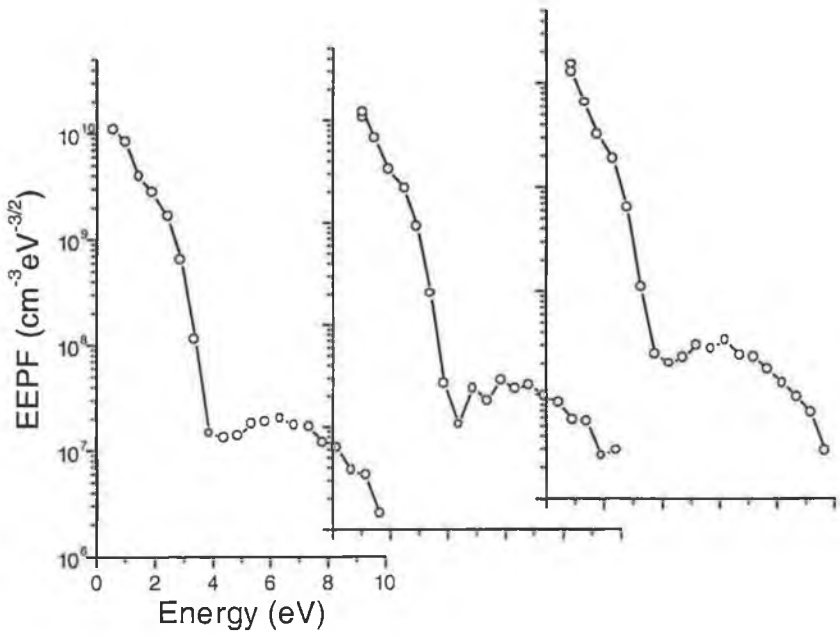

Figure 2.10: EEPFs measured in a 100 mTorr, 10 watt nitrogen plasma. The leftmost graph indicates the scaling.

As was stated in section 2.3.3, Measurement of the EEPF is essential in such discharges because the electrons are not in thermal equilibrium and therefore cannot be assumed to have a Maxwellian (single temperature) distribution. It will be shown in following chapters that EEPF measurements in argon are seldom Maxwellian. Examination of the separate temperature groups in the plasma then requires an accurate measurement of the distribution function. Since the EEPF is obtained by differentiating the *IV* characteristic, the characteristic must be as noise-free as possible since obtaining the second derivative will amplify any noise present. The high energy 'tail' observed in many distribution function measurements often has a low density so probe measurements require sufficient dynamic range to detect these populations. The probe system has proven very successful in these measurements. Figure 2.11 shows an EEPF measured in system 1 using a probe/reference probe setup. This EEDF is measured in the midplane of a high-voltage argon discharge. A dynamic range of five orders of magnitude is obtained, allowing analysis of the 'hot' component in the plasma. Further details of these measurements are in Chapter 3. Previous measurements made in these types of discharges have not been very successful due to insufficient dynamic range and the low densities of the hotter electron populations in the plasma [22].

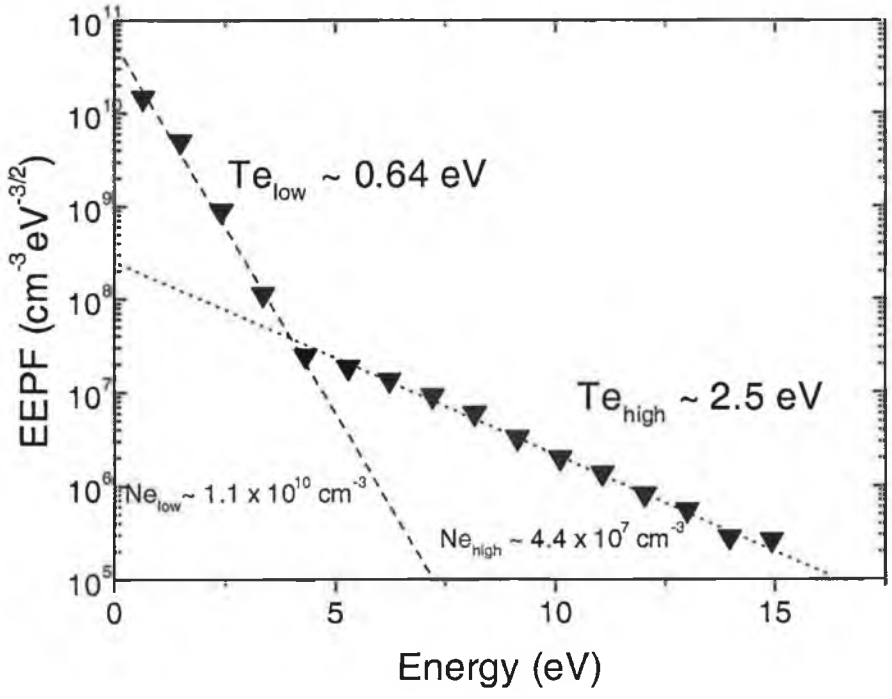

Figure 2.11: EEPF measured in the midplane of an argon discharge at 100 watts.

2.4 The Retarding Field Energy Analyser

Introduction

Capacitively coupled rf discharges with the asymmetric electrode geometry are frequently used for applications such as plasma enhanced deposition and etching. Consequently, the ion energy distribution (IED) behind a capacitive rf sheath is of special interest with regard to plasma processing. The following section describes the design and implementation of a simple retarding field energy analyser with a view to comparison of the data with that obtained from the Langmuir probe.

2.4.1 Theory of Operation

The retarding field energy analyser operates by measuring the plasma ion (or electron) current drawn to a flat collector plate as a function of a retarding or discriminating electrostatic field. This retarding field is generated by applying a potential between fine wire mesh grids placed in front of the collector. The grids are held parallel to the collector and are mounted in a closed cylindrical housing of some form with an entrance hole at one end. The housing is earthed relative to the plasma. Several separate grids are commonly employed. The first grid, called the repeller, is biased with a large potential V_r, (relative to a plasma potential) with a polarity opposite to that of the measured particle species. This is to remove the non-measured charged particle species' contribution to the collector current. The next grid, called the discriminator, is biased with a variable potential with the same polarity as the measured species. Only charged particles with energy greater than the discriminating voltage ($E > eV_d$) will pass through the discriminator grid to reach the collector. Taking the differential of the collector current I_c as a function of the discriminator voltage V_d, gives the particle energy distribution.

The most versatile analyser configuration has four grids, in addition to the collector [23]. An extra grid is placed directly in front of the collector in order to suppress secondary electrons generated by energetic ions or electrons hitting the collector. This secondary grid is usually biased several volts more negative than the collector - which itself is normally biased with some appropriate potential to ensure the collection of the measured species and prevent space charge forming between the grids. The last grid is an earth or screen grid placed across the entrance zone or orifice of the analyser. This defines a constant equipotential surface to prevent the electric field of the repeller grid from bowing out into the plasma and distorting the sheath [24].

2.4.2 Design Criteria

(i)The analyser should measure the energy distributions at the ground electrode surface. Building the analyser into or behind the electrode removes any size restrictions, and it does not perturb the plasma. The large thermal mass (heat dump) of the electrode also negates the need for additional cooling.

(ii)The analyser should require the minimal number of components, and be inexpensive to fabricate and maintain.

(iii)The design should allow for flexibility in the configuration, i.e. the number of grids and their spacing.

(iv)The design should facilitate easy maintenance and replacement of damaged or contaminated grid meshes.

(v)An adjustable orifice is required to limit the plasma entering analyser so leading to detrimental space charge effects. The standard approach is replaceable orifice plates with varying hole sizes. Note the orifice also defines the acceptance angle of particles that can be measured by the analyser.

(vi)The mechanical/vacuum housing should be separate from the electrical components, i.e. allow for differential vacuum pumping of analyser.

(vii)The components and material should be compatible with high vacuum and reactive/oxidizing gases. The grids, spacers and collector should also have a low secondary electron yield. In addition low vapour pressure materials that might lead to contamination of the grids should be avoided, i.e. no glue or resins.

(viii)The analyser should be compact with minimal grid/collector capacitance. Specifically it should have a time response of less than 0.02ms (i.e. a frequency response of 50 MHz or more) to permit time resolved measurements during an rf (13.56 MHz) cycle.

Other design factors: The grid material and transparency (mesh hole size and wire size) are critical in minimizing the generation of secondary electrons. Nickel has a low secondary emission coefficient and low reactivity. The mesh transparency should also be as high as possible (at least 50%) to minimize collisions. However the mesh hole size should be less than the Debye length of the plasma in the entrance zone. For expected plasma parameters a nickel mesh with a 0.04mm aperture and 60% transmission is appropriate.

Together with the mesh hole size, the spacing between the grids is a major factor in determining the energy resolution of the analyser. Sakai and Katsumata [25]

demonstrated that increasing the grid spacing may improve the energy resolution. Conway *et al* found that the distance between the repeller and discriminator was the primary factor to affect the resolution [26]. In this case, a repeller to discriminator distance of 1mm was used with all other grid separations set to 0.5 mm.

2.4.3 Analyser Design

The analyser described here uses features drawn from a previous successful analyser employed with a helicon rf plasma source [26]. The essence of the design is a compact grid stack with grid meshes clamped between copper spacers/contacts and thin insulator discs. The analyser underwent a series of modifications during operation to improve grid access and ease of assembly. The final version is the one that is described here. Figure 2.12 is an engineering drawing showing a cross-section of the analyser assembled into the ground electrode. The analyser and housing consists of three distinct parts, (i) the base plate and grid stack, (ii) the ground electrode, and (iii) the connector flange. The ground electrode is a detachable flat stainless steel plate that forms part of the vacuum chamber and the RF circuit. The analyser is housed in a 2.5 cm wide hole bored in the ground electrode as shown in figure 2.12. The electrode essentially forms the side walls of the analyser housing. The analyser itself is under vacuum and is pumped through a small vent hole in the detachable front base plate. The vacuum seal and electrical feed-through is provided by the 'O'-ring sealed connector flange bolted to the back face of the ground electrode. The analyser opening is defined by an interchangeable orifice plate with a range of hole diameters from 0.5mm to 2.0mm. The orifice plate is 'wire-cut' from 0.1mm thick stainless steel shim and is intended to sit directly behind the larger diameter base plate opening. There is provision however for a second orifice plate to be attached to the front of the base plate. Following the orifice plate is the grid stack that consists of a series of layers of nickel mesh, copper grid supports/spacers and insulating washers. The layers are repeated as many times as necessary to form the required number of grids. In this case, one earth grid, three biased grids and a collector. The grid is a single layer of electro-formed nickel mesh with 500 wires per inch (0.004 mm thick, 0.0ll mm wire diameter, 0.04 mm nominal aperture) and a transparency of 60%. Electrical contact to the mesh is made via a 0.4mm thick copper ring (wire-cut) with an inside diameter of 10.0 mm and an outside diameter of 14.0 mm. A 4mm long tag protrudes from the outside edge to provide a solder point for the connecting wires. The copper rings also act as grid spacers. The spacing between

individual grids can be adjusted by doubling up with more spacers or replacing the spacers with thinner ones. The inside diameter of the analyser is chosen to be several times the overall depth (the distance from the orifice to the collector) so as to minimize the liberation of secondary electrons from the copper spacers. Note that the acceptance angle of the analyser orifice is also a factor here. The insulating washers are single layers of 50 μm thick Kapton (polyimide) film. Kapton film has a maximum operating temperature of 320°C and is easy to cut. Mica is an alternative material with better electrical and thermal properties, but is more fragile mechanically. The inside and outside diameters of the insulator washers are 9.0 mm and 16.0 mm, chosen to give at least a 0.5 mm overlap with the inner and outer edges of the copper spacers. This allows for minor misalignments in the positioning of adjacent spacers without endangering their electrical isolation. The final grid, the collector, is not a mesh but a solid copper disc 0.4 mm thick and 14.0 mm diameter. The grid stack is secured by a 1.5 mm thick stainless steel clamp plate and four M2 screws. The clamp plate has a central hole to allow electrical connection to the back of the collector plate, as well as four cut-outs around its periphery to allow access to the grid solder tags underneath. The electrical connections to the grids are made via 30 AWG (0.25 mm diameter) single strand Kynar coated wires (0.5 mm diam.) to a 4 pin LEMO OB self latching socket. The LEMO socket is vacuum sealed into the stainless steel connector flange with an 'O'-ring and epoxy glue.

2.4.4 Bias Circuit and Data Acquisition

The analyser bias circuit and buffer amplifier are shown in figure 2.13. To test the operation of the analyser four separate power supplies were used. A power supply (to bias the grids V_r and V_s) and voltage amplifier circuit are incorporated into one unit for use with the device. The buffer amplifier circuit is enclosed in a metal box and mounted on the blanking plate directly at the back of the analyser (see figure 2.3 in section 2.2 for a schematic of the diagnostic setup). The collector bias V_c, floats above the current measuring resistor R_m (1kΩ to 100kΩ) and is generated by a series of 9V alkaline batteries also enclosed in a screened metal box. Special attention is paid to the ground connections and the screening of all the power supply cables. 100 μH inductors (similar to the rf chokes used in the Langmuir probe) are connected in series with each of the power supplies to prevent possible RF pickup on the grid cables from capacitively coupling to the collector. The collector current is measured as a voltage drop across the

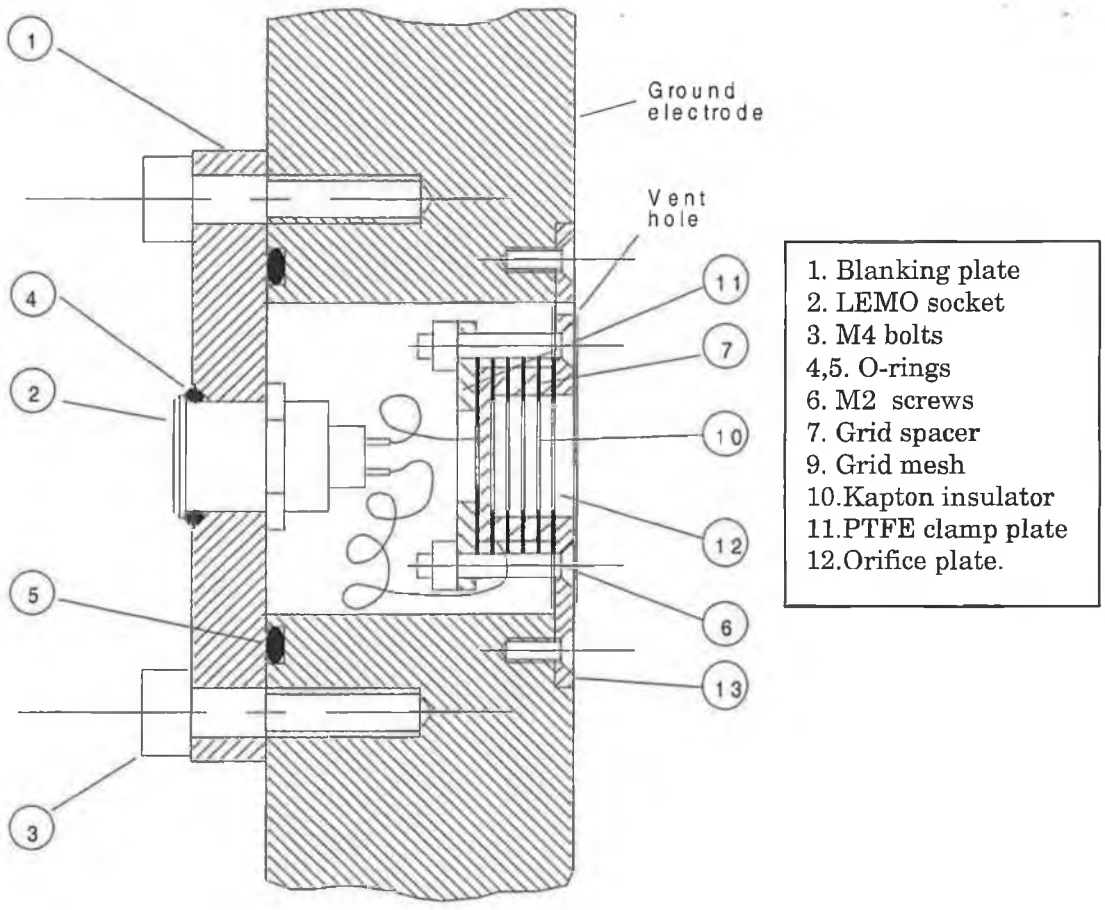

Figure 2.12: Engineering drawing of the analyser in the ground electrode of the capacitive system.

resistor R_m. using a INA117P (Burr-Brown) unity gain buffer amplifier (200V common mode rejection, 200 kHz bandwidth, powered by two 9V batteries) to decouple the bias circuit from the data acquisition. The collector signal is generally only a few mV so it is necessary to amplify the collector signal with an additional amplifier, an INA118P (Burr-Brown) precision instrumentation amplifier with an externally set gain (using resistor R_g).

For the preliminary results and bias optimization a chart recorder was used to plot the collector current against the discriminator voltage. However to obtain the energy distributions it is necessary to differentiate I_c relative to V_d. This is best achieved by sweeping V_d and sampling I_c with a data acquisition system and the numerically differentiating on a computer. The system employed here is a PC with a Bytronic MPIBM3 multi-function I/0 card. The acquisition card has an 8 channel 12 bit Analog to Digital Converter (ADC) and a 2 channel 12 bit Digital to Analog Converter (DAC), controlled via a purpose-written 'C' program. A 50 Volt discriminator sweep

potential is generated from a staircase ramp from the DAC with a programmable output voltage from -5Volts to 5Volts and a PB50 (Apex Corp.) power amplifier with a set gain of 10. The voltage step is 24mV (100V divided by 12 bits).

The collector current signal is sampled many (typically between 100 and 2000) times per voltage step with the ADC (programmable range of 0-5V). Several amplifier steps are required to bring the collector signal (of the order of 1μA, often less) up to a suitable level for measuring with the ADC. The *IV* curve is then differentiated using a 3 point gradient and the result smoothed with a 5 point moving average.

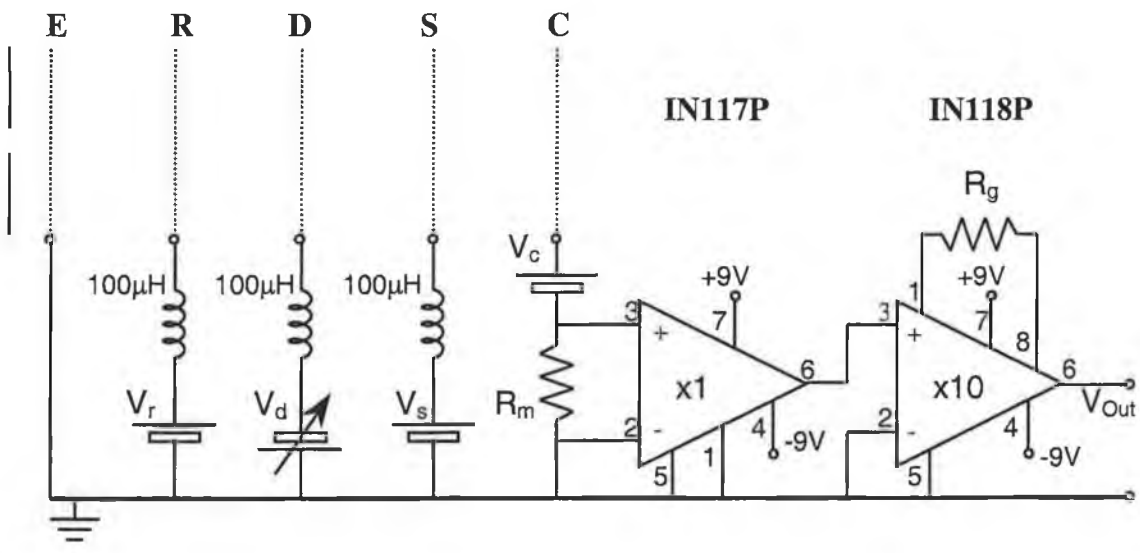

Figure 2.13: Grid bias and buffer amplifier circuit.

2.4.5 Analyser Operation

Figure 2.14 shows the individual grid currents I_r, I_d, I_s and I_c, (measured across a 100kΩ resistor) as a function of grid bias from –60 Volts to 60 Volts for an argon plasma at 3 mTorr and 48 watts of RF power. As expected the ion and electron saturation currents drop between successive grids due to the finite transmission of the mesh. However, all the grid curves display an extra kink in the electron current at around +30V bias that coincides roughly with the maximum ion energy. These kinks were also observed with other retarding field analysers and appear to be an inherent feature [23].

A standard Langmuir probe does not show any kinks or jumps in electron current around the plasma potential. Normally ions repelled by the positive probe bias form a sheath (positive space charge) which moderates the electron flow to the probe. However in the analyser, the presence of another grid (the earth grid in the case of I_r) modifies the sheath. As the discriminating grid bias increases the repelled ions are drawn to the adjacent floating grid (that is invariably at a lower potential when allowed to float) and so removed. For the plasmas encountered here, the ion energy distribution is a fairly sharp single peak above 8 mTorr so as the grid bias approaches the maximum ion energy all the ions are suddenly reflected and the electron current increases.

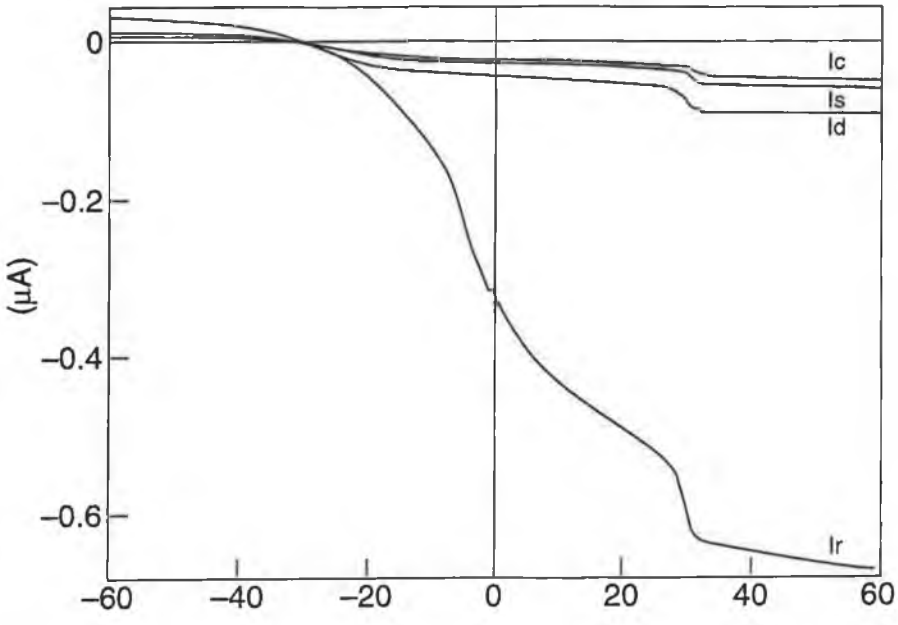

Figure 2.14: Grid current *versus* grid bias in argon at 3mTorr, 48 Watts.

2.4.6 Ion Discriminator Mode

Figure 2.15 shows a typical potential distribution along the axis of the analyser with the four grids biased for ion discrimination mode. For electron discrimination mode the grid potentials are essentially reversed - except that the suppressor grid should be at a lower potential than the collector. To operate correctly in ion discriminator mode the grid biases need to be optimized in a logical manner:

(i) Discriminator: The maximum V_d should be at least one and a half times the expected plasma potential (typically 35-45 Volts).

(ii) Repeller: Select a large negative potential for V_c so as to remove all primary (from the plasma) electrons, but not too large as it will accelerate ions unnecessarily.

(iii) Collector: V_c, should be fixed at a slightly negative voltage. Increase V_c negative to maximize I_c at zero V_d, but keep $|V_c| < |V_r|$. V_c has to be sufficiently negative to draw the ions to the collector, but not too large or else it will accelerate the ions above the impact energy threshold for secondary electron generation. Then again V_c should not be too small otherwise the suppressor grid will take too much of the ion current.

(iv) Suppressor: Increase V_s negative until I_c goes to zero at very large positive V_d. In all cases $|V_s| > |V_c|$, i.e. sufficiently more negative than the collector to reflect all secondary electrons back to the collector. V_s can be made more negative than V_r but it is still important to retain the separate repeller grid at the beginning to prevent internal ionization due to electron-neutral collisions.

It may be necessary to adjust V_r, V_c and V_s to optimize the secondary electron suppression with changes in plasma conditions, such as changing gas pressure and power. Figure 2.16 is a plot of I_c against positive V_d for various values of V_r, from 0 to -80V. V_c and V_s, are both set to zero (argon gas at 4 mTorr, 30 watts of rf power). The figure shows that a repeller bias slightly more than -80V is required to effectively remove the primary electrons at this gas pressure. The presence of secondary electrons is clearly seen as the dip in I_c at zero V_d.

With V_r = -90 Volts, V_c = -62 Volts and V_s = -63.5 Volts, figure 2.17 shows the analyser operating correctly (i.e. I_c goes to zero at large V_d and the absence of peaks and dips in I_c at lower V_d) for 4 mTorr argon gas pressure and 40 watts of rf power. Figure 2.17 also shows the current drawn by the other grids, I_s, I_d and I_r, as a function of the discriminator bias V_d. All the grids, except the suppressor, draw a positive ion current. In the ion discriminator mode the negative repeller reflects all the primary plasma electrons collected by the earth grid and accelerates the ions, some of which collide with the repeller grid resulting in a positive current. The majority of ions pass through the repeller to the discriminator and again some collide resulting in a positive current. Ions with sufficient energy pass through the discriminator and are accelerated to the negative suppressor grid, passing straight through to land on the collector. I_s is negative indicating that it is drawing secondary electrons emitted from the collector by the

impact of high energy ions. Figure 2.15 shows schematically the flow of ion and electron current.

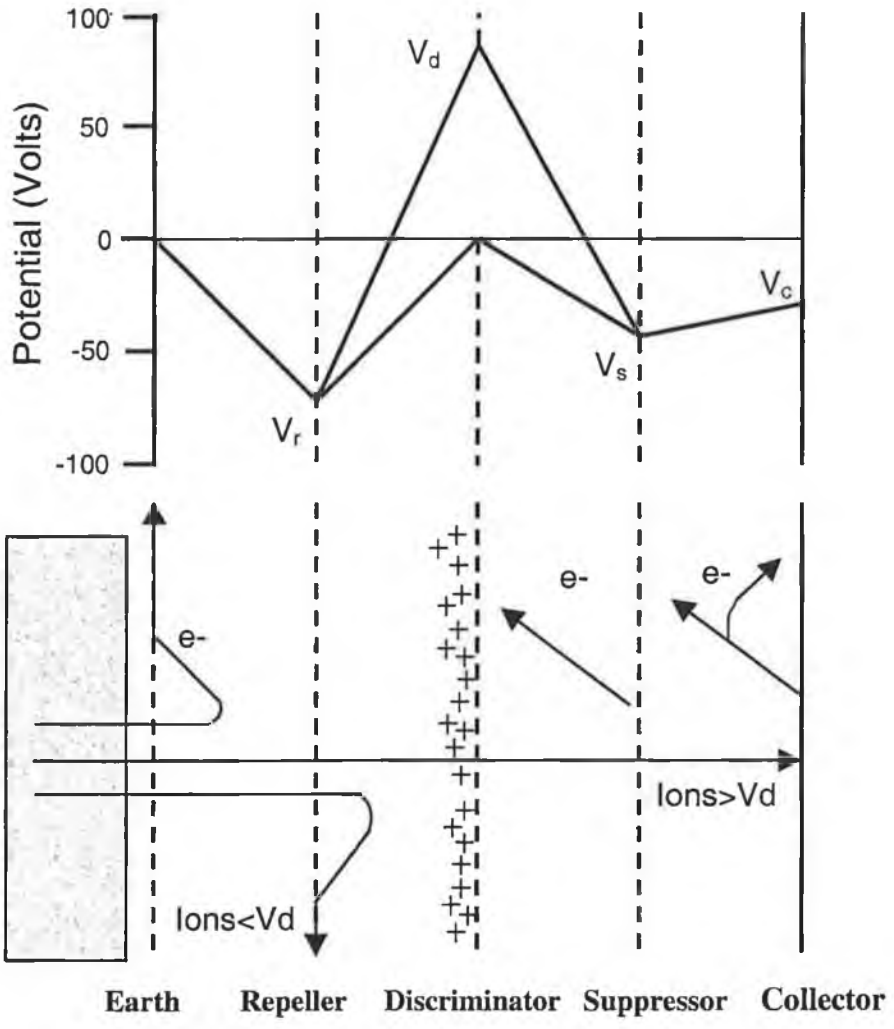

Figure 2.15: Bias distribution along analyser axis for ion collection.

From the shape of the I_c curve the ion energy distribution (IED) can be deduced as a single and fairly narrow peaked distribution with a minimum energy of around 25eV and a maximum energy around 30eV. As the discriminator potential V_d increases from zero, the low energy ions are reflected back on to the repeller grid causing I_r to rise and I_d and I_c to decrease. However as V_d approaches +23V (just below the IED base energy) both I_d and I_r begin to "roll-off" and there appears to be a slight plateau in I_c. The reason for this is possibly the sudden rise in the number of ions with energies just below the discriminator potential, which, effectively pile-up in front of the grid creating a positive space charge. This space charge raises the apparent potential barrier above that of the actual grid, thus increasing ion reflection (hence I_r) and reducing ion

collisions with the discriminator (I_d). However, once V_d rises above the real minimum ion energy, I_d saturates and I_r rises more slowly giving rise to the kink.

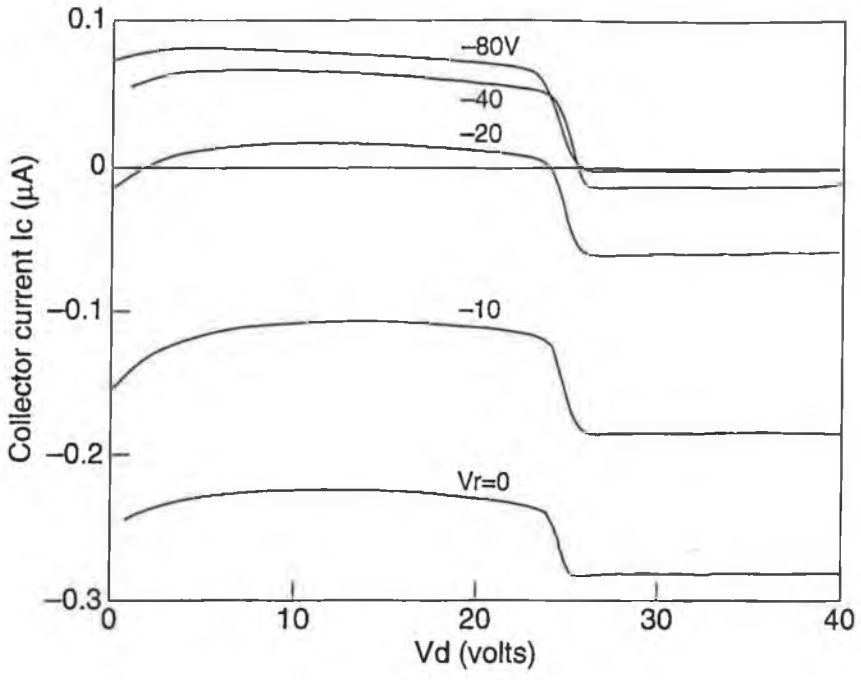

Figure 2.16: Collector current I_c as a function of discriminator bias V_d for various repeller biases V_r.

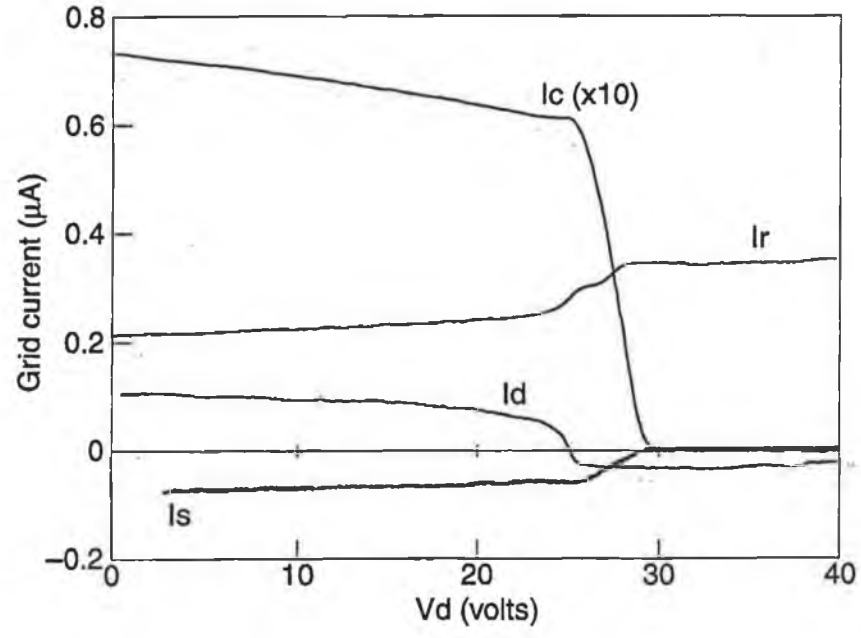

Figure 2.17: Grid currents vs discriminator bias V_d - ion collection mode. V_r -90V, V_c = -62V, V_s, = -63.5V, 4 mTorr argon, 40 watts rf power.

I_r is negative, probably because the 1.5V potential difference between the collector and the suppressor grid is, under these conditions, insufficient for a complete and effective suppression of all secondary electrons across the full range of the discriminator voltage. The energies of the ions impacting on the collector is: $E = E_i - e|V_d| + e|V_c|$, where E_i is the initial ion energy before the discriminator grid. Once V_d exceeds the peak ion energy the mean energy and the flux of the ions reaching the collector drops sharply and so the production of secondary electrons falls and I_s rises back towards zero.

Figure 2.18 shows a typical *IV* characteristic and ion energy distribution determined by numerically differentiating the *IV* curve. The conditions are 10 Watts at 10 mTorr of argon. There are 200 samples per voltage step (24mV per step) and the IED curve is smoothed with a five-point average. There is a small negative offset in the buffer amplifier chain that accounts for the negative collector current at high discriminator voltages. This is accounted for in the acquisition software. This does not affect the measured ion energy distribution. Typical full width at half-maximum values are 1.6–2.5 eV which indicates and energy resolution of 0.8-1.2 eV.

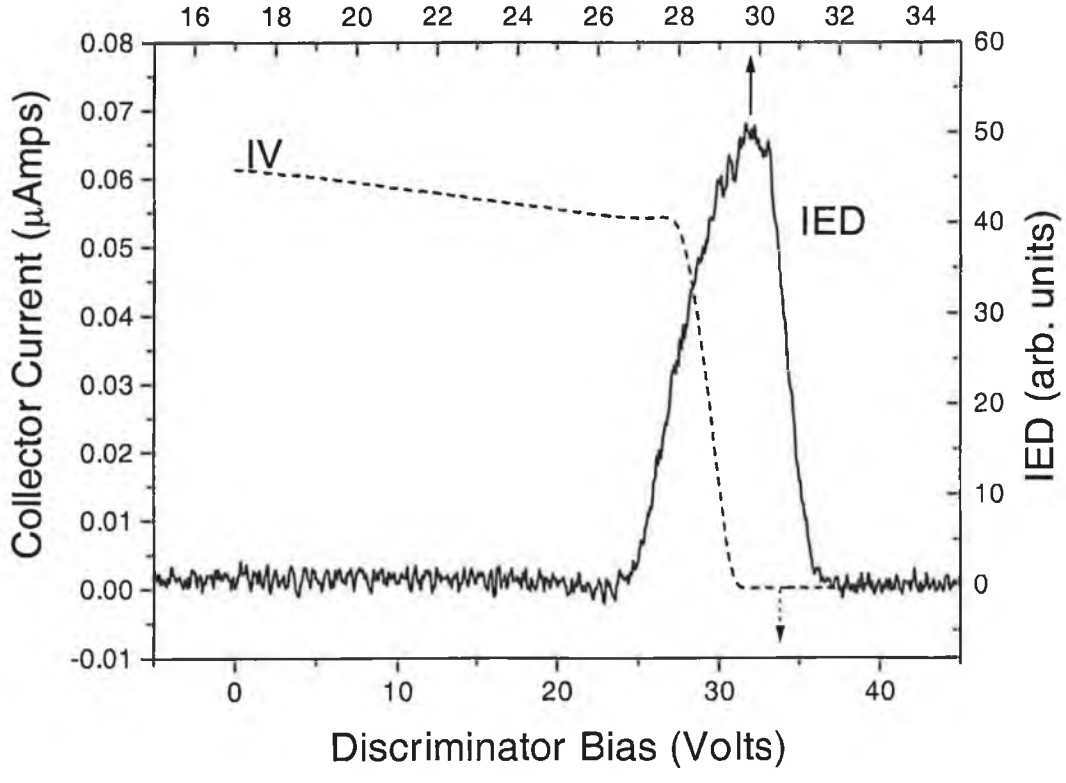

Figure 2.18: Typical *IV* characteristic and ion energy distribution.

2.4.7 Electron Discriminator Mode

The analyser may also be used to measure the electron flux to the grounded electrode. Figure 2.19 shows the potential distribution along the axis of the analyser operating in electron mode. In this case the repeller bias is set to a positive potential greater than the plasma potential to repel the ions. The discriminator bias is swept from a slightly positive to a large negative potential. The suppressor and collector biases are both set to a small positive potential to attract the electrons to the collector, though the suppressor bias is set at a slightly lower positive potential than the collector.

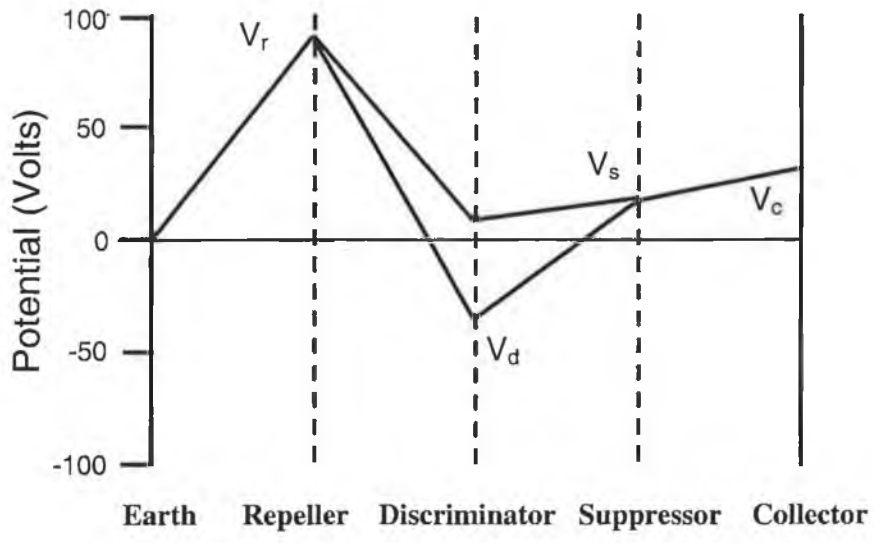

Figure 2.19: Bias distribution along analyser axis for electron collection.

The collector current and discriminator potential are recorded as described in section 2.4.4. The situation in the electron mode is different from that in ion mode in that the electrons will follow the rf potential instantaneously, however, the measurements reported here are averaged over many rf cycles. Fluctuations at the rf frequency at 13.56 MHz cannot be resolved because the frequency response of the analyser is presently too low.

The electron temperature may be extracted from the analyser current-voltage characteristic by plotting the logarithm of the collector current *versus* retarding potential. The slope of the characteristic is

$$\frac{d(\ln I_c)}{dV_D} = \frac{e}{kT} \qquad 2.4.1$$

A typical semilog plot of the collector current *versus* the retarding potential is shown in figure 2.20(a) for helium at 300 mTorr and 10 watts rf power and (b) helium at 300 mTorr and 50 watts rf power.

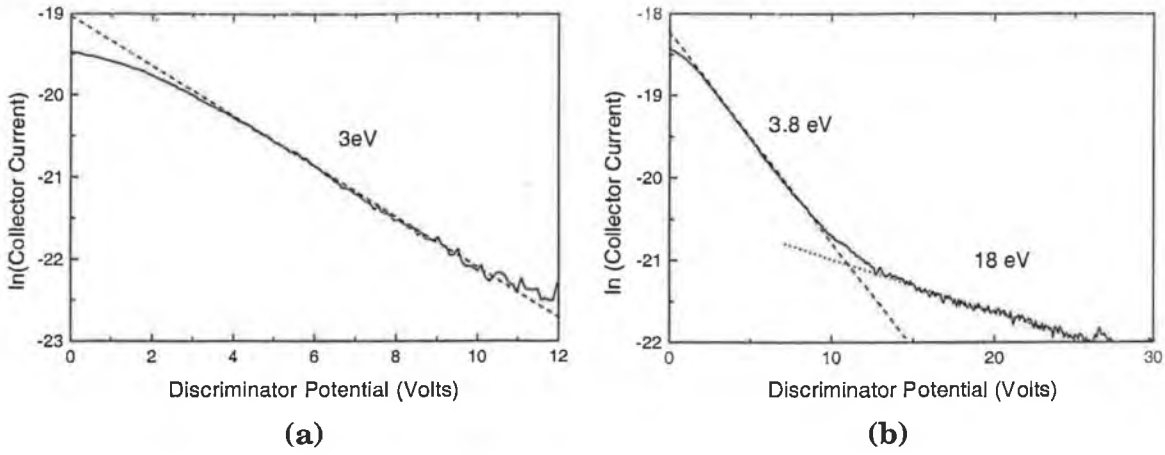

Figure 2.20: Plot of the logarithm of the electron current *versus* retarding potential for helium at 300 mTorr, (a) 10 watts and (b) 50 watts.

With regard to electron energy measurements made in this manner, it is a common misconception that the positive space-charge sheath adjacent to the grounded electrode/analyser surface prevents low-energy electrons from reaching the analyser [26,27]. This is the result of a disregard of the expansion and contraction of the rf sheath during the rf cycle. The collapse of the sheath during the most positive part of the rf cycle allows the plasma to 'touch' the electrode surface. Indeed, there is evidence for field reversal in the sheath at the time of collapse [21,28]. This field reversal accelerates electrons out of the plasma when the sheath contracts, so allowing the electron loss to balance the ion loss to the walls. This is further complicated by the fact that some electrons will also escape when the sheath voltage is nonzero (i.e. at low negative potentials, fast electrons may overcome the potential barrier and escape)

Mahony *et al* performed measurements using probes and temporally resolved optical emission that attributed near electrode emission to field reversal at the powered electrode in a GEC cell [29]. The electron beam measurements of Sato and Lieberman showed direct evidence of a field reversal that accelerates electrons out of the plasma during sheath collapse [30]. Recent electric field measurements by Czarnetski *et al* showed evidence for field reversal in a hydrogen discharge in a GEC cell. Similar evidence for helium was not obvious, possibly due to limitations on the lowest measurable sheath field [31].

The concept of an escaping electron distribution was discussed by Vender using a PIC simulation of an rf discharge at low pressures [28,32]. From this work came the realisation that the electron sheath interaction is a great deal more complex than was previously assumed. The escaping electron distribution at low pressure was found to

depend on sheath velocity, hence on sheath width. A hotter escaping electron distribution was measured at the electrode than was evident in the plasma bulk.

Langmuir probe measurements of the electron distribution are the most common method of determining the electron temperature in rf plasmas. Simply recording the time-average current collected by the probe cannot give accurate information on the electron distribution in the plasma as the rf component of the sheath voltage distorts the electron distribution. Therefore, the rf modulation of the sheath is nullified (as was described in section 2.3.4) and an undistorted distribution is obtained. No such precaution is taken with the energy analyser described here, so we can assume that the motion of the rf sheath in front of the analyser affects the measured electron energy distributions.

Measurement of the EEPF in a helium discharge using a Langmuir probe indicates a change from a single Maxwellian energy distribution of around 3 eV at relatively low rf power to a bi-Maxwellian at higher discharge powers. This is a manifestation of the α-γ transition discussed in detail for argon in Chapter 3. Figure 2.20 shows a single Maxwellian distribution at low rf power in comparison with a clear two-temperature distribution at higher powers. Figure 2.21 shows the EEPF's measured in helium compared to the corresponding electron temperatures measured using the analyser in the grounded electrode. Both the bulk and the high-energy 'tail' measured by the analyser at high powers exceeds that measured by the probe by several electron Volts. The exiting electron distribution is hotter as a consequence of passing through the sheath. Further study is necessary to fully understand the effect of the sheath on the electron distribution. This in turn may aid in further understanding of the operation of all electrostatic probes.

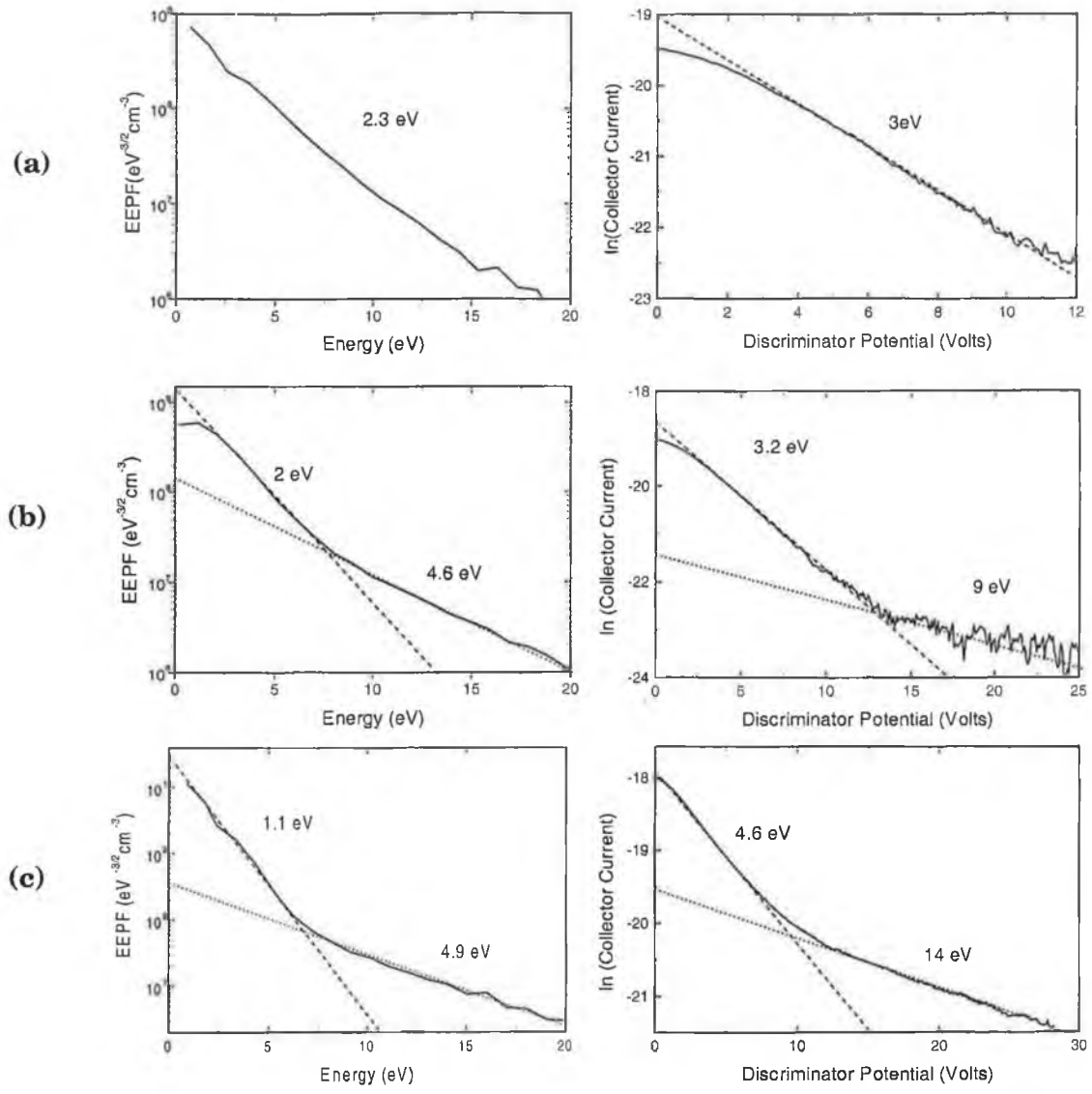

Figure 2.21: EEPF and semilog plots of the collector current versus voltage in helium at 300 mTorr at (a) 10 watts, (b) 25 watts and (c) 100 watts rf power.

2.4.8 Results and Discussion

Figure 2.22 shows the ion energy distribution as a function of pressure. Below 10 mTorr, the IED widens and eventually splits into the saddle-shape characteristic of other measurements made at the ground electrode in such discharges [27]. This has been explained by Wild and Koidl as being due to the modulation of the rf sheath [33]. Figure 2.23 shows a series of *IV* characteristics measured as the input power to the plasma was varied. It is clear that the ion saturation current increases with power, indicating an increase in ion density with power as expected. The negative currents at higher powers are due to an excess of electrons (due to insufficient Vr) and more secondary emission from the secondary grid. During an experiment, the repeller and suppressor bias was adjusted for every measurement to remove these negative currents.

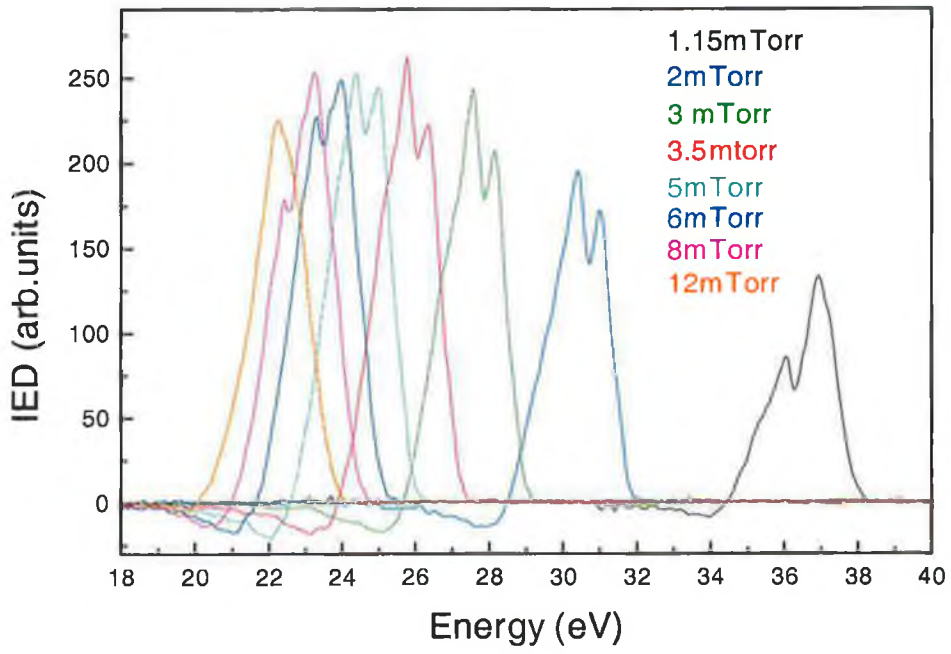

Figure 2.22: Ion energy distributions with varying pressure.

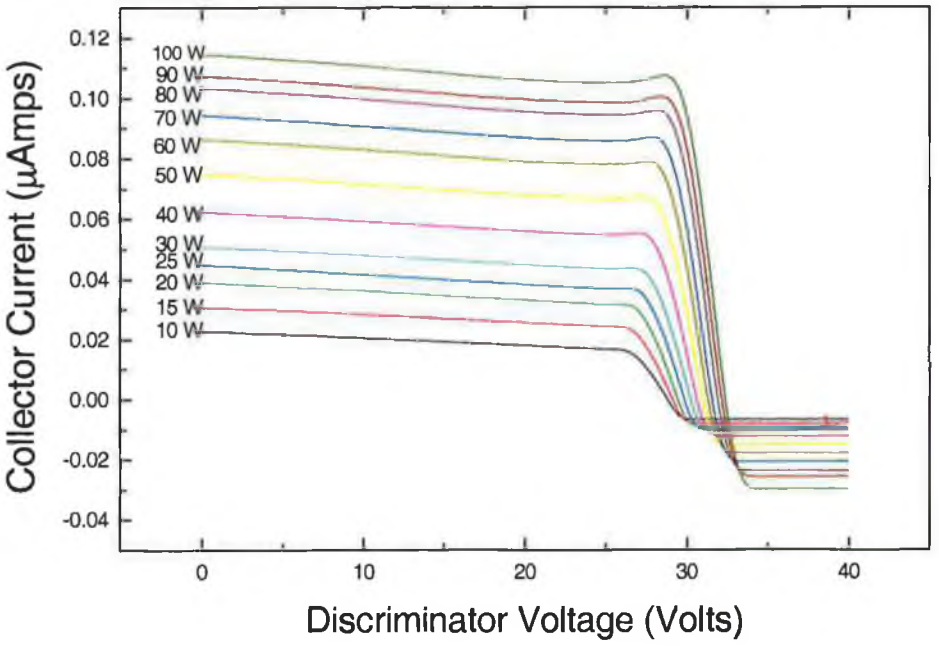

Figure 2.23: Measured *IV* characteristics with varying input power in argon at 10 mTorr.

The plasma potential is equivalent to the voltage dropped across the ground electrode sheath so the average ion energy should be approximately equal to the plasma potential. This provides an opportunity to compare data with a Langmuir probe-see figure 2.24.

Figure (a) shows a plot of ion density made using the Langmuir probe compared with the maximum ion current from the analyser. While an absolute measurement of ion density from the analyser has not been made, the same trends are evident for the same plasma conditions. Part (b) shows estimations of plasma potential from both devices. It is clear that both devices respond in the same way to changes in the discharge operating conditions.

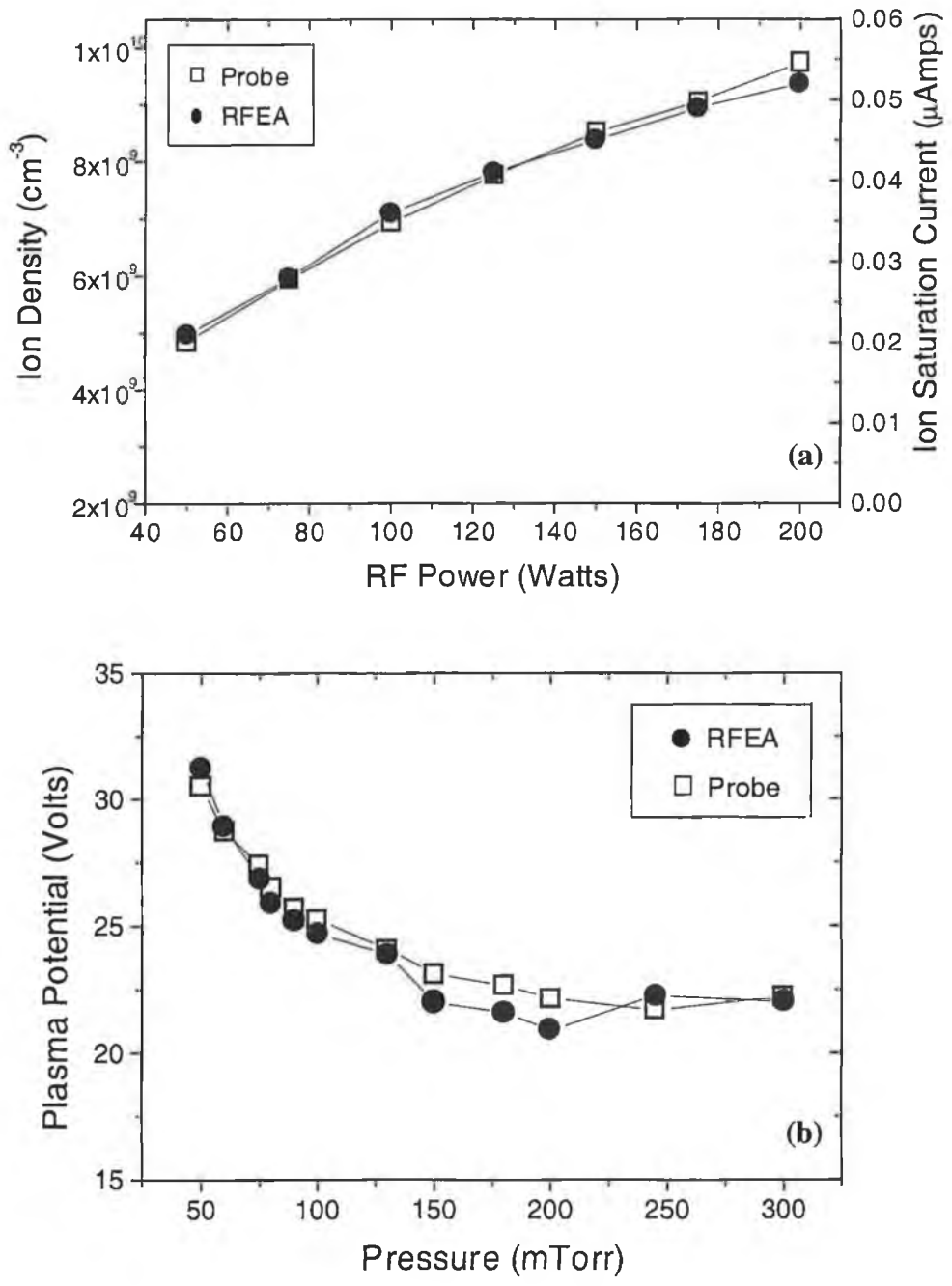

Figure 2.24: Comparison of the Langmuir probe and the RFEA. (a) Ion density and ion saturation currents at 10 mTorr and (b) plasma density measurements made at 50 watts.

2.5 Microwave Interferometry

Introduction

In some plasmas it is not possible to use electrostatic probes to determine plasma parameters so a method that does not perturb the discharge is required. Using electromagnetic waves as a probe into the plasma is a useful method of determining plasma density, provided that their intensity is not so great that they can perturb the plasma. This section deals with the use of the refractive index of the plasma, that is, the changes to free space propagation of the electromagnetic waves due to the electrical properties of the plasma. Interferometry is the primary technique for measuring the change in a plasma's refractive index. Here, this technique is used to determine the density along the plasma mid plane with a view to comparison with the Langmuir probe measurements.

2.5.1 Theory

Consider electromagnetic wave propagation in an infinite, uniform Lorentz plasma [34]. This means that the electrons are assumed to interact with each other through collective space charge forces while the ions and neutrals remain at rest. For the moment we assume no collisional damping due to ions and neutrals. The equation of motions for the electrons is

$$m\ddot{\xi} = -eE \qquad 2.5.1$$

where E is the electric field, e the charge on the electron and ξ is the spatial displacement. If we assume an oscillating electric field that varies as $e^{i\omega t}$, the steady-state solution is

$$\xi = \frac{e}{m\omega^2}E \qquad 2.5.2$$

The current density is

$$J = ne\dot{\xi} = -i\frac{ne^2}{m\omega}E \qquad 2.5.3$$

This is the Ohm's law form $J=\sigma E$, having the conductivity

$$\sigma = -i\frac{ne^2}{m\omega} \qquad 2.5.4$$

For wave propagation in a linear medium, a complex conductivity may be replaced by a complex dielectric constant that is given by κ [35]

$$\kappa = 1 - i\frac{\sigma}{\varepsilon\omega_0} = 1 - \frac{ne^2}{\varepsilon_0 m\omega^2} = 1 - \frac{\omega_p^{\,2}}{\omega^2} \qquad 2.5.5$$

where ω_p is the plasma frequency and ω is the wave frequency. If we take a plane electromagnetic wave travelling in the z direction and varying as $\exp(i\omega t - \gamma z)$, where $\gamma = \alpha + i\beta$ is the complex propagation coefficient and α and β are the attenuation and phase coefficients. The dispersion relation for such a wave is:

$$\gamma = i\kappa^{1/2}\frac{\omega}{c} \qquad 2.5.6$$

For low frequencies ($\omega < \omega_p$) the effective dielectric constant is negative and the wave is attenuated without phase shift. For high frequencies ($\omega > \omega_p$) the plasma becomes a relatively low-loss dielectric and the wave is propagated without attenuation. The phase coefficient becomes

$$\beta = \left(1 - \frac{\omega_p^{\,2}}{\omega^2}\right)^{1/2}\frac{\omega}{c} \cong \frac{\omega}{c} \qquad 2.5.7$$

when $\omega^2 >> \omega_p^{\,2}$. The phase velocity in this case is

$$v_\phi = \frac{\omega}{\beta} = \frac{1}{\left(1 - \frac{\omega_p^{\,2}}{\omega^2}\right)^{1/2}}c \qquad 2.5.8$$

At high frequencies, the refractive index N, becomes

$$N = \frac{c}{v_\phi} = \frac{\beta c}{\omega} = \left(1 - \frac{\omega_p^{\,2}}{\omega^2}\right)^{1/2} \qquad 2.5.9$$

The effect of ions and neutrals in a plasma may be accounted for by including a viscous damping term in the equation of motion

$$m\ddot{\xi} = -eE - \nu m\dot{\xi} \qquad 2.5.10$$

where ν is the collision frequency for momentum transfer. The solution of 2.5.1 gives a corrected expression for the refractive index [34]

$$N^2 = 1 + \frac{\omega_p^{\,2}}{\omega^2}\left(\frac{1}{1 - \frac{i\nu}{\omega}}\right) \qquad 2.5.11$$

However, in the limit $\nu^2 << \omega^2 - \omega_p^2$, the collision frequency is much less than the microwave frequency and the effects of collisional damping may be neglected. The refractive index may be approximated as

$$N \approx \left(1 - \frac{\omega_p^2}{\omega^2}\right)^{1/2} \qquad 2.5.12$$

where ω_p, the plasma frequency, is $e^2 n/m\varepsilon_0$. Consider a situation where we wish to measure the refractive index of a plasma that is in the path of one arm of a two-beam interferometer (such as the Mach-Zehnder configuration, see section 2.5.2). The total phase lag in the plasma arm will be

$$\phi = \int k dl = \int_0^l N(l)\frac{\omega}{c} dl \qquad 2.5.13$$

where k is the phase shift per unit length. A significant proportion of the length of this arm along which the integration is taken is outside the plasma. Also, the reference arm has a length and corresponding phase lag that may not be known. These effects are removed by comparing the phase difference between the two arms with and without plasma present. The phase change is then that induced by the plasma in the plasma arm, i.e

$$\Delta\phi = \int (k_{plasma} - k_0) dl = \int (N-1)\frac{\omega}{c} dl \qquad 2.5.14$$

It is assumed that in the absence of a plasma $k_0 = \omega/c$, i.e. the wave propagates effectively in vacuo. The integral may now be considered to be limited to the part that lies in the plasma.

This measurement of the phase shift provides a measure of the mean refractive index along the line of the interferometer beam through the plasma. When the plasma refractive index is given by equation 2.5.12 we can rewrite it as

$$N^2 = 1 - \frac{\omega_p^2}{\omega^2} = 1 - \frac{n_e}{n_c} \qquad 2.5.15$$

Where n_c is called the cut-off density

$$n_c = \frac{\omega m \varepsilon_0}{e^2} \qquad 2.5.16$$

If the density, n_e, exceeds n_c, then N^2 becomes negative and the wave is not propagating but evanescent, falling off exponentially with distance. Thus, this cut-off density is a critical density below which the plasma is a nearly transparent dielectric and above

which it is opaque and will attenuate the microwave beam. Very little power will be transmitted through the plasma and the interferometer will not function.

For $n_e<n_c$ the interferometer will give a measure of electron density from

$$\Delta\phi = \frac{\omega}{c}\int_0^l \left[\left[1-\frac{n_e(l)}{n_c}\right]^{\frac{1}{2}} - 1\right] dl \qquad 2.5.17$$

which is a line average along the beam path. If the plasma density is low, $n_e<<n_c$, then this may be approximated by

$$N \approx 1 - \frac{1}{2}\left(\frac{n_e}{n_c}\right) \qquad 2.5.18$$

and the phase shift becomes

$$\Delta\phi = \frac{\omega}{2cn_c}\int_0^l n_e(l)dl \qquad 2.5.19$$

If the phase shift is linearly proportional to the line-averaged electron density, the average density then becomes

$$n_e = \frac{\int_0^L n_e(l)dl}{L} = \frac{2cn_c}{\omega}\frac{\Delta\phi}{L} \qquad 2.5.20$$

$$\Rightarrow n_e = \frac{2c\omega\varepsilon_0 m}{e^2}\frac{\Delta\phi}{L} \qquad 2.5.21$$

This in turn may be simplified to [36,37]

$$n_e = 118.4\frac{\omega}{2\pi L}\Delta\phi \qquad 2.5.22$$

where $\omega/2\pi$ is in Hertz, $\Delta\phi$ is in radians, L is in cm and n_e is in cm^{-3}. This provides an estimation of the average plasma density once the phase difference is known.

2.5.2 Principle of Operation

A schematic of the simple microwave interferometer used here is shown in figure 2.25. This measures the phase difference, $\Delta\phi$, between the reference and plasma arms of the interferometer that is caused by the presence of the plasma in the chamber between the two horn antennas. This interferometer is of the Mach-Zehnder configuration and uses one of the simplest detection techniques [38]. This has advantages over the more complicated heterodyne interferometers, the main ones being simplicity and speed. In this configuration the time response is limited only by the

detector response so it is useful when studying pulsed plasmas [39]. The main disadvantage is an ambiguity in phase-shifts which exceed 180° or 360°. This situation is not encountered on this system.

A microwave signal output from the source (an Avantek YIG oscillator) passes through a coupler that splits the wave between the transmission and primary paths. The transmission path passes the wave to a horn that passes the wave through the plasma and be received by the horn opposite. The wave then passes to the magic tee junction. The primary wave passes through the fine attenuator, phase changer and several isolators before arriving at the opposite side of the magic tee (see figure 2.26). This device allows the waves entering it via arms 1 and 3 to be split between arms 2 and 4.

The phase shift, $\Delta\phi$, is measured using the variable phase changer, positioned as shown in figure 2.25. This shift is measured using the "null-field" approach, i.e. the phase is set to zero with no plasma present. When a plasma is present, the phase is nulled again and the difference in the two measurements is $\Delta\phi$.

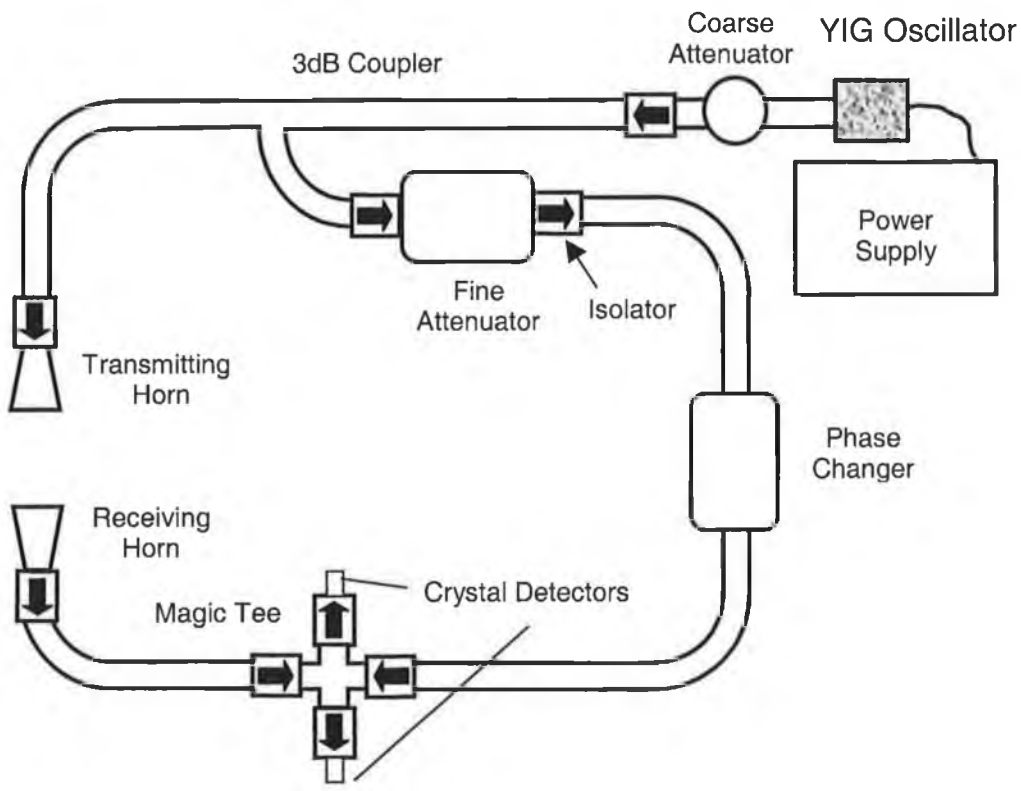

Figure 2.25: The interferometer configuration.

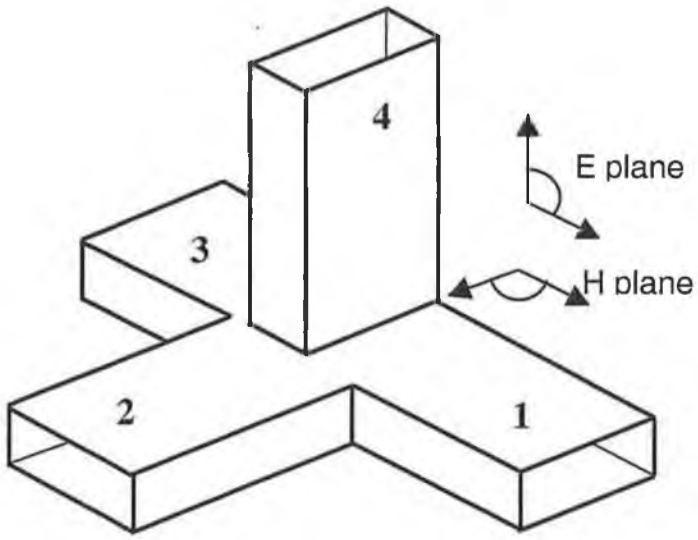

Figure 2.26: The hybrid 'magic' tee junction.

The relationship between the voltage output by the diode detectors and the phase shift caused by the plasma is determined by the output of the magic tee shown in figure 2.24. The electric field magnitudes at points 1, 2, 3 and 4 are given by [34,40,41]

$$S_1=S \sin \omega t \qquad 2.5.23$$

$$S_3=S \sin(\omega t+\phi) \qquad 2.5.24$$

$$S_2=S_1+S_3=2S \sin(\omega t+\phi/2)\cos(\phi/2) \qquad 2.5.25$$

$$S_4=S_1-S_3=2S \cos(\omega t+\phi/2)\sin(\phi/2) \qquad 2.5.26$$

The square law detectors attached at arms 2 and 4 produce a dc voltage signal that is proportional to the electric field intensity. Their outputs are given by

$$S_2^2=S^2(1+\cos\phi) \qquad 2.5.27$$

$$S_4^2=S^2(1-\cos\phi) \qquad 2.5.28$$

The difference between these signals is

$$V_{detected}=2S^2\cos\phi \qquad 2.5.29$$

By zeroing the output of the interferometer when no plasma is present, the detected signal is given by

$$V_{detected}=2S^2\cos(\pi/2+\Delta\phi) \qquad 2.5.30$$

$$=2S^2\sin(\Delta\phi)$$

$$\approx 2S^2\Delta\phi$$

for small values of $\Delta\phi$.

The microwaves were passed through the plasma via two windows on opposite sides of the system (system 2). The horns were placed against the windows and surrounded by Eccosorb™ sponge to prevent microwave emission into the laboratory. The interferometer sections were tightly joined together to avoid waveguide mismatching and isolators were included to remove only reflected signals. The microwave source produces a frequency range varying from 7–16 GHz depending on the input current. Figure 2.27 shows the frequency plotted as a function of input current. The linear relationship shown in figure 2.28 was found. An 11.5 GHz signal was chosen as this resulted in a cut-off density of $4.97 \times 10^{11} cm^{-3}$, allowing measurement over a practical density range.

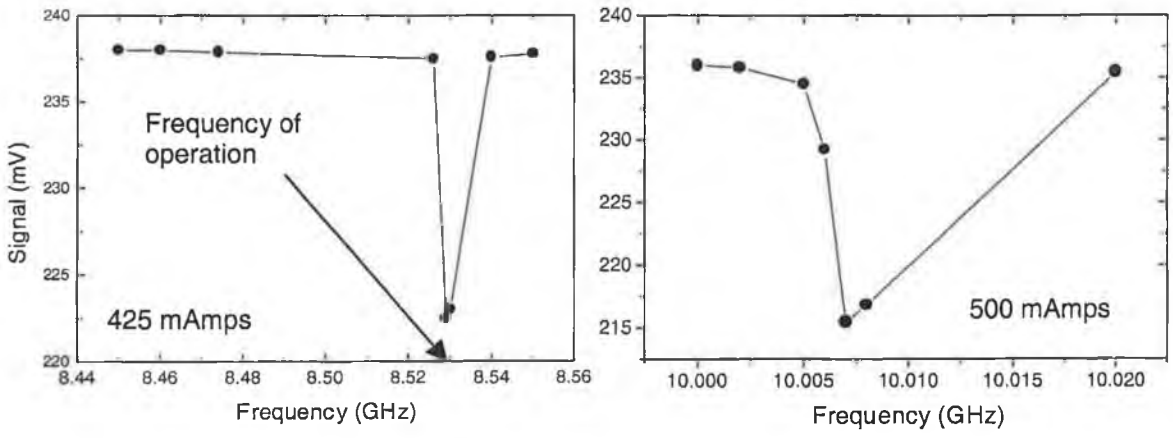

Figure 2.27: Frequency calibration, the signal measured by the detector drops when the frequency of the signal is found.

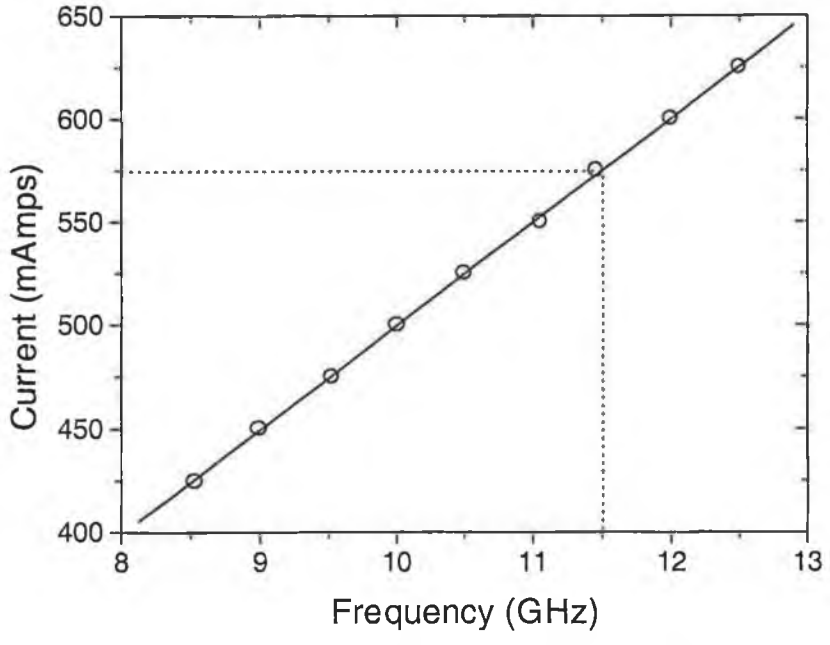

Figure 2.28: Input current versus frequency for the Avantek YIG oscillator.

Two HP 8474B crystal detectors were connected as shown in figure 2.25 to arms 2 and 4 of the magic tee to measure the output signals. It is necessary to check that these diodes are both well-matched (i.e. have equal sensitivity) and have a square law response. Should one or both of these conditions not be met, care must be taken to compensate for this. Figure 2.29 shows the well-matched output of both detectors versus input signal. Equal sensitivity of both detectors may easily be obtained by attenuating the signal from the most sensitive detector or by multiplying the output by a scale constant before subtracting one signal from the other.

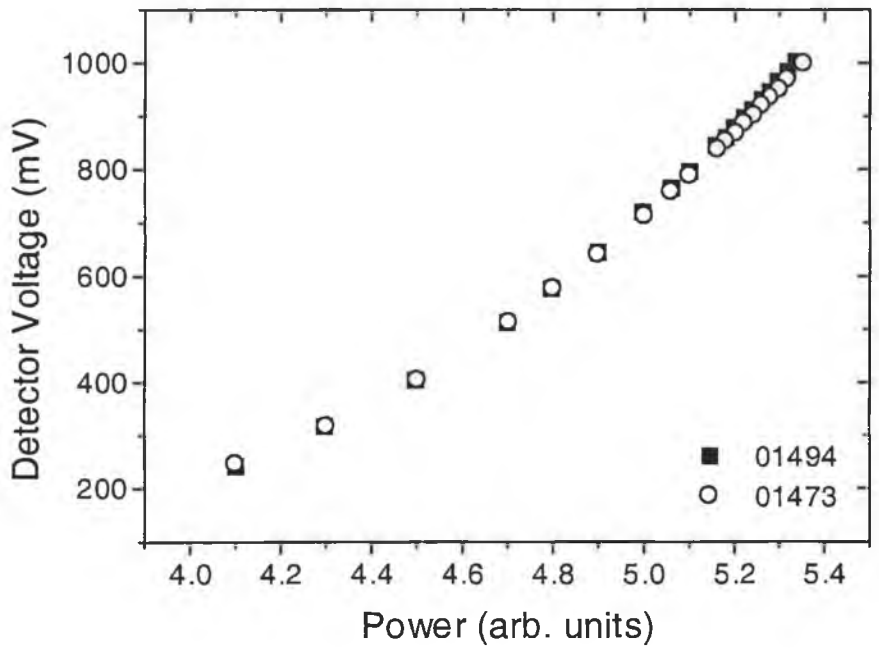

Figure 2.29: Comparison of detector sensitivities.

At certain signal levels the detectors may not operate perfectly in square law fashion, so it is necessary to calibrate each detector separately to convert the detector response to an equivalent square-law response [42]. The response of a square-law detector may be given by

$$I = (kV)^m \qquad 2.5.31$$

where I is the signal intensity, V is the detector signal, k is a constant and m=2 for a square-law detector

$$k = \frac{I_{max}}{V_{max}{}^m} \qquad 2.5.32$$

$$\Rightarrow I = \frac{I_{max}}{V_{max}{}^m} \cdot V^m \qquad 2.5.33$$

$$\Rightarrow \frac{I}{I_{\max}} = \left(\frac{V}{V_{\max}} \right)^m \qquad 2.5.34$$

$$\log \frac{I}{I_{\max}} = m \log \left(\frac{V}{V_{\max}} \right) \qquad 2.5.35$$

As this is in the form $y=mx$, a graph of log I/I_{max} *versus* log V/V_{max} should be a straight line with slope of 2 for a square law detector. Figure 2.30 shows plots of I/I_{max} versus V/V_{max} for the two detectors that verify their square-law operation.

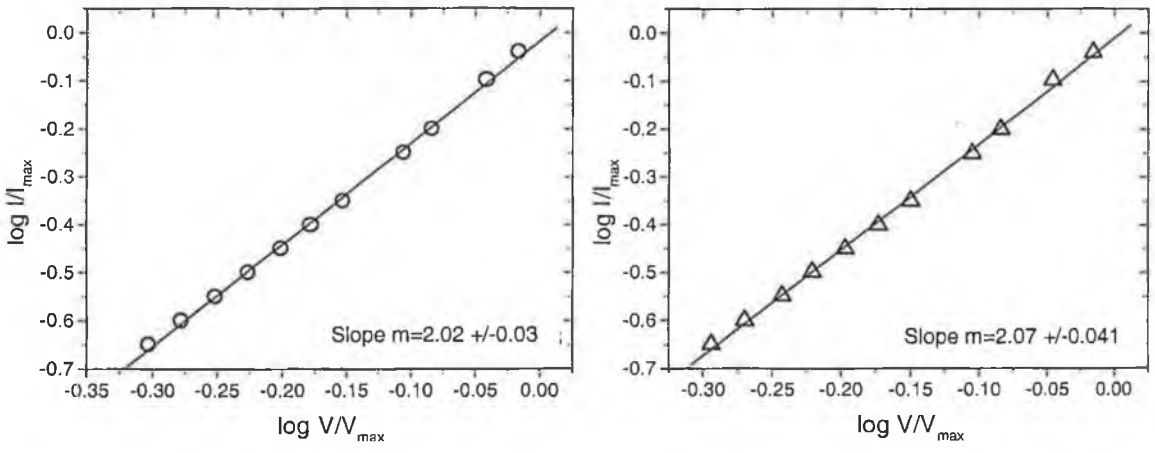

Figure 2.30: Plots of I/I_{max} versus V/V_{max} for the two HP crystal detectors.

The theory described in section 2.5.1 relies on the assumption that the effect of the neutral gas density on the phase shift is negligible. This was tested by observing the phase change as gas was allowed into the chamber, without a plasma present. The maximum phase change due to neutrals was measured to be 8 degrees at 300 mTorr. However, at 50mTorr, a phase change was not measured, implying that phase changes of less than 2 degrees were present due to neutrals at low pressure. When a phase change due to neutrals was measurable, it was subtracted from the phase change due to the presence of a plasma and the average electron density calculated using equation 2.5.22. A Bessel function is observed to roughly approximate the radial density profiles in the reactor, see Chapter 5. The central electron density was inferred from the line averaged interferometer measurement by plotting a Bessel function with the same area as the line average. The maximum density value of this Bessel function was then taken as the central electron density value measured using the interferometer.

2.5.3 Results and Discussion

Figure 2.31 shows a comparison of ion densities measured with the Langmuir probe and electron density with the microwave interferometer for a range of powers and pressures. At higher pressures above 70 watts rf power, the measured electron density starts to approach the cutoff density defined in section 2.5.1, so the interferometer ceases to be a useful method here.

Other comparisons of probe and interferometer measurements made in rf discharges have shown that the probe begins to underestimate the electron density at pressures above 100 mTorr [9,39]. This is due to the neglect of collisions in the probe theory. A surprising degree of agreement is found here at 300 mTorr that contradicts the previous measurements which found a factor of two difference in the density values. The reasons for this are not yet clear and further work is required to clarify this issue.

It should be noted that the interferometer requires further calibration [39] and that the analysis in its present form only gives the average electron density. Further work could include development of the technique to measure absolute electron densities that would allow more precise comparisons with probe data.

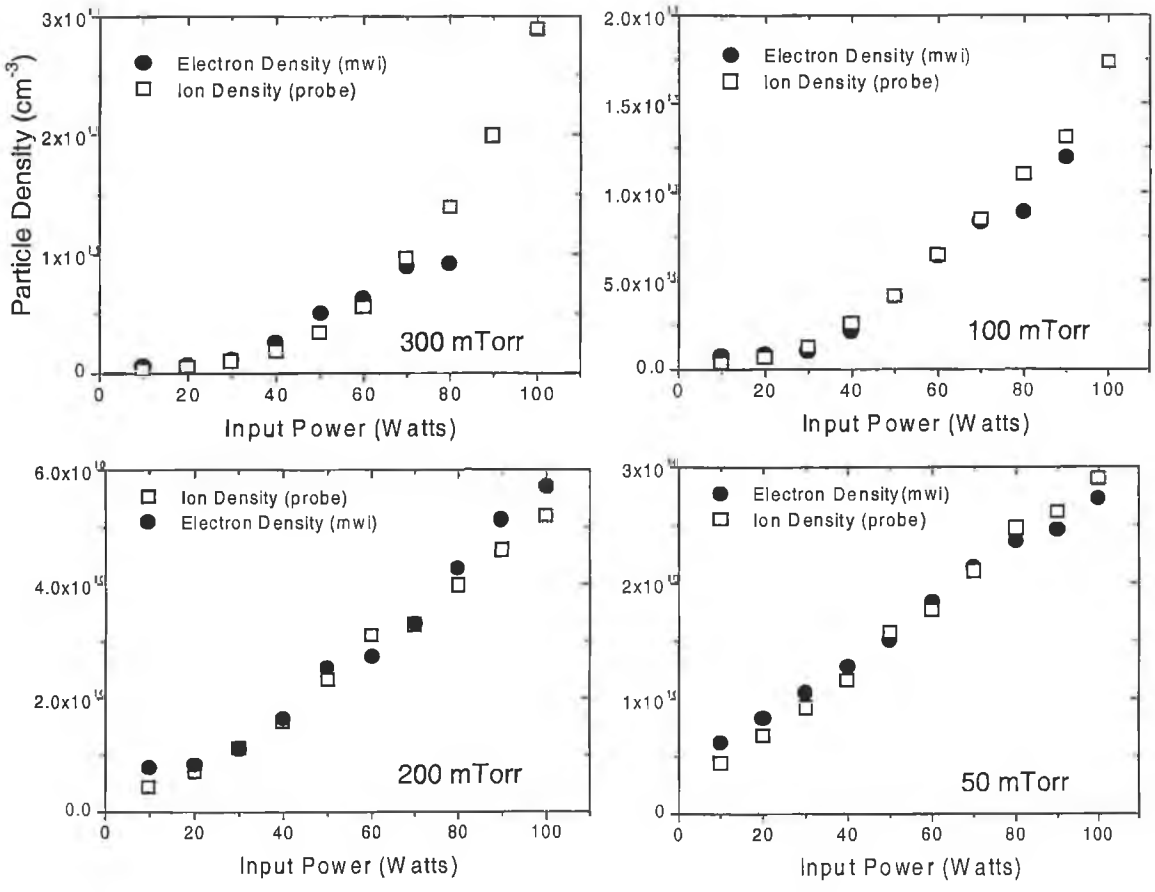

Figure 2.31: Comparison of interferometer density measurements with the ion density measured from the Langmuir probe over a range of power and pressure.

2.6 The Current -Voltage Monitor

Introduction

Monitoring of process parameters in rf plasmas is of great interest to the plasma processing community, where reproducibility and process control are of the utmost importance. Use of current-voltage monitors is rapidly becoming more widespread as such tools have the advantage that they are a robust, non-invasive and inexpensive element in the plasma process.

2.6.1 Current and Voltage Probes

The electrical current in an rf plasma is varying, so it is straightforward to take advantage of the resulting rapidly varying magnetic induction to measure the current. The simplest method of doing this is to place a pickup coil or loop in an area where the current is flowing. In the coil the changing magnetic field causes an electromotive force. A measure of the flux may thus be obtained by taking the integral of the induced electromotive force. The most commonly used pickup coil arrangement is the Rogowski coil. This is essentially a multiturn solenoid shaped into a torus, which encircles the current to be measured. Often the coil is wrapped around a metallic former that increases the coupling between the conductor and the coil. The coil is surrounded with an electrostatic shield to exclude noise resulting from capacitive coupling to large time varying voltage fluctuations. A coil plus an equivalent circuit for its operation as a current transformer is shown in figure 2.32 [43].

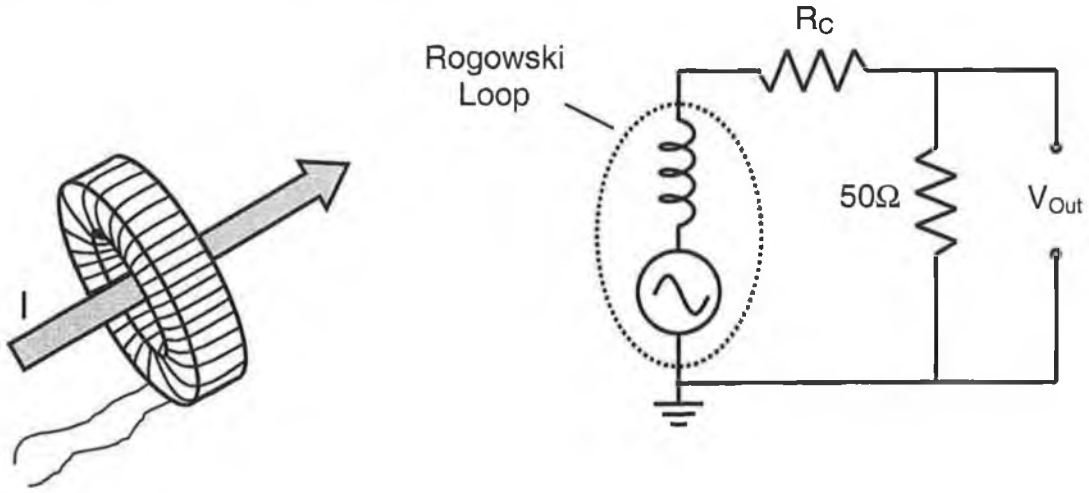

Figure 2.32: A Rogowski coil and its equivalent circuit for operation as a current transformer.

A measurement of the voltage on the powered electrode is also required. A standard resistive divider probe may not be used to measure this because loading of the signal occurs. A derivative voltage probe is used instead. This only transmits the ac

component of the signal so we have a direct measurement of the rf voltage. To ensure that this probe draws negligible current, its impedance must be high. A capacitance of 3pF has an impedance of 3.9kΩ at 13.56MHz. A typical voltage measurement circuit is shown in figure 2.33. The voltage probe is also connected between the matching unit and the powered electrode. The current probe is connected between the voltage probe and the powered electrode to ensure that any loading caused by the voltage probe will not affect the current measurements.

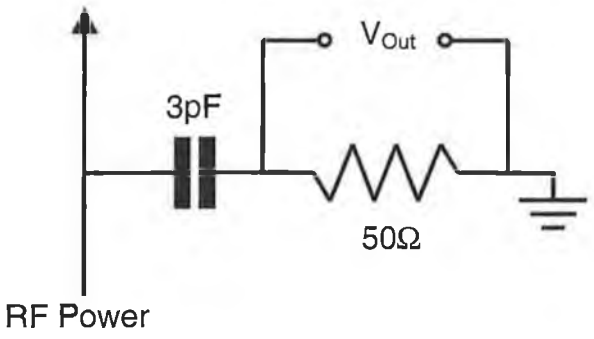

Figure 2.33: Voltage probe equivalent circuit.

Commercial current and voltage probes of these types are readily available. Current measurements on system 1 are made using a Pearson™ 10:1 current monitor. To study the α-γ transition (Chapter 3, section 3.3.2) a prototype of the Scientific Systems™ plasma-impedance monitor is used. This incorporates a current and voltage monitor based on the derivative probes of the GEC workers [44-48]. A schematic of the current voltage monitor is shown in figure 2.34. A derivative probe has the advantage of producing larger signals at the harmonics and thus improving their signal-to-noise ratio [46].

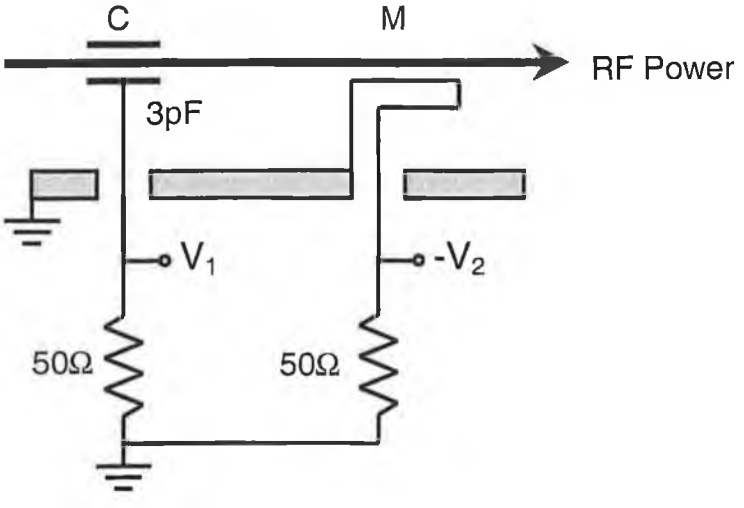

Figure 2.34: Schematic diagram of the current-voltage monitor.

2.6.2 Calibration and Harmonic Analysis

In order to make accurate voltage, current and power measurements, it is necessary to calibrate the probes for the fundamental and the relevant harmonic components in terms of both amplitude and phase. The current and voltage amplitude calibration is straightforward; a linear relationship between actual and measured voltage (and current) amplitudes is typical for the fundamental and the harmonics. In this work as in others, phase calibration is more difficult and subject to errors than amplitude calibration [46]. Phase measurements are performed on probe pairs because we are interested solely in the phase difference between voltage and current. The same sign convention protocol for the GEC cell is used; that is voltage angle minus current angle is the phase angle.

A calibration procedure was developed whereby a capacitive load, which has a phase angle of -90°, was used. The most convenient procedure uses the reaction chamber as a calibration standard [48]. Care must be taken to avoid discharge initiation by the calibration signal. Consequently, the calibration procedure was performed at low voltages. For an ideal capacitor, the phase signal should be –90°. A phase signal of approximately –75° was found on the reaction chamber of experimental system 1. This offset of 15° may be attributed to systematic errors in the measurement system. The largest source of error is the so-called 'transit time' error [45,46]. This is due to differences in the propagation delay times of the current and voltage signals. A phase difference of a few degrees is induced at 13.56MHz due to the finite speed of propagation of the signal. Using short and identical length cables reduces this phase offset. The transit-time error is accounted for by storing the phase offset, $\Delta\phi$, at 13.56MHz. This offset is then used to correct the measured phase. At the N^{th} harmonic, $N\Delta\phi$ is subtracted from the measured phase to obtain a complete, corrected, phase dataset.

Other systematic sources of error include cross talk, rf interference and unequal dispersion in the cables or oscilloscope channels. Capacitive coupling between the power lead and the case of the probe can lead to a spurious signal being added to the current signal, shifting its phase [45]. This type of error may be minimised by ensuring a good ground connection between the *IV* probe case and ground. The phase calculation (and correction) process was verified using several reactive loads (with ϕ = +90° and -90°). Measurements of the phase offset made over a six-month period have shown drift of a few degrees, see figure 2.35. To minimise and maintain consistent phase

corrections, the same cables were always used and a calibration run performed on the system prior to an experiment. Day-to-day phase error drifts of a couple of degrees were common. The GEC workers have also observed this and the cause is not certain [46].

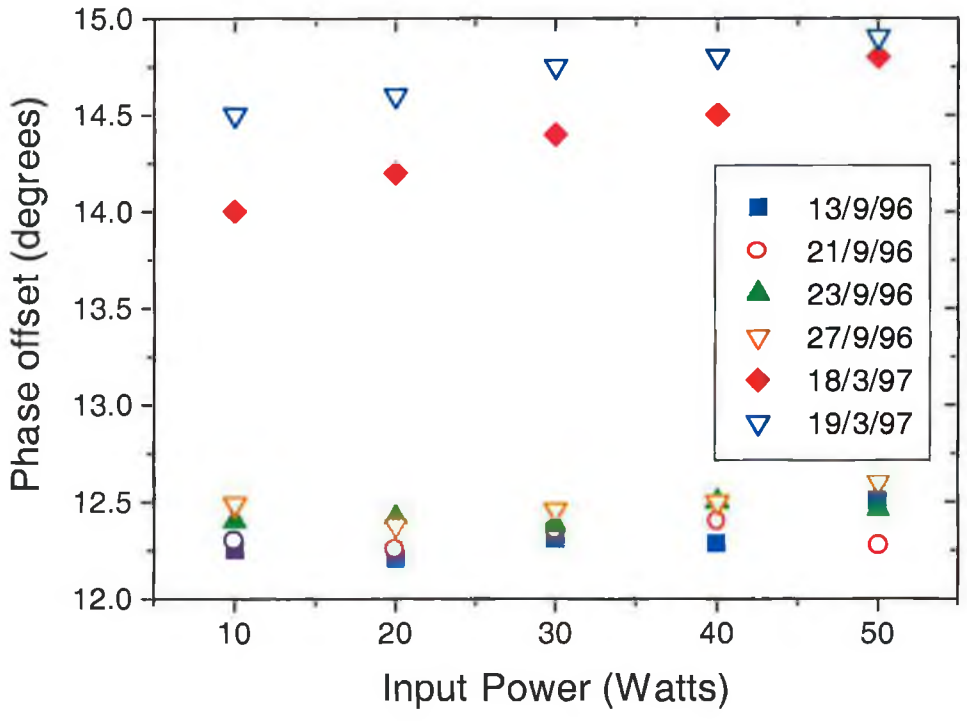

Figure 2.35: Phase offset measured over a six-month period.

Over a range of rf frequencies, loads such as the reaction chamber may not be purely capacitive. This can result in difficulty in determining the correct sign of the phase of the load at harmonics of the rf frequency. A Hewlett-Packard vector impedance analyser (HP 4193A) was used to measure the resonant frequency of the chamber. Figure 2.36 shows a sharp resonance at 33.15MHz, so the phase correction after the second harmonic (27.12MHz) is to +90° instead of -90°.

The current and voltage waveforms are digitised using a digital storage oscilloscope and downloaded using a HPIB (Hewlett-Packard Interface Bus) card. Once the actual phase difference between the voltage and current waveforms is known, the power may be estimated using

$$P = V_{rms} I_{rms} \cos\phi \qquad 2.6.1$$

where ϕ is the phase difference between voltage and current.

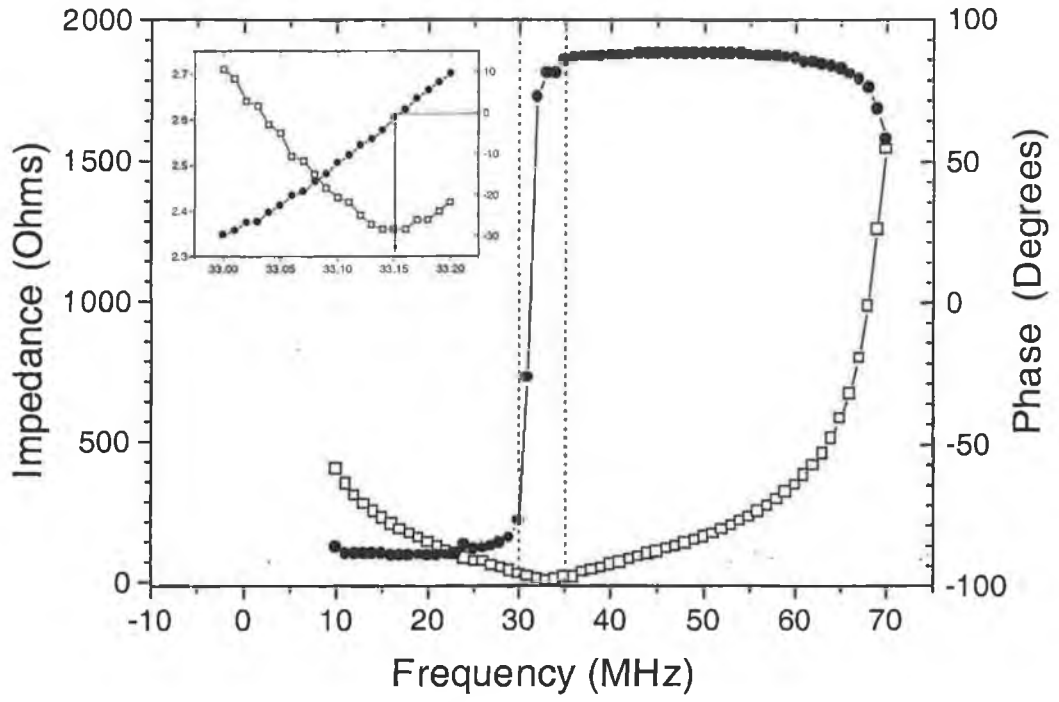

Figure 2.36: Frequency dependence of the impedance and phase on the empty chamber (system 1). Solid circles are phase measurements, open squares are impedance values. Inset: resonant frequency is at the zero-crossing of the phase and the minimum impedance value.

To obtain information about the harmonic content of the waveforms, a discrete Fourier transform of the data was taken. For periodic signals $y(t)=y(t+T_0)$ the Fourier series is [49]

$$y(t) = \frac{a_0}{2} + \sum_{k=1}^{\infty} a_k \cos\left(\frac{2\pi kt}{T_0}\right) + \sum_{k=1}^{\infty} b_k \sin\left(\frac{2\pi kt}{T_0}\right) \qquad 2.6.2$$

with the Fourier coefficients given by

$$a_k = \frac{2}{T_0}\int_{-T_0/2}^{T_0/2} y(t)\cos\left(\frac{2\pi kt}{T_0}\right)dt \qquad 2.6.3$$

$$b_k = \frac{2}{T_0}\int_{-T_0/2}^{T_0/2} y(t)\sin\left(\frac{2\pi kt}{T_0}\right)dt \qquad 2.6.4$$

The amplitudes of the different terms of the transform give the contribution of the harmonics to the signal. The phase of each harmonic is calculated by

$$\phi = \arctan\frac{b_k}{a_k} \qquad 2.6.5$$

Plasmas generated in parallel-plate systems are expected to have mostly reactive impedance. Deviations from a phase of -90° are due to the plasma impedance having both resistive and reactive components. The argon plasmas generated here have a phase of approximately -85°. The fact that the phase is so close to -90° makes the calculation of phase (equation 2.6.5) very sensitive to errors. For this reason, several phase error measurements were made and an average value found. Reconstructing the original waveform using the Fourier coefficients and calculated phase checks the validity of the discrete Fourier transform algorithm. Figure 2.37 shows a typical voltage waveform, its harmonic amplitudes and the reconstructed waveform.

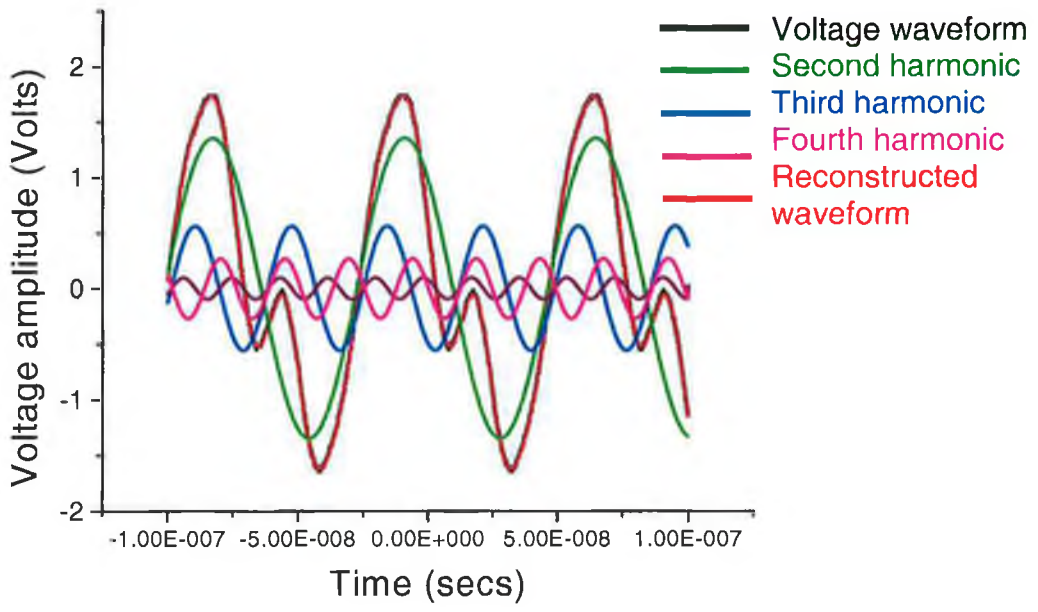

Figure 2.37: Voltage waveform plus its harmonics and reconstructed waveform.

It may be seen in figure 2.37 that the voltage waveform may contain several harmonic components. It is important to mention at this point that the digitising oscilloscope has a bandwidth of 100 MHz, this means that in this experiment only up to the third harmonic (40.68 MHz) may be fully sampled [50].

The absolute value of the total discharge impedance is the voltage divided by the current. Determination of the amplitudes and phases of the fundamental and relevant harmonics allows a measurement of the resistive and reactive components of the plasma impedance. This allows measurement of the power dissipation in the discharge volume and the sheath [51].

In order to characterise the discharge, the actual values of current and voltage in the plasma require definition. The voltage and current measured at the powered

electrode are not strictly the actual plasma current and voltage because of stray impedance between the electrode surface and measurement point. Some of the measured current is drawn not by the plasma but by parasitic capacitances in the electrode assembly. The measured voltage will also differ from the actual voltage because of a voltage drop along the power lead. Parasitic resistances dissipate power, so values of power obtained from the measured current and voltage values may be larger than the actual power dissipated in the plasma. [44,45]

Characterisation of chamber parasitics using equivalent circuits has been carried out in detail by several workers [44,45]. The relative error in measurements due to these parasitics has been estimated as approximately 15% [45].

If electrical measurements are to be used as an operating parameter only, i.e. to ensure reproducibility of discharge conditions, then corrections for parasitics may not be strictly necessary. Consequently, estimation of and correction for chamber parasitics are not performed in this work. In any case, the lack of a ground shield around the powered electrode in system 1 greatly reduces its parasitic capacitance, so the measured current and voltage may be assumed to be close to the actual values. However, corrections for parasitics are essential if measured electrical parameters are to be compared with theoretically predicted values.

2.6.3 Results and Discussion

In a parallel plate system the impedance may be simply modelled by a series combination of capacitances representing the sheaths with a resistance between them that represents the power dissipation between the electrodes. Increasing the rf power lowers the resistive component of the plasma due to the increase in plasma density. Increasing the rf power also increases the reactance as the higher rf voltages thicken the sheaths. This may be seen in figure 2.38, where the resistive and reactive contributions to the plasma impedance are plotted.

Phase and calculated power measurements are shown as a function of voltage amplitude in figure 2.39. Increasing the rf voltage causes the input power to rise and there is a corresponding increase in the absolute value of the phase angle. These measurements also reflect the decreasing plasma resistivity (expected with the increase in plasma density) and sheath capacitance.

The contribution of the harmonics to the discharge power is less than 10%, in agreement with the GEC workers. It is therefore assumed that power deposition in the

plasma may be estimated from the fundamental components to reasonable accuracy [51,52]. Signals at the harmonic frequencies arise because the impedance of the plasma is non-linear. Non-linear phenomena in plasmas are usually regarded as inconvenient effects in modeling. However, plasma diagnostics have been developed using non-linear properties such as self-excited electron resonance spectroscopy (SEERS) [53].

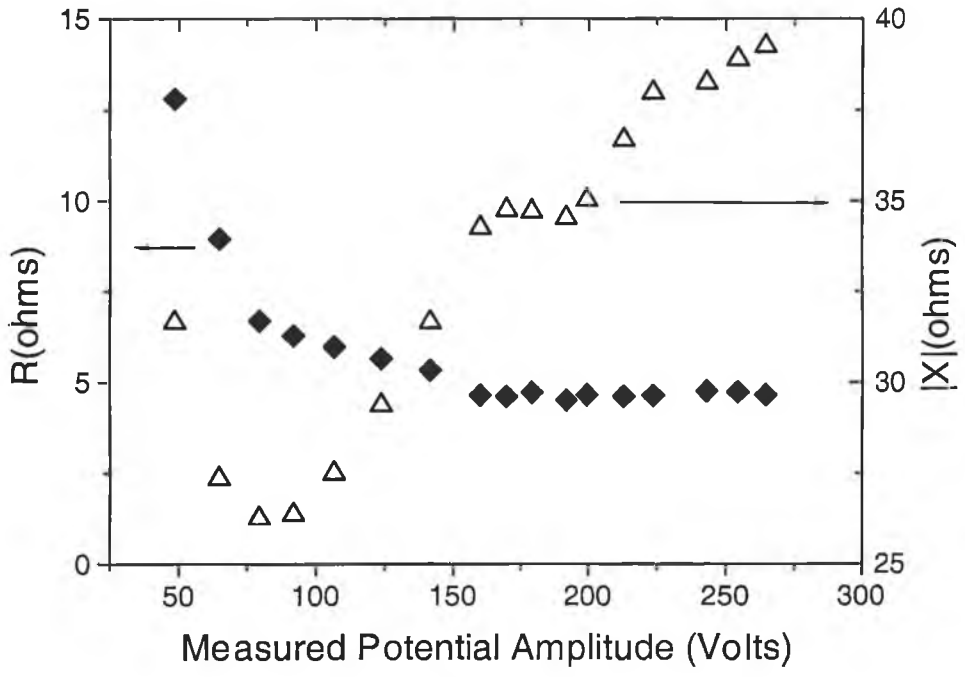

Figure 2.38: Resistive component R, and absolute value of the reactive component, $|X|$ of the complex impedance $Z=R+jX$, as a function of the applied potential in argon at 300 mTorr.

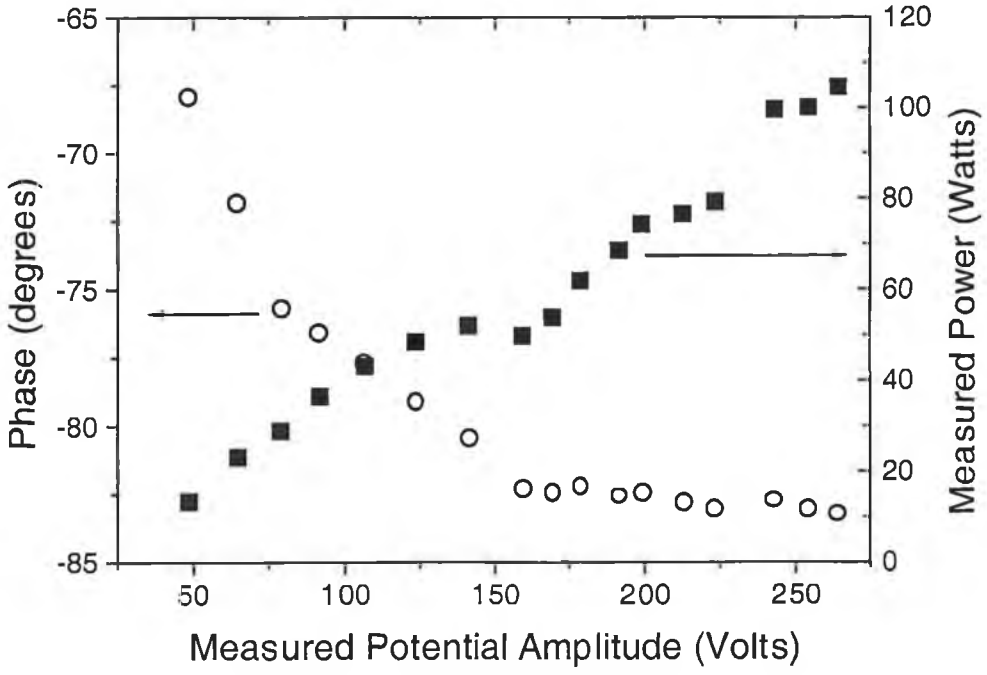

Figure 2.39: Discharge power and phase angle as a function of applied potential in argon at 300 mTorr.

Multiples of the fundamental frequencies are always present in the voltage and current waveforms in rf discharges. The incidence of certain rf voltage harmonics has been observed to indicate endpoint in certain etching processes, so indicating the possibilities for completely non-invasive *in situ* diagnostics for plasma processing [54-56].

2.7 Concluding Remarks

This chapter detailed the experimental systems examined in this thesis. The primary diagnostic used in this work is the Langmuir probe due to it ability of making spatially resolved measurements and for determination of the EEPF. A retarding field energy analyser and microwave interferometer were used to measure plasma parameters for the purpose of comparison with the probe measurements. Comparisons between probe measurements of the electron density and plasma potential and the same quantities using the interferometer and analyser were in good agreement, so reinforcing the confidence in the Langmuir probe as a reliable diagnostic tool.

Measurement of the electron energy using the energy analyser yielded hotter distributions than that of the Langmuir probe. This is attributed to the effect of the space charge sheath on the escaping electron distribution.

Current and voltage measurements on the powered electrode were made in a similar method to the GEC workers. In agreement with these workers, the contribution of the higher harmonics to the power deposited in the plasma was found to be less than 10 %.

References

[1] F. Chen in *Plasma Diagnostic Techniques*, edited by R.H. Huddlestone and S.L. Leonard, Academic Press, New York, (1965).

[2] J.G. Laframboise, UTIAS Report No. 100, (1966).

[3] I. Langmuir and H. Mott-Smith, Phys. Rev. 28, 727, (1926).

[4] B.E. Cherrington, Plasma Chem. and Plasma Processing, 2(2), 133-140, (1982).

[5] L. Schott in *Plasma Diagnostics*, edited by W.L. Holtgreven, North Holland, Amsterdam, (1968).

[6] C. Bohm and J. Perrin, J. Phys. D: Applied Phys. 24, 865, (1991).

[7] M. B. Hopkins and W.G. Graham, Rev. Sci. Instrum. 57(9), 2210, (1986).

[8] M.B. Hopkins, W.G. Graham and T.J. Griffin, Rev. Sci. Instrum. 58(3), 475, (1987).

[9] R.A. Doyle, PhD Thesis, Dublin City University, (1994).

[10] Scientific Systems Smartprobe™ Manual, (1997).

[11] V.A. Godyak, R.B. Piejak and B.M. Alexandrovich, J. Appl. Phys., 73(8), 3657, (1993).

[12] C.M. Deegan, J.P. Goss, D. Vender and M.B. Hopkins Appl. Phys. Letts., 74(4), 1969, (1999).

[13] V. Godyak, R. Piejak and B.M. Alexandrovich, Plasma Sci. Sources and Technology, 1, 36-58, (1992).

[14] M. Lieberman and A. Lichtenberg, *Principles of Plasma Discharges and Materials Processing*, Wiley Interscience, (1994).

[15] M.J. Druyvestyn, Z. Phys., 64, 781-798, (1930).

[16] J. Scanlan, PhD Thesis, Dublin City University, (1991).

[17] J.L. Wilson, J. B. O. Caughman, P.L. Nuygen and D. N. Ruzic, J. Vac. Sci. Technol. A, 7, 972, (1989).

[18] B.M. Annartone and N St.J Braithwaite, Meas. Sci. Technol. 2, 795-800, (1991).

[19] R.R.J. Gagné and A. Cantin, J.Appl.Phys., 43(6), 2639, (1972).

[20] P.A. Chatterton, J.A. Rees, W.L. Wu and K. Al-Assadi, Vacuum, 42(7) 489-493, (1991).

[21] M.M. Turner and M. B. Hopkins, Phys. Rev. Letts., 69(24), 3511, (1992).

[22] V.A. Godyak, R.B. Piejak and B.M. Alexandrovich, Phys. Rev. Letts. 68, 40, (1992).

[23] G. D. Conway and A. J. Perry, Report No. ANU-PRL-TR-02/96, (1996).

[24] C. Bohm and J. Perrin, Rev. Sci. Instrum. 64, 31, (1993).

[25] Y. Sakai and I. Katsumaka, Jap. J. Appl. Phys. 24, 337, (1985).

[26] G. D. Conway, A. J. Perry and R. W. Boswell, Plasm. Sces. Sci. Technol. 7, 337-347, (1998).

[27] S. G. Ingram and N. St. J. Braithwaite, J. Phys. D: Appl. Phys. 21, 1496, 1988.

[28] D.Vender and R. Boswell, J. Vac. Sci. Technol., 18, 725, (1992).

[29] C. M. O. Mahony, R. Al. Wazzan and W. G. Graham, Appl. Phys. Letts., 71(5), 608, (1997).

[30] A. H. Sato and M. A. Lieberman, J. Appl. Phys., 68(12), 6117, (1990).

[31] U. Czarnetski, D. Luggenholscher and H. F. Dobele, Plasma Sces. Sci. Technol., 8, 230-248, (1999).

[32] D. Vender, Ph.D. Thesis, The Australian National University, Canberra, (1990).

[33] C. Wild and P. Koidl, J. Appl. Phys., 69(5), 2909-2922, (1991).

[34] M. A. Heald and C. B. Wharton, *Plasma diagnostics with Microwaves*, Krieger Publishing Company, Huntington, New York, (1978).

[35] C. B. Wharton in *Plasma Diagnostic Techniques*, ed. R. H. Huddlestone and S. I. Leonard, Academic Press, New York, (1965).

[36] I. H. Hutchinson, *Principles of Plasma Diagnostics*, Cambridge University Press, (1990).

[37] H. Meuth and E. Sevillano, in *Plasma Diagnostics,* Vol.1, ed. O. Auciello and D. Flamm, Academic Press, (1988).

[38] E. Hotston and M. Seidl, Rev Sci. Instrum, 425, 22, (1965).

[39] L. J. Overzet, Journal of Research of the National Institute of Standards and Technology, 100, 4, 401-414, (1995).

[40] J. L. Kleber, MSc Thesis, University of Texas at Dallas, (1997).

[41] A. J. Baden-Fuller, *Microwaves, and Introduction to Microwave Theory and Techniques*, Pergamon Press, (1979).

[42] L. Lindberg and A. Eriksson, J. Phys. E: Sci. Instrum. 15, 548-554, (1982).

[43] S. L. Leonard in *Plasma Diagnostic Techniques*, eds. R.H. Huddlestone and S. L. Leonard,. Academic Press, New York, (1965).

[44] J. K. Olthoff, and K. E. Greenberg, J. Res. Natl. Inst. Stand. Technol., 100, 327, (1995).

[45] M. A. Sobolewski, J. Vac. Sci. Technol. A, 10, 3550, (1992).

[46] GEC Reference Cell Newsletter, ed. J. R. Roberts, (1991).

[47] J. R. Roberts, J. K. Olthof, R. J. van Brunt, J. R. Whetstone, SPIE, 1392, 428, (1990).

[48] P. A. Miller, SPIE, 1594, 179, (1991).

[49] I. Bull and R. Linke, Am. J. Phys. 64(7), 906, (1996).

[50] A. de Sa, *Principles of Electronic Instrumentation*, Edward Arnold Publishers, London, 1981.

[51] C. Beneking, J. Appl. Phys. 68(9), 4461-4473, (1990).

[52] P. Bletzinger and M.J. Flemming, J. Appl. Phys. 64, 4688, (1987).

[53] M. Klick, W. Rehak and M. Kammeyer, Jpn. J. Appl. Phys. 36, 4625-4631, (1997).

[54] M. Klick, J. Appl. Phys. 79(7), 3445, (1996).

[55] M. Surendra, Contributed paper M1A 2, 49th Gaseous Electronics Conference, Oct. (1996).

[56] W. Roth, R. Carlile, J. O' Hanlon, J. Vac. Sci. Technol. A, 15(6), 2930, (1997).

Chapter 3

Transitions in Heating Mechanisms

Introduction

One of the most important questions regarding the operation of rf discharges is the mechanism of electron heating. The aim of this chapter is to characterise and study the transitions in heating mechanisms that occur due to changes in the external operating parameters of the discharge. Particular attention is paid to the transition from a regime dominated by Ohmic heating to a secondary electron emission-dominated discharge, the so-called α-γ transition.

Measurements were made in the mid plane of capacitively coupled argon plasmas. A Langmuir probe was used to measure plasma parameters as a function of gas pressure, voltage and current.

3.1 Experiment

Argon plasmas were generated in the parallel plate capacitively coupled system described in detail in Chapter 2, section 2.1. The chamber dimensions and probe positions are shown in figure 3.1. The ground electrode touches the walls inside the chamber, the driven electrode is 240 mm in diameter and is electrically isolated from the rest of the chamber. The plate separation was varied from 4 to 8 cms.

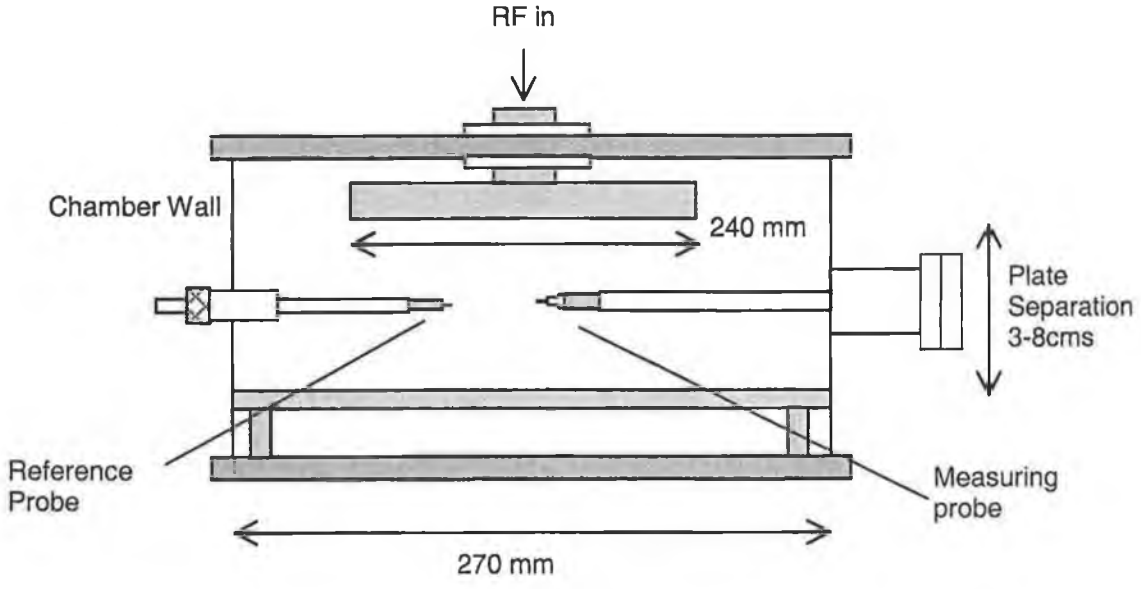

Figure 3.1: Chamber dimensions with probe positions (system 1).

The resistance between the plasma and ground electrode is non-negligible. Since the discharge electrodes are usually part of the probe circuit, it is important that their differential resistance, R_e, for the probe current measurement be much smaller than the differential resistance of the probe sheath, R_p. In rf discharges the conduction currents through the capacitive electrode sheaths are much smaller than the discharge currents so the rf sheath differential resistance can be comparable to the probe sheath resistance and consequently result in distortion to the measured EEPF. This distortion is manifest in the low energy part of the EEPF, since [1]

$$R_p = \left(\frac{dI_p}{dV_p} \right)^{-1} \approx \frac{T_e}{I_p} \qquad 3.1.1$$

R_p has its minimum value when the probe potential is equal to the plasma potential. Thus, $R_{pmin} \approx T_e/I_{e0} \propto T_e^{1/2}/n$, where I_{e0} is the electron saturation current to the probe. This situation is worsened by a two-temperature EEPF structure such as that measured in a low-pressure argon rf discharge, see figure 3.4. In this case the low temperature electron group with the temperature T_{elow} governs the minimum probe resistance, while the dc bias on the electrode makes it accessible to only the high temperature electron group, T_{ehigh}. Consequently, T_{ehigh} governs R_e. The resistances R_e and R_p are related to A_e and A_p, the electrode and probe areas respectively. The ratio of these areas must be very small if the rf electrode resistance is to be neglected, i.e.

$$\frac{A_p}{A_e} << \left(\frac{m_e T_{elow}}{M T_{ehigh}} \right)^{1/2} \frac{n_s}{n_p} << 10^{-5} \qquad 3.1.2$$

where n_s is the density at the plasma-sheath boundary, n_p is the plasma density measured by the probe, m_e and M are the electron and ion masses, respectively. For the systems used in this thesis, the ratio A_p/A_e is $\approx 10^{-5}$ (system 1) and $\approx 10^{-4}$ (system 2) so some distortion of the low energy part of the EEPF is expected. A large electrode area is required to achieve an acceptable value of A_p/A_e, this is not practical in most experiments so it follows that measurement of and correction for the ground electrode sheath resistance is necessary, particularly in discharges with a small powered electrode.

When drawing electron current, the probe alters the plasma potential by disturbing the balance between the ion current to both electrodes. The change in plasma potential as a function of probe current yields a value for the plasma-ground resistance, R_e [2]. This is measured in these experiments using a second reference probe that

monitors the changes in floating potential as the measuring probe is biased. Plotting the change in voltage of the reference probe *versus* the measuring probe's current yields a value for R_e, see figure 3.2 for typical measurements.

Neglecting this correction can lead to an overestimation of the average electron energy due to the shift in plasma potential. In the plasmas studied here, this may exceed 0.5 eV. Figure 3.3 shows a comparison of average electron energy measurement made with and without the correction for R_e.

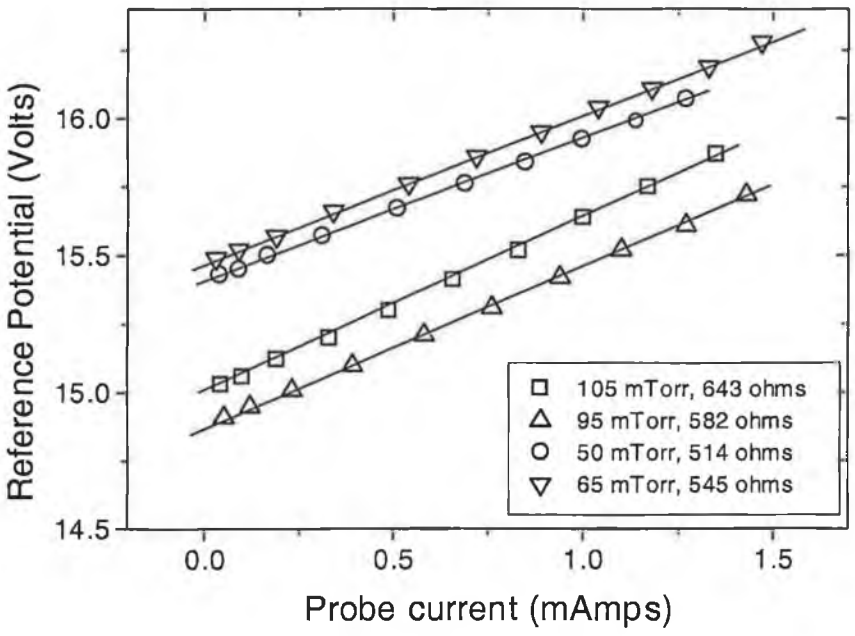

Figure 3.2: Sheath resistance measurements for argon at 1 Amp constant current.

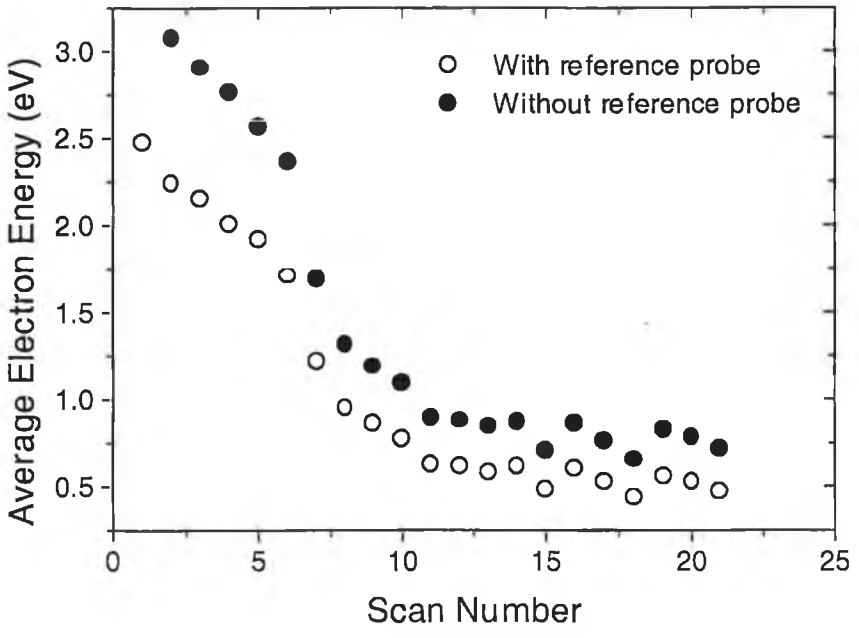

Figure 3.3: Comparison of electron energy measurements made in argon at 300 mTorr. Increasing scan number corresponds to increasing rf power (5-100 watts).

3.2 Heating Mechanisms in Parallel Plate Radio Frequency Discharges

Three primary heating mechanisms have been identified for electron heating in rf glow discharges: (i) secondary electron emission from the electrodes. These electrons are accelerated in the large sheath fields and enter the plasma; (ii) heating of the plasma electrons by the bulk electric field, and (iii) heating of the plasma electrons by the oscillating sheath electric field. The third mechanism is exclusive to rf discharges. There are two cases of sheath oscillation heating, collisionless sheath heating and collisional or Ohmic sheath heating. A discussion of sheath heating follows that considers primarily the collisionless case. Ohmic sheath heating is described in section 3.2.2.

3.2.1 Sheath Heating

In Chapter 1 the 'hard wall' model of the sheath was introduced. The process by which the ball interacts with the moving wall is called Fermi acceleration and was first used to explain the origin of cosmic rays [3]. This model has also been used to describe the collisionless heating of electrons by repeated interactions with the sheath electric field in rf plasmas [1,4].

The velocity of an electron reflected off the moving sheath is

$$v_r = -v + 2v_s \qquad 3.2.1$$

where v is the electron's initial velocity and v_s is the sheath velocity. When the electron collides repeatedly with the sheath there is a net energy gain if successive collisions with the sheath field occur at random oscillation phases. Sheath heating occurs when the sheath is considered almost collisionless while the plasma is considered collisional. In this regime, collisions in the plasma disrupt the ballistic motion of the two sheaths and the conditions for random phase are satisfied [5,6].

Several computer models of the rf sheath have been devised. A homogeneous sheath model was developed by Godyak and Popov [7]. Experiments devised to test this model showed discrepancies between experimental and theoretical sheath width values that increased with decreasing gas pressure [8]. This was attributed to the actual inhomogeneous ion distribution within the sheath between the plasma-sheath edge and the electrode. This inhomogeneity leads to a Child law variation in density across the sheath [9].

$$n = \frac{4}{9}\frac{\varepsilon_0}{e}\frac{V_o}{s^2}\left(\frac{x}{s}\right)^{-2/3} \qquad 3.2.2$$

where n is the density, x is the position in the sheath and s is the sheath width. The Child law for ions is modified due to the partial shielding of the positive space charge by the oscillating electrons [9]. Some authors have used a Child-Langmuir law for the ions within the sheath to model the sheath dynamics [10,11].

Monte Carlo and particle in cell (PIC) simulations have confirmed the existence of sheath heating in low-pressure capacitively coupled discharges [12-16]. Nitschke and Graves compared a fluid model that did not include stochastic heating with a PIC simulation that did [17]. The fluid simulation yielded half the electron power deposition, hence half the density compared to the PIC simulation. Adding stochastic heating to the fluid model resulted in closer agreement of the two techniques.

It is also clear from modelling work that space and time variations of the electron energy distributions near the sheath are important. Examination of the electron energy distributions at certain times in the rf cycle by Wood showed heating of the electrons during sheath expansion [18]. The time-varying, two temperature Maxwellian distributions used in this work were used to calculate values for power absorption that compared well with experimental values [18,19].

Ionisation is increased at the plasma-sheath edge due to the presence of higher energy electrons from sheath heating. This ionisation varies in space and time and most of the ionisation occurs along a path of fast electrons that are reflected off the sheath at the point in the rf cycle at which it is most rapidly expanding [20]. Ionisation at the sheath edge becomes more pronounced at higher pressures where the ionisation mean free path is shorter. This is discussed in more detail in the following section and in Chapter 5.

The first experimental evidence of energy exchange between the oscillating rf sheaths and the plasma electrons was obtained in experiments using resonance probes [21,22]. Sheath heating was first considered to have an important role in low pressure rf discharge maintenance by Godyak who studied the bi-Maxwellian feature of the EEPFs theoretically [23,24], with models [25] and experimentally [1,26]. Experimental measurements of the EEPF and plasma parameters in low pressure, capacitive rf discharges have been presented by several workers [27-29].

A typical EEPF for a pressure of 35 mTorr, gap length 4 cms and discharge current of 1.5 Amps is shown in figure 3.4. The EEPF may be represented as a sum of two Maxwellian distributions with corresponding temperatures T_{elow}=0.8 eV and T_{ehigh}=3.2 eV. These two groups have separate roles in the discharge. The low energy

group has a low electron-neutral cross section that corresponds to a low electron-neutral collision frequency:

$$\nu_{en} = Kn_g \qquad 3.2.3$$

where K is the rate constant (collision frequency per unit density) and n_g is the neutral gas density. For the EEPF in figure 3.4, $\nu_{en}=1.2\text{x}10^7\text{s}^{-1}$ for the low-energy electrons. This corresponds to a mean free path of 8 cms that is greater than the plasma length (4 cms). The low energy group originates from ionisation provided by the high-energy group and oscillates without collisions since $\nu_{en}^2 << \omega^2$. The low energy group cannot overcome the ambipolar potential barrier and so cannot reach the sheaths to be heated.

The high-energy electrons have a higher electron neutral collision frequency, $\nu_{en}=1.3\text{x}10^8\text{s}^{-1}$ with a mean free path of 4 mm that is less than the plasma length. These high-energy electrons interact with the neutral argon atoms through elastic, excitation and ionising collisions. As they can overcome the ambipolar potential barrier, compensate for their energy losses through interaction with the sheaths [26].

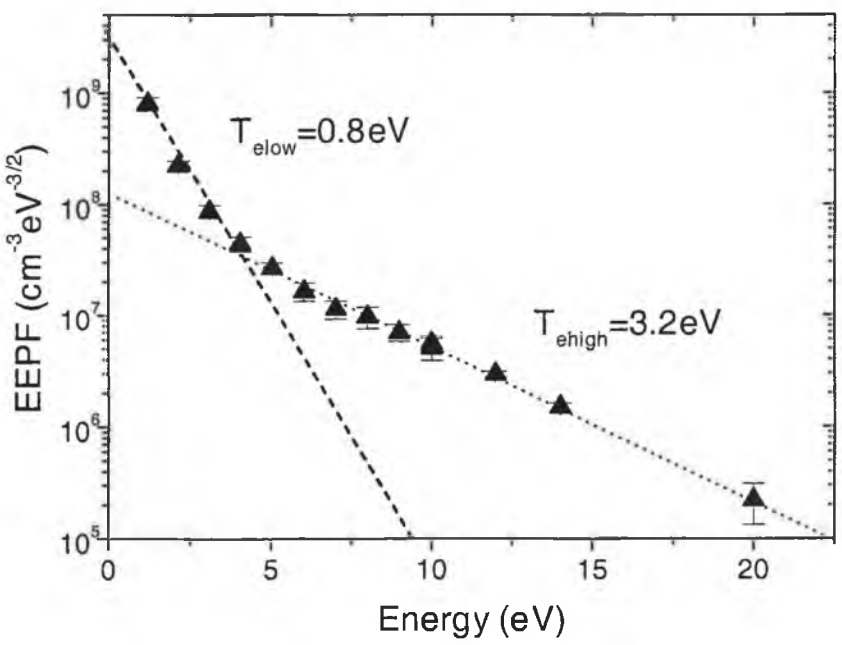

Figure 3.4: EEPF measured in the midplane of a 4 cm argon discharge at 35 mTorr and 1.5 Amps.

3.2.2 Ohmic Heating

Increasing the pressure on a low-current rf discharge causes a decrease in the mean free path. When the mean free path is less than the plasma dimensions the plasma becomes collisional. The discharge is now considered to be in the α mode. The main rf power dissipation process is Ohmic heating. Langmuir probe measurements of plasmas

in this regime yield electron temperatures of typically 2-4eV [1,29,30] and EEPFs of the Druyvesteyn form that is shown in figure 3.5. These EEPFs, with $\delta f/\delta\varepsilon \rightarrow 0$ as $\varepsilon \rightarrow 0$ (f is the EEPF, ε is the electron energy) are typical for argon plasmas in dc or low-frequency fields with no electron-electron interaction [31].

In this collisional regime, ionisation occurs in the plasma volume and at the plasma-sheath boundary. Bulk electrons with energies lower than the ionisation threshold are heated by the bulk plasma electric field and so contribute to ionisation. Enhanced emission at the plasma-sheath edge is observed. This may be attributed to ohmic sheath heating [12] and is consistent with an enhanced electron density and generation rate at the plasma-sheath boundary [Chapter 5]. As the rf sheath oscillates, the local plasma potential oscillates. During the positive part of the rf cycle when the sheath is retreating, the plasma potential near and in the sheath increases. Thermal electrons from the plasma diffuse or drift towards the electrodes. When the sheath expands, the electrons that followed the sheath in its retreat from the plasma are then in a region of lower plasma potential. These electrons are subsequently accelerated into the plasma, riding the wave of the lower plasma potential. The result is a high- energy tail in the EEPF at the sheath boundary [Chapter 5]. Since the sheath and plasma are collisional, the electrons being accelerated in to the plasma undergo collisions, imparting energy to the plasma [12]. Section 3.3.1 examines the transition from collisionless sheath heating to ohmic heating without considering the individual contributions of sheath and bulk heating in the latter regime.

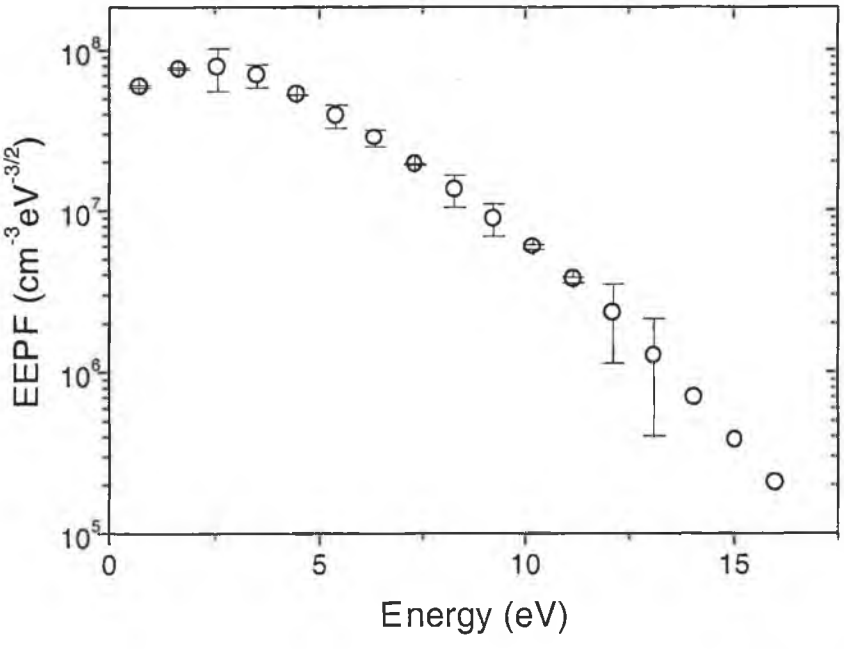

Figure 3.5: EEPF measured in the midplane of a 4 cm argon discharge at 100 mTorr and 1.5 Amps.

3.2.3 The γ Mode

Increasing the voltage (current, power) on an intermediate pressure (> 100 mTorr) rf discharge causes a dramatic change in both the appearance and properties of the discharge. Early observations of this were reported by Levitskii, who proposed that dramatic changes in the emission intensity and the electrical characteristics were due to distinctly different ionisation processes [32]. At relatively low rf voltages (typically < 100 Volts amplitude), ohmic heating is the dominant process. At higher discharge voltages, secondary electrons emitted from the electrode surface (hence the term γ mode as the secondary electron emission coefficient of a material is termed its 'γ') play more of a role in sustaining the discharge and may even dominate the bulk ionisation processes in the discharge. This regime of operation is analogous to the negative glow region of a dc column or a hollow-cathode discharge [12,33,34]

This high voltage mode has been investigated theoretically [35,36], using fluid models [37,38] and numerical simulations [39]. Experimental investigations of this regime have been performed in helium using Langmuir probes [40-42], optical emission spectroscopy [43] and Thomson Scattering [44]. Detailed studies in argon are described in [30] and section 3.2.2.

Figure 3.6 shows an EEPF measured in the midplane of a high-voltage argon rf discharge. The characteristic two-temperature structure is evident and has been measured in helium rf discharges [40,42]. There is a low-energy group with corresponding density of the same order as the plasma density, 1.1×10^{10}.

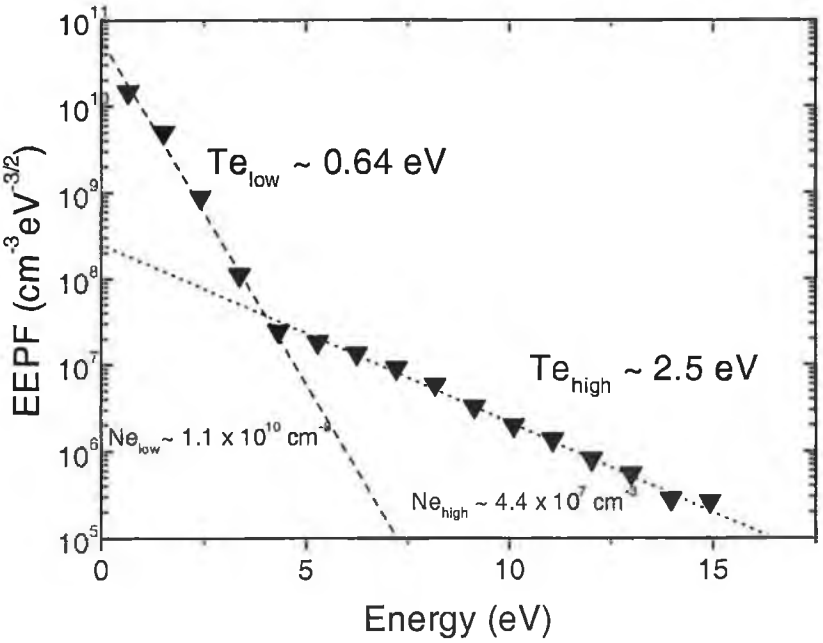

Figure 3.6: EEPF measured in the midplane of a 300 mTorr, 4 cm gap argon discharge at 200 Volts amplitude.

The high-energy group, with a temperature of 2.5 eV, has a density that is three orders of magnitude less than that of the low energy group. As is usually the case with probe measurements, electrons above the ionisation threshold for argon (15.75 eV) are scarcely detected, so the high-energy tail is only indirect evidence of secondaries and their progeny.

3.3 Transitions in Heating Modes

The point at which the discharge transits form one regime of operation to another may be seen in figure 3.7, where the EEPF changes shape as first the pressure rises in a constant current discharge, then as the voltage and current rise in a constant pressure discharge. Plasma parameters, the current-voltage characteristic and the appearance of the discharge itself also change markedly from one regime to another.

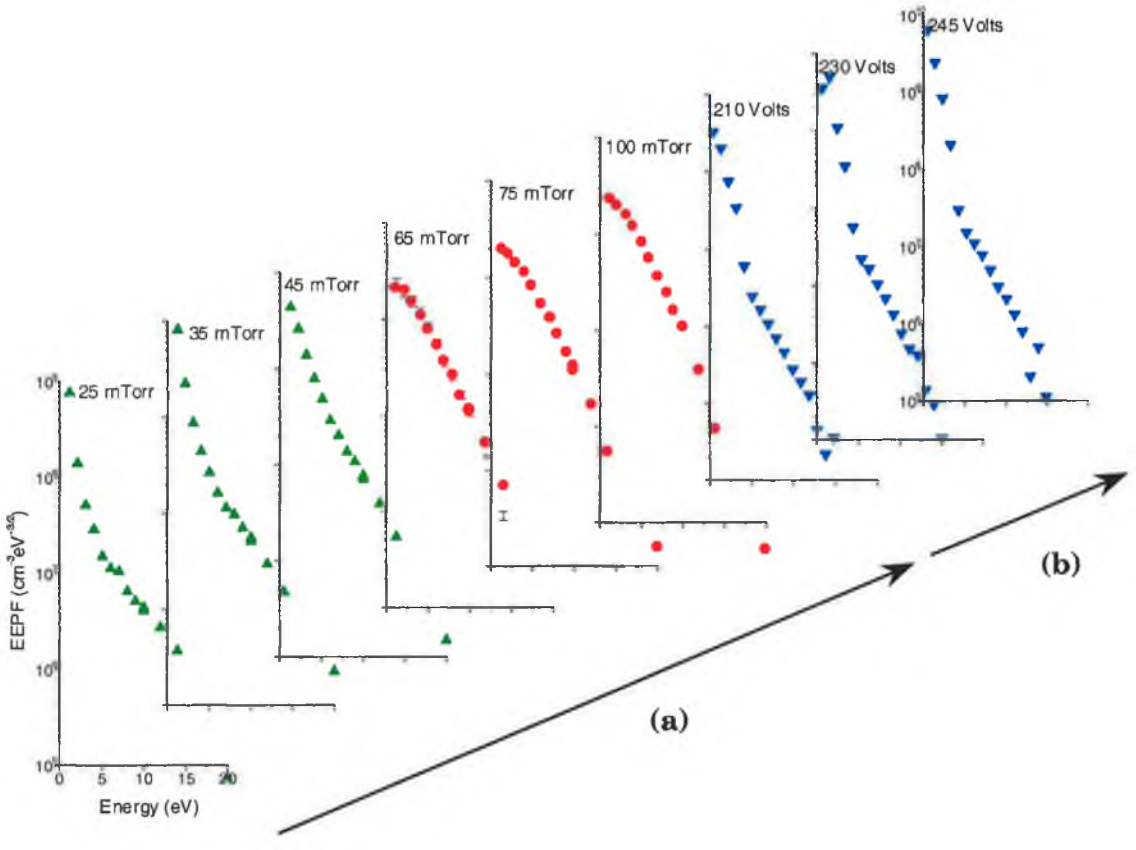

Figure 3.7: Evolution of the EEPF in the midplane of an argon discharge at (a) constant current, increasing pressure and (b) constant pressure (100 mTorr), increasing voltage and current.

3.3.1 The Transition from Sheath to Ohmic Heating

Measurements were made in the midplane of the argon discharge at gas pressures from 15 to 250 mTorr. Over this pressure range, the discharge current density

was maintained at 1.5 Amps (~ 3 mA/cm^2). Plasma parameters and the EEPF were measured for three electrode gaps over a range of pressures for the constant discharge current. The transition in heating mechanism was characterised by a decrease in the average electron energy as the pressure was decreased, see figure 3.8.

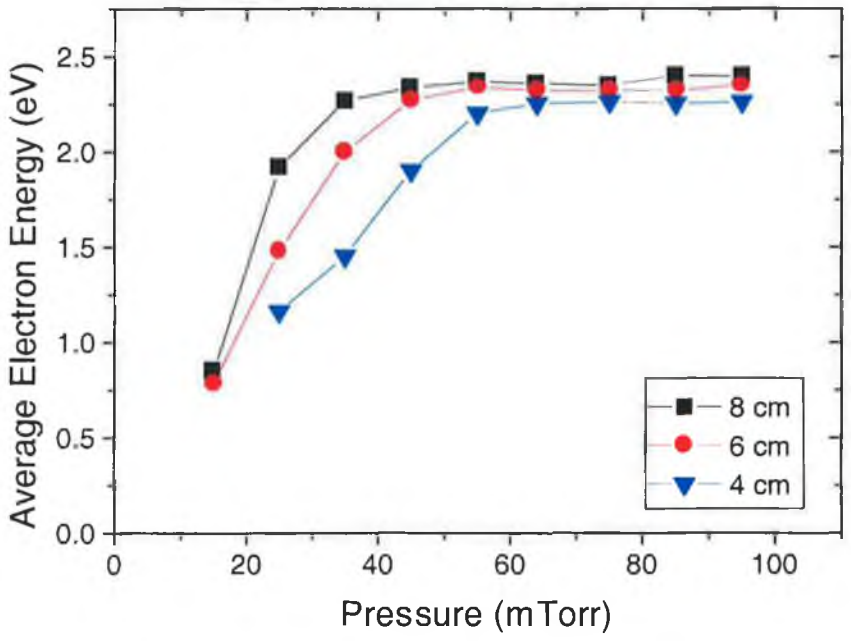

Figure 3.8: Average electron energy as a function of pressure for argon at a constant current of 1.5 Amps.

The average electron energy increases with increasing pressure due to the transition from sheath heating to ohmic heating. The increase in collisions and heating in the plasma bulk result in a higher average energy and more uniform energy distribution amongst the electrons.

At this point it should be noted that a comparison of the measured electron energy at the same pressure and current and different electrode gaps yields almost a factor of two decrease in energy as the gap length is decreased from 8 to 4 cms. Very low electron energies have been measured before in argon and the discrepancy between those and similar measurements were attributed to inadequate probe systems [26]. However, these measurements indicate that the electron energy may be a function of gap length. In weakly ionised plasma such as those studied in this thesis, the primary ionisation mechanism is electron impact ionisation. The primary loss mechanism in such plasmas is diffusion to the chamber walls. The production mechanism is a function of plasma volume, therefore of the spacing between the electrodes. The primary loss mechanism is diffusion to the walls and so is a surface effect that also depends on the gap between the electrodes. Although the production and loss mechanisms both scale

with electrode gap, the production process at constant current should scale up and down more rapidly than the loss process since it is a volume effect. This is consistent with the fact that higher densities are measured in the discharge for larger gaps at the same pressure and current (see figure 3.9) and may result in a higher average electron energy in larger discharges.

An increase in electron and ion density with pressure would normally be expected. However, at low currents and over the pressure range examined, the ion density measured at the discharge midplane decreased as the pressure was increased, see figure 3.9. At constant discharge current, the production rate is constant for all pressures examined. The decrease in density in the centre is due to an increase in the particle loss rate at higher pressures. The reasons for this become more apparent when the spatial density profiles are examined (see Chapter 5). At low pressures, the density profiles are symmetric about the midplane (figure 5.8). The resulting symmetric ambipolar potential distribution, with zero field in the middle, means that the electrons are effectively trapped in a potential well. This results in a low loss rate in the centre of the discharge. By contrast at high pressures the axial density profile is asymmetric (figure 5.8). Consequently the asymmetric ambipolar field in the centre means that for constant current, the electron loss rate higher than the low pressure case. The overall result is that the density in the centre is lower at high pressures, though the peak density in the plasma may be the same or higher.

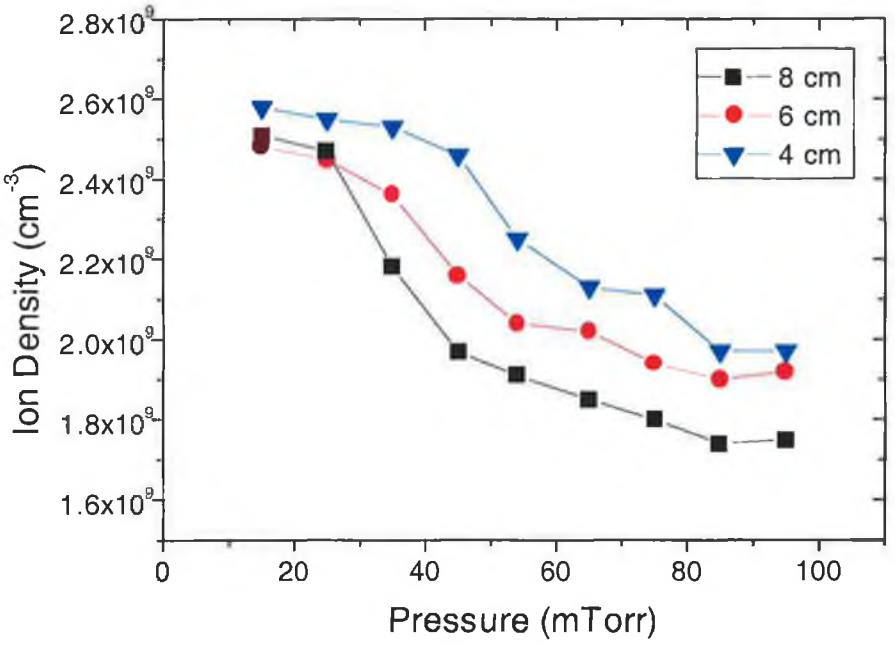

Figure 3.9: Ion density *versus* pressure for argon at a constant current of 1.5 Amps.

Figures 3.8 and 3.9 showed that the transition pressure decreases for increasing gap. The transition pressure is taken as the point of steepest slope on the electron energy *versus* pressure curve. The value of *pD* has been found to be approximately 200 mTorr cms for argon discharges [1,26,27]. Here, the *pD* parameters for gaps of 8, 6 and 4 cms are approximately 200, 180, and 190 mTorr cms. This confirms the scaling law for heating mode transitions described in [1]. Comparisons between experiment and simulation have shown agreement in the transition from sheath to ohmic heating [26,45,46].

The primary heating mechanisms in such plasmas determines the shape of the energy distribution function, so a change in shape indicates a transition from one mechanism to another. This was observed here for all electrode gaps, two of which are shown in figures 3.10 and 3.11. From these figures it is clear that the EEPF changes shape from a bi-Maxwellian, two-temperature distribution to a Druyvesteyn distribution at higher pressures and for smaller gap lengths.

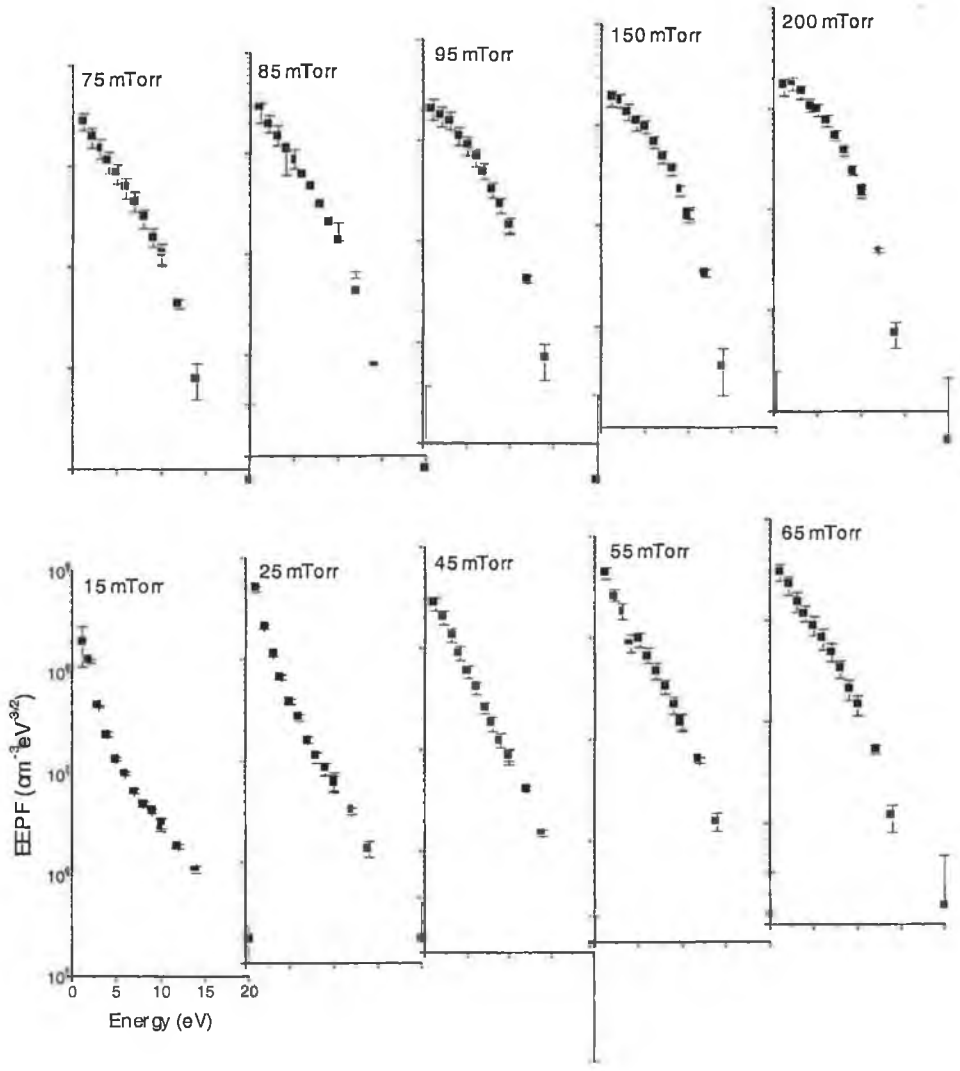

Figure 3.10: Evolution of the EEPF for an argon discharge with gap length 8 cms and constant discharge current of 1.5 Amps.

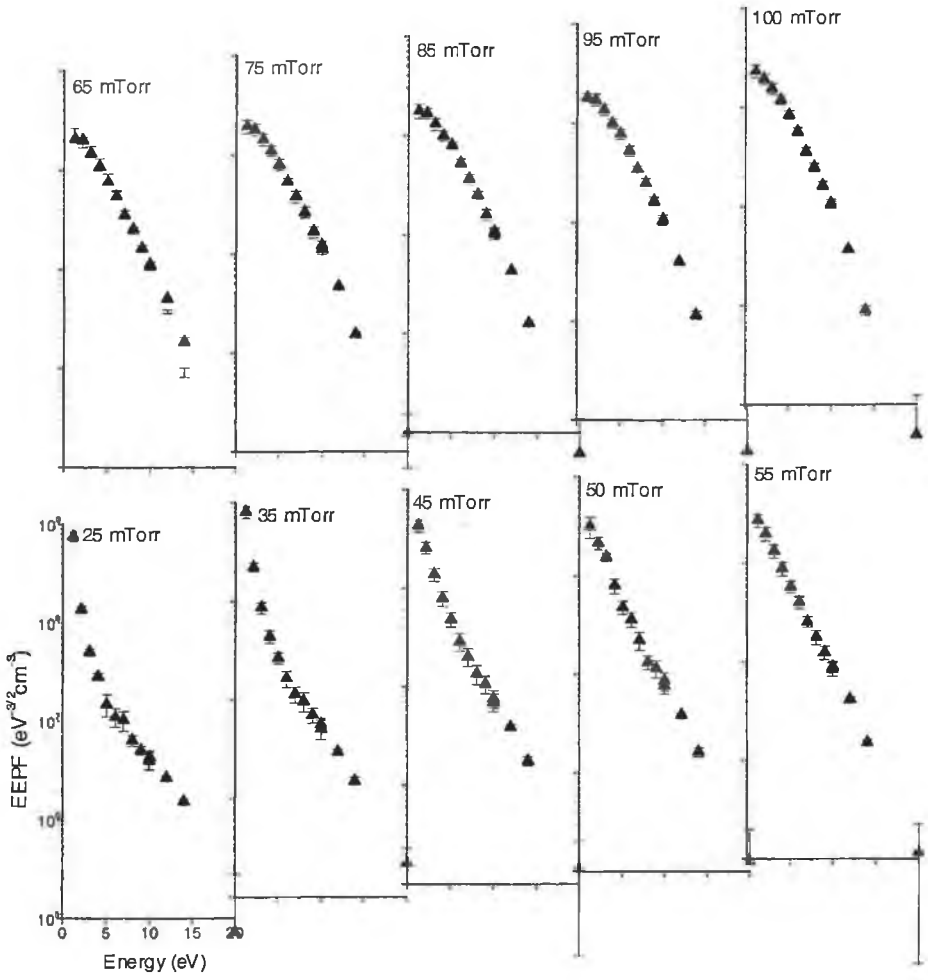

Figure 3.11: Evolution of the EEPF for an argon discharge with gap length 4 cms and constant discharge current of 1.5 Amps.

Similar measurements of the EEPF and plasma parameters in argon in system 2 also indicated a transition from the sheath heating regime to the ohmic heating regime. However, this occurred at a much larger *pD* of 750 mTorr cms. There was no measured change in transition pressure with gap. This is attributed to the discharge in system 2 not being as well confined as in system 1. The chamber dimensions in system 2 are a great deal larger than the electrode widths and gaps in the system, so the scaling law mentioned earlier would not apply in this chamber.

3.3.2 The α-γ Transition

Langmuir probe measurements were made is system 1, again with the probes in the discharge mid plane as shown in figure 3.1. In this experiment, the α-γ transition is studied at 100 and 300 mTorr.

Probe contamination can be a problem in high voltage discharges because the high sheath potentials required for secondary emission also result in contamination by sputtered material from the powered electrode. Care is taken to clean the probe by biasing it to > 100 Volts before every scan. This allows cleaning by electron bombardment. The probe will become contaminated if left biased close to the plasma potential for any time so the probe voltage is scanned in a non-sequential manner to avoid this [2].

Limitations on the energy resolution and dynamic range of electrostatic probes has made probe determination of the temperature of the low-energy component and detection of the high-energy 'tail' of the distribution function difficult to determine in the case of argon [40]. An improved probe system, the main features of which were discussed in sections 2.3 and 3.1, has resulted in measurement of bi-Maxwellian distribution functions for argon at high voltages, allowing examination of the high-energy group in the plasma.

As the potential (current and power) to the argon rf discharge is increased, a marked increase in emission intensity is noticed. This correlates well with distinct changes in electron and ion density and average electron energy. Figure 3.12 shows the average energy and the ion density measurements at 100 and 300 mTorr. The average electron energy in the α mode is approximately 2.5 eV, while the ion density increases linearly with increasing rf potential. At both pressure settings, the α-γ transition is characterised by a sharp increase in plasma density coupled with a decrease in electron energy. This point corresponds to a transition voltage of approximately 150 Volts for the 300-mTorr discharge and 200 Volts for the 100-mTorr discharge. These potential values correspond well with typical 'cathode fall' voltages in dc discharges [12,40].

At both pressure settings the EEPF measured in the plasma midplane evolves from a Druyvesteyn to a bi-Maxwellian distribution. This is shown in figures 3.13 (300 mTorr) and 3.14 (100 mTorr). The transition voltages obtained from the measured plasma parameters agree well with the change in form of the EEPF. As the distributions measured are distinctly non-Maxwellian, the electron temperature may not be accurately defined by the electron retardation part of the probe characteristic. It follows that

accurate measurement of the EEPF is important as it allows examination of the separate electron populations in the plasma.

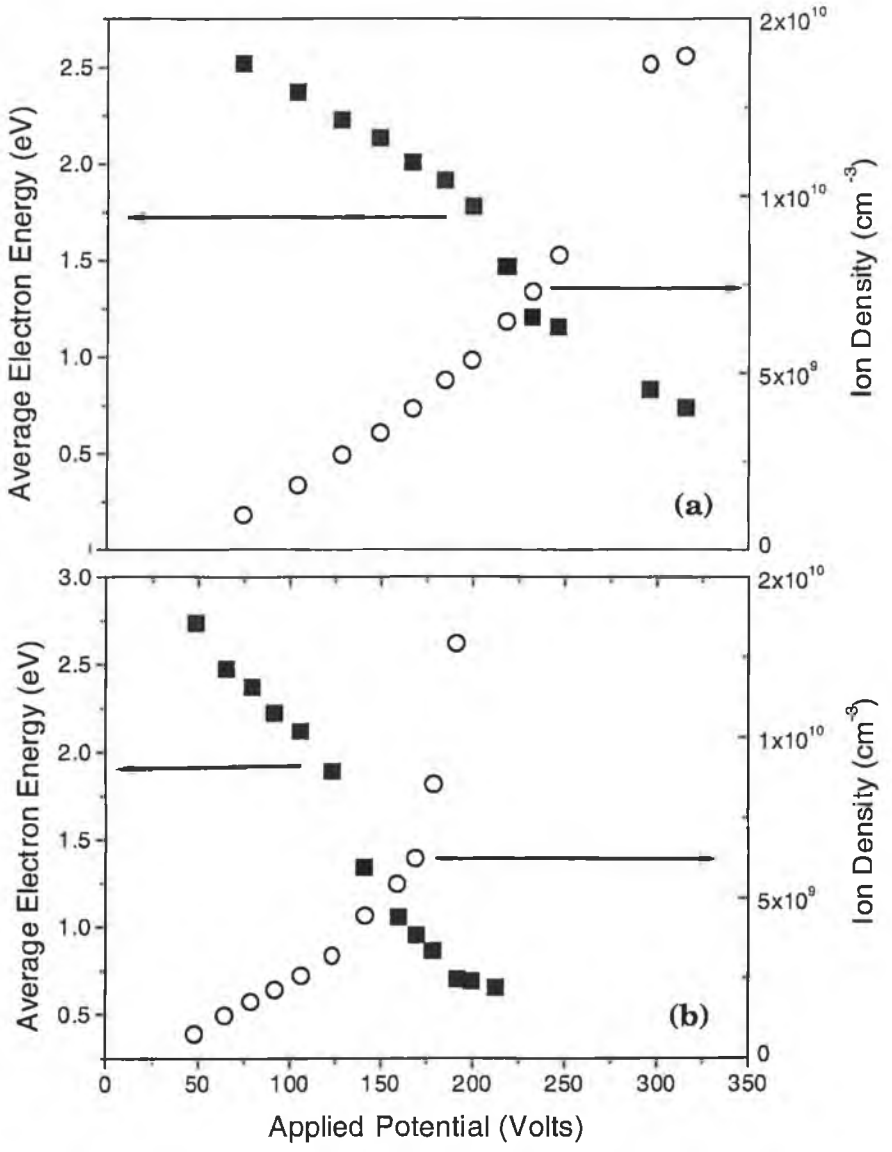

Figure 3.12: Average electron energy and ion density as a function of applied rf potential amplitude for a (a)100mTorr and (b) 300 mTorr argon rf discharge. Gap length is 3cms.

Figure 3.15 shows the densities of the bulk electrons (in the α mode) and the 'hot' (the high-energy tail of the EEPF) and 'cold' (the low-energy component of the EEPF) electron groups at 100 and 300 mTorr. The average density of the hot group at 300 mTorr is 1.5 x 10 ^{7} cm^{-3}, three times lower than that of the hot group at 100 mTorr. This is a consequence of the shorter mean free path for collisions at the higher pressure setting, resulting in increased loss of the hot electrons' energy via inelastic collisions.

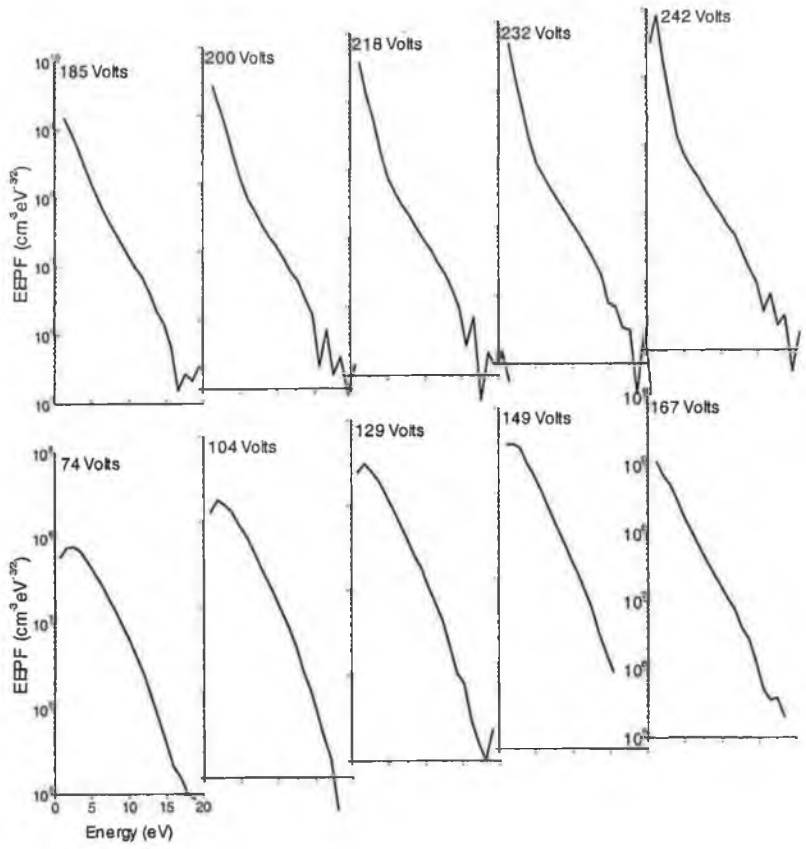

Figure 3.13: Evolution of the EEPF with applied rf potential at 100 mTorr. Gap length is 3cms.

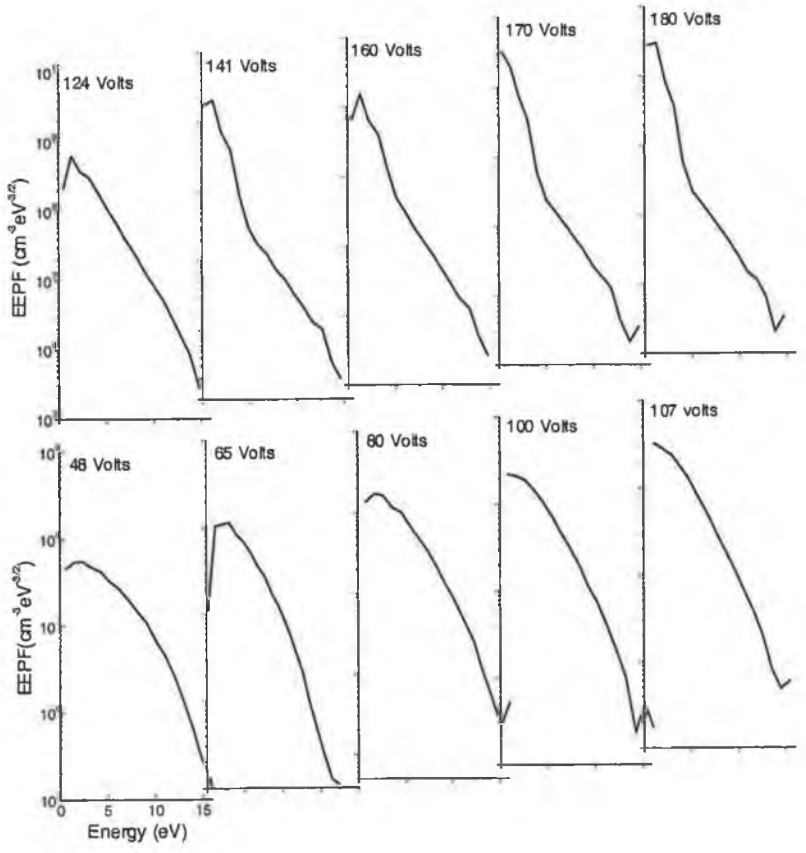

Figure 3.14: Evolution of the EEPF with applied rf potential at 300 mTorr. Gap length is 3cms.

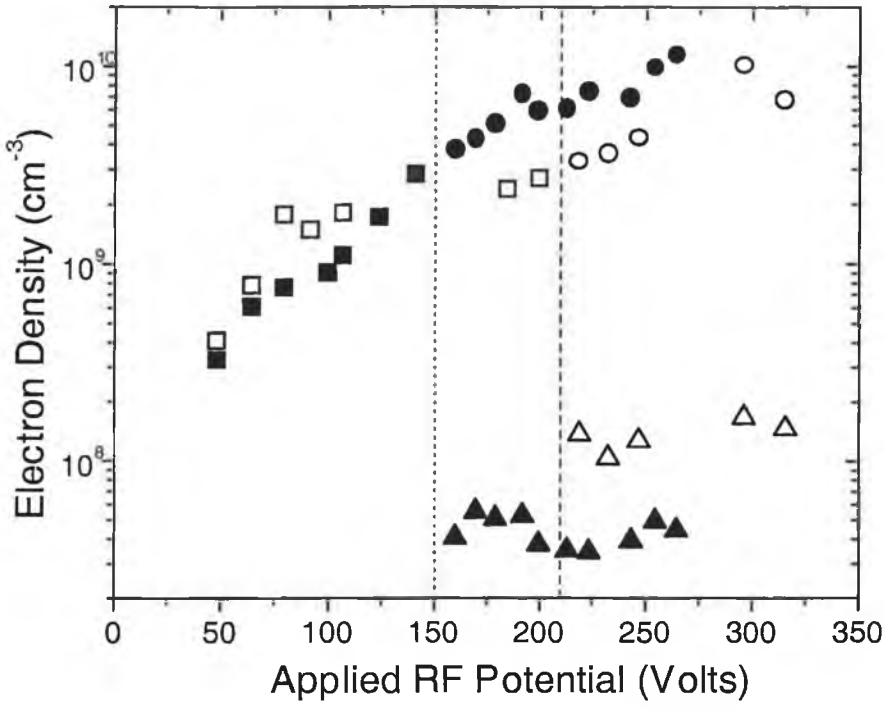

Figure 3.15: Electron densities, determined from the EEPF, at 100 (open symbols) and 300 mTorr (closed symbols),□ /■, bulk density in the α mode; ○/●, low-energy group;△/▲, high-energy group; dotted line, transition point at 300 mTorr; dashed line, transition point at 100 mTorr.

The departure from a linear current-voltage characteristic with the onset of the γ-mode has been observed in this experiment and by others [47-49]. Figure 3.16 shows three distinct regions in the current-voltage characteristic. In both the α and γ-mode plasma, the current-voltage characteristic is approximately linear. The flat section of the curve indicates the transition from one regime to another. The increase in density as a result of the secondary injection into the plasma results in the low energy electron group cooling down because more electrons are carrying the same current. Once the current increases after the transition, the temperature of the bulk electrons also increases.

Measurements made by Lisovskii of this transition have reported a decrease in sheath width as the discharge changes from the α to the γ mode [50]. Using experimental values of electron density, electron temperature and sheath voltage, the sheath width is estimated using [9,51]

$$s = 1.36\frac{\sqrt{2}}{3}\lambda_{De}\left(\frac{2V_0}{T_e}\right)^{3/4} \qquad 3.3.1$$

where $\lambda_{De}=743(T_e/n_e)^{1/2}$ is the electron Debye length, V_o is the sheath potential and T_e is the electron temperature in eV. Figure 3.17 shows the estimated sheath width *versus* the

applied rf potential for the 300 mTorr discharge. The sheath capacitance decreases as the sheath widens with increasing rf voltage. During the transition, the average electron energy decreases with increasing rf voltage such that the rf current remains almost constant and the overall discharge impedance increases despite the increase in plasma density. Once the discharge is in the γ mode, the sheath narrows and the impedance decreases.

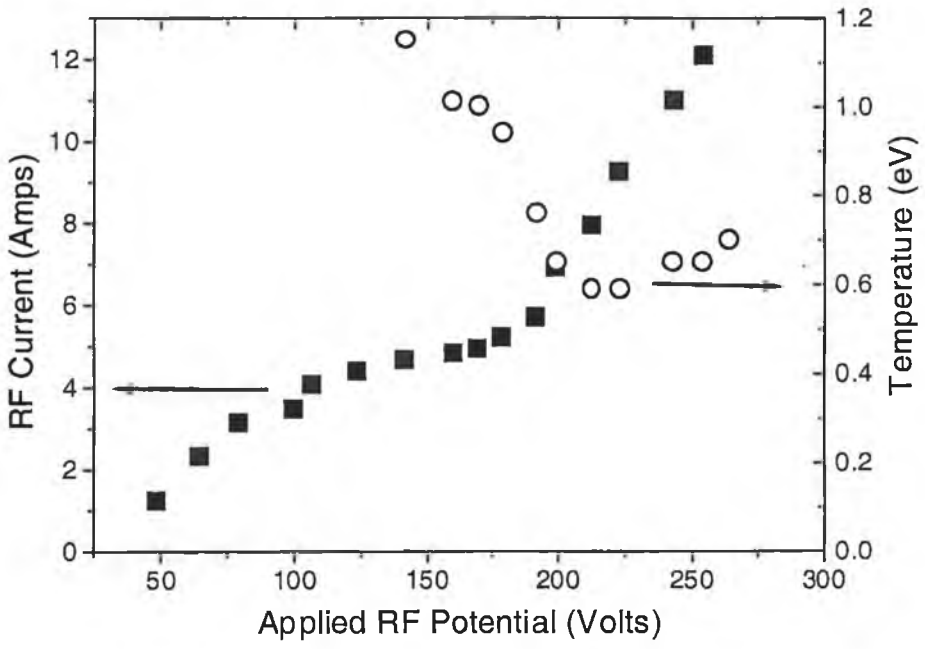

Figure 3.16: Measured rf current and temperature of the low-energy group *versus* applied potential for argon at 300 mTorr.

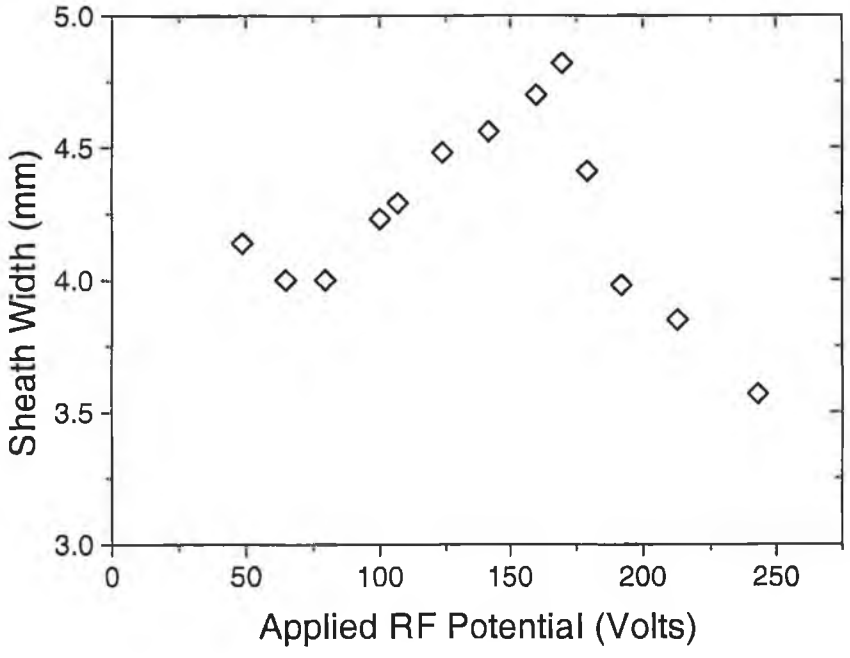

Figure 3.17: Sheath width as a function of applied potential for argon at 300 mTorr.

Measurements of the α-γ transition were also made for a 7 cm discharge at 100 mTorr. Experiments have shown that the transition voltage depends on discharge gap as well as pressure. The evolution of average electron energy and ion density is shown in figure 3.18. It is clear that the transition to the γ mode occurs at a lower voltage for a larger electrode gap; 150 Volts for a 7 cm discharge compared to 200 volts for a 3 cm discharge. Figure 3.19 shows similar measurements of the α-γ transition made in system 2.

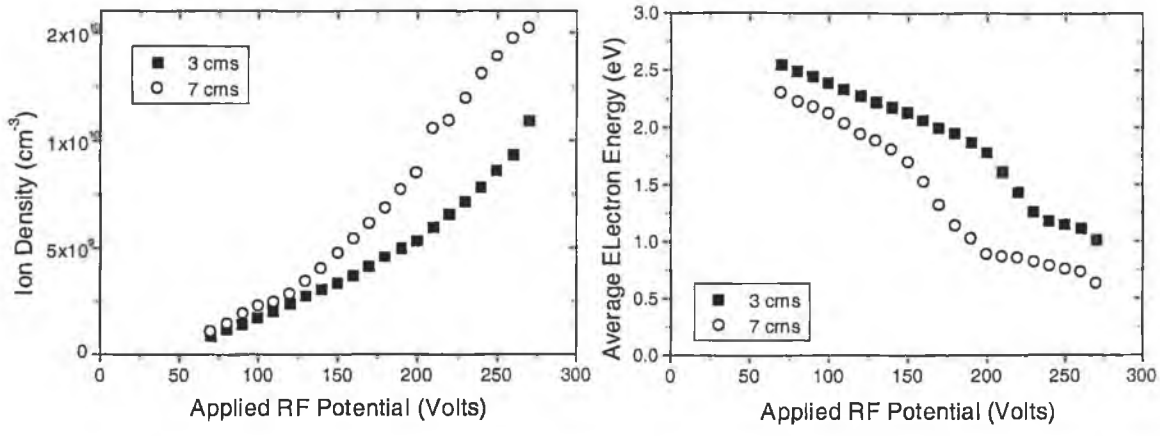

Figure 3.18: Average electron energy and ion density as a function of applied rf potential for a 7 cm discharge at 100 mTorr.

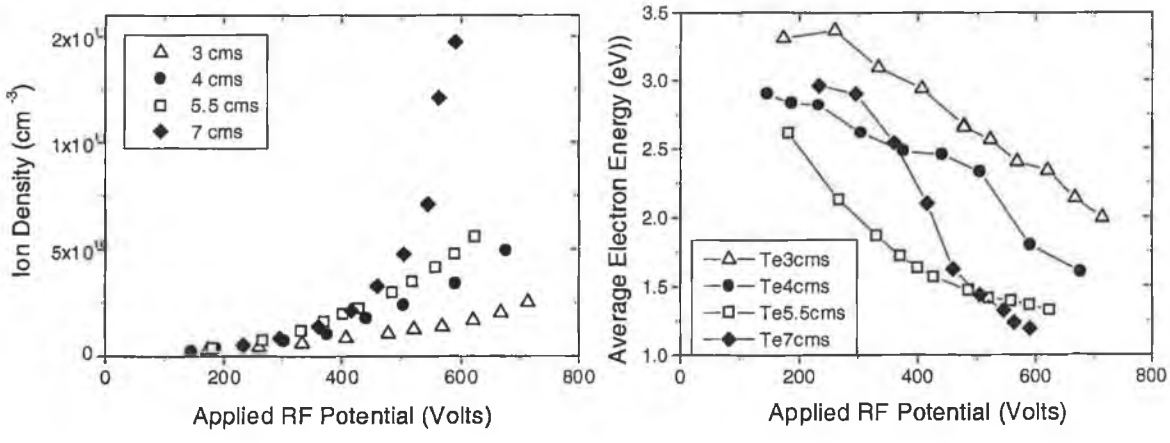

Figure 3.19: Average electron energy and ion density as a function of applied rf potential for several discharge gaps in system 2 at 300 mTorr.

3.4 Concluding Remarks

The aim of this chapter was to characterise the transitions in heating mechanisms in a capacitively coupled discharge. These transitions are clearly observed as changes in the measured plasma parameters and the EEPF. Measurements of the transition from sheath to ohmic heating are in good agreement with others and the *pD* parameter

defining the transition was found to be approximately constant for three electrode gaps. This parameter is a valid method of defining the transition only if the discharge is well confined.

At low pressures the plasma is sustained by the heating of some of the plasma electrons at the oscillating sheath edge, the cooler bulk electrons remain in the main body of the plasma, unable to gain energy from the sheaths. Thus, experimental measurements of a bi-Maxwellian EEPF are considered to be a manifestation of a plasma sustained by sheath heating. Direct experimental evidence of sheath heating has not yet been obtained using Langmuir probes. Evidence that this mechanism is one of the primary processes in low-pressure discharges is found mostly in the modelling work referenced in this thesis.

Increasing the applied voltage on an intermediate pressure discharge results in a transition to a so-called secondary electron emission dominated regime. The transition potential compares well with a typical 'cathode fall' potential in a dc discharge. The appearance of a high-energy 'tail' in the probability function is understood to be the result of high-energy electron penetration into the plasma volume. At higher pressures, less high-energy electrons are evident due to a decrease of the interaction mean free path.

In the γ mode, secondary electrons that are produced at the powered electrode by ion impact, are then accelerated across the sheath and perform ionisation. This occurs at neutral pressures at or greater than 100 mTorr, as at these pressures the conditions are favourable for a cascade of ionising collisions in the sheath. This results in a narrowing of the sheath width on transition to the γ mode. The discharge current is non-linear with voltage due to the changes in sheath capacitance that arise as it first increases, then decreases in width. The decrease in bulk electron temperature results in the discharge remaining constant in the transition region despite the increase in plasma density.

It is clear from these measurements that the capacitive discharge has several regimes of operation. In this chapter, all measurements were made in the discharge midplane with a view to examining the transitions in regimes. The appearance of the discharge in different regimes suggests that the spatial distribution of density, temperature and the corresponding ionisation profiles should vary significantly with changes in operating parameters. This is investigated in Chapter 5.

References

[1] V.A. Godyak, R. B. Piejak and B. M. Alexandrovich, Plasm. Sces. Sci. Technol., 1, 36-58, (1992).

[2] M. B. Hopkins, J. Res. Natl. Inst. Stand. Technol., 100, 1995, 415.

[3] E. Fermi, Phys. Rev. 75, 1169, (1949).

[4] M.A. Lieberman and V.A. Godyak, Memorandum No. UCB/ERL M97/65, (1997).

[5] M. Surrendra, D.B.Graves and I.J. Morley, Appl. Phys. Lett. 56, 1022, (1990).

[6] D. Vender, Ph.D. Thesis, The Australian National University, Canberra, (1990).

[7] V.A. Godyak and O.A. Popov, Sov. J. Plasm. Phys. 5, 227, (1979).

[8] V.A. Godyak, O.A. Popov and A.H. Hanna, Proceedings of the XIII International Conference of Phenomena in Ionised Gases, Berlin, (1997).

[9] M.A. Lieberman and A.J. Lichtenberg, *Principles of Plasma Discharges and Materials Processing*, Wiley Interscience, (1994).

[10] H.R. Koenig and L.I. Maissel, IBM Jour. Res. Dev., 14, 168, (1970).

[11] W. Pennebaker, IBM J. Res. Dev., 23, 16, (1979).

[12] M.J. Kushner, IEEE Trans. Plasma Sci., PS-14, 188, (1986).

[13] M. Surrendra and D.B. Graves, Phys. Rev. Lett., 66, 1669, (1991).

[14] D.Vender and R. Boswell, J. Vac. Sci. Technol., 18, 725, (1992).

[15] A.E. Wendt and W.N.G. Hitchon, J. Appl. Phys. 71, 4718, (1992).

[16] M. Surendra and D. Vender, Appl Phys. Lett., 65, 153, (1994).

[17] T.E. Nitschke and D.B. Graves, J.Appl.Phys, 76, 5646, (1994).

[18] B.P. Wood, M.A. Lieberman and A.J. Lichtenberg, IEEE Trans. Plasm. Sci, 23, 89, (1995).

[19] V.A. Godyak, R.B. Piejak and B.M. Alexandrovich, IEEE Trans.Plasm. Sci., 19, 660, (1991).

[20] D.Vender and R.W.Boswell, IEEE Trans. Plasm. Sci., 18, 725, (1990).

[21] R.W. Gould, Phys. Lett. 11, 236, (1964).

[22] R.S. Harp and F.W. Crawford, J. Appl. Phys., 35, 3436, (1964).

[23] V.A. Godyak, Sov. Phys. Tech. Phys., 16, 1073, (1972).

[24] V.A. Godyak, *Soviet Radio Frequency Discharge Research*, Delphic Associates, Falls Church, VA, (1986).

[25] V.A. Godyak, Sov. J. Plasma Phys., 2, 78, (1976).

[26] V.A.Godyak, R.B. Piejak and B.M. Alexandrovich, Phys. Rev. Letts., 65(8), 996-999, (1990).

[27] R. A. Doyle, PhD Thesis, Dublin City University, (1994).

[28] J. Scanlan, PhD Thesis, Dublin City University, (1989).

[29] J. McFarland, C.M.O. Mahony, P.G. Steen and W.G. Graham, Europhysics conference abstracts, 22H, 152, (1998).

[30] C. M. Deegan, J. P. Goss, D. Vender and M. Hopkins, Appl. Phys. Letts. 74(4), 1969, (1999).

[31] E. V. Karoulina, J. Phys. D:Appl. Phys. 21, 411, (1988).

[32] S.M. Leviitski, Sov. Phys. Tech. Phys. 2, 887, (1957).

[33] Y.Raizer, M.N.Schneider and N.A.Yatsenko, *Radio Frequency Capacitive Discharges, CRC Press*, (1995).

[34] Y. Raizer, *Gas Discharge Physics*, Springer-Verlag, New York, (1987).

[35] V.A. Godyak and A.S. Khanneh, IEEE Transactions on Plasma Science, PS-14, 2, 112, (1986).

[36] Y. Raizer and M.N. Schneider, Sov. J. Plasma Phys. 17(11), 789, (1991).

[37] I. Odrobina and M. Kando, Proceeding of the Eleventh International Conference of Gas Discharges and their Applications, Tokyo, 11th-15th September, (1995).

[38] I. Odrobina and M. Kando, Plasm. Sces. Sci. Technol., 5, 517-522, (1996).

[39] Y. Raizer and M.N. Schneider, J.Phys. D. Appl. Phys. 27, 1457-1464, (1994).

[40] V.A. Godyak, R.B. Piejak and B.M. Alexandrovich, Phys. Rev. Letts., 68(1), 40, (1992).

[41] A. Melzer, R. Flohr and A. Piel, Plasma Sces. Sci. Technol., 4(3), 424-431, (1995).

[42] G. Dilecce, M. Capitelli and S. De Benedictis, J. Appl. Phys., 69, 1121, (1991).

[43] R. Flohr and A. Piel, Phys. Rev. Letts, 70, 8, 1108, (1993).

[44] H-J.Weßeling and B.Kronast, J. Phys. D. Appl. Phyys. 29, 1035-1039, (1996).

[45] M.M. Turner, R.A. Doyle and M.B. Hopkins, Appl. Phys. Lett., 62, 3247-3249, (1993).

[46] V. Vahedi, C.K. Birdsall, M.A. Lieberman, G.DiPeso and T.D.Rognlien, Plasma. Sci. Technol., 2, 273, (1995).

[47] V. A. Lisovskii, V. D. Egorenkov, and O. V. Krasnikov, Tech. Phys. Lett. 19, 11, (1993).

[48] N. Kropotov, V. Lisovskii, Y. Kachanov, V.D Egorenkov and V. I. Rarenik, Sov. Tech. Phys. Lett. 15, 11, (1989).

[49] N.A. Yaksenko, Sov. Phys. Tech. Phys. 26(6), 678, (1982).

[50] V. A. Lisovskii, Tech. Phys. 43(5), 526, (1998).

[51] M. A. Lieberman, IEEE Trans. Plasm. Sci., 16(6), 638, (1988).

Chapter 4

Diffusion Modeling and Determination of Ionisation Profiles

Introduction

The purpose of this chapter is to discuss diffusion, the fundamental loss process in an electropositive, weakly ionised plasma. The geometry of the experimental systems in this work is well approximated by a cylinder of radius R and length Z. Simple one- and two-dimensional models are devised and used to simulate the diffusion process in a cylindrical geometry. The effect of the ionisation (source) profile is also examined. Assuming that the primary generation process is electron impact ionisation and the primary loss process is diffusion, the ionisation profile is determined from experimentally measured density profiles using a reconstruction technique similar to those used for deconvolution in spectroscopy.

4.1 Diffusion and Transport in a Weakly Ionised Plasma

Transport processes in plasmas depend on the degree of ionisation. A weakly ionised plasma is one in which the collision frequency of ions and electrons with neutral atoms is much greater than that of collisions of ions and electrons with one another [1]

$$\nu_{en} >> \nu_{ei}, \nu_{ee} \qquad 4.1.1$$

and

$$\nu_{in} >> \nu_{ii}, \frac{m_e}{m_i}\nu_{ei} \qquad 4.1.2$$

Where ν is the collision frequency and the subscripts *e*, *i*, and *n* denote electrons, ions and neutrals respectively. A highly ionised plasma is described by the reverse inequalities. The plasmas examined in this thesis have a typical degree of ionisation of $1x10^{-6}$ and so are weakly ionised.

Any weakly ionised plasma will have a density gradient; the plasma will diffuse to the low-density regions. Fick's law of diffusion describes 'free' diffusion i.e. diffusion in the absence of an external force such as an electric field

$$\Gamma = nu = -D\nabla n \qquad 4.1.3$$

where Γ is the particle flux, n is the particle density, D is the diffusion constant and u is the particle velocity [2-6]. In plasmas Fick's law is not necessarily the primary diffusion process as the plasma is spreading out as a result of both the density gradient and the electric field forces. The particle flux becomes

$$\Gamma = \pm \mu n_e E - D \nabla n \qquad 4.1.4$$

where $\mu = q/m\nu_m$ is the particle mobility and E is the electric field.

4.2.1 Ambipolar Diffusion

The primary production mechanism in this type of plasma is electron impact ionisation. The main loss mechanism is recombination at the chamber walls. This implies that the particle density at the walls is zero. Since the mobility of the electrons is much greater than that of ions ($\mu \propto 1/m$), the diffusion rates of ions and electrons must adjust so that both species diffuse at the same rate. The electrons have higher thermal velocities and leave the plasma first. The positive charge left behind results in an electric field that slows the electron loss and accelerates the ion loss. To find this field, the particle flux Γ, is set equal to $\Gamma_i = \Gamma_e$ and substituted into equation 4.1.4

$$\Gamma = \mu_i n E - D_i \nabla n = -\mu_e n E - D_e \nabla n \qquad 4.2.1$$

This gives

$$E = \frac{(D_i - D_e)}{(\mu_i + \mu_e)} \frac{\nabla n}{n} \qquad 4.2.2$$

The particle flux then becomes

$$\Gamma = \mu_i \frac{D_i - D_e}{\mu_i + \mu_e} \frac{\nabla n}{n} - D_i \nabla n \qquad 4.2.3$$

$$= -\frac{\mu_i D_e + \mu_e D_i}{\mu_i + \mu_e} \nabla n \qquad 4.2.4$$

This is Fick's law with the ambipolar diffusion coefficient

$$D_A = \frac{\mu_i D_e + \mu_e D_i}{\mu_i + \mu_e} \qquad 4.2.5$$

Since $D_e >> D_i$, and $\mu_e >> \mu_i$, and using the Einstein relation $D_e/\mu_e = kT/e$, equation 4.2.2 becomes

$$E_A \approx -\frac{D_e}{\mu_e} \frac{\nabla n}{n} \approx \frac{-kT}{e} \frac{\nabla n}{n} \qquad 4.2.6$$

Thus, the ambipolar electric field, E_A is in the opposite direction to the density gradient, it reduces the electron directed velocity [4,5]. Since E = -grad φ, where φ = potential;

$$\varphi - \varphi_o = \frac{kT}{e} \ln\left(\frac{n}{n_{max}}\right) \qquad 4.2.7$$

At a low density at the boundary, $n << n_{max}$, this potential distribution exceeds T_e/e. We get a distribution for electrons which corresponds to the Boltzmann equation

$$n = n_{max} \exp\left[\frac{e(\varphi - \varphi_0)}{kT}\right] \qquad 4.2.8$$

Since $D_e >> D_i$ and $\mu_e >> \mu_i$, $D_A \approx D_i + \mu_e D_i/\mu_e$, equation 4.2.5 becomes

$$D_A \approx D_i\left(1 + \frac{T_e}{T_i}\right) \qquad 4.2.9$$

Therefore, the ambipolar diffusion coefficient is less than the free diffusion coefficient and greater than the ion diffusion coefficient. Hence the ion motion is mobility dominated and electron motion is governed by Boltzmann equilibrium.

4.2.2 Diffusion in a One-Dimensional Slab

If we consider the equation of continuity

$$\frac{dn}{dt} + \nabla \bullet \Gamma = 0 \qquad 4.2.10$$

With $\Gamma = -D_A \nabla n$. In one dimension

$$\frac{dn}{dt} = -\frac{d\Gamma}{dx} \qquad 4.2.11$$

Since $\Gamma = -D_A dn/dx$

$$\frac{d\Gamma}{dt} - D_A \frac{d^2 n}{dx^2} = 0 \qquad 4.2.12$$

It is necessary to solve equation 4.2.12 for n. Since n is a function of both position (x) and time (t), separation of variables results in an equation of the form

$$n(x,t) = T(t)X(x) \qquad 4.2.13$$

Differentiating gives

$$\frac{dn}{dt} = T(t) + X(x)\frac{dT}{dt} \qquad 4.2.14$$

$$\frac{dn}{dx} = T(t)\frac{dX}{dx} \qquad 4.2.15$$

$$\frac{d^2n}{dx^2} = T(t)\frac{d^2X}{dx^2} \qquad 4.2.16$$

Substituting 4.2.14 and 4.2.16 into equation 4.2.12

$$X(x)\frac{dT}{dt} - D_A T(t)\frac{d^2X}{dx^2} = 0 \qquad 4.2.17$$

Dividing by $X(x).T(t)$ gives an equation of the form of 4.2.13

$$\frac{1}{T(t)}\frac{dT}{dt} - D_A\frac{1}{X(x)}\frac{d^2X}{dx^2} = 0 \qquad 4.2.18$$

The left and right hand sides are set equal to the same constant, $-1/\tau$, where τ is the decay time constant [2,3,6]. For the moment, we are concerned with the spatial part of the diffusion equation only. In this one dimensional geometry

$$\frac{d^2X}{dx^2} = \frac{1}{D_A\tau}X \qquad 4.2.19$$

In the geometry used to model the axial density profiles, this becomes

$$\frac{d^2Z}{dz^2} = \frac{1}{D_A\tau}Z \qquad 4.2.20$$

where Z is the gap length and z is the axial position. Equation 4.2.20 has a solution of the form

$$Z(z) = A\cos\left(\frac{Z}{(D_A\tau)^{1/2}}\right) + B\sin\left(\frac{Z}{(D_A\tau)^{1/2}}\right) \qquad 4.2.21$$

The boundary conditions are such that the density is zero at the powered electrode (n=0 at z=0) and the ground electrode (z=Z), where Z is the chamber length.

This implies that A=0 and

$$\frac{Z}{(D_A\tau)^{1/2}} = n\pi \qquad 4.2.22$$

$$\tau = \left(\frac{Z}{n\pi}\right)^2\frac{1}{D_A} \qquad 4.2.23$$

where n is an integer known as the mode number. Most cylindrically symmetric discharges have a single density maximum at or near the centre of the discharge so n=1. The density distribution is then given by

$$n(z) = n_{max}\sin\left(\frac{z\pi}{Z}\right) \qquad 4.2.24$$

where n_{max} is the maximum density [3].

4.2.3 Diffusion in a cylinder

In cylindrical geometry, the spatial part of the diffusion equation is

$$\frac{d^2R}{dr^2}+\frac{1}{r}\frac{dR}{dr}+\frac{1}{D_A\tau}R=0 \qquad 4.2.25$$

where R is the chamber radius and r the radial position. (This is the cylindrical co-ordinate form of equation 4.20 [3]). The solution is a Bessel function; $J_0(r)$ (see figure 4.1) This is similar to a damped cosine function [2,3]. The solution to 4.2.25 is

$$R(r)=J_0\left(\frac{r}{(D_A\tau)^{1/2}}\right) \qquad 4.2.26$$

In this case the boundary condition is $n=0$ at the chamber walls. To satisfy this, $R/(D_A\tau)^{1/2}$ must be equal to the first zero of J_0, i.e. 2.405.

It is important to mention at this point that this solution is valid only if the boundary conditions are met and if we can assume axial and azimuthal symmetry. This is found not to be the case in many of the experiments to be discussed.

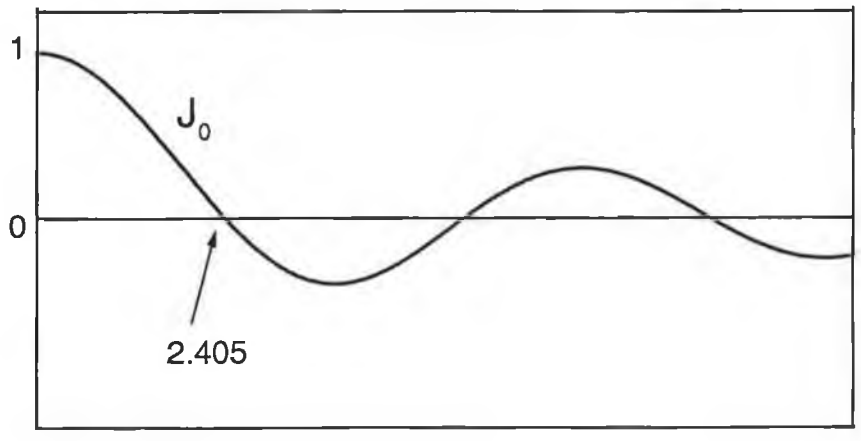

Figure 4.1: Zero-order Bessel function, J_0.

4.3 One-Dimensional Diffusion Simulation

At this stage it is useful to use a simple computer model to form a numerical solution density profiles under certain conditions. A computer code was devised in 'C' language to model the diffusion process. Writing Fick's law in one dimension, equation 4.2.11 gives

$$\frac{dn}{dt}=-D_A A\frac{dn}{dz} \qquad 4.3.1$$

where A is the area through which diffusion is occurring, perpendicular to the direction of the density gradient. Setting G, the concentration gradient equal to dn/dz and rewriting equation 4.3.1 gives

$$dn = -D_A AGdt \qquad 4.3.2$$

The model calculates the diffusion through a number of layers. In the case of the mth layer, the diffusion into it from the m+1st layer can be calculated as follows

$$dn_1 = -D_A A\frac{(n_m - n_{m+1})}{W}dt \qquad 4.3.3$$

where W is the width of a layer. (Note: G, the density gradient is estimated by taking the difference in particle counts in adjacent layers and dividing by the layer separation, W). The geometry for this simulation is described in figure 4.2.

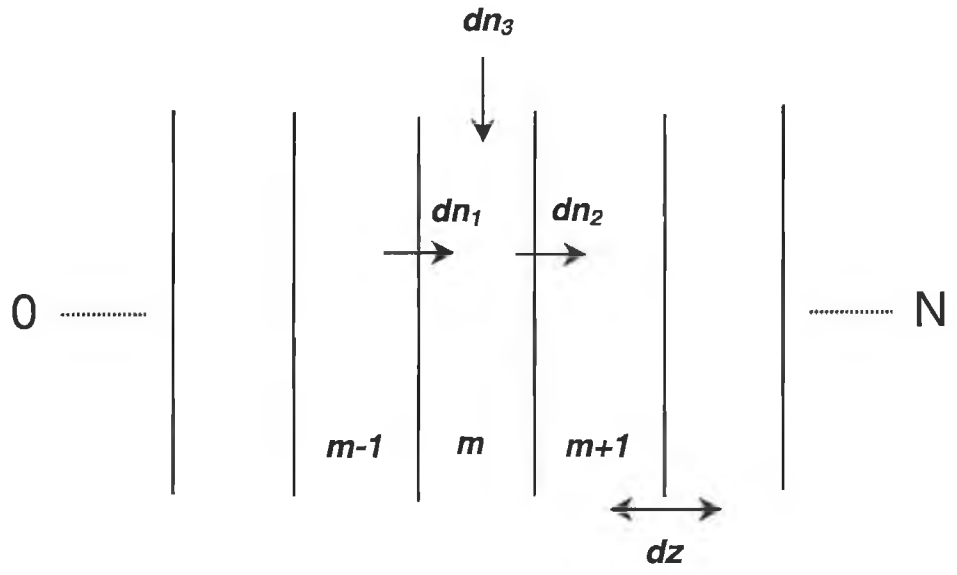

Figure 4.2: Geometry for the one dimensional (axial) simulation.

Similarly, the m-1st layer contributes

$$dn_2 = -D_A A\frac{(n_{m-1} - n_m)}{W}dt \qquad 4.3.4$$

Another process that causes n to vary in each layer is the production of new particles

$$dn_3 = G_r dt \qquad 4.3.5$$

where G_r is the generation rate.

The computer simulation consists of 200 layers. To provide particle sinks the program sets the particle count in the first and last layer to zero. The change in the number of particles in each layer is calculated using

$$dn_{total,m} = dn_{1,m} + dn_{2,m} + dn_{3,m} \qquad 4.3.6$$

where m denotes the layer. This change in particle number is then added to the existing values of n. The loss or gain from the $m+1$ and the $m-1$ layers into the m^{th} layer is also considered. This process advances the simulation one time-step, dt. The process is terminated when no further change in the density profile is observed.

A good test of the computer model is to compare the numerical density profiles with known analytic solutions, such as equation 4.2.24. To realise this with a computer simulation, each layer was set with an initial value of $1x10^6$ particles and sinks were set at the first and last layers. The program was then run for many time steps until the shape of the density profile converged. This is a sine function as predicted by equation 4.2.24 (see figure 4.3 E).

The solutions given in sections 4.2.2 and 4.2.3 are for a discharge decaying in time with no generating source present. There is a flat initial distribution that decays in time in the form of a sine or Bessel function. Figure 4.3 shows the results of the simulation run using this and other test conditions.

A further test of the model is to examine the temporal evolution of the density profile. Equation 4.2.18 shows that the diffusion equation has both temporal and spatial terms. The solution for the temporal part is an exponential function with the decay time constant, τ;

$$T = T_o e^{-t/\tau} \qquad 4.3.7$$

Where T is the density at time t and T_0 is the density at time t=0. The simulation is run with a sine profile to start and with sinks at both ends. Every 10,000 time-steps, the time and corresponding maximum density in the profile are recorded. Figure 4.4 shows an excellent fit between an exponential function and the simulation data points.

Figure 4.3 and 4.3 show the various tests of the one-dimensional model for several conditions. A constant uniform generation rate in every layer results in a parabolic density profile. This is in agreement with the numerical and analytic solutions obtained in reference [7] for negative ions in a low-pressure oxygen plasma. For a point generation source at the centre of the discharge, the density profile will be linear as shown by curve B in figure 4.3. This is in agreement with the analytic solution for such a point source given by Chen [2].

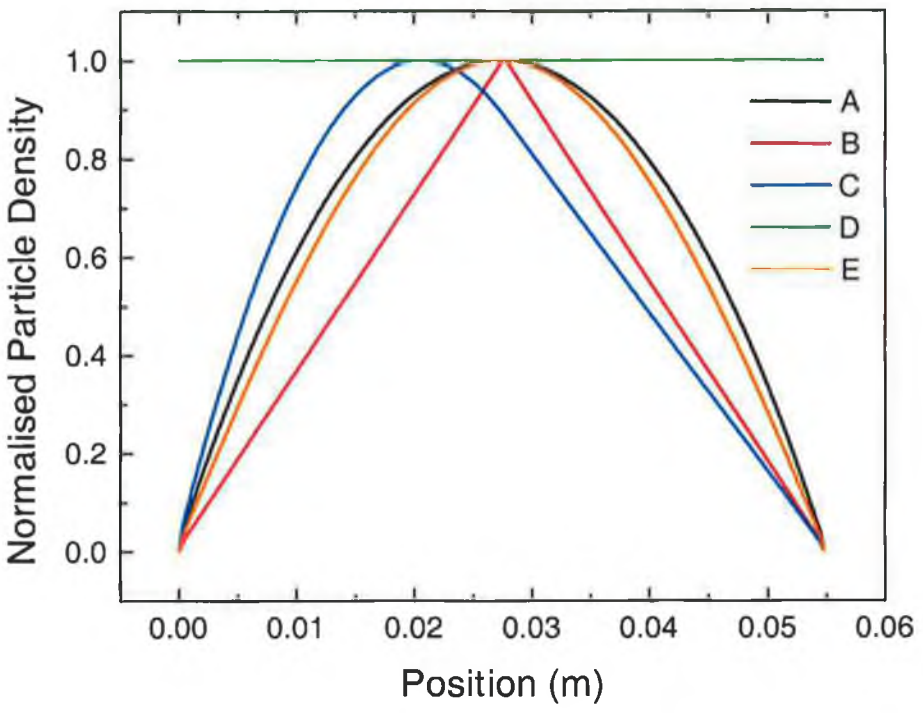

Figure 4.3: Results of the one dimensional simulation:
A: Source evenly distributed across gap, sinks at both ends (parabola).
B: Point source at centre of gap, sinks at both ends.
C: Source distributed from left edge to centre, sinks at both ends.
D: Evenly distributed source, no sinks.
E: No generating source (G=0), even distribution at start (sine).

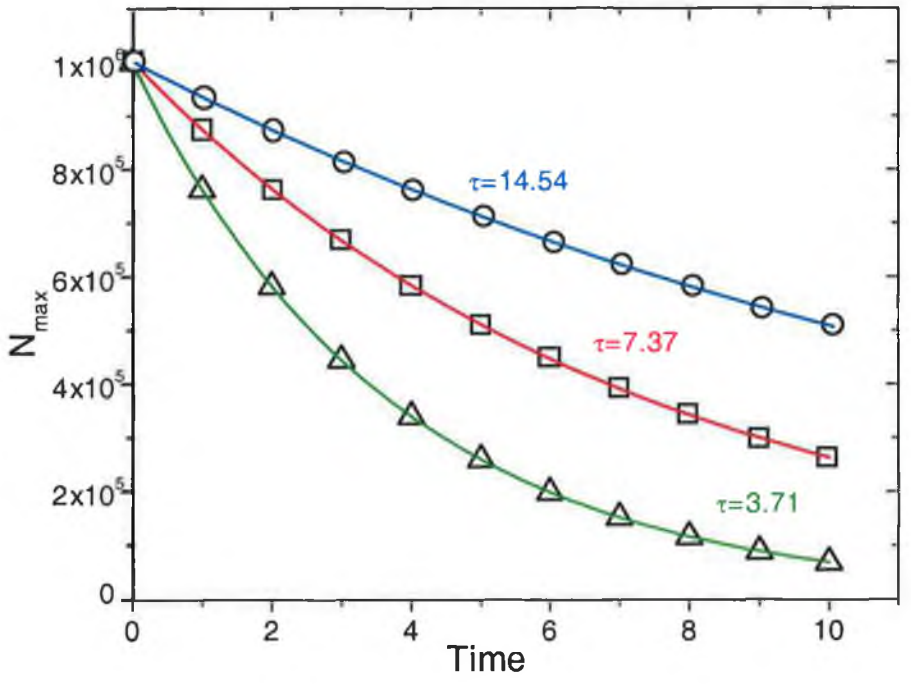

Figure 4.4: Plot of maximum density versus time for three diffusion rates and their exponential fits; D=5x10^5 (open circles), D=10^6 (squares), and D=2x10^6 (triangles).

A geometry consisting of a set of concentric rings was used to model radial diffusion. For simplicity the rings were evenly spaced by a distance, *dr*. The width of each ring is *dz*. The centre disc is of radius, *dr*.

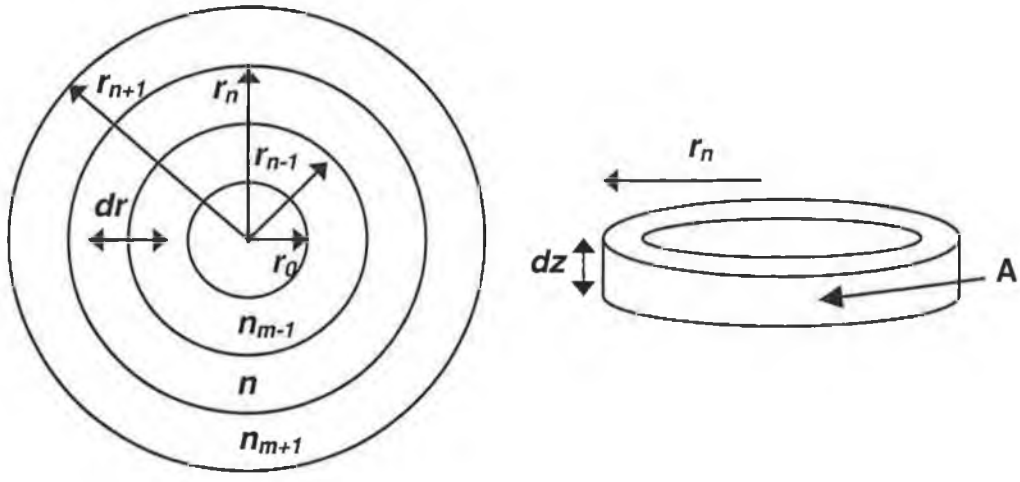

Figure 4.5: Radial geometry used in the simulation.

Consider Fick's law for diffusion across the boundary of ring m, and ring m+1

$$dn = DAGdt \tag{4.3.8}$$

A is the surface area of the side wall of the ring and is given by

$$A = 2\pi r_m dz \tag{4.3.9}$$

The density gradient G, is given by

$$G = \frac{\frac{n_{m+1}}{V_{m+1}} - \frac{n_m}{V_m}}{dr} \tag{4.3.10}$$

where V is the volume of the ring. Expressing V in terms of r gives

$$G = \frac{n_{m+1}}{\pi(r_{m+1}^2 - r_m^2)dz} - \frac{n_m}{\pi(r_m^2 - r_{m-1}^2)dz} \Big/ dr \tag{4.3.11}$$

Noting that

$$r_{m+1} = (m+2)dr \tag{4.3.12}$$

$$r_m = (m+1)dr$$

and

$$r_{m-1} = mdr$$

Then

$$G = \frac{1}{\pi dr^3 dz}\left(\frac{n_{m+1}}{2m+3} - \frac{n_m}{2m+1}\right) \qquad 4.3.13$$

Substituting 4.3.9 and 4.3.6 into 4.3.8 gives

$$dn_1 = -\frac{2D(m+1)}{dr^2}\left(\frac{n_{m+1}}{2m+3} - \frac{n_m}{2m+1}\right)dt \qquad 4.3.14$$

Similarly by considering the diffusion on the inner edge of the ring

$$dn_2 = -\frac{2Dm}{dr^2}\left(\frac{n_{m-1}}{2m-1} - \frac{n_m}{2m+1}\right)dt \qquad 4.3.15$$

The number of new particles generated in a ring per time step is given by

$$dn_3 = B_R V_m dt \qquad 4.3.16$$

where B_R is the generation rate per unit volume and V_m the volume of the ring. Substitution gives

$$dn_3 = \pi B_R dr^2 dz(2m+1)dt \qquad 4.3.17$$

Euler's method is used to calculate n_m as a function of time

$$n_m = n_m + dn_1 + dn_2 + dn_3 \qquad 4.3.18$$

$$n_{m-1} = n_{m-1} - dn_2 \qquad 4.3.19$$

$$n_{m+1} = n_{m+1} - dn_1 \qquad 4.3.20$$

$$t = t + dt \qquad 4.3.21$$

Note: dn_2 is set to zero for m equal to zero and dn_1 is zero for m equal to m_{max}.

As a test of the model all rings were filled with an equal concentration of particles, given by

$$n_m = \pi C dr^2 dz(2m+1) \qquad 4.3.22$$

where C is the concentration. After each iteration the number of particles in the outermost ring is set to zero, this ring forms the sink for the particles, there is no generation term, thus dn_3 is zero. The resulting distribution of particle density as a function of radius converges on the Bessel function solution predicted analytically [3]. See figure 4.6 for some tests of this model. Note that

$$C_m = \frac{n_m}{\pi dr^2 dz(2m+1)} \qquad 4.3.23$$

$$r_m = (m+1)dr \qquad 4.3.24$$

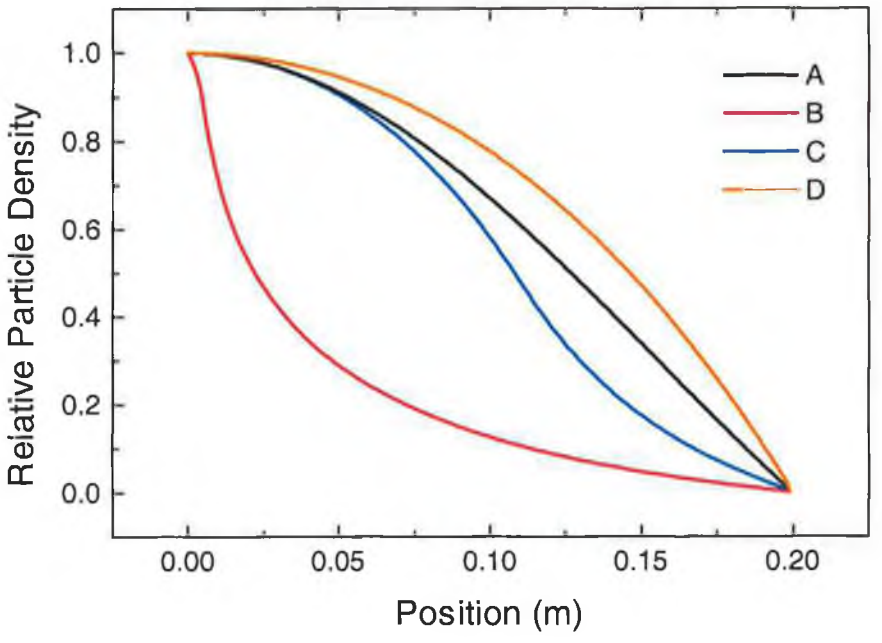

Figure 4.6: Results of radial one dimensional simulation
A: Source evenly distributed across gap, sinks at wall (Bessel function)
B: Point source at centre of chamber, sink at 0.2m
C: Source from 0 to 0.1m, no generation elsewhere.
D: No source, even distribution at start.

4.4 Two-Dimensional Diffusion Simulation

The axial and radial models can be combined to produce a two-dimensional diffusion model that describes diffusion in a chamber with azimuthal symmetry. The experimental system used has essentially this geometry, modified only by the ports.

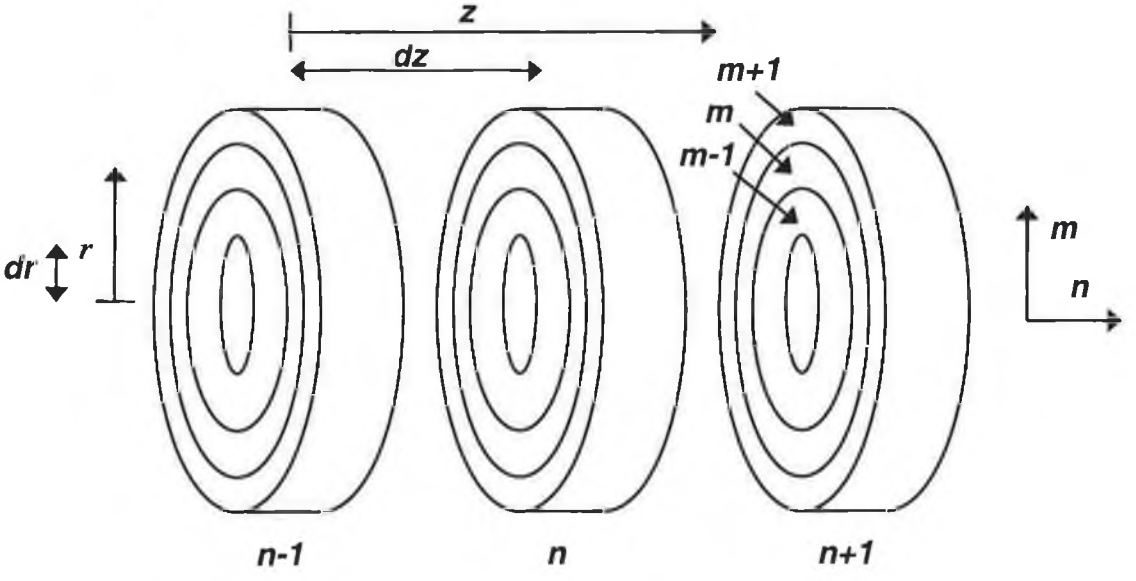

Figure 4.7: Two dimensional radial geometry.

Using a similar approach to that used for the radial model the axial diffusion from layer, *n-1*, to layer *n*, is given by

$$dn_4 = -\frac{1}{dz^2}\left(n_{n-1} - n_n\right)dt \qquad 4.4.1$$

and from layer, *n+1*, to layer *n*

$$dn_5 = -\frac{1}{dz^2}\left(n_{n+1} - n_n\right)dt \qquad 4.4.2$$

To advance a time step *dt*, dn_1, dn_2, dn_3, dn_4 and dn_4 are calculated for each cell, $n_{m,n}$. These values are stored in four separate arrays. The dn_x, below apply to cell *m,n*. The following Euler step is then taken

$$n_{n,m} = n_{n,m} + dn_1 + dn_2 + dn_3 + dn_4 + dn_5 \qquad 4.4.3$$

$$n_{n-1,m} = n_{n-1,m} - dn_4 \qquad 4.4.4$$

$$n_{n+1,m} = n_{n+1,m} - dn_5 \qquad 4.4.5$$

$$n_{n,m-1} = n_{n,m-1} - dn_2 \qquad 4.4.6$$

$$n_{n,m+1} = n_{n,m+1} - dn_1 \qquad 4.4.7$$

As a test of this 2D model, the same concentration was placed in all cells, and the generation rate set to zero, $dn_3=0$. The outer ring on every layer is forced to zero after each iteration. All the rings in the first and last layer are also set to zero after each iteration, this is analogous to the sinks at each electrode in a typical cylindrical chamber. The resulting distribution is sinusoidal along the Z-axis and a Bessel function along the radius, see figure 4.8. Due to the very large increase in the computation time required per iteration and limitations on array size, 50x50 cells are used.

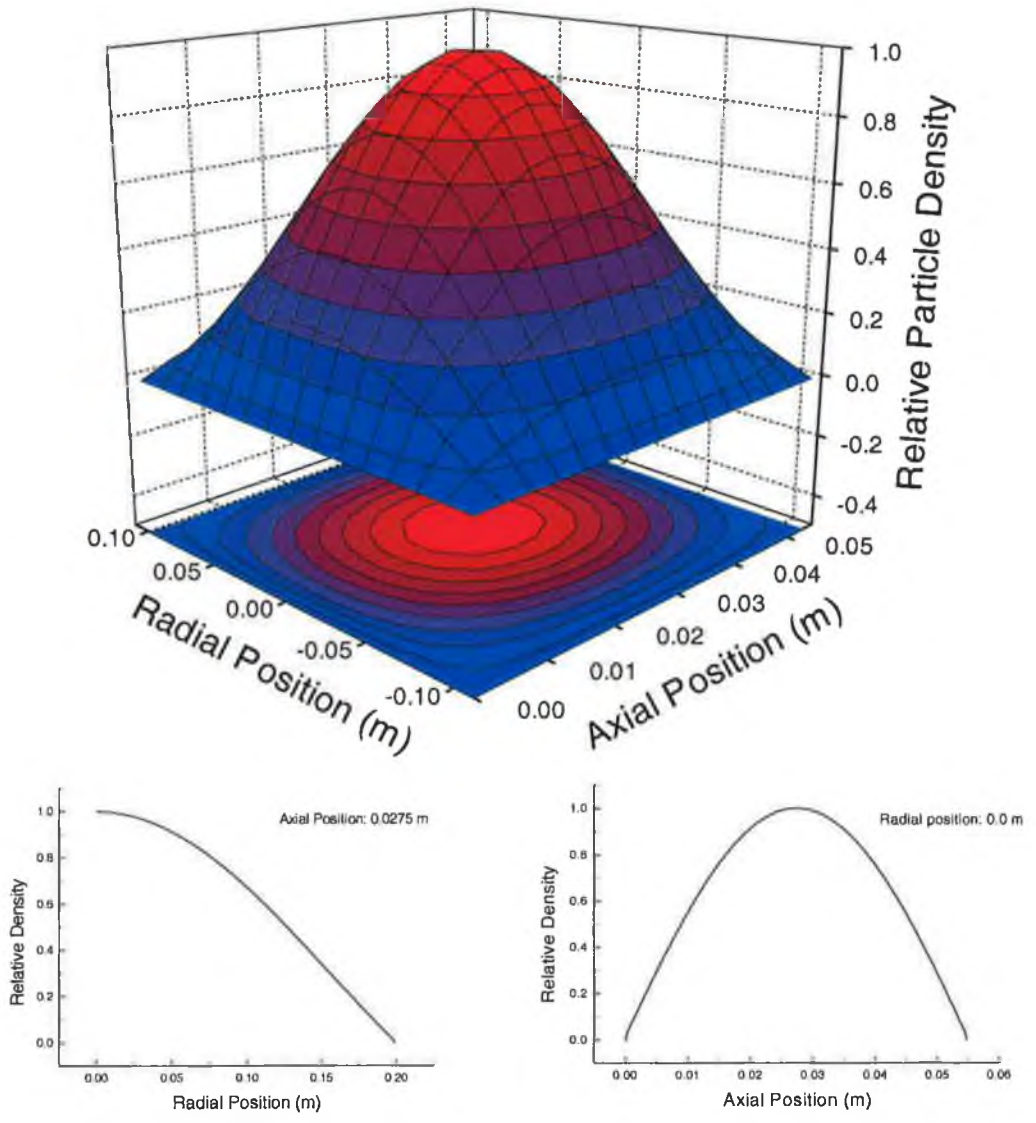

Figure 4.8: Two dimensional density profile estimated using the model with a flat initial distribution. Matrix size is 50x50 elements, converted to metres (approximate chamber dimensions).

4.5 Determination of Ionisation Profiles

Spatially resolved excitation profiles in capacitively coupled discharges have been measured in argon by Kitajima and co workers [8]. The main advantage of optical emission is that it may be time resolved to small fractions of the rf cycle. A disadvantage of optical emission studies is that actual ionisation profiles are not measured, the ionisation profile may only be considered as being similar to the excitation profile if there are similarities in the cross sections for the two processes.

An experimental method has been devised to extract the total ionisation profile in two dimensions. This is valid if the production process is ionisation and the loss process is ambipolar diffusion. As this procedure calculates the total production

(ionisation) term, processes such as two-step ionisation and ion neutral ionisation are included.

Using the simplifying assumptions of electron impact ionisation and ambipolar diffusion to the walls, the ionisation profile is determined from the density profiles using a purpose written 'C' program. Figure 4.9 illustrates the geometry of the measurements. One axial profile, taken along the middle of the discharge axis, plus three to six radial profiles, taken at either end and along the mid plane, are interpolated to form a two-dimensional 50x50 grid that represents the experimental density profile. The more data obtained the more accurate the density profile. However it was found that this procedure reproduced the two-dimensional experimental profiles with reasonable accuracy, so reducing the need to take large amounts of data.

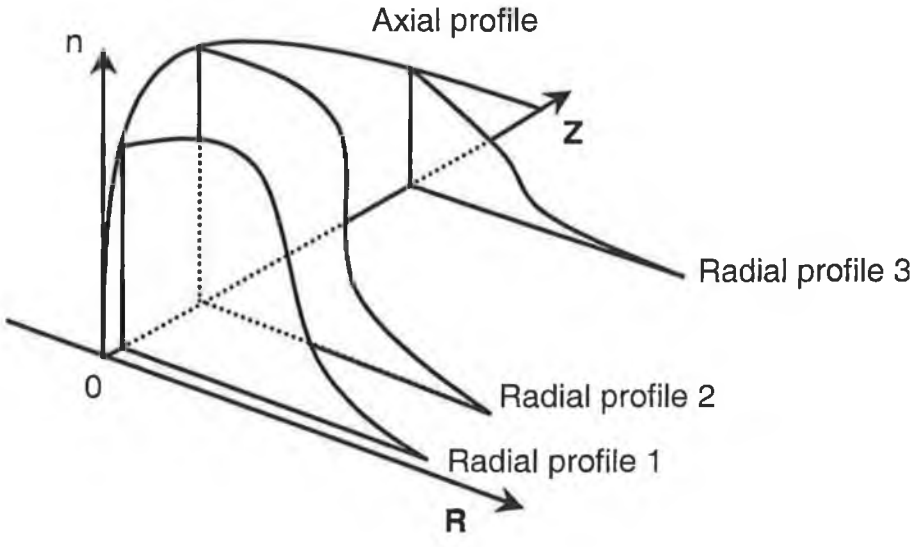

Figure 4.9: Geometry of the measurement scheme.

The algorithm works as follows:

(i) A 'first guess' of the ionisation profile is inserted into a 50x50 data array. This may simply be a flat distribution or the same as the density profile times some constant.

(ii) A density profile corresponding to the ionisation profile in part (i) is obtained using the two dimensional diffusion simulation described in section 4.4. The diffusion simulation continues until equilibrium is reached, i.e. no further change is measured in the density profile. This process yields a modeled density profile.

(iii) This modelled density profile is compared (point-for-point) with the experimental density profile. Should a difference be measured, the following correction is made on each point,

$$G_{new} = G_{old} \frac{N_{experiment}}{N_{model}} \qquad 4.5.1$$

Where G is the ionisation rate and N is the density value at each point. This technique is commonly known in spectroscopy as Gold's Ratio method [9] and is similar to the multiplicative algebraic reconstruction technique used in computed tomography [10].

(v) This technique can amplify scatter in the density profile so 9-point neighbourhood averaging is employed every few iterations.

(vi) Steps (ii) to (v) are repeated until the modelled density profile converges on the experimental density profile. The ionisation profile is then saved to a file.

Figure 4.10 (a) shows the experimental density profile and (b) the corresponding modelled density profile obtained on convergence. It is clear from this figure that the algorithm can accurately reproduce the experimental density profile.

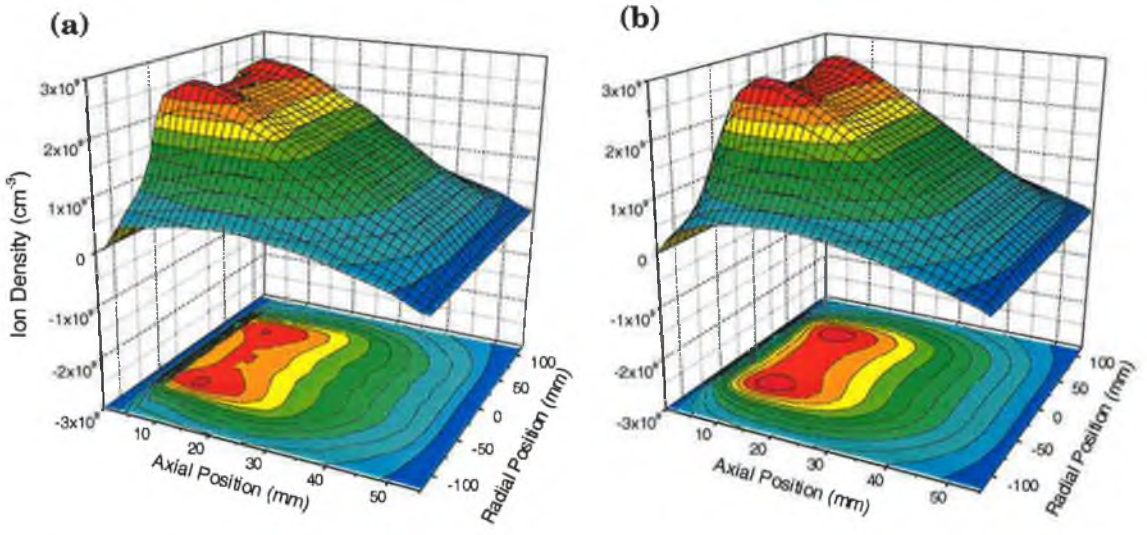

Figure 4.10: (a) Experimental ion density and (b) modelled ion density for a 300 mTorr, 5 watt argon discharge. The powered electrode edge is at 0 mm, ground electrode at 55 mm. The vertical axes are ion density in cm^{-3}.

The simple 55 mm by 120 mm geometry used in the simulation is a good approximation at the higher gas pressures because the plasma is well confined between the parallel plates. There was very little plasma observed or density measured outside this cylindrical plasma region. However, at lower pressures ($\leq$50 mTorr), the plasma diffuses into the surrounding area in the chamber due to the increase in mean free path.

An appreciable electron density may be measured in the chamber between the ground shield and the chamber wall. So at low pressures, a more realistic geometry is necessary to accurately determine the ionisation profile. Figure 4.11 shows the modified chamber geometry. This geometry allows particle diffusion along the sides of the powered electrode. The large probe port is taken into account to some extent by extending the radial wall of the chamber to 190 mm.

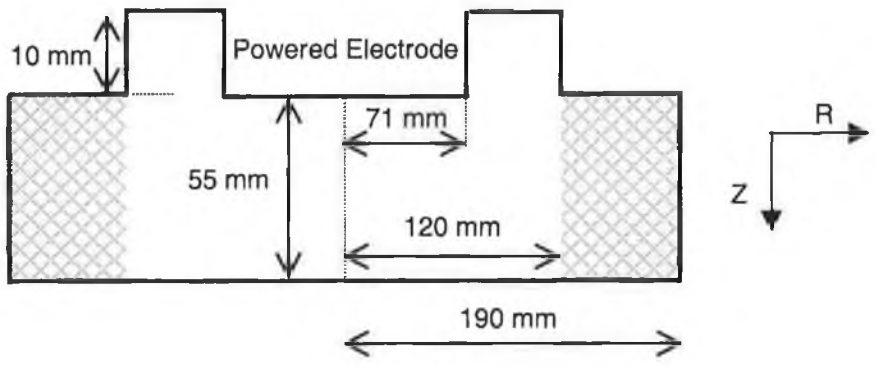

Figure 4.11: Modified chamber geometry. The crosshatched area indicates the probe port.

At higher pressures, the results from the simple cylindrical geometry and the modified geometry shown in figure 4.11 are almost identical, indicating that the plasma is reasonably well-confined and does not flow into the volume between the powered electrode and the chamber wall. This is consistent with observations of the discharge at the higher pressures. At low pressures, the modified geometry must be used. The two-dimensional experimental and modeled density profiles are shown in figure 4.12 (a) and (b) for a 10 mTorr, 100 watt discharge.

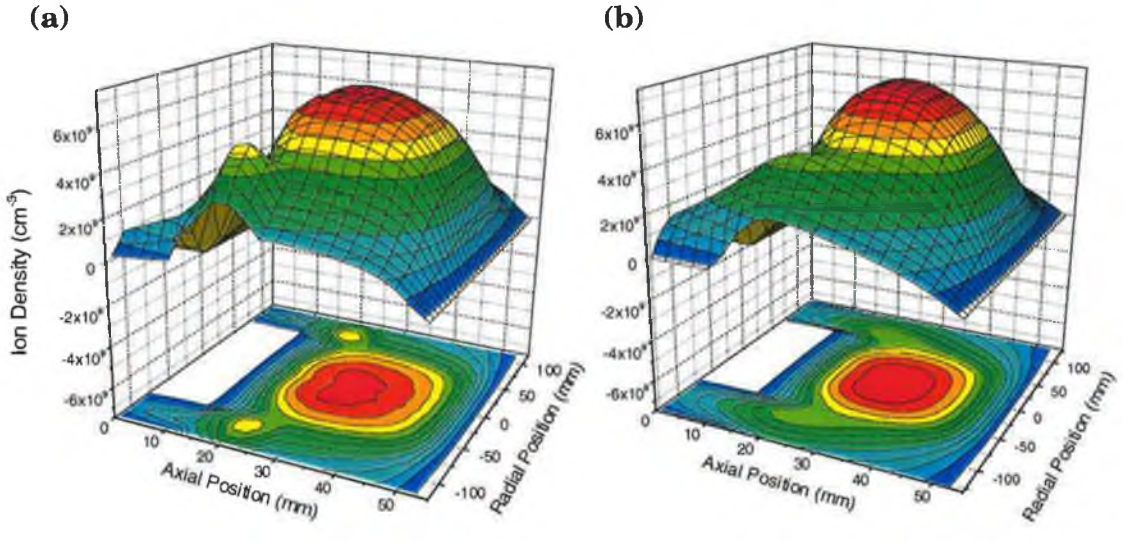

Figure 4.12: (a) experimental ion density and (b) modelled ion density for a 10 mTorr, 100 watt argon discharge. Powered electrode is at 0 mm, ground electrode at 55 mm.

References

[1] Golant, Zhilinsky, Sakharov and Brown (eds.), *Fundamentals of Plasma Physics*, Wiley Series in Plasma Physics, New York, (1980).

[2] M. Lieberman and A. Lichtenberg, *Principles of Plasma Discarges and Materials Processing*, Wiley, New York, (1994).

[3] F. F. Chen, *Introduction to Plasma Physics and Controlled Fusion*, Plenium Press, New York, (1984).

[4] L. B. Loeb, *Basic Processes of Gaseous Electronics*, University of California Press, Berkeley, (1960).

[5] A. von Engel, *Ionised Gases*, American Institute of Physics, New York, (1965).

[6] B. E. Cherrington, *Gaseous Electronics and Gas Lasers*, Pergamon, New York, (1979).

[7] D. Vender, W. W. Stoffels, E. Stoffels, G. M. W. Kroesen and F. J. de Hoog, Phys. Rev. E, 51(9), 2436, (1994).

[8] T. Kitajima, M. Izawa, N. Nakano and T. Makabe, J. Phys. D: Appl. Phys, 30, 1783-1789, (1997).

[9] P. A. Jansson, *Deconvolution*, Academic Press, (1984).

[10] G.T. Herman, *Image Reconstruction from Projections*, Academic Press, New York, (1980).

Chapter 5

Charged Particle and Ionisation Rate Profiles in an RF Plasma

Introduction

In order to further the understanding of the sustaining mechanisms in the rf capacitively coupled plasma, a spatial study was performed using the Langmuir probe. This chapter presents spatially resolved plasma parameter measurements in the context of the heating mechanisms discussed in Chapter 3. Spatially resolved measurements of electron energy, floating and plasma potential are presented in section 5.2. Section 5.3 presents ion density measurements and the corresponding ionisation distributions determined using the procedure described in Chapter 4. The evolution of the density and ionisation profiles with pressure is investigated.

5.1 Experiment

The system used for these measurements is the capacitive system described in Chapter 2, section 2.2. The Langmuir probe, mounted on top of the chamber, can be accurately moved both axially and radially, the z and r directions respectively. The gap between the electrodes is fixed at 55mm. This allows the Langmuir probe tip close access to the sheath region at the powered electrode. The height of the chamber means that the probe can only take readings from the centre of the electrode to the wall position. Since the walls of the chamber are at ground potential, with the only bias being on the powered electrode, radial and azimuthal symmetry are assumed. Figure 5.1 shows a simple sketch of the reactor. Deviations from the geometry described in Chapter 4 are due to the probe and exhaust ports. These are accounted for to a certain extent using the modified geometry shown in figure 4.11.

5.2 Electron Energy, Plasma Potential and Floating Potential

Figure 5.2 shows the electron temperature, floating and plasma potentials as a function of distance from the powered electrode in a 10 mTorr, 5 Watt plasma. It is apparent from the constant plasma potential that the discharge bulk is virtually field-free.

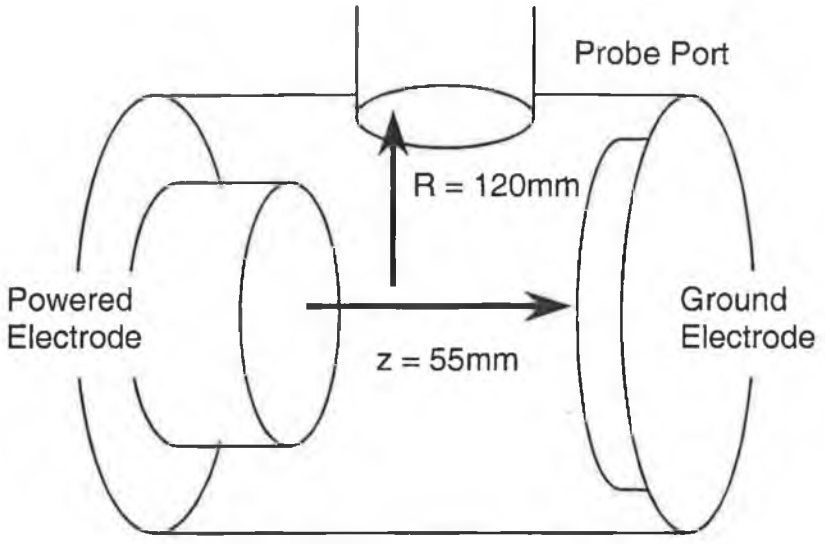

Figure 5.1: Sketch of chamber geometry indicating the co-ordinate system.

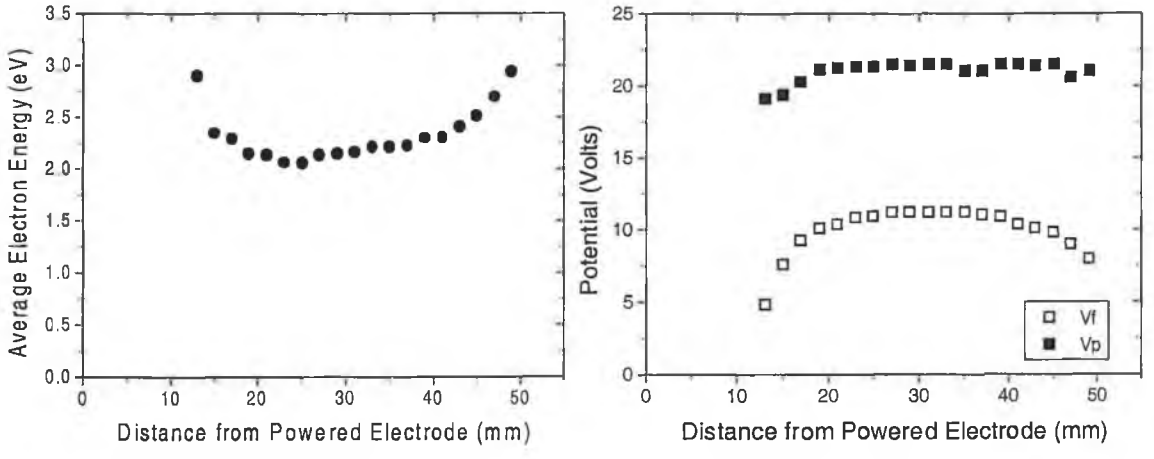

Figure 5.2: Electron energy, plasma and floating potentials as a function of z in argon at 10 mTorr and 5 Watts input power.

A near constant average energy of 2.2 eV is measured along the discharge axis. The constant energy is supported by the observation that the plasma appears as a fairly uniform, diffuse glow, see figure 5.5. Near the sheaths the average electron energy increases slightly, this is to be expected as the electrons are mainly heated by the oscillating sheath boundaries [1,2].

Increasing the pressure in a low-current discharge results in a transition to the collisional mode of operation known as ohmic heating (the α mode) that has been described in Chapter 3. Figure 5.5(a) shows the discharge appearance differs significantly from the low-pressure discharge. The time-average sheath width in a 300 mTorr, 5 Watt plasma is of the order of 4 mm (in comparison to approximately 13 mm

at 10mTorr). There is a narrow region of enhanced emission close to the powered electrode sheath while the bulk plasma is dimmer. This enhanced emission region indicates both higher electron energies and charged-particle densities near the sheath. This is evidenced by the spatially resolved measurements. Figure 5.3 shows the electron energy decreasing from 3.5 eV to 2.2 eV over a distance of approximately 5mm from the powered electrode sheath. This is consistent with the enhanced emission region shown in figure 5.5(a). The ionisation rate is sensitive to the electron temperature and therefore will have a maximum at the plasma-sheath boundary where the temperature is greatest. This temperature remains near constant across the rest of the plasma.

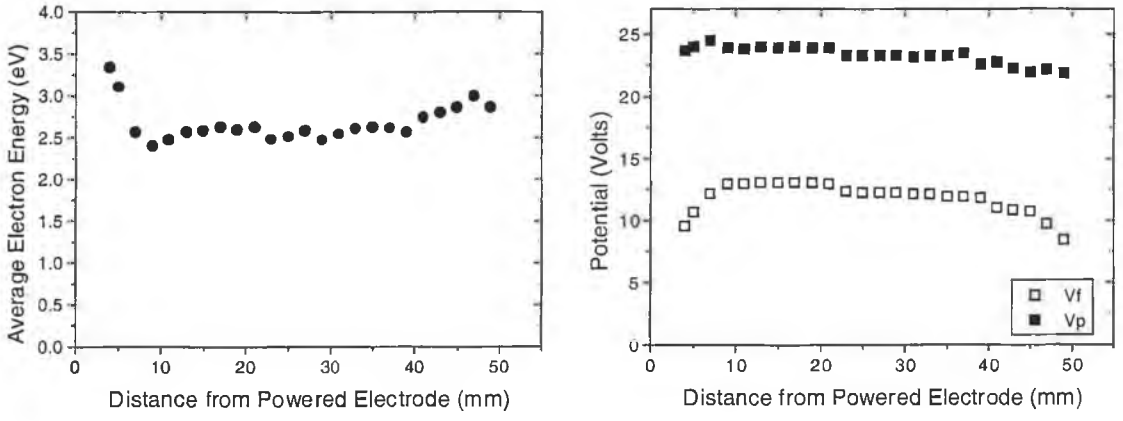

Figure 5.3: Electron energy, plasma and floating potentials as a function of z in argon at 300 mTorr and 5 Watts input power.

Measurements of energy and potentials in high power plasmas are shown in figure 5.4. Energy and potential gradients near the sheath edge are larger than in either of the previous measurements. The potential and energy values become constant a distance of approximately 3 mm from the powered sheath for the 300 mTorr case and 5 mm for the 10 mTorr case. The difference in sheath widths at the two pressures is apparent in the data presented in figure 5.4.

The most dramatic physical change is the marked change in light emission from the plasma when the power (voltage, current) is increased. Figure 5.5 (b) and (d) show high power plasmas at both 10 and 300 mTorr. A significant increase in the emission intensity is coupled with a change in colour. A spectroscopic study would be required to investigate this phenomenon.

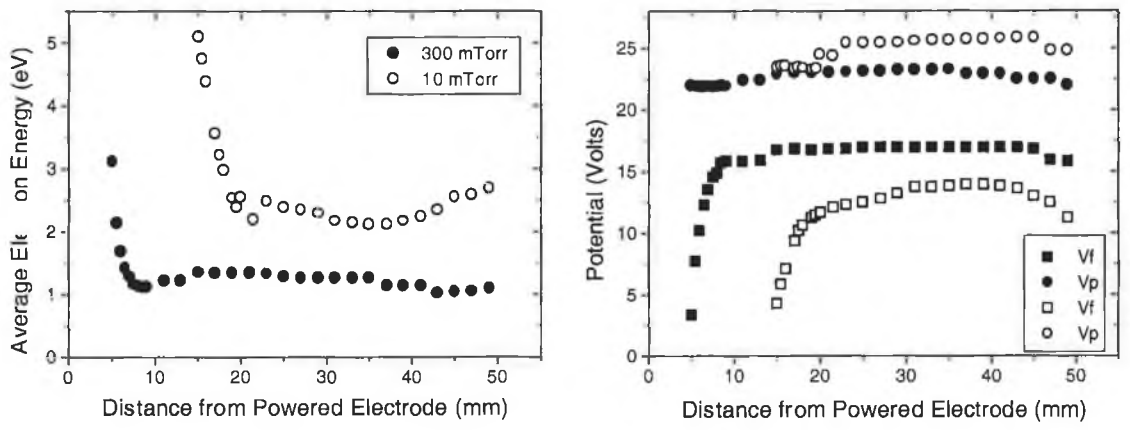

Figure 5.4: Electron temperature, plasma and floating potentials as a function of z at 10 mTorr, 100 Watts (open symbols) and 300 mTorr, 100 Watts (solid symbols).

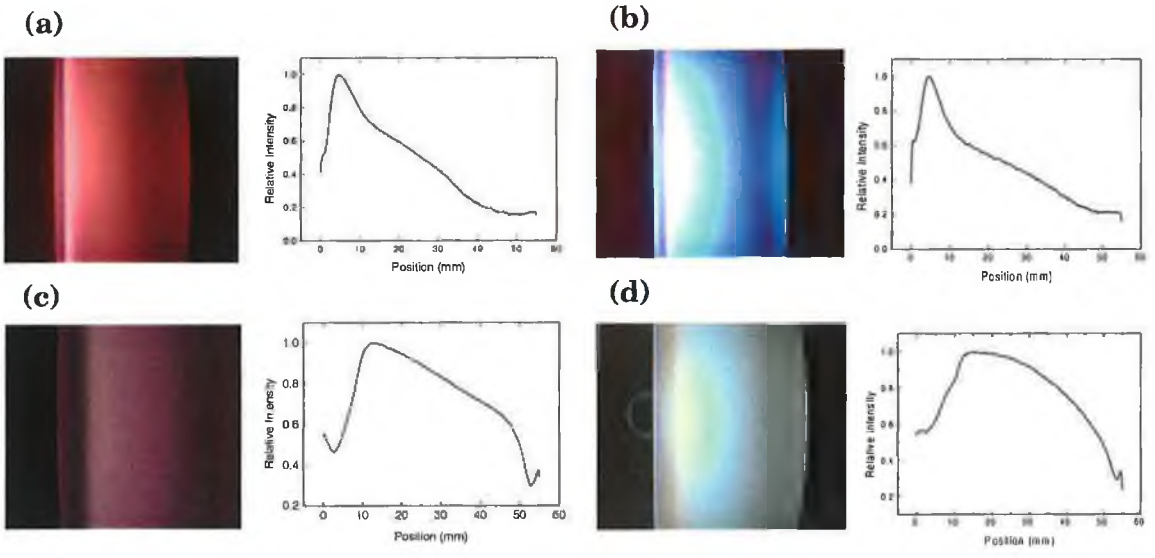

Figure 5.5: Pictures of an argon rf discharge at (a) 300 mTorr, 5 Watts, (b) 300 mTorr, 100 Watts, (c) 10 mTorr, 5 Watts and (d) 10 mTorr, 100 Watts.

5.3 Charged Particle Profiles

Spatially resolved plasma parameter measurements have been performed by several workers using various diagnostic methods. Optical emission measurements of two-dimensional excitation profiles have been performed in a capacitively coupled system in argon under 'α mode' conditions by Kitajima *et al* [1]. Axial and radial measurements of the plasma parameters using a Langmuir probe have been made by Overzet and Hopkins in a GEC reactor [2] and by Oelerlich-Hill *et al* in an asymmetric system [3]. Spatially resolved measurements of electron density have been made using a microwave interferometer system, also in a GEC cell [4].

As the distance between the electrodes in this system is much less than the chamber radius, particle losses to the chamber wall are assumed to be axially dominated [5]. Radial measurements of electron density have been made that indicate peaks in density just inside the powered electrode edge [2,4], so the two-dimensional algorithm described in Chapter 4 is used to analyse and extract the ionisation profile from the density measurements. This is done from 10 to 300 mTorr at rf powers of 5 and 100 watts. This facilitates a spatial examination of the rf discharge operating in the regimes described in Chapter 3. The large rf sheath and small electrode gap in the GEC cell has limited probe studies to 100 mTorr or higher. To the best of the author's knowledge there are no reported two-dimensional probe measurements at very low pressures in the GEC cell.

For nonequilibrium plasmas, where the electron temperature is much higher than the ion temperature [6], equation 4.2.9 reduces to the following expression for the ambipolar diffusion coefficient, D_A

$$D_A = \mu_i T_e \qquad 5.2.1$$

Where μ_i is the ion mobility and T_e is the electron temperature in eV. The ion mobility was taken from data in [7] and the electron temperature from the Langmuir probe measurements at the discharge centre (referred to in this work as the average electron energy). A plot of the ambipolar diffusion coefficients *versus* pressure for 5 and 100 Watts is shown in figure 5.6. Equation 5.2.1 implies that the diffusion coefficient will change in space as the electron temperature changes, a discussion of this is left to section 5.5.3.

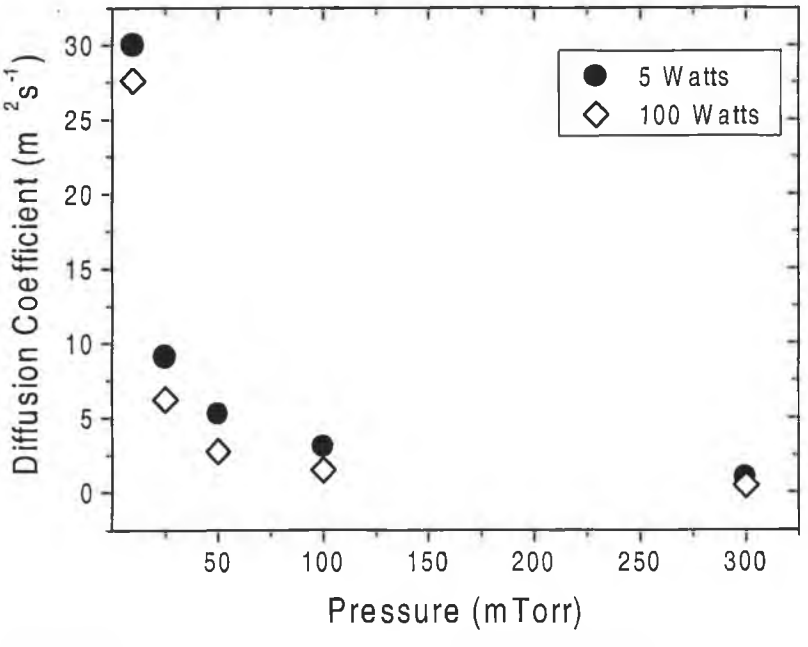

Figure 5.6: Calculated ambipolar diffusion coefficients versus pressure in argon.

5.3.1 Low Discharge Power

Figure 5.7 shows the variations of axial and near-electrode radial density profiles with pressure for low power (5 watt) argon discharges. At higher pressures and low power, the axial density profile is strongly asymmetric, which is consistent with the emission profiles shown in figure 5.5. The radial density profiles show off-axis maxima, similar to that in reference [2]. At pressures lower than 50 mTorr, the axial ion density profile becomes more symmetrical in shape. At these pressures the radial density profile measured near the powered electrode (from 5mm to 14 mm from the electrode) also shows a plateau in the ion density at 70 mm, the approximate position of the edge of the powered electrode.

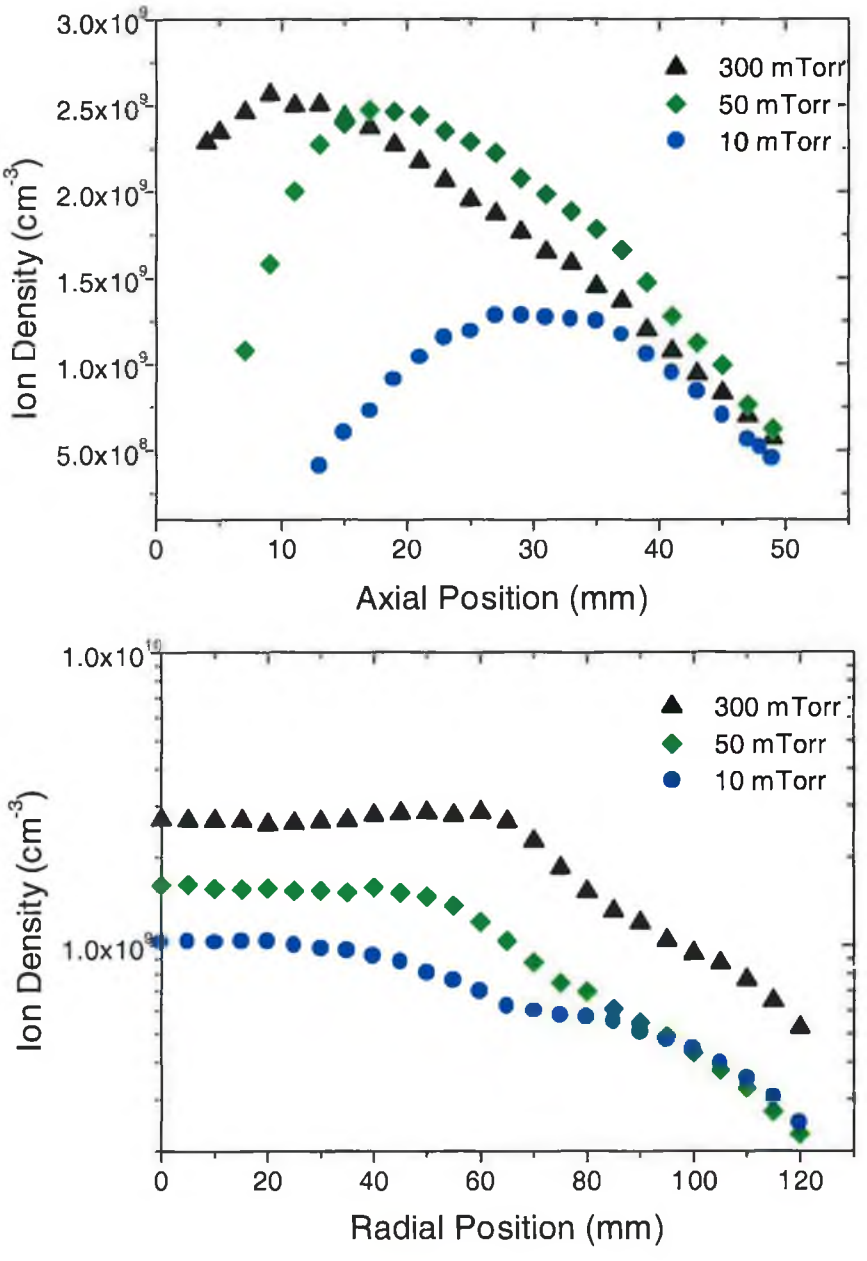

Figure 5.7: Axial and radial density profiles in argon at 5 watts rf power.

5.3.2 High Discharge Power

Increasing the power on the argon discharge has a significant effect on the density profiles in both the axial and radial directions. Apart from a significant increase in density, at high and low pressures the density profile in the axial direction flattens out along the discharge axis. The off-axis radial density peaks are enhanced at this higher power and the minimum in the density profile observed near the electrode edge at low pressures is more apparent here.

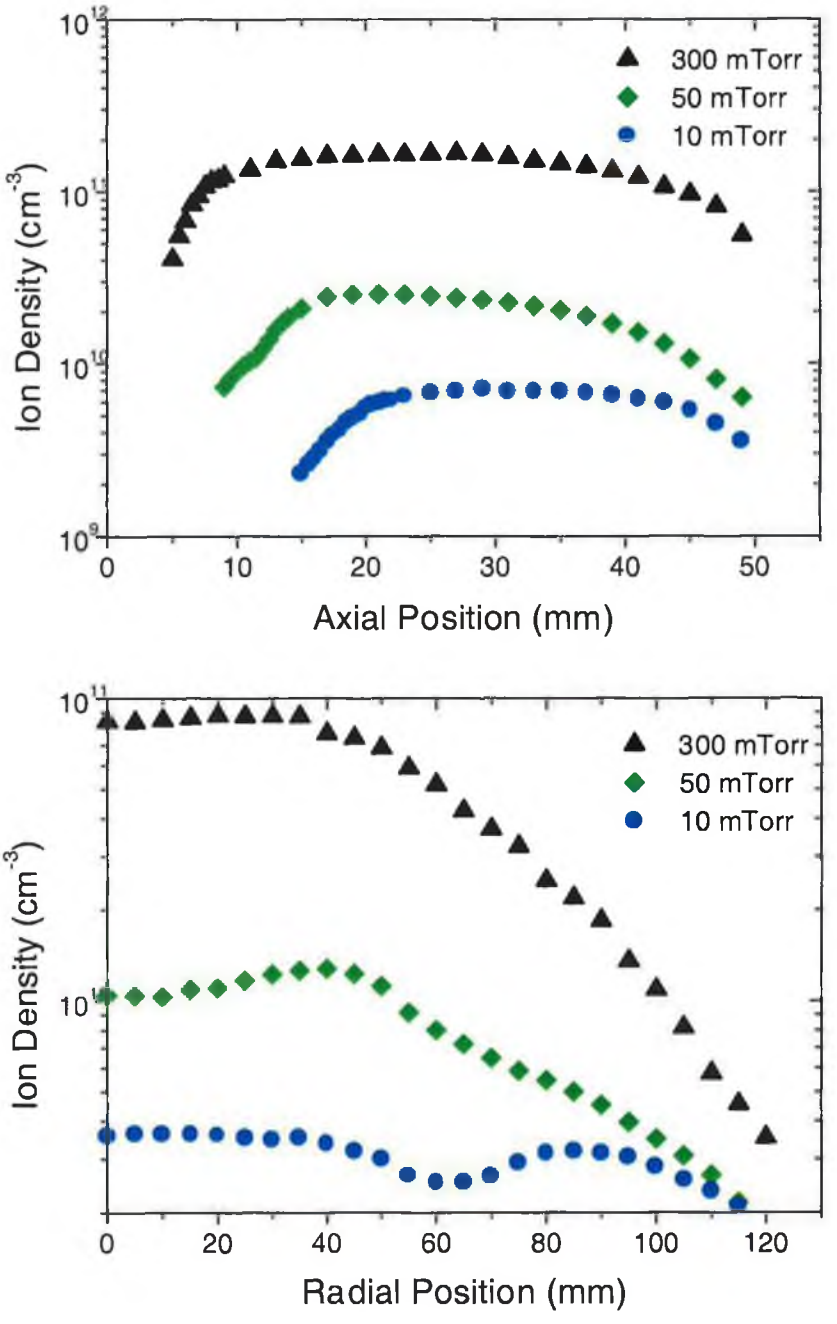

Figure 5.8: Axial and radial density profiles in argon at 100 watts rf power.

The minimum in ion density near the (radial) electrode edge shown in figures 5.7 and 5.8 corresponds to an increase of the average electron energy measured by the probe (see figure 5.14). The reason for this is that the sheath in front of the powered electrode is not perfectly flat across its radius. The parameter measurements and the photograph in figure 5.9(b) indicate that the sheath is thicker at the edge of the powered electrode. A radial measurement at a fixed distance from the powered electrode would then exhibit a decrease in density and increase in electron energy at the region of increased sheath thickness. The reason for the thickening of the sheath is likely to be partly due to the perturbation of the electric field at the electrode edges due to the presence of the ground shield. Radial optical emission measurements by Pender *et al* indicate the presence of large radial and axial fields near the electrode edges in a GEC cell [8].

Figure 5.9 shows a plot of the lines of equal potential in the chamber without a plasma. It is clear that the electric field is enhanced at the edges. The presence of a plasma will modify the field in the bulk but recent electric field measurements by Czarnetski and co-workers have shown a strong perturbation in the field near the ground shield in a GEC cell [9].

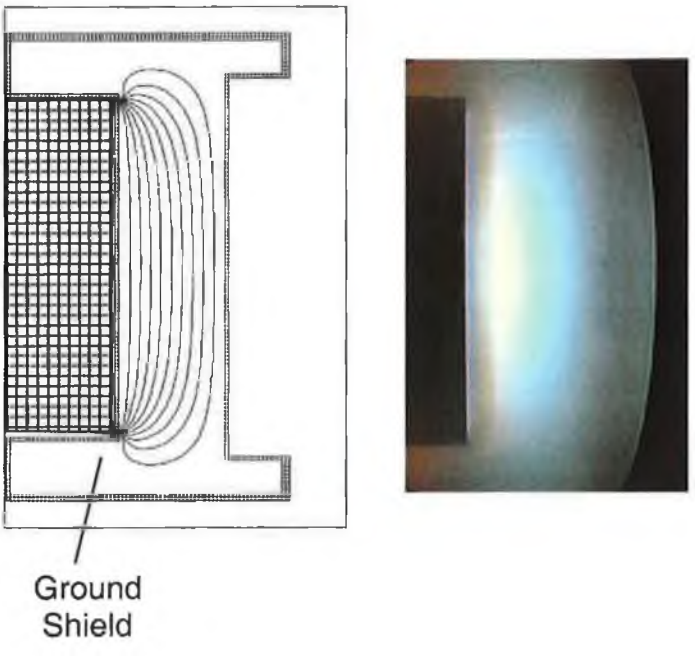

Figure 5.9: Electric field lines in an evacuated chamber. The powered electrode is at 100 Volts. The increase in sheath width is visible near the powered electrode edge.

5.4 Ionisation Profiles

5.4.1 Low Discharge Power

Figure 5.9 (a)–(e) shows the density and ionisation profiles for argon at 5 watts rf power. It is clear from this figure that at higher pressures, most of the ionisation occurs at the plasma-sheath boundary next to the powered electrode. This is consistent with the enhanced emission profile at the higher pressures and has been attributed to a type of sheath heating known as 'wave riding' or ohmic sheath heating [10]. Ionisation at the sheath edge at higher pressure results in an asymmetric density profile because the ionisation mean free path is low. A similar two-dimensional ionisation rate has been predicted by Passchier and Goedheer using a fluid model of an argon rf discharge at 500 mTorr [11]. On decreasing the pressure, we see an increase in ionisation first at the plasma-ground sheath boundary then in the plasma bulk itself, figure 5.10(d)-(e).

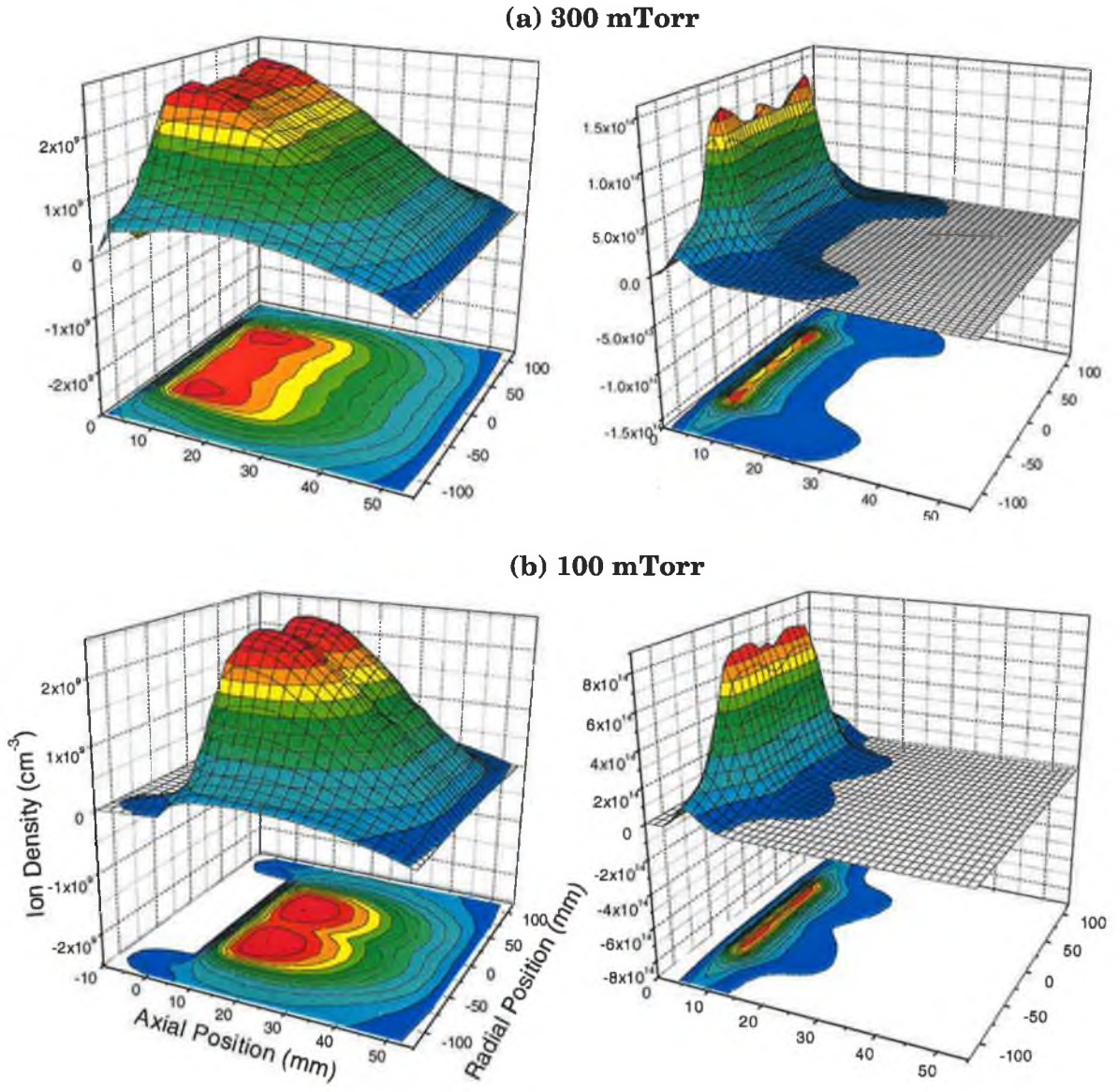

Figure 5.10: Density (left) and ionisation profiles (right) for argon at 5 watts.

(c) 50 mTorr

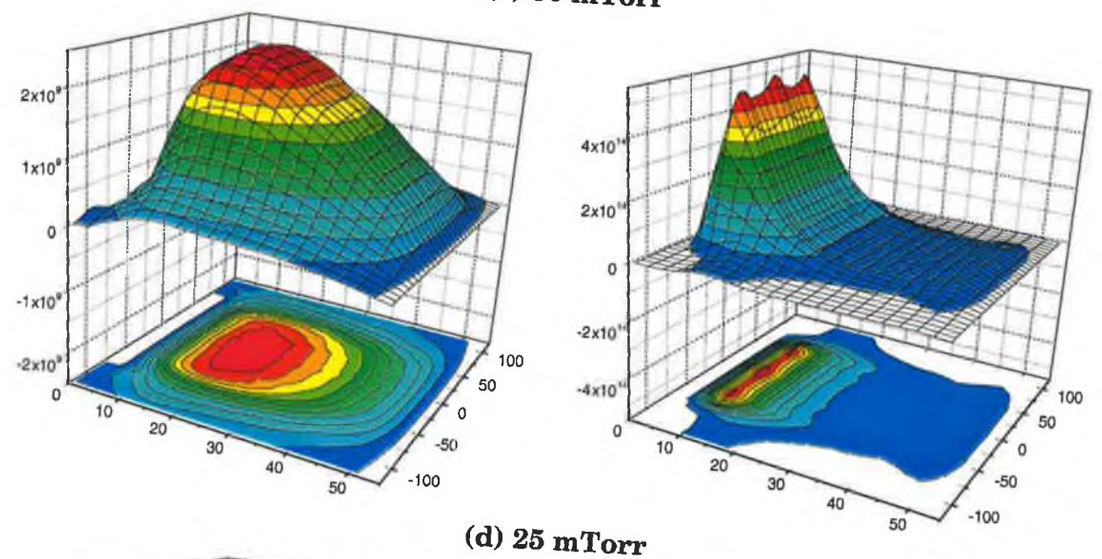

(d) 25 mTorr

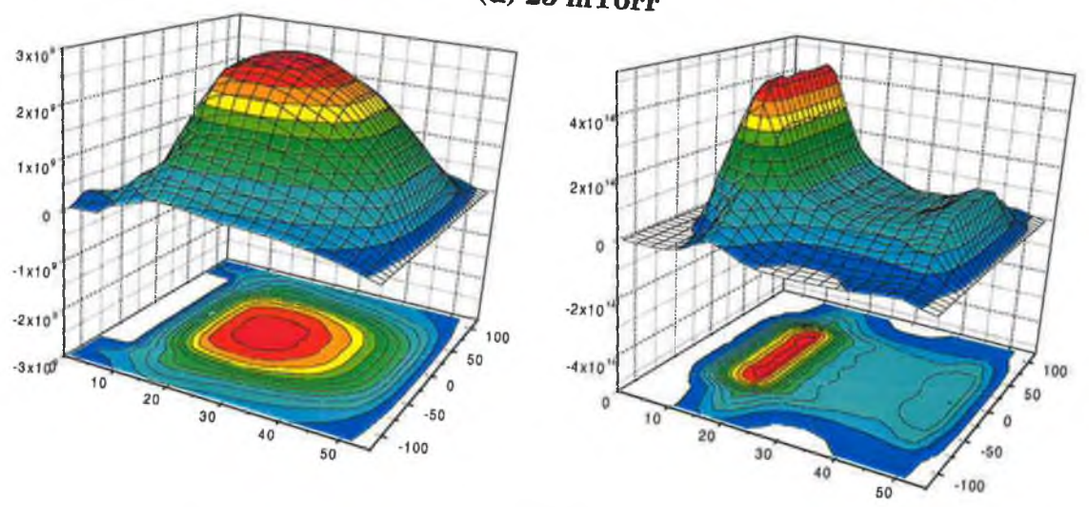

(e) 10 mTorr

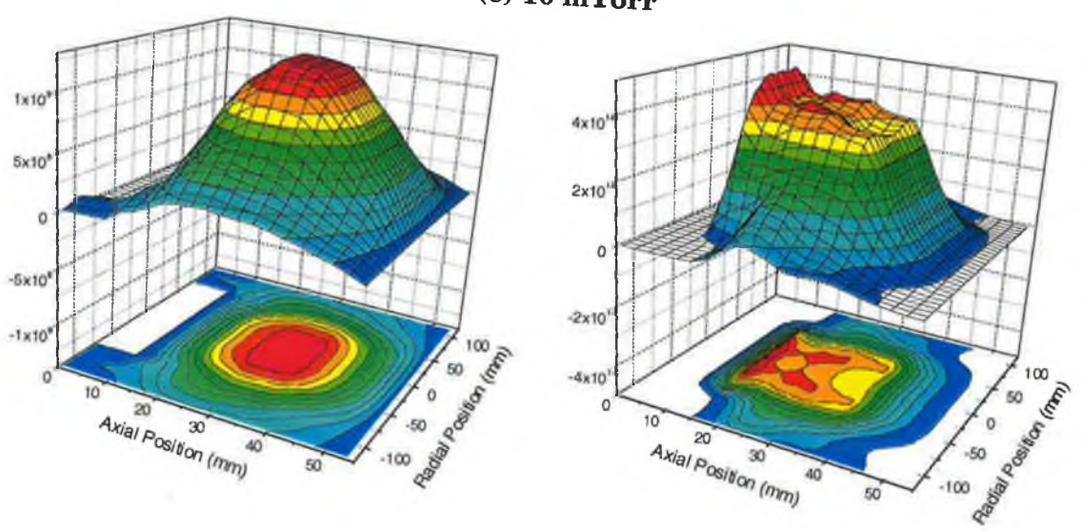

Figure 5.10 (continued): Density (left) and ionisation profiles (right) for argon at 5 Watts.

5.4.2 High Discharge Power

At the higher power setting, the discharge is in a regime of operation where secondary electrons should play a larger role. There is a distinct increase in ionisation at both the powered and ground sheath edges as well as in the discharge bulk. Also very apparent are the off-axis density peaks at 300, 100 and 50 mTorr see figure 5.11 (a), (b) and (c). The enhancement of ionisation in front of the electrodes may be attributed in part to secondary electron emission from the electrodes and an enhancement of sheath heating at low pressures due to the increase in the rf field at the sheath edge. At the higher pressures, the ionisation would be expected to still be concentrated at the sheath edges.

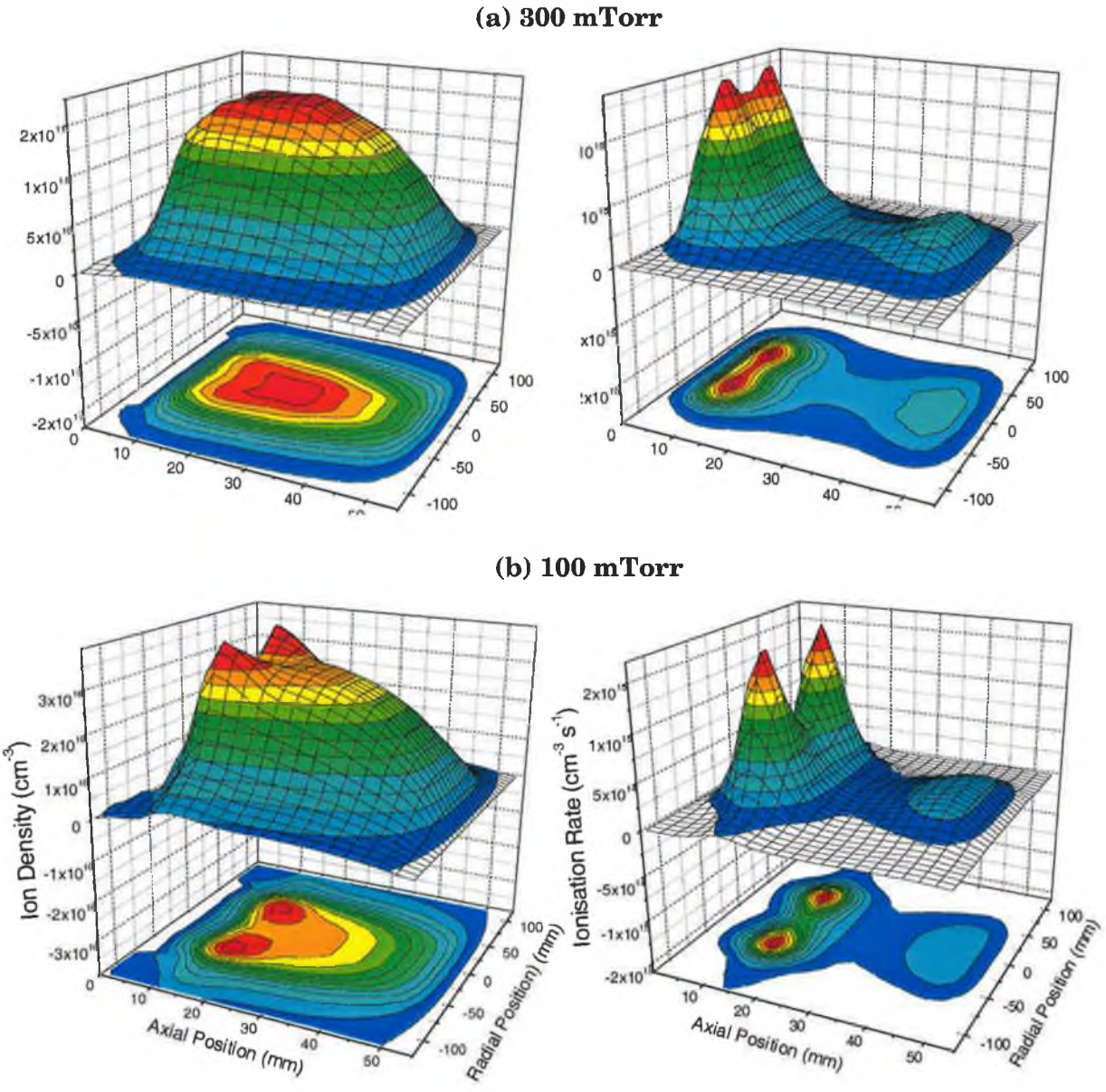

Figure 5.11: Density(left) and ionisation (right) profiles in argon at 100 Watts. The units on the y axes are cm^{-3} and $cm^{-3}\ s^{-1}$ respectively.

(c) 50 mTorr

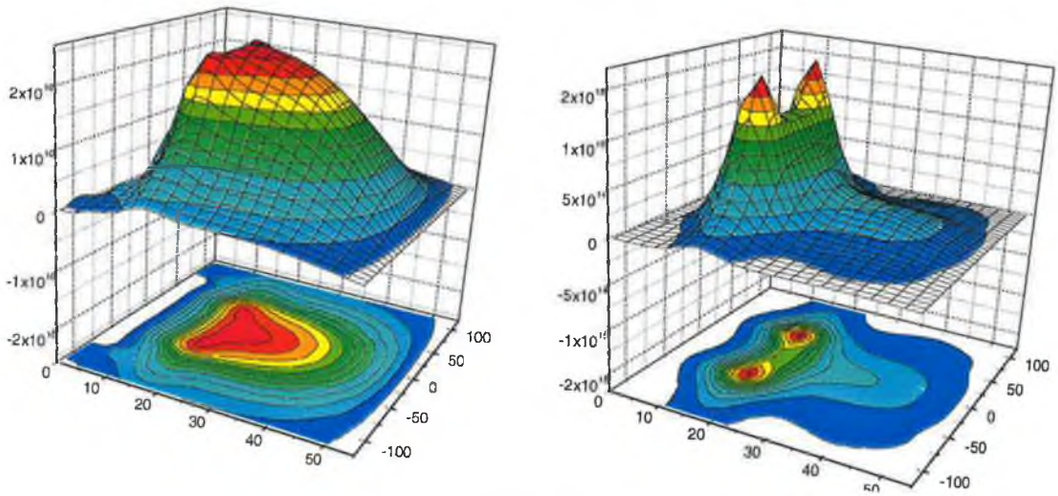

(d) 25 mTorr

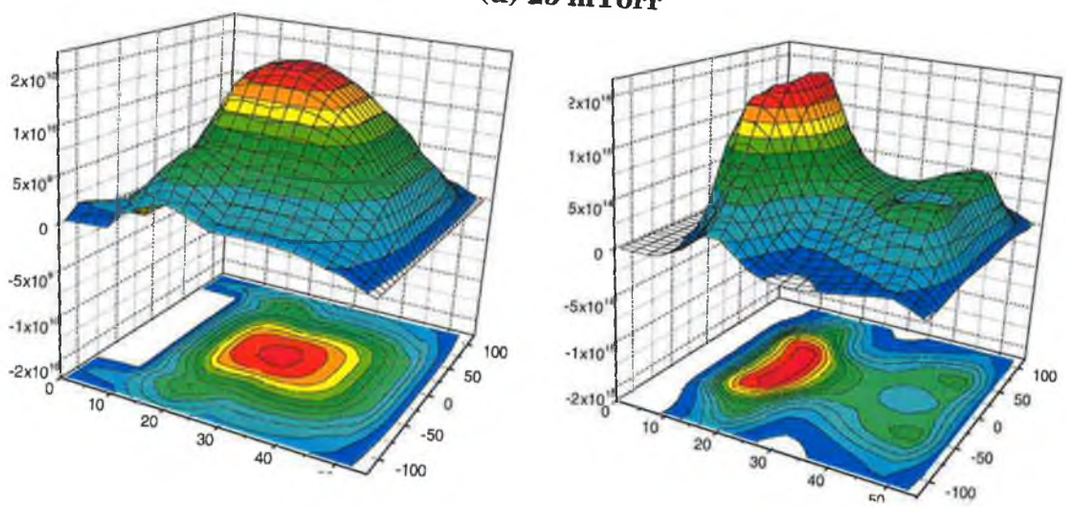

(e) 10 mTorr

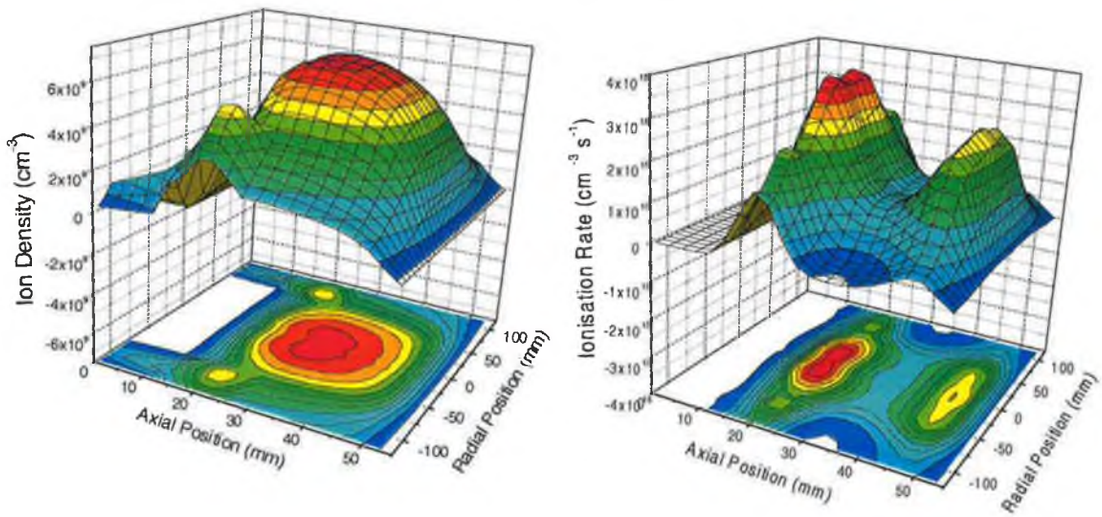

Figure 5.11(continued): Density(left) and ionisation (right) profiles in argon at 100 watts. Vertical axes are in cm^{-3} and $cm^{-3}\ s^{-1}$ respectively.

Experimental measurements of the radial density profile in a GEC reactor have been made using a Langmuir probe by Overzet and Hopkins [2] and by microwave interferometry by Lukas *et al* [4]. Here, the measurements were restricted to the higher pressure (>100 mTorr) range and the off-axis density peaks were just inside the powered electrode radius, in good agreement with figures 5.10 (a) and (b). The reason given in [2] for these peaks was an enhancement of the electric field strength at the electrode edge due to the proximity of the ground shield. This explanation is further supported by references [8,9].

A quantitative explanation for these off-axis peaks may lie in the computer simulations that allow observation of the field intensity in the presence of a plasma. Boeuf and Pitchford used a two dimensional numerical fluid model for argon in the GEC reference reactor geometry [12]. Alas, the lowest pressure examined in this work is also 100 mTorr, above the limit where collisionless heating does not play a significant role in the discharge. However, at high pressures (>100 mTorr) favourable comparisons were drawn between these simulation results and those of reference [2]. A further parametric study of the off-axis density maxima was performed. Increasing the rf voltage enhanced the off-axis density. A comparison of figures 5.10 and 5.11 indicate that this is also true of this discharge. However, the authors concluded that an enhanced radial electric field was not responsible for the off-axis peak in density as no such structure was observed when the electrode gap was increased [12]. These measurements show that off-axis peaks do exist in gaps larger than 2.5 cm (the GEC cell gap). It has already been mentioned that an enhancement of the electric field has been measured in a GEC cell in a helium plasma [9]. It is concluded that an enhancement in the radial electric field is a plausible explanation for the radial non-uniformity in density, though the electric field distribution in the chamber at low pressures is not yet clear.

Measurement of off-axis density peaks have also been noted by Lymberpoulos and Economou [13] and attributed to a radial electric field that develops as the more mobile electrons diffuse into the surrounding chamber from between the two electrodes. Away from the edge of the electrode the electric field is directed axially and heats the electrons near the plasma-sheath interface. This is consistent with the measured increase in electron energy near the powered electrode sheath (see section 5.2). Near the electrode edges the electrons acquire extra energy due to the increased radial field, so an increase in the measured electron energy would be expected near the electrode

edge. Measurements of the average electron energy shown in figure 5.12 for the 300 mTorr discharge show that the average energy does increase in the vicinity of the edge of the powered electrode.

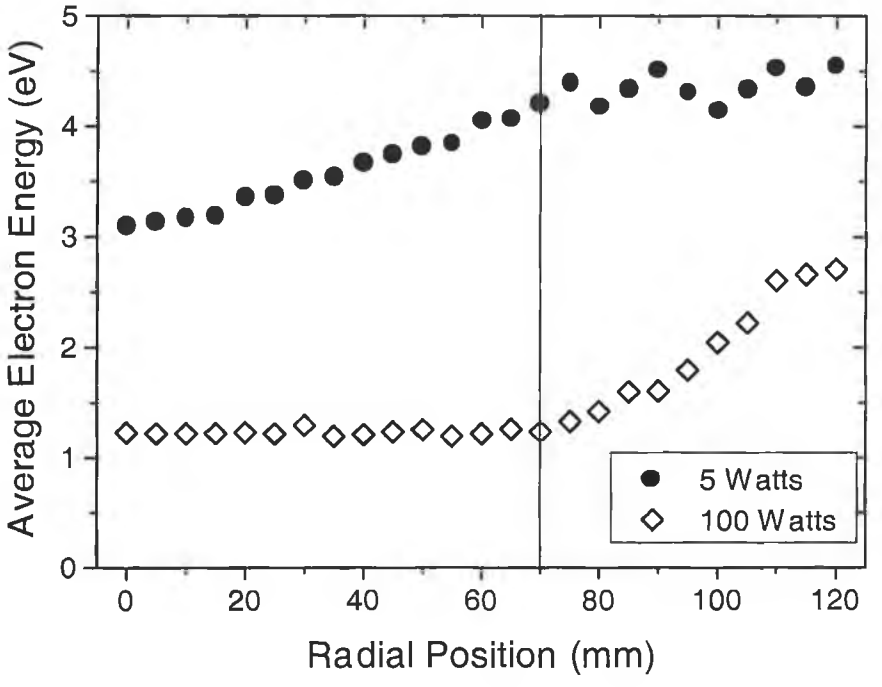

Figure 5.12: The variation in average electron energy with radial position at 300 mTorr.

This increase in electron energy has implications for the diffusion simulation as the ambipolar diffusion coefficient used here is directly dependent on electron energy, see equation 5.2.1 (T_e is the average electron energy measured by the probe). The analysis algorithm described in Chapter 4 assumes a uniform diffusion coefficient throughout the plasma. The effect of including the increasing electron energy in the axial and radial directions would be to enhance the ionisation profiles in the regions of higher energy i.e. at the axial and the radial boundaries. The overall result of this would be to increase the total generation rate derived from the density profiles. This is shown in section 5.5.3.

5.5 Particle Balance

Figure 5.13 shows the total number of ions generated per second under the conditions presented in figures 5.10 and 5.11. The generation rate increases at lower pressure, this is consistent with a higher average electron energy measured in the discharge bulk at low pressures.

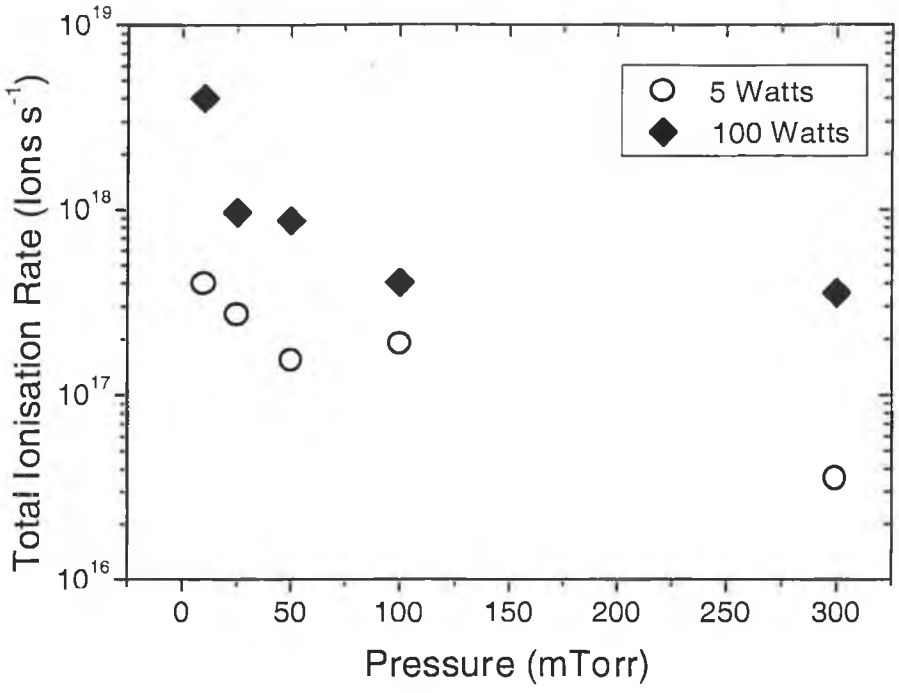

Figure 5.13: Total number of ions generated per second versus gas pressure.

5.5.1 Uniform Discharge Model

Using the chamber dimensions and the measured plasma parameters, a simple particle balance calculation may be used to estimate the number of charged particles created per second by [14]

$$K_{iz} n_e n_g V = u_B n_s A_{eff} \qquad 5.5.1$$

where K_{iz} is the ionisation rate constant, n_e is the electron density, n_g is the neutral gas density, u_B is the Bohm velocity, n_s is the density at the sheath edge, V is the discharge volume and A_{eff} is the effective loss area i.e. the area of the chamber walls plus the electrodes.

Tables 5.1 (a) and (b) contain the experimental generation and calculated loss rates. The value of n_s used is the ion density measured closest to the sheath by the probe. A large discrepancy exists between experiment and calculation, particularly at 300 mTorr. The significant discrepancy in the experimental values may be attributed to several factors. Equation 5.5.1 is a very simple expression for particle balance. It assumes a uniform density distribution in a cylindrical plasma volume. The geometry of the system is considered on obtaining the generation rate from experimental data but a simple cylinder is used in the calculation. At 300 mTorr, the experimental value is derived from density measurements that are likely to be underestimated by a factor of two (see Chapter 3). This would result in an experimental underestimation of the

generation rate and is probably part of the reason why the experimental and calculated values are so dissimilar at 300 mTorr.

(a)

Pressure mTorr	Ionisation Ions $m^{-3}s^{-1}$ (Experiment)	Ionisation Ions $m^{-3}s^{-1}$ (Calculated)
300	$3.54x10^{16}$	$2.6x10^{18}$
100	$1.87x10^{17}$	$1.92x10^{18}$
50	$1.53x10^{17}$	$3.12x10^{18}$
25	$2.7x10^{17}$	$3.11x10^{18}$
10	$3.9x10^{17}$	$1.5x10^{18}$

(b)

Pressure (mTorr)	Ionisation Ions $m^{-3}s^{-1}$ (Experiment)	Ionisation Ions $m^{-3}s^{-1}$ (Calculated)
300	$5.34x10^{17}$	$7.9x10^{19}$
100	$4.0x10^{17}$	$3.3x10^{19}$
50	$8.64x10^{17}$	$3.1x10^{19}$
25	$9.6x10^{17}$	$1.48x10^{19}$
10	$4.0x10^{18}$	$7.7x10^{18}$

Table 5.1: Comparison of experimental and calculated values for the generation rate at (a) 5 watts and (b) 100 watts.

5.5.2 Non Uniform Discharge Model

It is clear from the spatial density measurements that the plasmas studied here are not well approximated by a flat density distribution, particularly at higher pressures. In Chapter 4, the density profile in one and two dimensions for a cylindrical geometry was obtained for several analytic solutions. Rewriting the result for the 2-D nonuniform case

$$n_i(r,z) = n_0 J_0\left(\frac{\chi_{01} r}{R}\right)\sin\left(\frac{\pi z}{Z}\right) \qquad 5.5.2$$

where n_0 is the experimentally measured ion density, J_0 is the first order Bessel function and $\chi_{01}=2.405$ is the first zero of the Bessel function. The overall particle balance in a cylinder is given by [14]

$$\oint_S \Gamma_i \cdot dS = K_{iz} n_g \int_0^Z \int_0^R n_i 2\pi r dr dz \qquad 5.2.3$$

where Γ_i is the particle flux. Substituting equation 5.2.2 into the right hand side of this and integrating gives the generation rate. Values for this are compared with experimental values and those of the uniform model in table 5.2 (a) and (b).

5.5.3 Effect of the Temperature Gradient

A considerable source of error in the experimental analysis is that the estimation of the diffusion coefficient assumed a constant bulk electron temperature (as was measured in the centre of the discharge). In fact the spatially resolved measurements have indicated significant increases in electron energy close to the sheaths and the edges of the electrode. Hence the ionisation rate should increase in these regions. The difference between the bulk electron energy and the maximum electron energy was between a factor of 0.5 and a factor of 4. Figure 5.14 shows a two dimensional electron energy profile as was measured in a 10 mTorr discharge at 100 watts. Variations in the energy measurement were similar for many of the conditions examined. The increase in electron energy near the edge of the powered electrode sheath (at z~13 mm) coincides with the minimum in ion density that was shown in section 5.3 for the same conditions. This increase in energy may be attributed to an increased electric field in this region and is most evident at 10 mTorr and 25 mTorr.

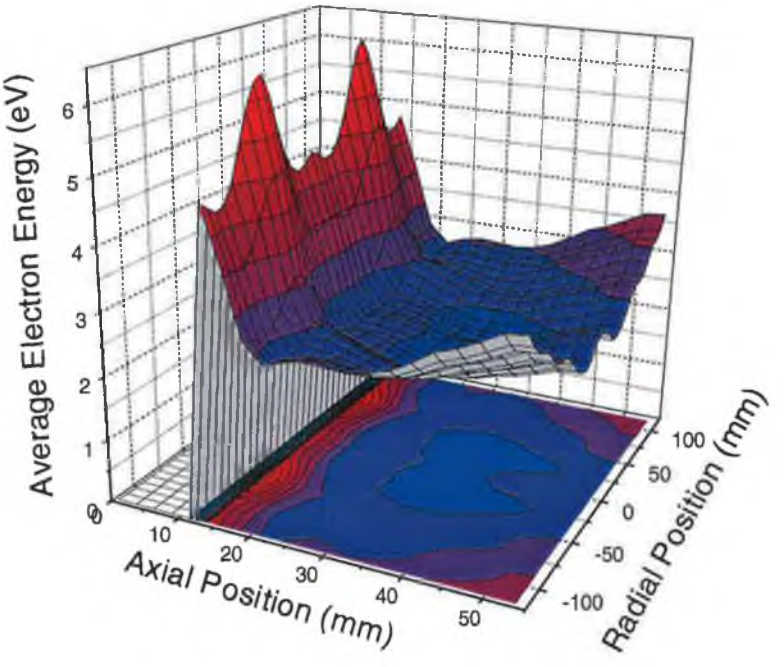

Figure 5.14: Surface plot of average electron energy in argon at 10 mTorr, 100 watts.

An increase in generation rate is observed when the spatial variation of electron energy is taken into account in the analysis algorithm. Table 5.2 (a) and (b) show an increase in the experimental ionisation rate (of approximately 20 %) when the electron energy variation is taken into account. A comparison of tables 5.1 (b) and 5.2 (b) shows that the ionisation rates increase significantly for the 100 watt data. This is due to the larger energy gradients present in the high power plasmas. Table 5.2 also shows the generation rates calculated using the nonuniform model. At 5 watts, the nonuniform model agrees more closely with the experimental value at 10 mTorr only. At higher pressures, none of the measured density profiles resemble a cosine so this nonuniform model would not be expected to apply here. At 100 watts, the density profiles in this case are more symmetric. By including the effect of the varying electron energy better agreement with the uniform particle balance calculation is observed (Table 5.2 (b)). In this case, the uniform calculation is a better approximation due to the almost uniform density profile measured along the discharge axis.

(a)

Pressure (mTorr)	**Ionisation Ions $m^{-3}s^{-1}$ (Experiment)**	**Ionisation Ions $m^{-3}s^{-1}$ (Nonuniform)**	**Ionisation Ions $m^{-3}s^{-1}$ (Uniform)**
300	$6.5x10^{16}$	$9.84x10^{19}$	$2.6x10^{18}$
100	$1.8x10^{17}$	$3.25x10^{19}$	$1.92x10^{18}$
50	$1.96x10^{17}$	$9.8x10^{18}$	$3.12x10^{18}$
25	$3.83x10^{17}$	$5.72x10^{18}$	$3.11x10^{18}$
10	$4.75x10^{17}$	$1.19x10^{18}$	$1.5x10^{18}$

(b)

Pressure (mTorr)	**Ionisation Ions $m^{-3}s^{-1}$ (Experiment)**	**Ionisation Ions $m^{-3}s^{-1}$ (Nonuniform)**	**Ionisation Ions $m^{-3}s^{-1}$ (Uniform)**
300	$8.8x10^{17}$	$6.84x10^{20}$	$7.9x10^{19}$
100	$1.04x10^{18}$	$7.18x10^{19}$	$3.3x10^{19}$
50	$1.37x10^{18}$	$2.4x10^{19}$	$3.1x10^{19}$
25	$2.33x10^{18}$	$1.6x10^{19}$	$1.48x10^{19}$
10	$6.46x10^{18}$	$1.67x10^{18}$	$7.7x10^{18}$

Table 5.2: Comparison of experimental and calculated values for the generation rate at (a) 5 Watts and (b) 100 Watts. The experimental values take the spatial variation of electron energy into account.

5.6 Concluding Remarks

This chapter detailed the spatial characterisation of an argon plasma over a range of pressures. The ionisation profiles were determined from the two dimensional density profiles, allowing some interesting features to be examined. Off axis peaks in the density profiles were measured. These are attributed to a perturbation of the electric field in the vicinity of the edge of the powered electrode edge due to the presence of the ground shield. This results in an enhancement of electron heating and consequently the ionisation rate in that region. Increasing the rf power enhances this effect.

Higher pressure plasmas exhibit asymmetric density distributions, corresponding to an ionisation distribution that is concentrated at the edge of the powered electrode sheath. At low powers and high pressures the primary heating mechanism is therefore ohmic sheath heating.

As the pressure is decreased, ionisation occurs to a greater extent in the bulk and at the ground sheath edges as the ionisation mean free path increases. The 10 mTorr, low power discharge exhibits the most uniform ionisation profile. In this instance the electron energy measurements indicate heating at the sheath edges. However, the ionisation mean free path at 10 mTorr is of the order of 30 mm, so significant ionisation in the discharge centre is measured.

The ionisation profiles at higher powers indicate a considerable increase in ionisation near the sheath edges for all pressures settings. At 300 and 100 mTorr, there is an enhancement of the ionisation at the ground sheath edge and in the discharge bulk. This is attributed to an increase in secondary electrons emitted from both electrodes, though the actual extent to which secondaries contribute to ionisation cannot be determined from these measurements. At the lower pressures, the ionisation increases at the sheath edges and in the bulk. At 10 mTorr and 25 mTorr, a minimum in density and maximum in energy are measured near the powered sheath edge. This would be consistent with an increase in the electric field in this region. Further work is required to investigate if a significant field exists in this part of the discharge.

The uniform and nonuniform particle balance equations may not always accurately represent the generation rate in this discharge due to simplifying assumptions that are rarely applicable. The larger discrepancy at 300 mTorr is also attributed to the experimental underestimation of ion density that results in an underestimation of the experimental ionisation rate.

Comparison of the total number of ions generated and simple particle balance calculations resulted in a difference of at least an order of magnitude. Including the effect of the electron energy variation in the calculation of the diffusion coefficient resulted in a significant increase in the experimental generation rate. This correction was found to be important at high discharge powers. The 'flattening' of the ion density profile at high discharge power resulted in better agreement with the uniform model generation rate in terms of the particle balance. The nonuniform model was found to be most applicable in the low-pressure, low power discharge.

References

[1] T. Kitajima, M. Izawa, N. Nakano and T. Makabe, J. Phys. D: Appl. Phys, 30, 1783-1789, (1997).

[2] L. J. Overzet and M. B. Hopkins, Appl. Phys. Lett, 63(18), 2454, (1993).

[3] G. Oelerich-Hill, I. Pukropski and M. Kujawka, J.Phys.D: Appl. Phys. 24, 593-601, (1991).

[4] Ch.Lukas, V. Schulz-Von der Gathen and H. F. Dobele, Plasma Sces. Sci Technol., 8, 94-99, (1999).

[5] D. Vender, W. W. Stoffels, E. Stoffels, G. M. W Krosen and F. J. de Hoog, Phys Rev E, 51(5), 2436, (1994).

[6] Y. Raizer and M. N. Schneider, *Gas Discharge Physics*, Springer-Verlag, (1991).

[7] S. C. Brown, *Basic Data of Plasma Physics*, AIP Press, New York, (1994).

[8] J. Pender, M. Buie, T. Vincent, J. Holloway, M. Elta and M. Brake, J. Appl. Phys. 74(5), 3590, (1993).

[9] U. Czarnetski, D. Luggenholscher and H. F. Dobele, Plasma Sces. Sci. Technol., 8, 230-248, (1999).

[10] M.J. Kushner, IEEE Trans. Plasma Sci., PS-14, 188, (1986).

[11] J. D. Passchier and W. J. Goedheer, J. Appl. Phys. 74(6), 3744, (1993).

[12] J. P. Boeuf and L. C. Pitchford, Phys. Rev. E 51(2), 1376, (1994).

[13] D. P. Lymberpoulos and D. J. Econmou. J. Res. Natl. Inst. St. Technol., 100(4), 473, (1995).

[14] M.A. Lieberman and A.J. Lichtenberg, *Principles of Plasma Discharges and Materials Processing*, Wiley Interscience, (1994).

Chapter 6

The Electron Energy Probability Function

Introduction

The importance of accurate measurement of the electron energy probability function (EEPF) was discussed in Chapters 2 and 3. It is common practice to define the slope of the log of the probe current versus the probe potential as the 'electron temperature'. Since the electron energy probability function is not Maxwellian in capacitive rf plasmas the concept of electron temperature is not fully applicable. The electron temperature deduced from the probe *IV* characteristic can characterise no more than the mean electron energy and can only be used for calculations of excitation and ionisation rates if the EEPF is Maxwellian.

This chapter discusses spatially-resolved measurements of the EEPF in argon for several regimes of operation. Comparisons are drawn between bulk and near-sheath measurements. The rate coefficients for ionisation are calculated using the measured EEPF and the argon cross section for ionisation.

6.1 Measurement of Particle Density

Three methods of determining particle density are possible using a Langmuir probe; from the ion saturation current, the electron saturation current and the integral of the measured EEPF. In this thesis the second method is ruled out because the electron saturation region of the probe *IV* curve is not always well defined. However, the ion saturation current is well defined and constant for probe potentials a few volts below the floating potential (see figure 2.6) so the measured particle densities presented are deduced from this. Godyak has stated that the integral of the EEPF is a more accurate measure of the electron density [1]. A comparison of electron and ion densities measured from the ion saturation current and electron densities measured from integrating the EEPF are shown in figure 6.1. Over a wide range of input powers, there is a factor of two difference in the electron and ion densities determined from the relevant saturation currents. However, the electron density measured from the EEPF agrees very well with the ion density measurement, so reinforcing our belief that the ion

density measurement is a more accurate reflection of the charged particle density in the plasma.

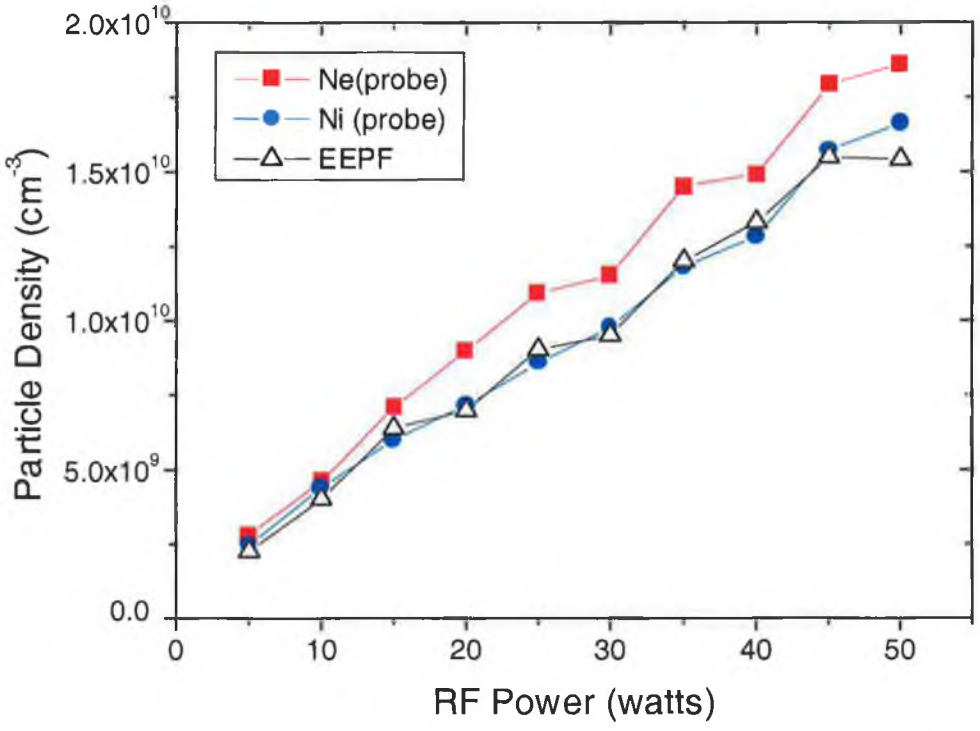

Figure 6.1: Ion and electron density measured from the Langmuir probe characteristic compared with electron density from the EEPF. Measurements are made in the centre of a 25 mTorr argon discharge.

6.2 Low Discharge Power

Spatially resolved probe measurements were made along the axis of a 5 watt argon plasma in system 2. The discharge gap was 55 mm as before.

Results for two neutral pressures, 10 mTorr and 300 mTorr, are presented in this section. These are chosen so as to be on both sides of the transition from collisionless sheath to ohmic heating. The EEPFs for 10 mTorr exhibit the bi-Maxwellian structure typical of sheath heating. Figure 6.2(a) shows a surface plot of the EEPFs measured across the discharge gap. A plot of three EEPFs shown in figure 6.2(b) shows that they almost coincide over the measured energy range. The EEPFs in 6.2(b) are plotted versus total energy, the kinetic plus the ambipolar potential energy. The ambipolar potential that arises in the plasma due to the charge gradient is plotted for the 10 mTorr case in figure 6.3. In this case there exists a potential well that effectively confines low energy electrons in the middle of the discharge.

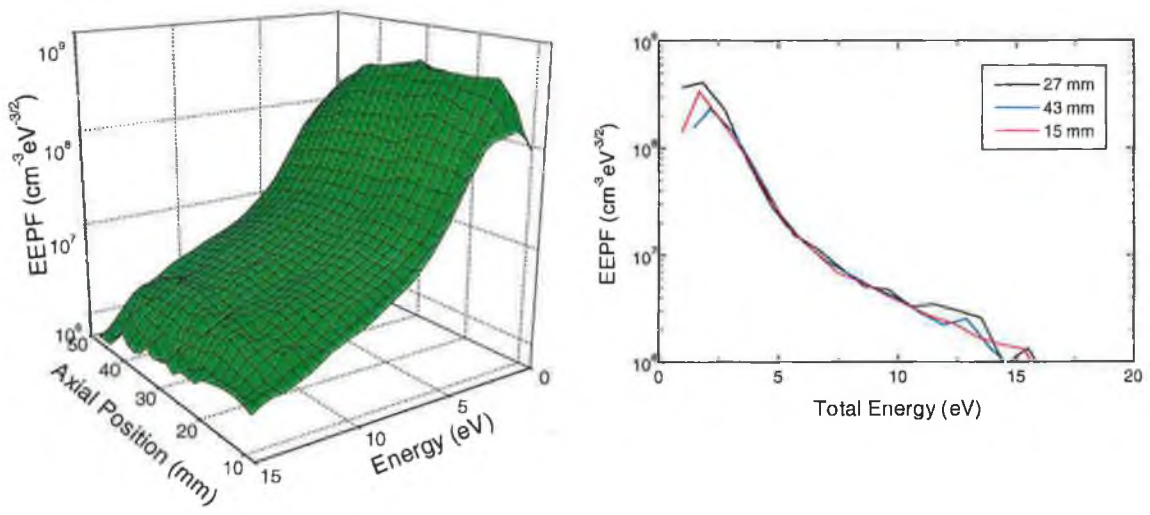

Figure 6.2: (a) Surface Plot of the EEPF in the axial direction and (b) selected EEPFs for argon at 25 mTorr, 5 watts.

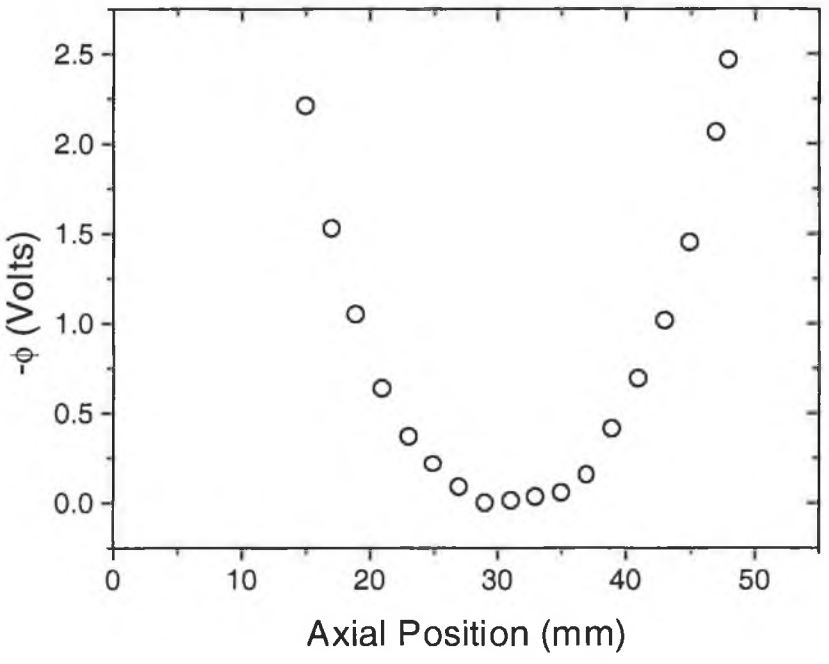

Figure 6.3: Plot of the ambipolar potential along the discharge axis.

The EEPFs shown in figure 6.4(a) are for the 300 mTorr plasma. They are Druyvesteyn shape typical of a collisional discharge. In this case, the asymmetric density distribution shown in figure 5.7 for these conditions is also evident in the spatial evolution of the EEPF. Figure 6.4(b) shows that the EEPFs (again *versus* total energy) coincide at low energies only. The EEPF measured closest to the powered electrode shows more high energy electrons than in the midplane of the discharge.

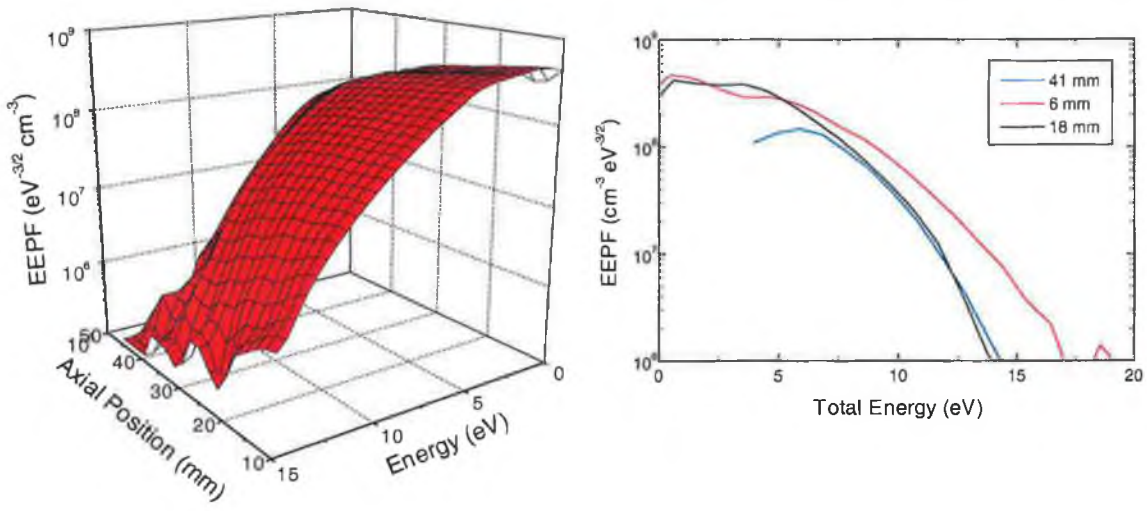

Figure 6.4: (a) Surface Plot of the EEPF in the axial direction and (b) selected EEPFs for argon at 300 mTorr, 5 watts.

The nonlocal approach proposed by Bernstein and Holstein has recently been used to describe the electron behaviour in rf plasmas [2,3]. The EEPFs measured at 10 mTorr (figure 6.2) are typical of that measured in a nonlocal regime, where the electron distribution function is not in equilibrium with the local electric field [3]. The nonlocal regime is applicable if the electron energy relaxation length is comparable to or larger than the characteristic chamber dimension L/π (1.75 cm in this case) [3,4]. The electron energy relaxation length λ_ε is given by [4]

$$\lambda_\varepsilon = \sqrt{\lambda\lambda^*} \qquad 6.2.1$$

where λ and λ^* are the mean free paths for elastic and inelastic collisions, respectively. Equation 6.2.1 is applicable for diffusion-like electron motion and little anisotropy in the energy distribution function [4,5]. With the highest electron energy of 15 eV and a pressure of 10 mTorr, λ_ε has a value of the order of 9 cm. A significant feature of the 10 mTorr, 5 watt discharge is that although the electron heating occurs at the sheath edges (see figure 5.2), much of the ionisation occurs in the plasma bulk where the rf and ambipolar fields are at a minimum or zero (figure 5.10(e)). This may be attributed to the nonlocal electron kinetics where the EEPF is insensitive to the electric fields in the discharge. The concomitance of the EEPF along the discharge axis confirms the uniform ionisation along the axis, a quantitative discussion of this will be presented in section 6.4.

The EEPFs at 300 mTorr in figure 6.4(b) exhibit characteristics of both nonlocal and local behaviour. At low energy the (normalised) EEPFs coincide but at higher energies the EEPF measured near the powered electrode indicates an increase in

electron temperature (where the rf field is larger). This is consistent with the higher average electron energy measured near the powered electrode at 300 mTorr (figure 5.3).

The simultaneous local and nonlocal characteristics of the EEPF are due to the difference in electron energy relaxation length for low and high-energy electron groups. The low energy group is affected only by elastic collisions with neutrals and electron-electron collisions. Here, the typical energy relaxation length for electrons at less than 11.55 eV is of the order of 1 cm. The high-energy electrons are affected by inelastic collisions such as excitation and ionisation; the energy relaxation for 20 eV electrons is 3 mm. Hence, the 300 mTorr EEPFs near the sheath are local functions of the electric field. As the EEPF determines the ionisation balance, the ionisation and plasma density profiles are expected to have maxima at or near the sheath region. This is clearly the case in Chapter 5, figure 5.10(a).

6.3 High Discharge Power

The transition from low current to high current discharges was shown in Chapter 3. Spatially resolved EEPF measurements of a 300 mTorr, 100watt discharge are shown in figure 6.5. Nearer to the powered electrode an enhancement of the high-energy tail is measured-see figure 6.6. This tail in the EEPF is due to secondary emission from the electrodes as a result of ion acceleration through the large voltage (typically a few hundred volts) across the sheath.

Figure 6.6 shows that there are less high energy electrons in the discharge mid plane. This is expected as ionisation occurs mainly at the plasma-sheath boundary with little or none in the middle of the discharge. A distinguishing feature of these EEPFs is the structure measured near the sheath edge, see figure 6.5. This structure is also evident in the low pressure, high power discharges. As the sheath edge is not stationary in space, it is possible that, during a measurement, the compensation electrode on the probe is not immersed in the plasma at all times during the rf cycle. This would result in distortion of the probe *IV* characteristic. It is therefore possible that the local potential modulation of the plasma at the sheath edge results in the structure in the EEPF.

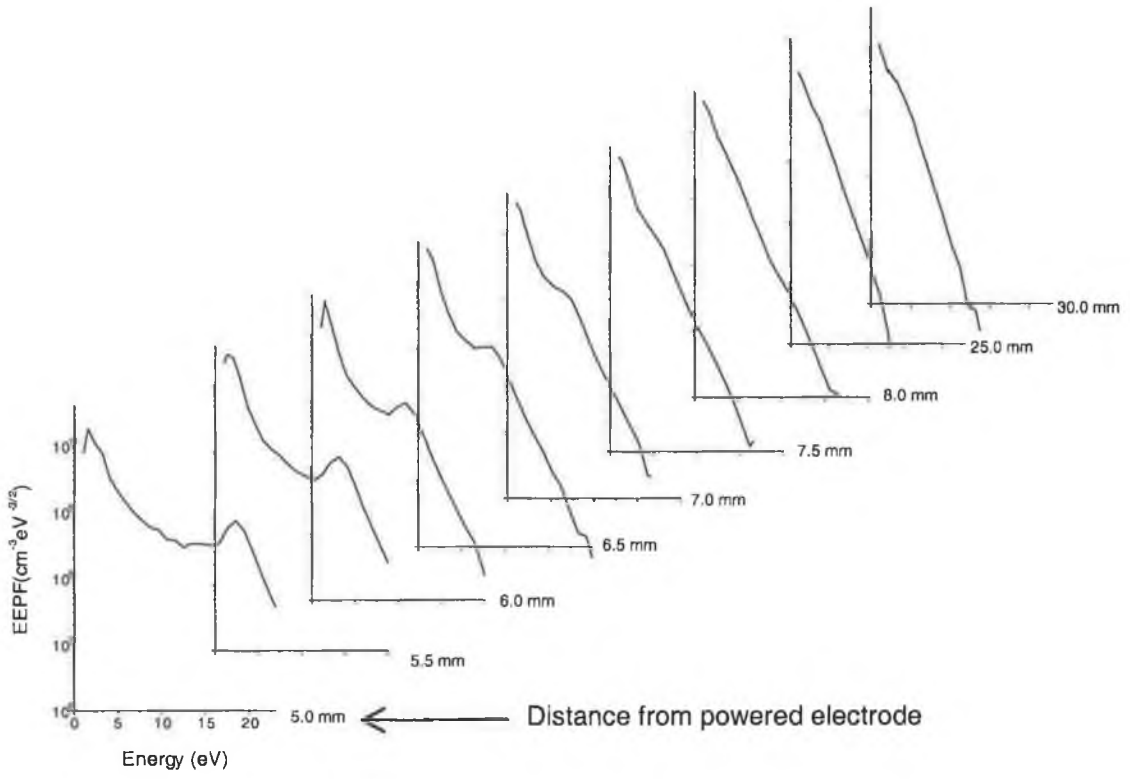

Figure 6.5: EEPFs measured in 300 mTorr argon discharge at 100 watts.

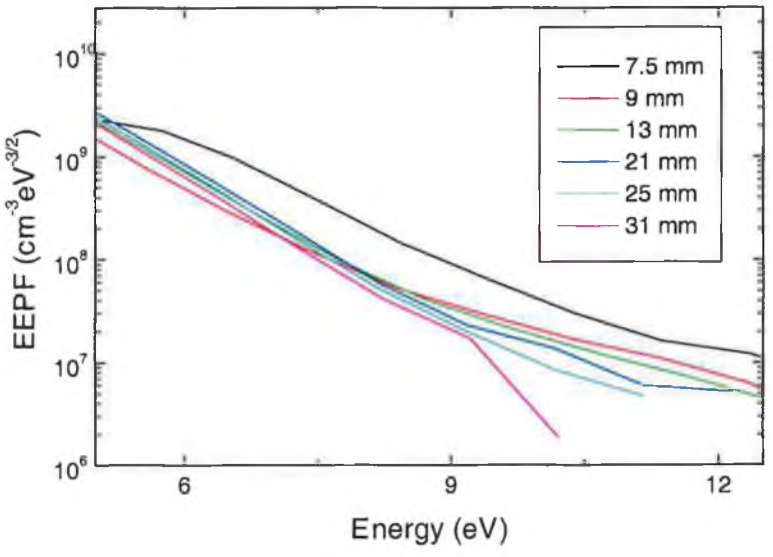

Figure 6.6: Close-up of EEPFs measured in 300 mTorr argon at 100 watts. Legend denotes distance from powered electrode.

Measurements by Raymont and Twiddy have indicated similar structures in a low pressure mercury vapour discharge [6]. Near the cathode, a second peak in the EEPF was measured at 14 eV. The peak was not evident a short distance from the cathode and was attributed to a group of fast electrons accelerated in the cathodic part of the discharge.

Other measurements by the same authors yielded similar structures in the presence of standing striations [7]. Electron distribution functions measured by

Alexandrov *et al* n a helium discharge positive column at 300 mTorr show a second peak at 20 eV close to the cathode [8]. Again, an EEDF measurement further from the cathode shows no second peak. The authors concluded that the second peak was due to the presence of a group of secondary electrons.

We rule out striations as a source of the EEPF structure because they were not present in the discharges examined. Measurements in a dc column are not susceptible to rf interference in the way that measurements made here are. However, time-resolved probe measurements made by Ruzic and Wilson in a capacitive rf discharge have shown evidence of an electron beam component at the plasma potential minima and maxima [9]. A comparison of measurements near to the powered electrode and at the discharge mid plane showed a degradation of the beam components as the probe was moved away from the powered electrode.

The near sheath structure was not evident in discharges operating at low powers so the possibility remains that it has some physical explanation other than distortion to the probe characteristic. While rf distortion is still a likely explanation, the possibility of an electron beam should not be ruled out, at least at low pressures. Clearly, further study is required to resolve this issue.

6.4 Calculation of Rate Coefficients

The collision frequency and rate constants for ionisation may be calculated by integrating over the electron velocity distribution function. The collision frequency, ν and rate constant, K are given by [10]

$$\nu_{iz} = n_g K_{iz} = n_g \langle \sigma(v_R) v_R \rangle_{v_1 v_2} \qquad 6.4.1$$

$$= n_g \int d^3 v_1 d^3 v_2 f_1(v_1) f_2(v_2) \sigma(v_R) v_R \qquad 6.4.2$$

where the distributions are normalised, v_1 and v_2 are the velocities of the incident and target particles respectively and $v_R=|v_1-v_2|$. The subscript *iz* indicates ionisation constants. Consider electron-neutral collisions only. Since the incident particle velocity is much greater than the target (neutral) velocity, $v_R \approx |v_1|$. If the electron distribution is assumed to be a Maxwellian then the rate constant is

$$K_{iz}(T_e) = \langle \sigma_{iz}(v) v \rangle_v \qquad 6.4.3$$

$$= \left(\frac{m}{2\pi k T_e} \right)^{3/2} \int_0^\infty \sigma(v) v \exp\left(\frac{-mv^2}{2kT_e} \right) 4\pi v^2 dv \qquad 6.4.4$$

Where m and T_e are the electron mass and temperature and v is written instead of v_1.

As the measured EEPF is rarely Maxwellian a more general approach is to weight the ionisation cross section with the electron distribution function and to numerically integrate the result. The average electron energy in argon plasmas is of the order of 3 eV but the electrons do have a distribution of energies. The ionisation threshold of argon is 15.76 eV so only the tail of the distribution function and the cross section values near threshold contribute to the rate constant for ionisation.

The Thomson cross section for ionisation is given by [10]

$$\sigma_{iz} = \pi\left(\frac{e}{4\pi\varepsilon_0}\right)^2 \frac{1}{\varepsilon}\left(\frac{1}{\varepsilon_{iz}} - \frac{1}{\varepsilon}\right) \qquad \varepsilon > \varepsilon_{iz} \qquad 6.4.5$$

where σ_{iz} is the cross section and ε_{iz} is the ionisation threshold energy. This expression is an approximation to experimentally determined cross sections [10 and references therein] but it reasonably follows the experimental cross section for argon, ε_{iz}=15.76 eV, so it is used here to calculate the ionisation rate coefficients.

Figure 6.7(a) shows an EEPF measured in the mid plane of the 300 mTorr, 5 watt discharge. A Druyvesteyn curve is fit to this data as shown. The curve is preferentially fit to the 'tail' of the EEPF as this is most relevant to the ionisation. This fit is normalised, multiplied by the ionisation cross section (shown in part (b) of figure 6.7) and then multiplied by the electron velocity. The result is then numerically integrated to give the rate constant (equation 2.3.27). In the case of a bi-Maxwellian distribution, an exponential is fitted to the tail of the distribution function and the integral calculated in the same manner.

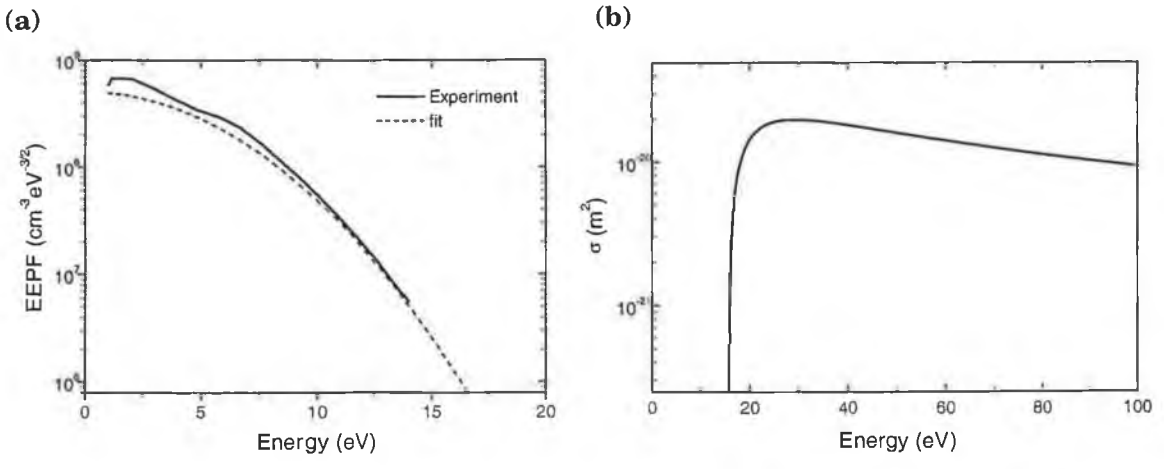

Figure 6.7: (a) Measured EEPF plus analytical fit and (b) ionisation cross section obtained using equation 6.4.5.

The collision frequency is calculated using equation 6.4.1. The particle generation rate, G is considered to be entirely due to ionisation by electron-neutral collisions

$$G = \nu_{iz} n_e \qquad 6.4.6$$

Chapter 4 described a method of calculating the ionisation rate in two dimensions for a range of discharge conditions. This approach does not require knowledge of the ionisation cross sections or the EEDF. The ionisation rate is calculated using the particle density and the diffusion coefficient only. Figure 6.8(a) shows the central axial ionisation distribution (continuous curve) for the 300 mTorr, 5 watt discharge, calculated using this technique. The points plotted are the generation rates obtained using the integration procedure and equation 6.4.6. Excellent agreement between the two quantities is achieved. This supports the analysis algorithm described in Chapter 4 as an accurate method of determining the ionisation profiles. As the integral method only accounts for (electron impact) ground state ionisation, the implication here is that other ionisation processes are not significant. Figure 6.8(b) shows the central ionisation profile of the 10 mTorr, 5 watt data. The agreement here is less good but the trend is the same, a significant ionisation rate is measured along the axis, even though the heating occurs at the sheath edges. The lower calculated value may be due to an uncertainty in the form of the EEDF at higher energies or the neglect of the contribution of other ionisation processes in the calculation. However, it is unlikely that two-step ionisation will occur at low pressures.

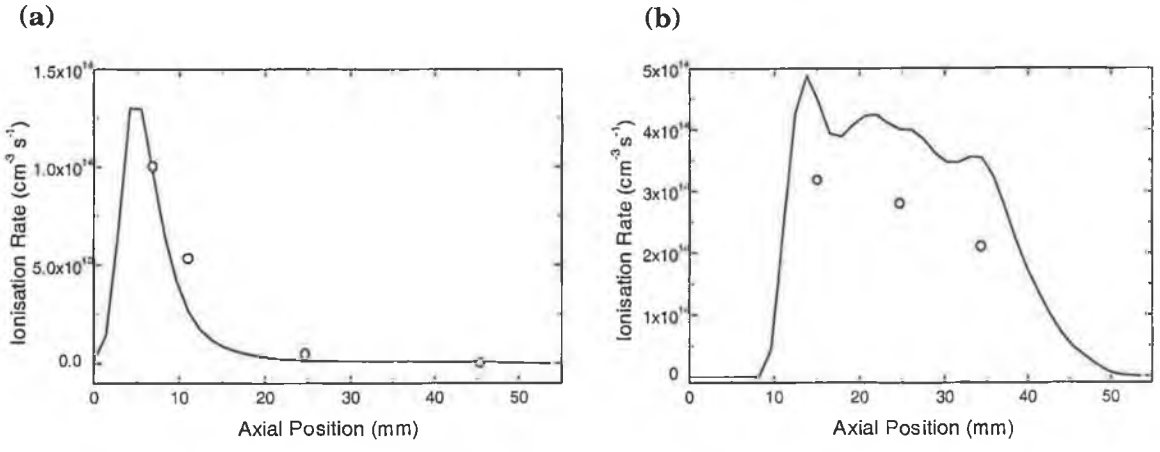

Figure 6.8: Generated and calculated ionisation rate profiles for (a) 300 mTorr, 5 watt and (b) 10 mTorr, 5 watt discharges. Lines are the profiles generated in Chapter 5 and open circles are results of the integration procedure and equation 6.4.6.

The evolution of the EEPF from low discharge power to high discharge power has been shown in Chapter 3 and sections 6.2 and 6.3. The fit used to calculate the rate constant is generated from the tail of the corresponding EEDFs. Figure 6.9 shows the central axial ionisation profiles for (a) the 300 mTorr, 100 watt and (b) 10 mTorr, 100 watt discharges respectively. Again, the open circles indicate the results of the integral calculation.

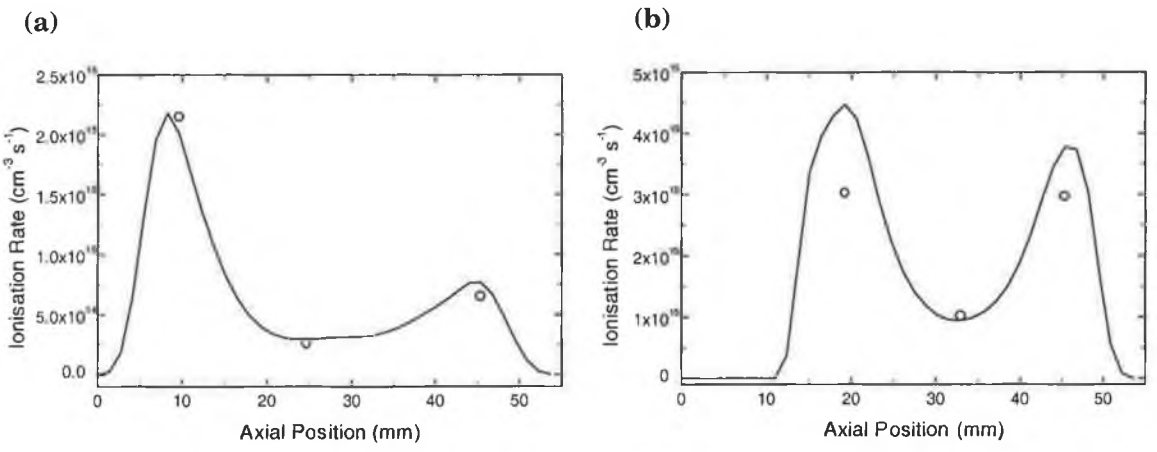

Figure 6.9: Generated and calculated ionisation rate profiles for (a) 300 mTorr, 100 watt and (b) 10 mTorr, 100 watt discharges. Lines are the profiles generated in Chapter 5 and open circles are results of the integration procedure and equation 6.4.6.

Figures 6.8 and 6.9 show the generated ionisation rate profiles assuming a uniform electron temperature. Taking the temperature variation into account results in an increase in the ionisation rate near the powered electrode sheath in most cases. Figure 6.10 shows the same quantities as the previous figure plus the ionisation profile that takes the temperature variation into account. It is clear that again, more realistic comparisons may be made if the temperature variation is taken into consideration.

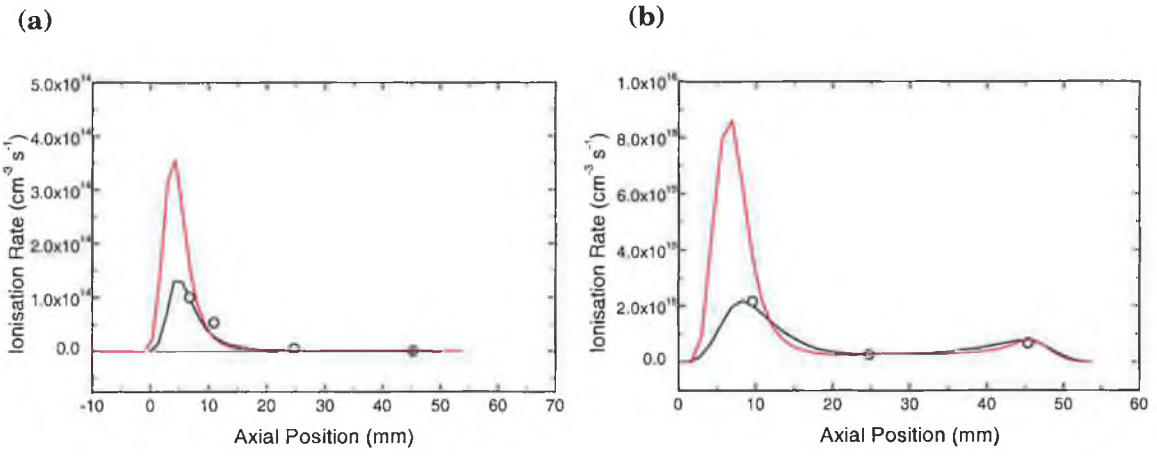

Figure 6.10: Generated and calculated ionisation rate profiles for an (a) 300 mTorr, 5 watt and (b) 300 mTorr, 100 watt discharge. The red line is the adjusted generation rate, other symbols as before.

The conclusion drawn from these comparisons is that the primary production process in capacitive argon rf plasmas studied here is by electron impact ionisation from the ground state. This process is not always the dominant production mechanism in capacitive discharges. Fluid simulations of glow discharges have shown that metastable ionisation is the main electron production mechanism in a 1 Torr argon discharge [11].

Calculation of the rate coefficient using the EEDF is limited since it gives information on electron neutral ionisation only. The main benefit of the new technique developed is that it extracts ionisation rates pertaining to the total ionisation in a discharge. It follows that it could be used to determine when other ionisation processes (e.g. ion-neutral and two step ionisation) are important. This technique would also allow the determination of the temporal evolution of the ionisation rate of pulsed plasmas and discharge afterglows.

References

[1] V. A. Godyak, R. B. Piejak and B. M. Alexandrovich, J. Appl. Phys., 73(8), 3657, (1993).

[2] I. B. Bernstein and T. Holstein, Phys. Rev. 94, 1475, (1954).

[3] V. A. Godyak and R. B. Piejak, Appl. Phys. Letts., 63(23), 3137, (1993).

[4] U. Kortshagen and L. D. Tsendin, Appl. Phys. Letts., 65(11), 1355, (1994).

[5] V. I. Kolobov, D. F. Beale, L. J. Mahoney and A. E. Wendt, Appl. Phys. Letts., 65(5), 537, (1994).

[6] S. W. Rayment and N. D. Twiddy, Proc. Roy. Soc. A, 340, 87-98, (1968).

[7] S. W. Rayment and N. D. Twiddy, Brit. J. Appl. Phys. (J Phys. D), 2(2), 1747, (1969).

[8] V. M. Alexandrov, Ute Flender, N. B. Kolokolov, O. V. Rykova and K. Wieseman, Plasma Sces. Sci. Technol. 5, 523, (1996).

[9] D. N. Ruzic and J. L. Wilson, J. Vac. Sci. Technol. A, 8(5), 3746, (1990).

[10] M. A. Lieberman and A. Lichtenberg, *Principles of Plasma Discarges and Materials Processing*, Wiley, New York, (1994).

[11] D. P. Lymberpoulos and D. J. Economou, J. Appl. Phys., 73(8), 3668, (1993).

Conclusion

A comprehensive investigation of capacitive rf plasmas is completed using several diagnostic methods and simple models of the production and loss processes. The electron heating mechanisms particular to rf plasmas are characterised via measurement of the plasma parameters.

The primary diagnostic used here is a Langmuir probe. This allows spatial characterisation and measurement of the electron distribution function. Improvements in the probe technique are such that detection of high energy electrons in high voltage argon discharges are possible. The probe technique is checked by comparison with the density measurements of a microwave interferometer. It is further validated by comparisons of the probe plasma potential and that of an ion energy analyser. To date, it has been commonly thought that only high energy electrons could be detected by such an analyser. This is due to the neglect of the period of sheath collapse when part or all of the electron distribution may escape the plasma. Operation of the analyser in electron collection mode results in hotter electron temperatures than that measured by the Langmuir probe. It is proposed that this is due to the effect of the sheath on the escaping electron distribution. This process is further complicated by the fact that it is a time-averaged measurement. Further development of the measurement system to allow time-resolved measurements would allow closer study of this process that should lead to an improved understanding of electron characteristics measured with Langmuir probes.

Transitions in heating mechanisms are characterised for a capacitive argon plasma. The evolution of plasma parameters and the EDF in the discharge centre are in good agreement with the experiments and simulations of others. The transition from collisionless sheath heating to ohmic heating is well characterised by the product of the neutral pressure and the electrode gap, provided that the discharge was well confined between the electrodes. The α–γ transition is investigated. Measurement of the EDF allows separation and examination of the electron populations in the discharge. The non-linear behaviour of the current-voltage characteristic during the transition is consistent with the changes in plasma parameters and the estimated sheath width. While it is clear that the α–γ transition is also dependent on neutral pressure and discharge gap, further study is required to investigate if a scaling law similar to that of the previous transition may be applied.

A simple model of diffusion was developed and found to be in agreement with analytic models and experiments. The measured density profiles and the diffusion model are incorporated in a reconstruction technique to determine the ionisation distribution in two dimensions.

To further understanding of the heating mechanisms, a spatial study is presented over a range of neutral pressures. High and low power discharges were investigated in an effort to distinguish the heating mechanisms. Spatial variations in electron energy are consistent with the observed light emission. Measurements indicate that most heating occurs at the sheath edges regardless of the operating pressure or power. The axial density distribution changes from symmetric to asymmetric at high pressures. The radial density profiles indicated off-axis density peaks that are attributed to enhancement of the electric field near the electrode edge.

The evolution of the ionisation rate profiles is determined. For low power discharges, the axial ionisation profile indicates a peak in production at the powered sheath edge. At high pressures this is attributed to ohmic sheath heating. As the pressure is lowered, the ionisation becomes more evenly distributed along the discharge axis. This is due to the large mean free path for ionisation (> 3 cm) at the lowest operating pressure. At high power an enhancement in ionisation at the plasma-sheath edges is attributed to secondary emission from the electrodes, particularly in the higher pressure discharge where the mean free path is low. Disagreement between the ionisation rates obtained from the data and that of particle balance calculations are attributed to both the simplicity of the particle balance and the neglect of the variation in electron temperature in the experimental data. Including the variation in electron temperature is important at high discharge powers where significant temperature gradients exist.

The spatial variation of the electron energy distribution function is examined. The variation in form of the EEPF across the high pressure discharge is attributed to the combination of nonlocal and local electron kinetics. The nonlocal regime is found to be a good model of discharge behaviour at low pressures. Finally, the ionisation rate is calculated by weighting the ionisation cross section with the EDF. The calculated rate is in good agreement with the ionisation profiles obtained from the density measurements. Hence there is now a method of determining the ionisation rate that is independent of EDF measurement and that includes all ionisation processes, not just ground state ionisation by electron-neutral collisions. Use of the two techniques in

tandem to determine the relative contributions of different processes (ion-neutral ionisation, two step ionisation) is now a distinct possibility, provided the relevant cross sections and energy distribution functions are known.